

Metal oxide/carbon hybrid anode materials for lithium-ion batteries

Dissertation
zur Erlangung des Grades
des Doktors der Naturwissenschaften
der Naturwissenschaftlich-Technischen Fakultät
der Universität des Saarlandes

von

Öznil Budak

Saarbrücken

2020

Tag des Kolloquiums: 16. April 2021

Dekan: Prof. Dr. Jörn Erik Walter

Berichtersteller/in: Prof. Dr. Guido Kickelbick
Priv.-Doz. Dr.-Ing. Guido Falk

Vorsitzende/r: Prof. Dr. Tobias Kraus

Akad. Mitarbeiter/in: Dr.-Ing. Frank Aubertin

List of content

Tag des Kolloquiums.....	i
List of content.....	ii
Acknowledgments.....	iv
Abstract	v
Zusammenfassung.....	vi
1. Introduction.....	1
2. Lithium-ion batteries.....	2
2.1. History of lithium-ion batteries.....	2
2.2. Basic working principle of a lithium-ion cell.....	4
2.3. Essential definitions and measurement techniques for batteries.....	5
2.4. Electrolytes.....	7
2.4.1. <i>Liquid electrolytes</i>	7
2.4.2. <i>Organic and inorganic solid electrolytes</i>	10
2.5. Positive electrodes (Cathodes).....	15
2.5.1. <i>Layered family</i>	16
2.5.2. <i>Spinel oxide family</i>	23
2.5.3. <i>Polyanion (Oivine) family</i>	25
2.6. Negative electrodes (Anodes).....	28
2.6.1. <i>Intercalation/insertion type anodes</i>	29
2.6.2. <i>Formation type anodes</i>	34
2.6.3. <i>Displacement type anodes</i>	37
3. Hybrid materials for lithium-ion battery.....	41
4. Overview of the conducted investigations.....	45
5. Results and discussion.....	47
5.1. Vanadium (III) oxide/carbon core/shell hybrids as an anode for lithium-ion batteries.....	47
5.2. Carbide-derived niobium pentoxide with an enhanced charge storage capacity for use as a lithium-ion battery electrode.....	65
5.3. Titanium niobium oxide $Ti_2Nb_{10}O_{29}$ /carbon hybrid electrodes derived by mechanochemically synthesized carbide for high-performance lithium-ion batteries.....	88

6.	Summary, conclusions and outlook	110
	References	113

Acknowledgments

I kindly thank my supervisor Prof. Dr. Guido Kickelbick, who gave me the honor to be his Ph.D. student and enlighten my way of achieving the goal of finishing my doctoral work. I will also always be grateful to Prof. Dr. Eduard Arzt, CEO of the INM, for his continuing support. This thesis was part of the COSH-CDC project (PR-1173/5) by the German Research Foundation (DFG, Deutsche Forschungsgemeinschaft).

I want to express my appreciation to Dr. -Ing. Habil. Guido Falk from Saarland University for his efforts to be the second review for my doctoral work.

During my time of almost four years working at the INM, it has been my pleasure and honor to learn and work with wonderful and incredible people. My special thanks to Dr. Mesut Aslan, my great mentor in the laboratory. I am also grateful to my kind INM colleagues: Dr. Pattarachai Srimuk, Dr. Soumyadip Choudhury, Dr. Choonsoo Kim, Dr. Marco Zeiger, Dr. Simon Fleischmann, Dr. Nicolas Jäckel, Dr. Benjamin Krüner, Dr. Rafael Linzmeyer Zornitta, Anna Schreiber, Hwirim Shim, Robert Drumm, Prof. Dr. Volker Presser. The work would have been difficult without great contributions from master students and intern students (in alphabetical order): Bixian Ying, Declan Siewert, and Jaehoon Choi.

I am also grateful for the opportunity to network and collaborate with great scientists. Particularly, I thank Prof. Dr. Helmut Ehrenberg, one of the pioneers in the energy storage field, for the great discussion. Many thanks also to Dr. Robert Haberkorn from Saarland University, Prof. Bastian J.M. Etzold from the Technical University of Darmstadt, and Prof. Dr. Lars Borchardt from Ruhr-University Bochum for meaningful discussions.

Finally, my life would be impossible if it were not for the unconditional support from my big “Budak” family. I am really thankful to them for teaching me how to overcome unfair points in life. Other enormous thanks, I owe to my life partner for his unconditional support and for showing me the path with his limitless love.

Abstract

The global warming fact has been calling for a change in our current energy infrastructure, which is based on fossil fuels. Lithium-ion batteries (LIBs) are one of our main tools that can serve our society for the desired transition from non-renewable energy sources to renewable ones, for instance, by opening the door of e-mobility with their high energy efficiency. However, the current state-of-art revealed that the electrode architecture has a crucial role in the obtained electrochemical performance of LIBs. In the traditional composite electrodes based on a physical admixture of components, particle-to-particle contact loss occurs between the electrochemically active metal oxide and conductive carbon additive, eventuate in poor electrochemical performance. On the other hand, hybrid electrode architecture provides nanoscopic chemical blending between the metal oxide and carbon, resulting in advanced electrochemical performance due to a continuous conductive network. However, the synthesis techniques for hybrid materials are limited to wet chemical synthesis. Therefore, the aim of this doctoral work is to explore novel synthesis approaches for the metal oxide/carbon hybrid materials and investigate their performances for LIBs with the comparison of their composite counterparts. For that purpose, this dissertation investigates the promising anode candidates for LIBs, namely, V_2O_3 , Nb_2O_5 , and $Ti_2Nb_{10}O_{29}$, which were synthesized from their relatively cheap carbide sources via a new synthesis approach, chloroxidation or simple CO_2 oxidation. The successfully-synthesized carbide-derived metal oxide/carbon hybrids displayed advanced rate handling abilities and cyclic stabilities compared to their counterparts.

Zusammenfassung

Die Tatsache der globalen Erwärmung hat eine Änderung unserer gegenwärtigen Energieinfrastruktur, die auf fossilen Brennstoffen basiert, erforderlich gemacht. Lithium-Ionen-Batterien (LIBs) sind eines unserer Hauptinstrumente, die unserer Gesellschaft für den gewünschten Übergang von nicht erneuerbaren Energiequellen zu erneuerbaren Energiequellen dienen können, indem sie zum Beispiel mit ihrer hohen Energiedichte und Effizienz die Tür zur E-Mobilität öffnen. Der derzeitige Stand der Technik hat jedoch gezeigt, dass die Elektrodenarchitektur eine entscheidende Rolle bei der erzielten elektrochemischen Leistung von LIBs spielt. Bei den traditionellen Verbundelektroden, die auf einer physikalischen Beimischung von Komponenten basieren, tritt ein Kontaktverlust von Partikel zu Partikel zwischen dem elektrochemisch aktiven Metalloxid und dem leitfähigen Kohlenstoffzusatz auf, was zu einer schlechten elektrochemischen Leistung führt. Andererseits bietet die hybride Elektrodenarchitektur eine nanoskopische chemische Mischung zwischen dem Metalloxid und dem Kohlenstoff, was zu einer verbesserten elektrochemischen Leistung aufgrund eines kontinuierlichen leitfähigen Netzwerks führt. Die Syntheseverfahren für Hybridmaterialien sind jedoch auf die nasschemische Synthese beschränkt. Ziel dieser Doktorarbeit ist es daher, neue Syntheseansätze für die Metalloxid/Kohlenstoff-Hybridmaterialien zu erforschen und ihre Leistungen für LIBs im Vergleich zu ihren Verbundwerkstoff-Pendants zu untersuchen. Zu diesem Zweck wurden vielversprechende Anodenmaterialien für LIBs, nämlich V_2O_3 , Nb_2O_5 und $Ti_2Nb_{10}O_{29}$, mit Hilfe eines neuen Syntheseansatzes aus relativ billigen Karbidquellen mittels Chloroxidation oder einfachen CO_2 -Oxidation synthetisiert. Die aus dem Karbid hergestellten Metalloxid/Kohlenstoff-Hybride wiesen im Vergleich zu ihren Pendants fortgeschrittene Ratenhandhabungsfähigkeiten und zyklische Stabilitäten auf.

1. Introduction

Decarbonization of our future energy supply makes it necessary to develop new forms of energy production and storage. After the recognition that global climate change is a great threat to human societies and the planet, the European Council is committed to reducing greenhouse gas emissions to 80-95% compared to 1990 levels by 2050.[1] Furthermore, in 2015, the first legally binding global climate change agreement, the Paris Agreement, was signed to keeping the increase in global average temperature below 2°C, with respect to pre-industrial levels.[2] For the limiting of global climate change resulting from burning fossil energy fuels, renewable energy sources, such as solar, wind, biomass, geothermal, and hydro-power, have played a crucial role. Those renewable energy sources can serve the desire for low-carbon consumption energy production with their potential of zero or almost zero greenhouse gas emissions.[3] However, the intermittent nature of renewable energy sources and high dependency on the geographic location brings along the requirements of energy transmission systems, and as well energy storage systems (ESS). Such systems compensate for energy fluctuation by storing the surplus energy when the electricity supply is higher than demand and releasing the stored energy when demand becomes higher than supply.[4]

The working principle of the electrochemical energy storage systems is based on carrying charge (e.g., electron, ion) between electrodes or only one way from one electrode to another, which is determinative on the rechargeability. Depending on the requirements for the application, either high energy provider batteries or high-power supplier capacitors can be chosen (**Figure 1A**). The charge storage mechanism for capacitors and electrical double-layer capacitors (EDLCs) comprises ion adsorption and desorption, i.e., non-Faradaic process.[5] This process has the characteristic responses in cyclic voltammetry like rectangular shape (**Figure 1B**). On the other hand, the Faradaic reaction, where oxidation or reduction reaction occurs via charge transfer, is the charge storage mechanism for batteries.[6] In this mechanism, the electrochemistry responses show sharp or broad redox peaks (**Figure 1C**).

Lead-acid (Pb-acid) rechargeable batteries possess lead and lead oxide as electrodes and aqueous sulfuric acid or a gel as an electrolyte. Lead-acid batteries still have a large share in the battery market (e.g., used in internal combustion engine cars). Although the production cost of Pb-acid batteries is low, their low specific energy and low-temperature capability are their drawbacks.[7] Nickel-cadmium (Ni-Cd) rechargeable batteries were used in portable devices for 50 years; however, the memory effect problem, which causes capacity loss if not

given a periodic full discharge cycle, and toxicity (Cd) is the main concern. Later, Nickel-metal-hydride (Ni-MH) rechargeable batteries came to play in the market. Its specific energy is higher than that of the Ni-Cd batteries, but their limited cycle life hindered their success in the battery market.[8] The highest specific energy can be obtained from Li-metal batteries, yet lithium dendrite formation is the main issue for safety hazards.[7] The history of lithium-ion batteries (LIBs) has begun by developing the insertion/intercalation type electrode materials to prevent dendrite formation. Ever since the LIBs had released to the market in 1991, research and industry sections have been continuously developing LIBs. As one can see these days, LIBs have become an integral part of our daily life, powering cellphones, laptops, and electronic devices. In particular, the transition of the transport sector from the internal combustion engine to electric vehicles leads to higher demands of LIBs. Thus, moving towards a more sustainable energy society will need the improvement of the energy and power of LIBs.

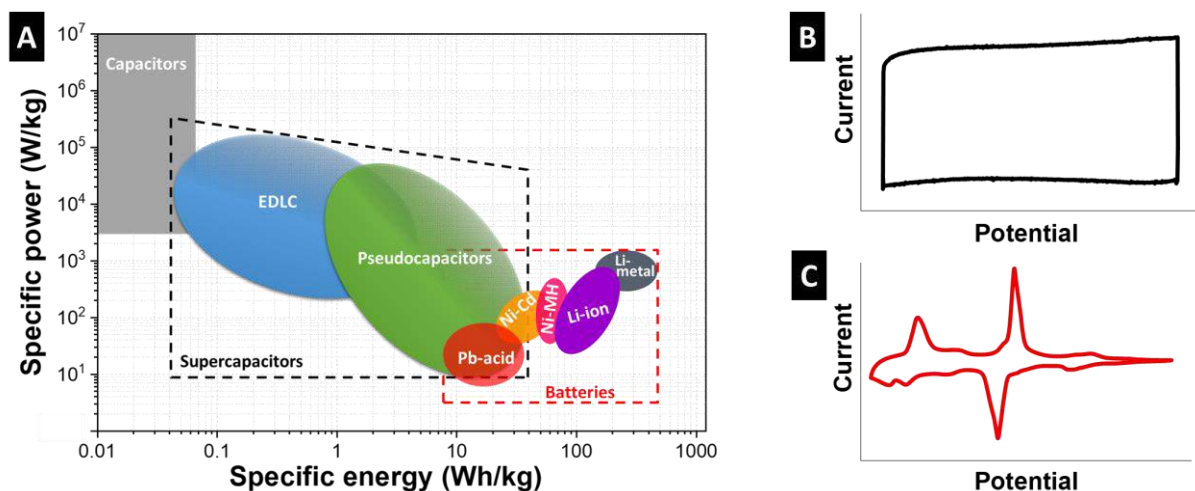


Figure 1. A) Ragone chart of the current electrochemical energy storage systems. Voltage profile of B) capacitor and C) battery. The Ragone chart is inspired by Ref. [9].

2. Lithium-ion batteries

2.1. History of lithium-ion batteries

One can start the history of batteries with a prehistoric battery, the so-called Parthian Battery (ca. 150 BC), which is a clay jar consisting of an iron rod surrounded by a copper cylinder soaked in vinegar or an electrolytic solution. However, the purpose of the Parthian Battery remains unclear whether it is a galvanic cell or not. Later, another history-line on batteries starts with the discovery of Alessandro Volta in 1799 on the voltaic cell, which involves zinc and copper plates separated by cardboard soaked in saltwater.[8] Although the timeline of

the batteries is unclear when exactly it has begun, the use of batteries in our modern lives is undeniable. Nowadays, most of the battery market is covered by lithium-ion batteries due to their high energy-to-weight ratio and long operational life.

The history of rechargeable lithium-ion batteries cannot be separated from non-rechargeable lithium-metal batteries. The first lithium-metal battery is consisting of lithium metal and manganese dioxide as electrodes was invented in 1962. It was introduced to the battery market by Sanyo in 1972.[7] There are advantages of using a metallic lithium electrode, such as that lithium is the lightest metal, has a high theoretical capacity of 3860 Ah/g, and a very low electrode potential (-3.04 V vs. standard hydrogen electrode (SHE)). However, large volume change and high reactivity of lithium during the electrochemical process leads to dendrite growing resulting in short-circuiting, thermal runaway, and hence catch fire. The inherent instability of the metallic lithium shifted the research to alternative electrode materials. However, early research was first focused on replacing the displacement type cathodes.[10] A breakthrough from lithium-metal batteries to lithium-ion batteries was obtained by introducing the intercalation/insertion-type electrode of TiS_2 by Whittingham in 1976 at Exxon.[11] However, the cut-off voltage was low as 2.5 V vs. Li/Li^+ , which prevents to reach to the high energy density battery. Goodenough et al. introduced LiCoO_2 as a high voltage applicable (4 V vs. Li/Li^+) insertion type electrode in 1980.[12] In the same year as the first insertion electrode introduced to the battery society, Besenhard et al. also revealed that Li^+ ions intercalate into graphite.[13] However, graphite was not preferred due to its lower theoretical capacity of 372 mAh/g compared to metallic lithium, and co-solvent intercalation of propylene carbonate-based electrolyte leads to graphene layer exfoliation resulting in capacity loss.[10] Moli Energy produced the first rechargeable lithium-based battery by using metallic lithium and molybdenum sulfide in 1985, but severe battery explosions because of the aforementioned lithium dendrite growing led to revisit intercalation type electrode materials.[7] In the same year, Yoshino et al. offered to use petroleum coke as a less graphitized carbon due to its low structural destruction than that of graphite.[14] Thereby, the first lithium-ion battery, which was built with petroleum coke as a negative electrode, LiCoO_2 as a positive electrode, and propylene carbonate-based electrolyte, was introduced to the battery market in 1991 by Sony.[7] The graphite came to play only after the discovery of ethylene carbonate (EC), which can suppress graphene layer exfoliation. However, the EC-based electrolyte can cause the formation of the solid-electrolyte interface.[15-17] In 1993,

Guyomard and Tarascon revealed LiPF_6 in EC/DMC electrolyte, which provides improved oxidation stability.[18] Since then, it has been the most favorable liquid electrolyte for the LIBs. Milestone discoveries until reaching to the lithium-ion batteries as we know them today is illustrated in **Figure 2**.

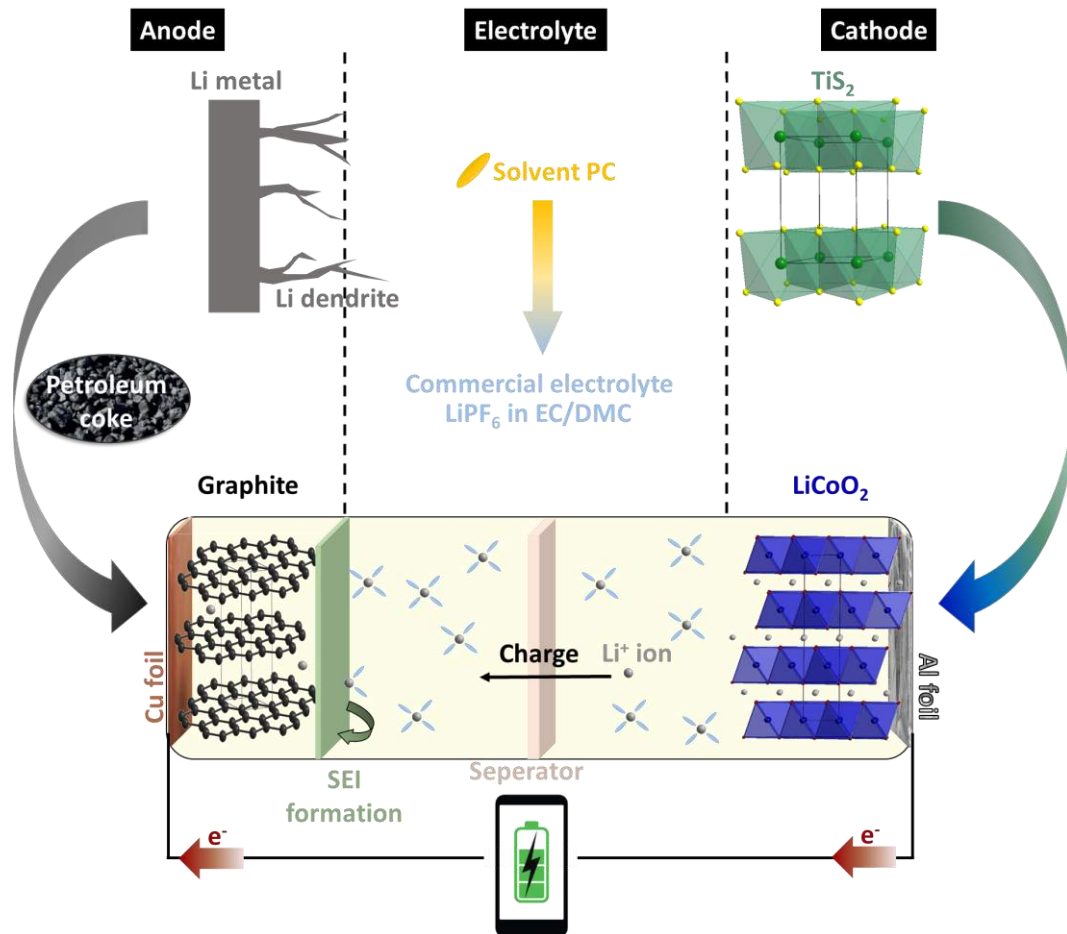


Figure 2. Milestone discoveries on the lithium-ion batteries with the charging process illustration (inspired by Ref. [10])

2.2. Basic working principle of a lithium-ion cell

A lithium-ion cell consists of four main parts: negative electrode (anode), electrolyte, separator, and positive electrode (cathode). The anode and cathode are defined for the discharge process, where the anode undergoes the oxidation reaction, and the reduction reaction occurs on the cathode side. For example, in a lithium-ion cell with graphite (C_6) as an anode and LiCoO_2 as a cathode, the half-reaction mechanism for each electrode during the charging process, as illustrated in **Figure 2** (below-part), can be given as follows:





During charging, the Li^+ ions release from the cathode to the electrolyte, then pass through the separator and get into the anode. At the same time, electrons are transferred via an external circuit from cathode to anode. During the discharging process, the lithium-ion cell undergoes the reverse of the charging process. The charge process requires applying an external power while discharging occurs spontaneously.

2.3. Essential definitions and measurement techniques for batteries

Understanding how a battery works and how to evaluate the performance of the electrochemical sources is highly correlated with the thermodynamics of the electrochemical process. In a galvanic cell, electrical energy is produced via an electrochemical reaction. During the so-called redox reaction, the electrons transfer from one species to another at the interface of the electrodes and electrolyte. The redox reaction is divided into two half-cell reactions: the oxidation reaction (**Equation 3**), where the electrons release by the anode, and the reduction reaction, where the electrons are accepted by the cathode (**Equation 4**). In the following equations, n stands for the number of electrons.



The overall reaction can be written as follows[19]:



At the equilibrium condition, the specific standard electrode potential can be derived from the thermodynamic data of the reaction, as following **Equation 6**:

$$E^0 = \frac{-\Delta G^0}{n \cdot F} \quad [\text{V}] \quad (6)$$

where ΔG^0 is standard Gibbs free energy, n is the number of the electrons, and F is the Faraday constant, which is the quantity of charge per mole of the electrons (**Equation 7**).

$$F = e \cdot N_A \quad (96485.3 \text{ C/mol or } 26.801 \text{ Ah/mol}) \quad (7)$$

For the non-standard conditions, the potential of the full-cell reaction can be given by the Nernst Equation (**Equation 8**), where E_{cell} stands for the cell potential at the temperature of interest, E_{cell}^0 is the standard cell potential at the equilibrium conditions, R is the universal gas constant, T is the absolute temperature, and Q_r is the reaction quotient.

$$E_{\text{cell}} = E_{\text{cell}}^0 - \frac{R \cdot T}{n \cdot F} \cdot \ln Q_r \quad [\text{V}] \quad (8)$$

There are also essential definitions, which will be given as the following:

Open circuit voltage (OCV): The voltage of a cell, which is neither on discharge nor charge, in other words, the state of the voltage of a cell that is not connected with an external circuit.

Charge capacity (Q): The total amount of charge available from a cell (**Equation 9**). An ampere is a unit of electrical current (I), which is defined as a rate of charge flow in an electric circuit.

$$Q = \int_{t_1}^{t_2} I(t) \cdot dt \quad [\text{Ah}] \quad (9)$$

Theoretical gravimetric capacity (Q_{th}): The amount of charge per weight of reactants (m_i), is given by **Equation 10**.

$$Q_{\text{th}} = \frac{n \cdot F}{\sum_i m_i} \quad [\text{Ah/kg}] \quad (10)$$

Specific energy (E_{sp}): The amount of electrical energy delivered per unit mass of a cell (**Equation 11**).

$$E_{\text{sp}} = \frac{n \cdot F \cdot \Delta E^0}{\sum_i m_i} \quad [\text{Wh/kg}] \quad (11)$$

Specific power (P_{sp}): The amount of power delivered per unit mass of a cell (**Equation 12**).

$$P_{\text{sp}} = \frac{I \cdot \Delta E^0}{\sum_i m_i} \quad [\text{W/kg}] \quad (12)$$

There are also terms of *energy density* and *power density*, which are the close terms to the *specific energy* and *specific power* with the difference is the use of a unit volume of a cell instead of a unit mass of a cell. Therefore, the unit of *energy density* and *power density* is Wh/l and W/l, respectively.

Specific current: The amount of charge per unit mass with the unit of measure of A/kg.

Current rate (C-rate): Describing the time frame for either a full charge or discharge, where C donates the theoretical or nominal charge capacity (**Equation 13**). For example, 1 C means that the transfer of all of the stored energy in one hour; in other words, the entire battery will be discharged in 1 h. Another example, C/10 (0.1 C), means that the full transfer of all stored energy in 10 h.

$$C = \frac{\text{discharge current}}{\text{nominal capacity}} \quad (13)$$

Cycle: One sequence of a complete discharging and charging process.

It is essential that, for battery evaluation, each parameter is correlated to the fundamental understanding of thermodynamic and kinetic of a particular system or interested materials. For example, the electrode potential (**Equation 6**) will be high or low, depending on the electrochemical potential of a material. At the cell level, the potential difference between

anode and cathode gives us an indication of how high the energy of such a battery is (**Equation 11**). Yet, the kinetic energy is the parameter that reflects how fast a battery can be during the charging/discharging. This can be seen in the very simple parameter of power (**Equation 12**). Another important parameter is cyclic stability. In common, the battery should have a long cycle life with as less as possible the performance decay.

There are several electrochemical techniques to be applied for testing of the electrochemical performance of a battery; however, the essential techniques for battery performance testing are cyclic voltammetry (CV) and galvanostatic cycling with potential limitation (GCPL).

Cyclic Voltammetry (CV): A method that provides information about the electrochemically active regions of the electrode during scanning of the potential between two given values at a fixed rate. It can also be a useful technique for spotting the parasitic reaction caused by the electrolyte decomposition. In other words, one can use CV to estimate the operating window of electrolyte, whether it is matching with interest electrode materials or not.

Galvanostatic cycling with potential limitation (GCPL): A method that provides information about potential changes in the working electrode against the reference electrode while keeping the current constant. The GCPL technique can be applied to perform rate handling capability and cyclic stability tests for LIBs. The rate handling capability tests give information about the speed of kinetics of the tested battery system by applying different specific currents/C-rates, while the cyclic stability tests provide information about the degradation rate of the battery for an extensive number of cycling via applying a constant current in a set range of potential.

2.4. Electrolytes

2.4.1. Liquid electrolytes

Organic liquid electrolytes for LIBs consists of three main classes of materials: (i) aprotic (nonaqueous) solvent, (ii) conducting lithium salt, and (iii) additives. An ideal solvent for lithium-ion battery applications should meet the following demands [20]:

- The solvent should be able to dissolve the salts in a sufficiently high concentration, thus, possessing a high permittivity (ϵ), which is a measure of the ability of a material to be polarized by the electric field.
- It should have a low viscosity (η) to provide facile ion transportation.

- The solvent must be inert toward all other cell components, such as electrodes and current collectors.
- It should be applicable to a wide temperature range. For example, exhibiting a low melting point (T_m) and as well a high boiling point (T_b).
- The solvent should have a high flash point (T_f) for safety reasons, while it is nontoxic and economical.

Organic esters have been leading to be a suitable liquid electrolyte for LIBs. **Table 1** presents the most used organic carbonate solvents and their physical properties for LIB applications. Ethylene carbonate (EC) and propylene carbonate (PC) take the attention due to their high boiling point, permittivity, flashing point. However, the EC solvent possesses a disadvantage of having a high melting point; therefore, the EC solvent is a solid at room temperature. After the recognition of the PC solvent causes an unstable solid-electrolyte interface (SEI) on the surface of the carbonaceous anodes, the interest of research shifted towards using the co-solvent approach. For instance, a small percentage (9%) of PC solvent mixing with EC can suppress the melting point of EC.[21] That is followed by using dimethyl carbonate (DMC) instead of PC as a co-solvent with the EC solvent.[18, 22] The linear carbonates, such as DMC and diethyl carbonate (DEC), bring along the advantage of forming a homogenous mixture with the EC solvent at any ratio. Moreover, suppressing the melting point of EC and lowering the viscosity can be counted as the other advantage of the linear carbonates.[20] Since then, ethyl methyl carbonate (EMC) and many more have been discovered as a co-solvent with the EC solvent for LIBs.[23]

Table 1. Organic carbonates as electrolyte solvents.[20]

Solvent	T_m (°C)	T_b (°C)	η at 25 °C (cP)	ϵ at 25 °C	T_f (°C)
Ethylene carbonate (EC)	36.4	248	1.9	89.8	160
Propylene carbonate (PC)	-48.8	242	2.5	64.9	132
Dimethyl carbonate (DMC)	4.6	91	0.6	3.1	18
Diethyl carbonate (DEC)	-74.3	126	0.8	2.8	31

The ideal lithium salt as a use in the electrolyte for LIBs must fulfill the following essential requirements [20]:

- The lithium salt must dissolve completely in an as-chosen solvent to ensure high Li⁺ ion mobility.
- The anion from the lithium salt should be stable against the oxidative decomposition at the positive electrode while inert to the electrolyte.
- It should also be inert with all other cell components, such as separator, current collectors, and cell packaging materials, etc.
- While it is stable against thermally induced with electrolyte, it should also be nontoxic and preferably economical.

The possible lithium salts for LIBs are limited compared with the wide spectrum of aprotic organic solvents. LiBF₄, LiPF₆, LiAsF₆, and LiClO₄ are in the group of the most used lithium salts for lithium-ion battery applications. The ionic conductivity (σ) of these salts in the PC solvent is lower than that of EC/DMC mixture solvents (**Table 2**). Although the conductivity of LiAsF₆ is higher than that of LiPF₆ salt in EC/DMC, it is not preferable due to the toxicity of As species.[24] Another high conductivity preserver in EC/DMC is LiClO₄ salt, which possesses high anodic stability like up to 5.1 V vs. Li/Li⁺; however, at high temperatures and high current rates, it reacts with the organic species from the solvent, resulting in safety issues.[22, 25] Even though the LiBF₄ salt is less toxic than LiAsF₆ salt and provides better safety than LiClO₄, the low ionic conductivity of LiBF₄ in EC/DMC is a drawback. Although LiPF₆ is known for its chemical and thermal instability, it has been commercialized by the use of stabilizer additives.[26] Even at room temperature, LiPF₆ generates solid LiF and PF₅ gas, which reacts with the organic solvents and deteriorates the stability of the SEI components (e.g., Li₂O, LiF, Li₂CO₃, polyolefins, and semicarbonates, etc.) on the graphite anode surface.[27] Different types of stabilizer additives have been used, such as a trace amount of LiF, tris(2,2,2-trifluoroethyl)phosphite (TTFP), fluorinated carbamate, and hexamethyl-phosphoramidate.[28]

Table 2. Lithium salts as electrolyte solutes.[20]

Salt	T_m (°C)	$T_{\text{decomposition}}$ (°C) in solution	σ (mS/cm) (1 M, 25 °C)	
			in PC	in EC/DMC
LiBF ₄	293	> 100	3.4	4.9
LiPF ₆	200	80 (EC/DMC)	5.8	10.7
LiAsF ₆	340	> 100	5.7	11.1
LiClO ₄	236	> 100	5.6	8.4

Ionic liquids can also be used as liquid electrolytes for LIBs. They have been suggested due to their wide electrochemical operating range, improved thermal stability, and low volatility.[29, 30] However, the presence of impurities in ionic liquids, such as residual solvents or water, causes undesirable side-reactions.[31] In addition, wetting of the separator, low ion transport abilities due to the high viscosity are reasons that they are not competitive replacement candidates for conventional organic liquid electrolytes, especially for industrial applications.[32, 33]

2.4.2. Organic and inorganic solid electrolytes

The state-of-art for LIBs still rely on flammable liquid electrolytes, which catch fire during overcharging or abused operation. Furthermore, rapid charging leads to lithium plating at the graphite anode and form dendrites that penetrate through the separator. Consequently, the internal short-circuit causes the fading of the life cycle of the battery and, eventually, explosion. Replacing liquid electrolytes with solid electrolyte systems has been investigated with the aim of solving such problems. However, there are some challenges remaining in the development of the solid-state electrolyte (i.e., low ionic conductivity, incompatibility with the lithium anode, and high contact resistance at the interface between electrode and electrolyte).

The solid-state battery has shown superior energy density greater than that of traditional LIBs. Cathode materials used in solid-state LIBs are not new but the same as cathode found in traditional LIBs, which will be discussed in the following sections. As for anodes in solid-state

LIBs, lithium metal, graphite, and lithium titanate are widely applied depended on the reduction potential of the selected solid electrolyte. Several key challenges, apart from poor ionic conductivity, are the following: volume change either in cathode or anode during the electrochemical process, low active mass loading in the cathode and anode, and poor contact electrode/electrolyte interface.

One of the solid-state electrolytes class is solid polymer electrolytes (SPEs); in other words, organic solid electrolytes. Non-volatility, improved safety, better overheat and overcharge allowance, decreasing the cell weight, reducing the cell price, suppressing dendrite formation for the case using metallic lithium anode, shape flexibility, and improved shock resistance can be given as advantages of SPEs compared to liquid electrolytes.[34] In the solid polymer electrolyte, the lithium salt, which is added to provide the lithium-ion conduction, is solvated by polymer chains.[35] One can easily think that SPEs may also act as a host for ions. In 1973, poly(ethylene oxide) (PEO) in alkali metal salts opened the solid polymer electrolyte systems using for LIBs.[36] Although PEO-based electrolytes provide excellent solubility for lithium salt, they suffer from low ionic conductivity. The PEO is a semicrystalline polymer, where the ion transport occurs from its amorphous domains (**Figure 3A**); therefore, most studies have been focused on increasing the ionic conductivity of PEO by decreasing the crystallinity of PEO.[37] Lithium salt choice is as essential as the polymer choice for SPEs. For example, the LiPF_6 salt is a great choice for liquid electrolyte systems; lithium trifluoromethanesulfonate (LiTf), lithium bis(trifluoromethanesulfonimide) (LiTFSI), lithium bis(trifluoromethanesulfonimide) (LiBETI), and lithium bis(fluorosulfonyl)amide (LiFSI) are offered as more preferable lithium salts for PEO-based SPEs due to exhibiting high solubility, high ionic conductivity, and high electrochemical stability.[38-40] The larger anions from the lithium salt aid to increase ionic conductivity, reduce the crystallinity, and increase the glass temperature (T_g) of PEO.[37] Polyester-based (e.g., polyethylene carbonate (PEC), poly(trimethylene carbonate) (PTMC), and poly(propylene carbonate) (PPC)), polycaprolactone (PCL), nitrile-based (e.g., succinonitrile, poly(acrylonitrile (PAN)-based) solid organic electrolytes are further examples of SPEs.

Lithium-ion transport in the organic solid electrolytes involves the migration of lithium ions in the solvent medium. According to the Stokes-Einstein equation, the conductivity of lithium in the organic electrolyte can be increased by increasing the ion dissociation in the solvent and reducing the viscosity of the solvent. As for the lithium-ion transport in the solid electrolyte,

lithium (mobile specie) in the crystalline solid must pass through the bottleneck point where the defined energetic barrier (so-called migration energy) is maximized. Ion conductivity increases with decreasing migration energy. The absolute lithium conductivity related to the activation energy of diffusion can be expressed by:

$$\sigma = \frac{\sigma_0}{T} e^{\frac{-E_A}{k_B T}} \quad (14)$$

Where E_A is the activation energy of diffusion, T is the temperature, and k_B is the Boltzmann constant. As noted, the ion concentration in the crystal is independent of the temperature and activation energy. The lithium-ion number of transfers is also another metric that reflects the diffusivity of the electrolyte. In the aprotic electrolyte, the number of lithium-ion transfer is between 0.2 and 0.5. Obviously, the number of the lithium-ion transfer in solid-state is much lower (2-5 times).[41] The ion diffusion mechanism is based on Schottky and Frenkel, which includes a vacancy mechanism and a relatively complicated diffusion mechanism. Some materials with special structure can achieve high ionic conductivity without a high concentration of defects, like materials with crystal framework composing of immobile ions and sub-lattices with mobile ions. For achieving the fast ionic conduction, three minimum criteria must be full filled: i) the number of sites available for mobile ions must be larger than the number of mobile species, ii) the migration barrier (kinetic energy) energies between available sites should be low enough for ion hopping from one to another site, and iii) those sites must be connected to form a continuous diffusion pathway (related to the grain boundary resistance). The latter is of great concern in the field of solid electrolyte because the grain boundary resistance is significantly higher than bulk resistance.[42]

On the other hand, it is generally accepted that the simple energy level approach commonly used to evaluate the stability window of Li-ion electrolytes (**Figure 3B**) has very limited applicability, especially when the formation of the solid-electrolyte interface (SEI) on the anode surface and the formation of the cathode electrolyte interface (CEI) on the surface of the cathode are discussed. Additionally, it became clear that the terms HOMO and LUMO should be avoided when talking about the electrochemical stability of electrolytes. Instead, it is safer to speak of the potential of electrolyte reduction at negative potentials and of the potential of electrolyte oxidation at positive potentials. Both SEI and CEI lead to an increase of the Li-ion diffusion and charge-transfer across the interfaces. However, the formation of SEI and CEI on the surface of the electrodes can be favorable as a passivation

layer, such as mitigation of parasitic reactions, reduction of the ion dissolution, and suppression of the volume change during lithiation/delithiation process.[43]

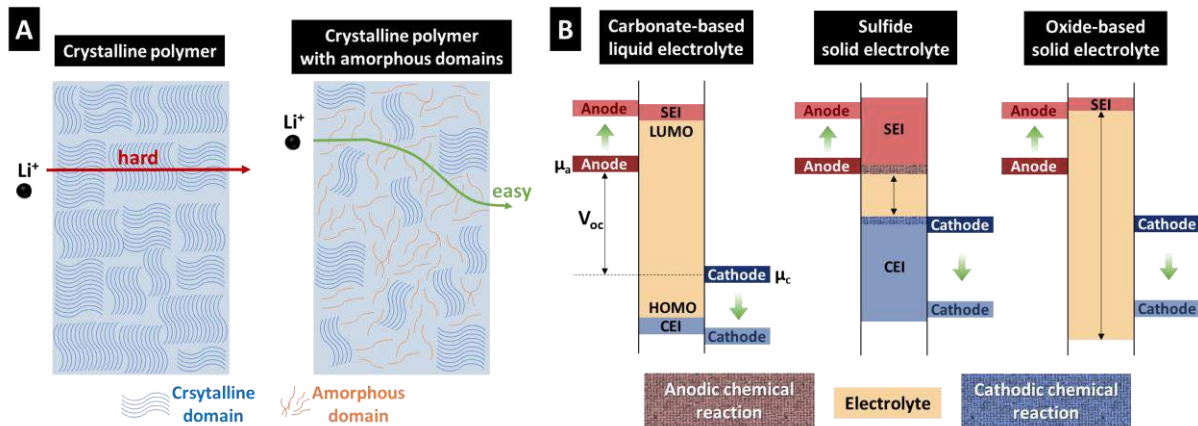


Figure 3. A) Schematic illustration of lithium-ion transfer across (left) a crystalline polymer and (right) a crystalline polymer with amorphous domains (inspired by [44]). B) Schematic band diagrams of the carbonate-based liquid electrolytes, sulfide-based solid electrolytes, and oxide-based solid electrolytes (inspired by [43]).

The ion transport pathway within bulk depends on the complex properties of the material, such as the structure, physical, and chemical properties of the material. For inorganic solid electrolytes, materials possess a periodic structure built from the coordination of polyhedrons. In ceramics, the ion transport pathway is provided via defect, ion interstitial, and vacancies from the structure. Within the bulk, the penalty energy for ion migration is most related to the fundamental structure of the material, which will be briefly discussed below.

Perovskite materials have the general formula of ABO_3 with the cubic unit cell. In the structure, A is the alkaline earth to the rare-earth element at the corner of the cube. The B is typically transition metal at the center of the structure, and the oxygen atom locates at the face-center position.[41] Lithium can occupy the A site of the structure via aliovalent doping (e.g., $Li_{3x}La_{0.66-x}M_{0.9-x}TiO_3$). Replace lithium at the A site lead to the modification of oxygen vacancies, which influence the ion conductivity.[45] Lithium diffuse by hopping in the ab plane to the adjacent vacancy. The representative perovskite solid electrolyte is $Li_{3x}La_{1.3-x}TiO_3$, which exhibits lithium conductivity of 0.07 mS/cm and bulk ion conductivity of 1 mS/cm. Although $Li_{3x}La_{1.3-x}TiO_3$ has high bulk ionic conductivity, it cannot be applied with lithium and graphite anode because of the limited potential window at 1.5 V vs. Li/Li⁺. [46, 47]

NASICON (sodium superionic conductor) compounds are generally rhombohedral structures, while monoclinic and orthorhombic phases have also been reported.[48] *NASICON* has a general formula of $AM^{4+}/M^{3+}(PO_4)_3$ where A is Li or Na, and M^{4+} can be Ti, Ge, Sn, Hf or Zr, and M^{3+} can be Cr, Al, Ga, Sc, Y, In or La.[49-52] In the structure, Li can occupy two distinct sites: one at the 6-fold coordination (octahedral) between two MO_6 octahedral, and another at 8-fold coordination between columns of MO_6 octahedra. The lithium diffusion is hopping between those two sites, which determine the ion conductivity. The large bottleneck site leads to lower activation energy and thus higher ionic conductivity.[53-55] To enlarge the bottleneck site, the element in the M^{3+} site should be large. By far, $Li_{1.3}Al_{0.3}Ti_{1.7}(PO_4)_3$ has the highest bulk conductivity (3 mS/cm).[56] However, one should keep in mind that a titanium-containing compound is not suitable for anode materials with active potential lower than 1.5 V vs. Li/Li⁺. [44]

Garnet is the oxides materials having a cubic unit cell. It has a general formula of $A_3B_2(XO_4)_3$, where A has 8-fold coordinated in the antiprismatic site. B is the 6-fold coordinated in the octahedral site. X is the 4-fold coordinated in the tetrahedral site. In lithium conducting garnet, lithium element occupies the tetrahedral position, for example, $Nd_3Te_2(LiO_4)_3$. [41] For obtaining better ionic conductivity at room temperature, more lithium is added alongside with the adjusting valence state of A and B. As for example, $La_3M_2(Li_{1.7}O_4)_3$ exhibits large lithium distribution in the tetrahedral and distorted octahedral site rendering higher lithium conductivity. However, having more lithium concentration located in the distorted octahedral site is crucial for increasing the total ionic conductivity.[57] For example, increasing lithium from $Li_3Ln_3Te_2O_{12}$ to $Li_7La_3M_2O_{12}$ cause more lithium distribution in the distorted octahedral and thus increase the ionic conductivity by 9-folds.[58]

Sulfide solid electrolyte is also known as thio-LISICON. It has been reported as the highest conductivity among all solid electrolytes. For example, $Li_{10}GeP_2S_{12}$ exhibits conductivity as high as liquid electrolyte (0.6 mS/cm).[59] The thio-LISICON has a general chemical formula of $Li_{10}MP_2S_{12}$ where M are Si, Ge, or Sn. Lithium atoms distribute in the octahedral voids originated along with the c, a, and b axis. As for the c axis, lithium is edge-shared with (P/Ge) S_4 tetrahedral. Another octahedra site is located by corner shared with PS_4 tetrahedral along a and b axis. The diffusion of lithium along the ab plan is estimated to be slower than the c direction. Thus, optimization of the octahedral space along c-direction leads to higher lithium conductivity.[41] For instance, substitution Ge with Sn or Si at the evaluated atomic ratio (e.g.,

$\text{Li}_{10}\text{Ge}_{0.95}\text{Si}_{0.05}\text{P}_2\text{S}_{12}$ with a conductivity of 0.83 mS/cm) lead to the optimum tunnel size.[60] Although thio-LISICON exhibits high lithium conductivity, it is difficult for cell assembling as it is sensitive to moisture. Further, it tends to react with the cathode material.[42]

Argyrodite or lithium argyrodite ($\text{Li}_6\text{PS}_5\text{X}$, where X is Cl, Br, or I) is the young introduced fast lithium-ion conductor materials.[61] The structure is built from tetrahedral close packing anion in the cubic unit cell. Tetrahedral PS_4 network creating an octahedral cage in which lithium is distributed around S or halide ion.[41] The diffusion between the octahedral cage results in low activation energy (0.2-0.3 eV), while lithium distribution and disordered S^{2-}/X^- sublattice will further increase the conductivity. However, there is an exceptional case where iodide in the structure decreases the ionic conductivity.[62]

Seemingly, the solid-state electrolyte has gained a lot of attention. However, the liquid organic electrolytes are still more practical, in particular, the manufacturing of the battery. Inorganic solid electrolytes are mostly brittle and thus not suitable for cylindrical cells. It is rather a fit in the pouch or prismatic cell. The transition from a traditional lithium-ion battery to an all-solid-state battery still far to reach. Not only low ionic conductivity is a challenge in materials development, but also the interface reaction between electrode materials and solid electrolyte. This leads to the artificial interface chemistry (so-called buffer interface) development that avoids the reaction between solid electrolyte and electrode materials (anode and cathode). Consequently, the cost of an all-solid-state battery might be higher than a traditional liquid electrolyte-based battery at the moment. Speaking of the energy density of the all-solid-state battery, it still has a large room for improvement. Regardless of the electrode materials, the all-solid-state battery delivers lower specific energy and specific power than that of liquid organic electrolyte-based battery systems.[63] A part of the issue is the contact resistance. In the electrode material (both cathode and anode), one needs to add a solid electrolyte apart from carbon conductive and a polymer binder.[43] Obviously, the dead mass at the cathode and anode is higher as compared with liquid electrolyte-based batteries.

2.5. Positive electrodes (Cathodes)

Intercalation chemistry materials have been around the corner of materials research for almost 180 years. Like few layers-metal disulfides (MS_2), various kinds of layer material were investigated for cation intercalation (e.g., Li^+ , Na^+ , and H^+). The first cathode material for rechargeable lithium-ion batteries was demonstrated by Whittingham at Exxon Corporation

using TiS_2 cathode vs. lithium metal anode in LiClO_4 salt dissolved in an organic solvent. The discharge cell voltage of that battery was lower than 2.5 V and had good reversibility, by means of one lithium insertion per one mol of TiS_2 . However, the cell had two main issues: first, the cell voltage was low and, thus, the cell showed low energy density; second, the lithium anode was prone to decay the performance because of dendrite formation during charging. Hence, seeking for intercalation chemistry to replace TiS_2 began and has been continued until now. [64, 65]

2.5.1. Layered family

Significant progress of research has been focused on the high specific capacity and high operational voltage positive (cathode) materials to meet the demand for reaching higher specific energy next-generation Li-ion batteries. Obtaining high specific energy is correlated with the energy difference between redox energies of anode and cathode. To better understand that the cathode needs to provide the stabilization of a higher oxidation state with a lower-lying energy band, where the anode needs to have the stabilization of lower oxidation states with a higher-lying energy band. According to John B. Goodenough, the top of the $\text{O}^{2-}:2p$ band lies at lower energy than that of the $\text{S}^{2-}:3p$ band. [66] This discovery shaded the light for the opportunity of using the oxides as a cathode due to lowering the redox energy by reaching lower-lying energy bands like $\text{Co}^{3+/4+}$ and $\text{Ni}^{3+/4+}$ (Figure 4). Thus, the possibility of enlarging the energy density was enabled by increasing the cell voltage as high as 4 V.

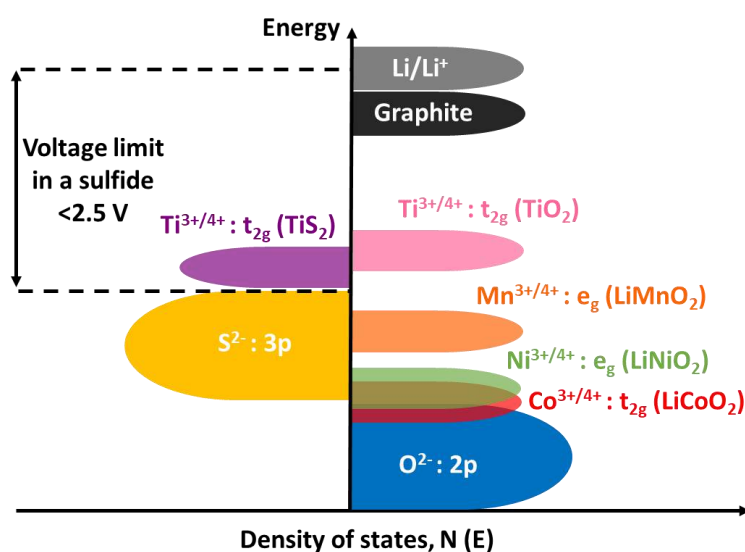


Figure 4. Positions of the redox energies relative to the top of the anion: p bands (inspired by [64]).

LiCoO₂ (LCO) as the first high voltage applicable oxide cathode with lithium metal anode and the electrolyte of LiBF₆ in propylene carbonate (PC) for LIBs was reported in 1980.[12] The crystal structure of LiCoO₂ has an α-NaFeO₂-type layered structure where monovalent Li⁺ and trivalent Co³⁺ ions are arrayed in serial (111) planes, and oxygen atoms are ordered in a cubic closed packed framework of $R\bar{3}m$ hexagonal space group (**Figure 5A**). Also, according to the surrounding Li⁺ environment and the number of unique oxide layer stacking, the most stable crystal structure of LCO is under the classification of O3-type. The symbol of “O” stands for the octahedral coordination environment of Li⁺ ions surrounded by six oxygen, and “3” represents different stacking of oxygen atoms in a single unit.[67] The good cation ordering property of LCO comes from the large charge and size difference between monovalent Li⁺ and trivalent Co³⁺ ions.[64] Besides, its electronic structure displays relatively high electronic conductivity due to possessing direct Co-Co interaction with the shared octahedral edges along the cobalt planes.[64, 68] However, the semi-conductor state of LiCoO₂ changes during the delithiation process, and it becomes the insulation-metal phase feature due to the introduction of electron holes into the low-spin Co^{3+/4+}:t_{2g} band.[69, 70] Apart from the conductivity, Co³⁺ provides stability to the structure owing to the fact of high octahedral-site stabilization energy (OSSE).[64] Although its theoretical capacity is as high as 272 mAh/g, the available capacity for the high-voltage operation has a limit of 140 mAh/g at 4.2 V vs. Li/Li⁺ because of the phase transition, surface degradation, and inhomogeneous reaction mechanism.[68, 71] The phase transition mechanism of Li_xCoO₂ occurs until 4.2 V vs. Li/Li⁺ alternately in between the hexagonal to the monoclinic when Li content in the structure nearly falls by half (x = 0.5) as called solid-solution reaction. Further delithiation (x < 0.45) of Li_xCoO₂ leads to another phase transition from O3-type to H1-3 and then to O1-type of CoO₂, where O1-type is a hexagonal single-layered and isostructural of CdI₂ phase, and H1-3 is a hybrid structure of O3- and O1-type.[72] This, as called a two-phase reaction, takes place over 4.2 V vs. Li/Li⁺. The further delithiation causes the oxygen release from the crystal lattice due to the decrease of Fermi level within the trivalent Co³⁺ t_{2g} band and then overlapping with the top of the 2p band of oxygen.[64, 73] The released oxygen in the cell induces an exothermic reaction with the flammable organic electrolyte resulting in safety hazards. Also, the high-voltage operation of LCO triggers organic electrolyte decomposition, the continuous formation of the cathode electrolyte interphase (CEI), and even Co dissolution.[74, 75] Therefore, the practical application of LCO for LIBs is limited to the upper cutoff potential of 4.2 V vs. Li/Li⁺. However,

recent studies reveal that the particle size of LCO has a dramatic impact on the rate of Li^+ ions diffusion, which affects power performance. Recently, Jena et al. demonstrated that LCO with larger particles shows inhomogeneous Li diffusion, and thus it shows a typical two-phase reaction over 4.2 V vs. Li/Li^+ . In contrast, LCO with small particles undergoes only the solid-solution reaction, even over 4.2 V vs. Li/Li^+ , and better rate handling performance enabling high power.[76] Additionally, the cobalt price increase year by year because Co is a rare element with a total deposition of 29 ppm in the Earth's crust.[77] Hiesh et al. also predicted that the cobalt price might increase annually by \$ 27.3/kg in 2030.[78] The researchers have started the investigation of replacing Co with other transition metals on account of the safety issues, the high-cost, and voltage-limited performance of LCO.

The analogous of LiCoO_2 can be written as LiMO_2 in which M represents transition metals such as Ti, V, Cr, Mn, Al, and Ni.[64, 79] Owing to the relatively low-cost of Ni than that of Co, Ohzuku et al. suggested LiNiO_2 (LNO) as a high-voltage (ca. 4 V vs. Li/Li^+) cathode material for LIBs in 1993.[80, 81] The LNO possesses the same structure as LCO; however, similar ionic radii of monovalent Li^+ and divalent Ni^{2+} raise the issue that Ni^{2+} ions take place in the lithium layer, so-called ionic mixing (**Figure 5B**).[82] Therefore, the suggested general formula of LNO is $\text{Li}_{1-x}\text{Ni}_{1+x}\text{O}_2$, where x depends on the synthesis conditions and has a direct impact on the reversible capacity.[83, 84] While LCO and LNO share the same theoretical capacity of 274 mAh/g, the practical capacity of LNO, over 200 mAh/g, is higher than that of LCO (ca. 140 mAh/g).[85] The oxidation of Ni^{2+} ions to the trivalent Ni^{3+} causes the local shrinkage of the inter-slab distance even at the first deintercalation process, which leads to irreversible capacity.[86] The in-depth delithiation process of $\text{Li}_{1-x}\text{Ni}_{1+x}\text{O}_2$ involves phase transformation like LCO, from hexagonal to monoclinic and again to hexagonal.[84] Similarly to LCO, in **Figure 4**, the $\text{Ni}^{3+/4+}$ band touch upon the top of the 2p band of O^{2-} , which provokes the oxygen release from the structure and hence severe safety issues (thermal runaway). Therefore, recently, the substitution of LNO with different transition metals plays a crucial role in improving structural stabilization and the electrochemical performance of layered oxides.

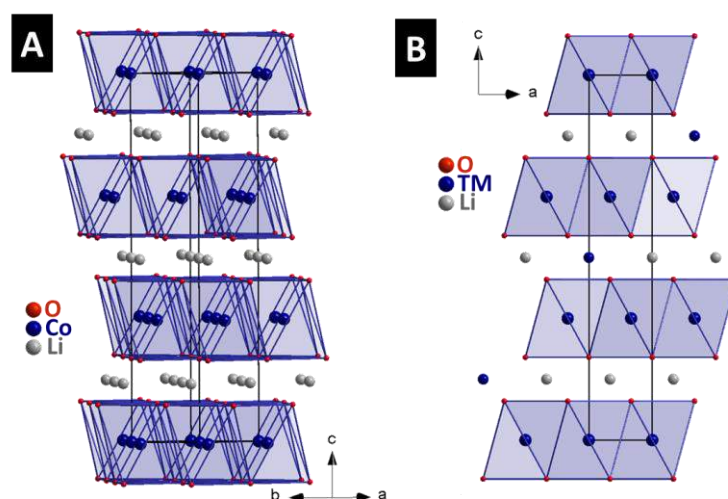


Figure 5. A) Structural illustration of LiCoO_2 . B) Structural illustration of partial cation mixed phase with TM (transition metal) ions in Li slab.

Recent strategies to improve thermal, structural and electrochemical stabilization of transition metal oxide layered cathode materials for LIBs are that using different transition metals to form binary or ternary metal oxides. The most promising ternary metal oxide family can be distinguished into two main classes: the ones with Ni, Co, and Al (NCA family) and those with Ni, Co, and Mn (NCM family).

NCA family cathodes can be generalized with the formula of $\text{LiNi}_{1-x-y}\text{Co}_x\text{Al}_y\text{O}_2$ (NCA), where $1-x-y$ can be equal or higher than 0.8.[87] Therefore, they are also known as Ni-rich cathode materials for LIBs. $\text{LiNi}_{0.8}\text{Co}_{0.15}\text{Al}_{0.05}\text{O}_2$ is the most widely researched material among NCA family cathodes for LIBs due to its relatively lower-toxicity and high energy-density (180-200 Wh/kg for the voltage window of 3.0-4.2 V vs. Li/Li^+).[88, 89] Therefore, it has been started using for commercial applications. For example, Tesla Motor Corporation recently uses the Panasonic NCA cathode in its Model S and Model X.[90] NCA also has the same $R\bar{3}m$ hexagonal layered structure as LNO. Instead of just Ni^{3+} , Co^{3+} and Al^{3+} are substituted in Ni^{3+} octahedral sites resulting in a slightly different lattice. The presence of Co^{3+} and Al^{3+} in the NCA structure provides the bond strength by stabilizing Ni^{3+} , which prevents the phase transition of NCA during the electrochemical process.[91-93] Although Al is an electrochemically inactive element, it increases the thermal stability and the capacity retention of NCA even at the low stoichiometric substitution of Al in the structure like 5%.[94, 95] However, the practical-obtained capacity of NCA is limited ca. 200 mAh/g, because of complex-inhomogeneous phase transformation during the lithiation/delithiation process.[96]

For instance, even during the first cycle, the surface structure starts changing: the layered hexagonal structure turns to a partially ordered spinel ($Fd\bar{3}m$) structure as a middle phase and then to a disordered electrochemically inactive NiO-like rock salt structure ($Fm\bar{3}m$), which is attributed to irreversible capacity lost from the first cycle.[96, 97] Moreover, overcharging or deep delithiation (over 4.2 V vs. Li/Li⁺) causes the same complex structure transformation from the outer surface (rock salt NiO) to the inner surface (layered hexagonal structure) of the NCA grains.[96] Therefore, the suggested discharge depth of NCA is set up to 60%.[98] Besides, the complex-inhomogeneous structural change causes a reduction of transition metal ions, resulting in oxygen loss due to balance the charge neutrality, and also microcrack formation occurs because of the anisotropic volume expansion/contraction.[96, 99] Liquid electrolyte can easily penetrate to the microcracks once the crack is initiated. Then the penetrated electrolyte leads to more NiO-like rock salt structure formation on the surface of the grains, eventuate in continuous capacity decay during the electrochemical cyclic process. Surface coating and bulk phase doping can be given as a modification method for NCA cathodes to improve their cyclic stability. The main goal of the surface coating method is to prevent direct contact between the active material and electrolyte and to lower the electron transport paths.[100] Carbon and its derivatives, due to their relatively low density (e.g., 1.06 g/cm³ for graphene) and conductivity properties [101, 102], oxides (e.g., SnO₂[103], TiO₂[104]), fluorides (e.g., AlF₃[105], MgF₂[106]), polymers (e.g., polyaniline[107]) and even the other cathode active materials (e.g., LiCoO₂[108], LiFePO₄[109]) for LIBs can be used for the surface coating of NCA. The bulk phase doping, which can be classified into two groups like cationic and anionic doping, focuses on improving the structural stability by decreasing the amount of occupancy of Ni²⁺ in the Li⁺ vacancy layer in the structure of NCA.[100] While the cationic doping can be carried out with Mn, Ti, Fe, Na, K [110-112], and so on, anionic doping of NCA is possible applying F⁻, Br⁻, S²⁻ [113-115], etc. By far, there is no one gold technique for solving the numerous challenges. Structure stability, mitigation of phase transformation, and thermal runaway can be solved by ionic substitution, while interface reactions require surface coating. The NCM family with the general formula of LiNi_{1-x-y}Co_xMn_yO₂ (NCM) crystallize in the $R\bar{3}m$ hexagonal layered structure system. The NCM cathode has been attracted great attention due to its high theoretical capacity (ca. 275 mAh/g) and low volume change of less than 2% during the lithiation/delithiation process for the potential lower than 4 V vs. Li/Li⁺.[116] LiNi_{0.33}Co_{0.33}Mn_{0.33}O₂ (NCM111 or NCM333), as a first member of the NCM family, was

introduced by Ohzuku et al. in 2001 with the specific capacity of 150 mAh/g in 3.5-4.2 V vs. Li/Li⁺, and 200 mAh/g in 3.5-5.0 V vs. Li/Li⁺. [117] After that, different Ni, Co, and Mn stoichiometry involving NCM family members can be exemplified with LiNi_{0.4}Co_{0.2}Mn_{0.4}O₂ (NCM424), LiNi_{0.5}Co_{0.2}Mn_{0.3}O₂ (NCM523), LiNi_{0.6}Co_{0.2}Mn_{0.2}O₂ (NCM622), and LiNi_{0.8}Co_{0.1}Mn_{0.1}O₂ (NCM811). Although there is a wide range of NCM cathodes, the recent research trend has been going in the direction of increasing Ni content and hence decreasing the Co content in NCM. Increasing the Ni content in NCM brings along the advantage of enlarging the specific capacity of NCM. On the other hand, decreasing the Co amount in NCM can be favor with lowering the cost of the cathode, which is 35% of the total cost for a lithium-ion cell. [98] At the operating voltage of 3.0-4.3 V vs. Li/Li⁺, NCM111 has a specific capacity of ca. 160 mAh/g, whereas the specific capacity of the Ni-rich NCM cathodes can be enhanced to 170 mAh/g for NCM523, to 180 mAh/g for NCM622, and even to 200 mAh/g for NCM811. [98] Besides, Mn in the NCM is electrochemically inactive but, Mn contributes to chemical stabilization of the NCM by decreasing the oxygen release from the lattice because of the well above energy band of Mn^{3+/4+} than the top of the O²⁻ p-band (**Figure 4**). [64] On the other hand, the low OSSE of Mn might cause a structural change from layered to spinel, leading to voltage decay during the lithiation/delithiation cyclic process. [64] The largest contribution to the structural stability of NMC results from Co, which also provides increasing conductivity causing in better rate capability. [64, 118] Considering the role of Ni in NCM cathodes, as mentioned above, increasing its stoichiometric amount in the structure enhances the specific capacity. However, it comes with the cost of lowering the thermal stability and capacity retention, as seen in **Figure 6A**. [118] Recent research has been shown that the poor electrochemical performance of NCM cathodes can be explained with these main reasons; cation mixing, phase transformation, microcracking, and cathode-electrolyte interphase parasitic reactions (**Figure 6B**). In an ideal $R\bar{3}m$ structure, the transition metal sites, and lithium sites should be separated; however, there can be a cation mixing of Ni (mostly), Co, and Mn in the Li slabs for NCM cathodes, just like LNO structure (**Figure 6B**). [119] This phenomenon can take place during material synthesis, but also during the delithiation process of NCM at a high operating voltage such as over 4.3 V vs. Li/Li⁺. [120, 121] The Ni occupancy in the Li slabs leads to narrowing the distance between the transition metal slabs, resulting in decreasing the lithium diffusion in the Li slabs, and hence poor electrochemical performance. In addition to that, delithiation of NCM particles at high operation voltage brings forth the

structural transformation from layered $R\bar{3}m$ structure to Li-deficient (disordered) spinel $Fd\bar{3}m$ structure by the cation mixing and further delithiation generates the formation of rock salt NiO ($Fm\bar{3}m$) structure via oxygen evolution.[121] While the rock salt cubic phase transformation occurs near the surface of the NCM cathode, the Li-deficient spinel phase appears in the subsurface (**Figure 6B**). The generated NiO on the surface of the NCM particles acts as a passivation layer that blocks the Li^+ ion diffusion, hence affecting adversely on the capacity retention.[119] Furthermore, potential higher than 4 V vs. Li/Li^+ causes a drastic volume change of NCM cathodes and, thus, mechanical stress on the particles that would generate microcracks.[122] The emergent microcracks lead to electrical contact loss between particles as well as the current collector and particles. Besides, the electrolyte penetrates into those microcracks, it gets into contact with the inner-fresh active material, resulting in new cathode-electrolyte interphase (CEI). The CEI formation occurs on the surface/interface of the cathode particles as a film, which lowers the Li^+ ion diffusion rate and even blocks the Li^+ ion paths. For example, LiO_2 , Li_2CO_3 , MF_x (M: transition metal), LiF , etc., can be the product for commercial ethylene carbonate (EC)-based electrolytes with lithium hexafluorophosphate (LiPF_6).[123] Even a trace amount of H_2O can trigger the HF generation, which causes the dissolution of the highly oxidative Ni^{4+} and even Co^{4+} into the electrolyte.[124] Therefore, further developments for NCM cathodes are required to maintain its high capacity and cyclic stability at high operating voltages. In order to achieve that, different modification techniques have been continuously proceeded, such as doping, surface coating, and compositional partitioning.[125-130]

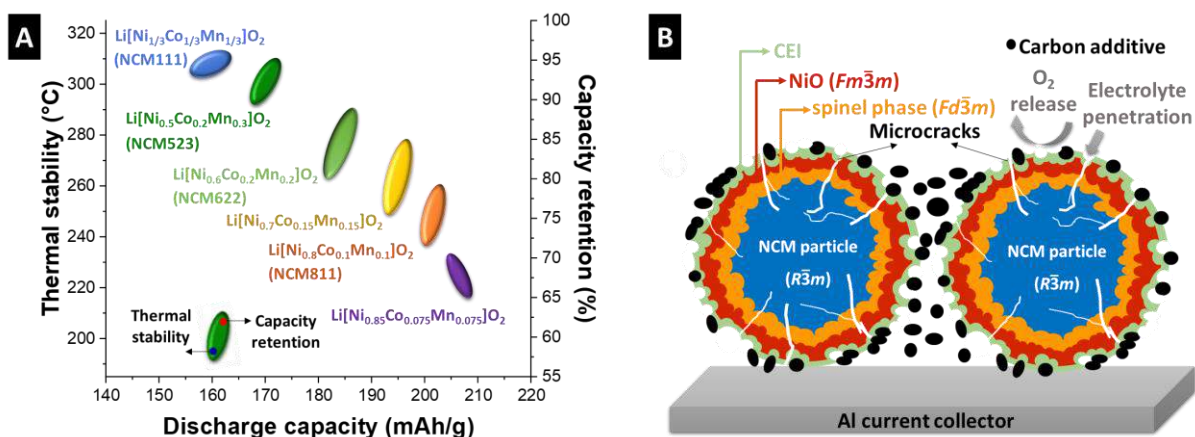


Figure 6. A) Relationship between discharge capacity, thermal stability, and capacity retention of the NCM electrodes (inspired by [118]). B) Degradation mechanism illustration of the NCM cathodes (inspired by [121]).

2.5.2. Spinel oxide family

Spinel cathodes can be crystallographically categorized with two main classes: cation-order spinel and cation disorder spinel. The cation-order spinels with the space group of $P4_332$ can be synthesized at low temperatures ($<650\text{ }^\circ\text{C}$); on the other hand, the cation-disordered, also known as the oxygen-deficient structures, can be obtained at high temperatures ($\geq 650\text{ }^\circ\text{C}$). [131] The cation-disordered spinel cathodes show better electrochemical performance compared to the cation-ordered spinel cathodes. [132]

The cation-disordered spinels have a general formula of AB_2O_4 , where the oxygen atoms occupy the $32e$ site, A stands for the cations on the tetrahedral sites ($8a$), and B refers to the cations on the octahedral sites ($16d$) in the cubic ($Fd\bar{3}m$) structure. [133] After discovering that spinel Fe_3O_4 can host material for Li^+ ion in the structure, spinel $\text{Li}_x\text{Mn}_2\text{O}_4$ (LMO) took a wide range of attention as a second class cathode for LIBs due to its low toxicity and low cost compared to layered cathodes. [134, 135] In the structure of LMO (see **Figure 7A**), the lithium atoms at the tetrahedral site ($8a$) share a face with the vacant octahedral sites ($16c$), which creates a three-dimensional empty channel for Li^+ ions migration. [136] That three-dimensional framework of LMO brings an advantage of fast lithium diffusion pathways and fast Li^+ ion conductivity, thus good rate capability; however, the theoretical capacity (148 mAh/g) and poor cyclic stability of LMO is its drawback. [137] The irreversible phase transformation for deeply discharging and the Mn dissolution can be responsible for the fast capacity fading of LMO (**Figure 7B**). [138]

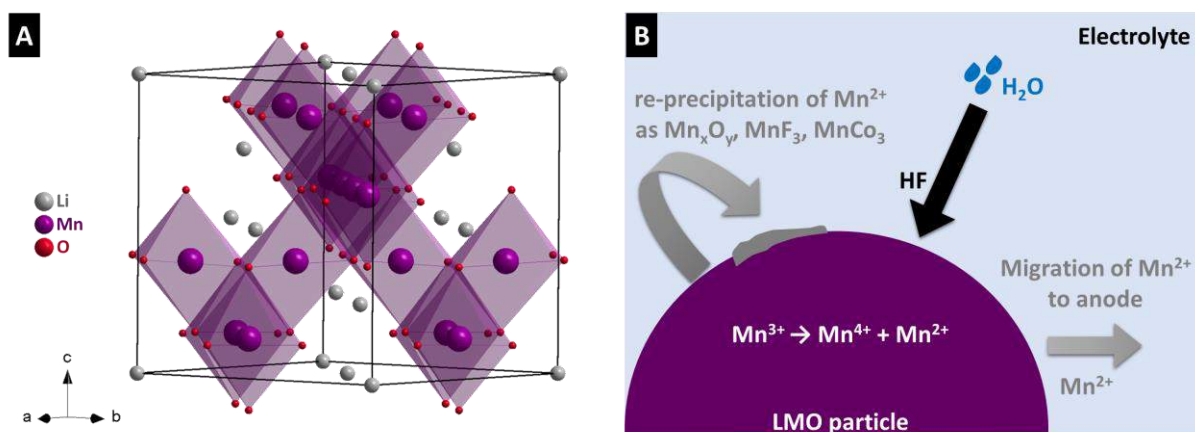


Figure 7. A) Structural illustration of LiMn_2O_4 . B) Illustration of the dissolution mechanism of spinel LiMn_2O_4 (inspired by [139]).

The lithium insertion/extraction of LMO can be divided into two regions; above and below 3 V vs. Li/Li^+ . [140] For the region above 3 V, during the lithium extraction, the $\text{Li}_x\text{Mn}_2\text{O}_4$ spinel structure transforms to the cubic $\lambda\text{-MnO}_2$ (Mn_2O_4 , $Fd\bar{3}m$) phase within two steps; the first step occurs at 3.9 V vs. Li/Li^+ (while $0.45 < x < 1.0$), and the second step takes place at 4.1 V vs. Li/Li^+ ($0.1 < x < 0.45$). [140] The obtained $\lambda\text{-MnO}_2$ phase crystallizes in the Mn_2O_4 spinel framework. [133] The unit cell contraction and expansion between those phases are small (7.6%), which provides structural stability to the LMO structure during lithiation/delithiation for the above 3 V region operated cells. [140, 141] For the below 3 V region, the studies revealed that additional lithium insertion into the LMO results in the two-phase reaction, where $\text{Li}_x\text{Mn}_2\text{O}_4$ transforms to tetragonal $\text{Li}_2\text{Mn}_2\text{O}_4$ ($I4_1/amd$) phase. [133] When the excess amount of Li^+ ion is introduced to the LMO structure, the population of Mn^{3+} ions in the structure increases. Such a case leads to Jahn-Teller distortion resulting in phase transformation of the structure and Mn disproportionation reaction on the surface of the electrode. The one reason for the poor cyclic stability of LMO at a deep-discharging state can be explained by large volume expansion (16%) during the phase transformation. [142] Hence, discharging below 3 V is avoided to be able to ensure better cyclic stability performance.

The Mn dissolution from LMO in acidic media is a well-known phenomenon even before its use for LIBs. [143] The trace amount of H_2O in the electrolyte might react with the commercially available organic electrolytes containing LiPF_6 salt, and resulting in HF production. The resulting HF reacts with the surface of the LMO particles and leads to Mn dissolution as Mn^{2+} ion in the organic electrolyte. Also, the lithiation process of LMO takes the

lead in manganese disproportionation reaction, where Mn^{3+} ions turn into Mn^{4+} and soluble Mn^{2+} ions (**Figure 7B**). Some of the Mn^{2+} ions migrate to the graphite anode and deposit on the surface of the anode, while some of the Mn^{2+} ions re-precipitate on the surface of the cathode and increase the electrode impedance.[139, 144-146]

Surface coating of LMO particles and cation substitution into the octahedral site (16d) of the LMO structure have been used as approaches to overcome the limiting factors of the electrochemical performance of LMO. The aim of the surface coating technique is that suppressing Mn dissolution by protecting the surface of LMO from the attack of HF. Different types of oxides (e.g., ZnO, ZrO_2 , Li_2ZrO_3 , Al_2O_3 , SiO [147-149], etc.), fluorides (e.g., YF_3 , and SrF_2 [150, 151]), and phosphates (e.g., $FePO_4$, and $AlPO_4$ [152, 153]) can be given as examples of the coating of the LMO surface. The goal of the cation substitution into the LMO structure is that decreasing the Mn^{3+} content and lowering the level of Mn^{2+} dissolution in the electrolyte. The different cations have been successfully substituted into the LMO structure, such as Co^{2+} , Al^{3+} , and Ni^{2+} , and the resulted general formula of the substituted LMO spinel is $LiM_xMn_{2-x}O_4$ (M : cation source and $0 \leq x \leq 1$).[154, 155] For instance, Ni-substituted $LiNi_xMn_{2-x}O_4$ (LNMO) has a great interest due to its high operation potential compared to LMO.

In an ideal structure of the LNMO spinel, the divalent state of Ni and the tetravalent state of Mn share the octahedral site (16d), while no trivalent state of Mn exists. In theory, the absence of the Mn^{3+} ions in the structure should lead to a Jahn-Teller distortion-free structure.[156] The electrochemically active Ni^{2+} contributes to the electrochemical process by Ni^{2+}/Ni^{3+} and Ni^{3+}/Ni^{4+} redox couples at around 4.7 V vs. Li/Li⁺. [157] Although the theoretical capacity of $LiNi_{0.5}Mn_{1.5}O_4$ is 147 mAh/g for the case of extraction of all Li^+ ions from the structure, the obtained-reversible capacity is about 135 mAh/g.[64, 158] The high electrochemical activation potential brings along the electrolyte decomposition for conventional organic electrolytes for LIBs, and also high-temperature synthesis causes the oxygen loss from LNMO, resulting in the formation of a rock salt Li_yNi_yO as an impurity phase, and increasing the Mn^{3+} content in the LNMO structure.[156, 158]

2.5.3. Polyanion (Olivine) family

The olivine structures are under crystallize in an orthorhombic space group with the general formula M_xAO_y , where M stands for the transition metal atoms in half of the octahedral site and A describes the atoms at the center of isolated tetrahedral geometry of polyanions (such

as $(\text{SO}_4)^{2-}$, $(\text{PO}_4)^{3-}$, $(\text{MoO}_4)^{2-}$, and $(\text{WO}_4)^{2-}$.[159, 160] The polyanions can provide a possibility to change the redox energy of the transition metal ions (see **Figure 8A**), and also, strong covalent bonding in the tetrahedral polyanions stabilize the entire structure.[160, 161] Hence, lithium transition metal phosphates with the general formula of LiMPO_4 (M: Fe, Mn, Co, Ni) and the theoretical capacity of ca. 167-171 mAh/g have been attracted much attention after the first discovery of LiFePO_4 (LFP) in 1997.[160, 162]

The progress on LFP cathodes shows that the $(\text{PO}_4)^{3-}$ polyanion in LFP structure conduce to lowering the Fermi energy level of $\text{Fe}^{3+}/\text{Fe}^{2+}$ redox couple to a useful level (3.4 V vs. Li/Li^+ for $\text{Fe}^{3+}/\text{Fe}^{2+}$), which is called an "inductive effect".[161, 163] In addition to that, the strong P-O covalent bonds in the $(\text{PO}_4)^{3-}$ polyanion provide high stability to the LFP structure (see **Figure 8B**), which prevents the oxygen evolution from the structure during the delithiation process. The excellent cyclic stability of LFP is correlated with the reversible phase transformation between LiFePO_4 and FePO_4 , which crystallize in the same space group (*Pbnm*). The LFP also exhibits a low volume change of 6% during the lithiation/delithiation process.[160] However, the lack of a continuous FeO_6 octahedral network in the LFP structure causes low electronic conductivity (ca. 10^{-9} S/cm), resulting in poor rate handling capability for high current rates.[164, 165] Therefore, recent investigations have been focused on improving the rate handling capability of LFP by coating the surface with conductive materials, such as carbon and its derivatives.[166-168] The optimization of carbon coating thickness has been shown as a critical factor. Thin carbon leads to poor rate capability performance due to an insufficient conductive network. A thick carbon layer restricts the Li^+ ion diffusion through the LFP, which leads to a loss of specific capacity.[167, 169] Still, the relatively low operational potential of LFP (ca. 3.4 V vs. Li/Li^+) compared to other cathode materials narrows down its use for high energy applications. Therefore, the research focus has moved to other LiMPO_4 family candidates, such as LiMnPO_4 and LiCoPO_4 , $\text{LiFe}_y\text{Mn}_{1-y}\text{PO}_4$.

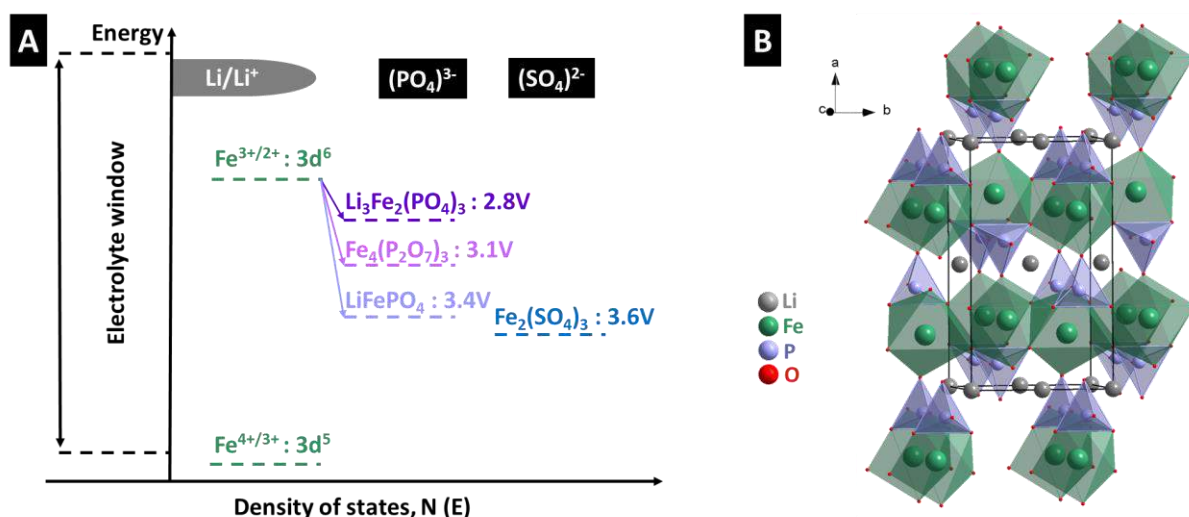


Figure 8. A) Schematic derivation of the energy diagram of Fe-based polyanion cathodes (inspired by [163]). B) Structural illustration of LiFePO₄.

LiMnPO₄ and LiCoPO₄ are considered as promising cathode material candidates for LIBs due to their high theoretical operational potentials, 4.1 V and 4.8 V vs. Li/Li⁺, respectively.[165, 170] Similarly to LiFePO₄, LiMnPO₄ possesses low electronic conductivity (1.8×10⁻⁸ S/cm) and exhibits performance decay at high current rates.[171] Decreasing the particle size, carbon coating, and Fe substitution to the LiMnPO₄ to form the LiMn_yFe_{1-y}PO₄ (LMFP) phase can be counted as methods to improve its electrochemical performance.[172-174] The well-engineered LiMn_yFe_{1-y}PO₄ results in the coexisting of Fe and Mn at the octahedral site (4c) and thus, partially increases the electronic conductivity, and therefore improved rate capability. However, the rapid capacity drop occurs at y > 0.8 due to increase of structure polarization.[160, 174] Therefore, LiMn_{0.8}Fe_{0.2}PO₄ has been accepted as the optimized phase for LMFP materials. Since the electronic conductivity of LMFP (2.3 × 10⁻³ S/cm) is still insufficient, carbon coating and reduction of particle size techniques have also been applied to LMFP cathodes. For example, recently, carbon-coated nanosized LiMn_{0.8}Fe_{0.2}PO₄ displays robust rate handling ability, like delivering a specific capacity of 110 mAh/g at a high rate of 10C.[175] Unlike the layer oxide cathodes, surface reactivity, and structural stability of polyanion materials are robust. However, the drawback of polyanion materials is the low intercalation potential, low electronic conductivity, and moderate capacity. For further improving this material by the transition metal substitution, nano-synthesis and carbon coating appear to be the best available option.

2.6. Negative electrodes (Anodes)

Since the beginning of the LIBs development, lithium metal was used as an anode due to its extremely high theoretical capacity (3,860 mAh/g), low density (0.59 g/cm³), and low negative electrochemical potential (-3.04 V vs. the standard hydrogen electrode (SHE)).[176] However, two major problems have been recognized; first, dendrite formation during Li deposition processes leading to internal short circuits resulting in safety hazards like a thermal runaway; second, low Coulombic efficiency (CE).[176, 177] The low CE can be partially solved using an excess amount of Li while avoiding the dendrite formation requires more advanced techniques. One of the approaches is based on using the different electrolyte systems to improve the stability of the solid electrolyte interface (SEI) on the Li metal, which is cracked during Li stripping at high currents, and the Li deposition process.[177] The research on Li metal anode is revisited and has been in intensive progress, but it is not yet ready for commercialization. Therefore, in the meantime, the alternative anodes for LIBs have been researched. To do so, one can find materials that react with lithium-ion via two different mechanisms. These mechanisms are insertion reaction and conversion reaction. By definition, the insertion reaction involves the insertion of guest ions (Li⁺) into a normally unoccupied interstitial site in the crystal structure. Strictly speaking, often when the host materials are layered materials (e.g., graphite), it is called intercalation reaction. Although the chemical composition of the original material can be changed (seen as solid solution), insertion/intercalation reaction does not result in their basic structural changes. Additionally, the interaction between lithium and host materials is rather ionic bonding instead of covalent bonding.

Conversion reaction or reconstitution reaction is the reaction between materials and lithium, which results in a new phase grow and the other disappear. The microstructure of one or more gets significantly changed or reconstruct the phase according to the chemical composition (known as phase diagram). The conversion reaction can be seen in two main types, including formation reaction and displacement reaction.[178] As for the formation reaction, it is the reaction where a new phase is formed in one electrode resulting in the modification of microstructure. The reaction mechanism can be seen in **Equation 15**:



In the anode materials, one can think of the alloying reaction as the formation reaction. For example, silicon is electrochemically reacted with lithium to form an alloy (Li_{4.4}Si) having an

amorphous structure. Another formation reaction can be seen in the lithium-sulfur battery, where S_8 ring molecule is converted to poly-sulfide and finally to LiS_2 .

The displacement reaction involves the displacement process, which results in two new phases in the electrode (**Equation 16**):



Specie A is reacted with BX by replacing B. The resulting products are AX and B, which are completely new phases compared with reactants. As noted, the main driving force of displacement reaction is determined by thermodynamic stability. The free energy of the formation of AX must be lower than that of BX. As an example of a displacement reaction, many metal oxides have been studied.[179] In the following sections, all mechanisms will be discussed in light of the state-of-the-art materials.

2.6.1. Intercalation/insertion type anodes

After Sony introduced the first lithium-ion battery to the market in 1991, the interest in carbonaceous compounds as a negative electrode for LIBs has been widely increased by years.[180] Although all carbonaceous materials (e.g., hard carbon, soft carbon, graphite, etc.) can be the host for lithium ions, their electrochemical performance as a negative electrode for LIBs is disparate from each other. The most used anode material, graphite, has a high theoretical capacity of 372 mAh/g within a potential range of 0 to 0.25 V vs. Li/Li^+ .[181] The most stable graphite structure arranged in ABAB stacking can be described as a layered hexagonal structure where the carbon atoms are located in a planar system, called graphene layers (**Figure 9A**).[182, 183] Although there is another graphite structure under the rhombohedral space group with ABCABC stacking order, both hexagonal as well as rhombohedral phases of graphite display similar capacities and intercalation mechanism. They transform into AA stacking by hosting the lithium in the center of carbon rings between the graphene layers.[184] The intercalation mechanism of lithium occurs with two-phase plateaus, which is well-known as a staging phenomenon (**Figure 9B**).[180, 184] The stage number describes the unoccupied graphene layers between two occupied by Li layers. The interplanar distance of graphene layers of the fully lithiated graphite (LiC_6 at stage I) enlarges to 3.70 Å compared to the initial state (3.35 Å).[185] Even though the theoretical lithium intercalation is fully reversible, the first cycle displays an irreversible capacity of around 10-20% when using organic electrolytes because of the solid-electrolyte interface (SEI) formation on the graphite

surface at ca. 0.8 V vs. Li/Li⁺ (**Figure 10A-B**).[184] The quality of SEI formation has a direct impact on the cyclic stability and safety aspects. The SEI film must exhibit a good Li⁺ conductivity and prevent Li⁺-solvent co-intercalation into the graphite layers.[186] The Li⁺-solvent co-intercalation leads to expanding the graphite matrix (ca. 150%), resulting in capacity fading due to graphite lattice deterioration (exfoliation).[187] Since 1990, ethylene carbonate (EC) based electrolytes with low viscosity solvents such as dimethyl carbonate (DMC) and diethyl carbonate (DEC) have been in use because of partially blocking excessive Li⁺-solvent co-intercalation by their effective film formation on the graphite surface.[16, 22, 188] The main drawback of graphite is its low operational potential, which triggers the lithium plating at high currents and low temperatures. When Li plating occurs on the graphite surface, it is accompanied by lithium and capacity loss, which is followed by additional SEI formation on the plated lithium surface. Also, further lithium deposition on the plated lithium grows as a so-called dendrite formation, which provokes the internal short-circuit and hence thermal runaway.[189]

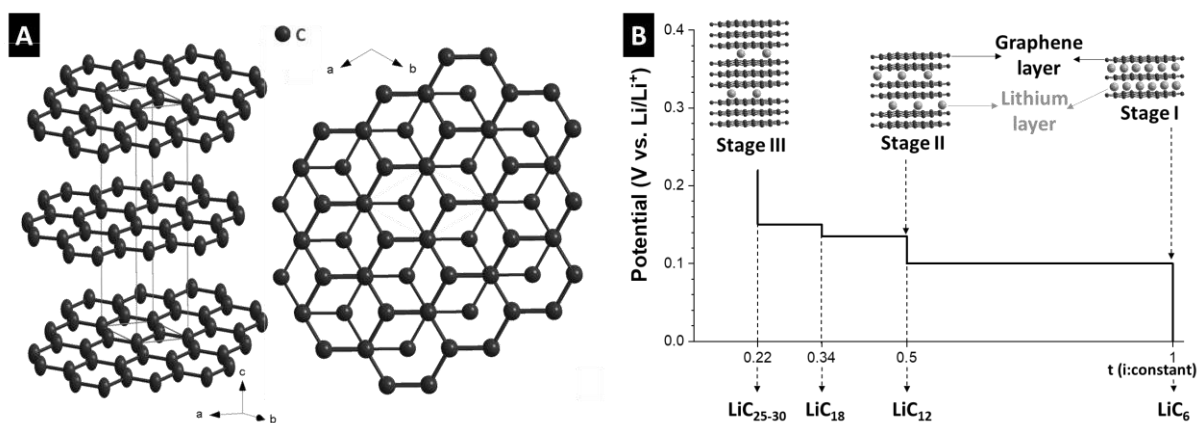


Figure 9. A) Structural illustration of graphite. B) Stage formation during lithiation into graphite (inspired by [184]).

Amorphous carbons, such as hard carbon (non-graphitizable) and soft carbon (graphitizable), has been used as an anode for LIBs. The hard carbon possesses small crystallites with several layers that are oriented randomly (**Figure 10B**).[190] The practical capacity of hard carbon is higher than that of the theoretical capacity of graphite due to capacitive contribution by lithium adsorption in the inner porosity.[191] However, the irreversible capacity is extremely high for the first cycle because of high surface area reactions such as additional SEI formation in the porous (**Figure 10B**). In addition to that, the lithium adsorption hysteresis occurs close

to 0 V vs. Li/Li^+ , which causes the lithium plating at high currents, eventuating in safety hazards; therefore, the obtainable specific capacity from hard carbon is limited for industrial applications.[192] On the other hand, soft carbon is known as low specific capacity carbon because of its smaller reversible capacity of 240-280 mAh/g.[184, 193] Due to those drawbacks of hard and soft carbon, the vast majority of commercial LIBs are built with a graphite anode.

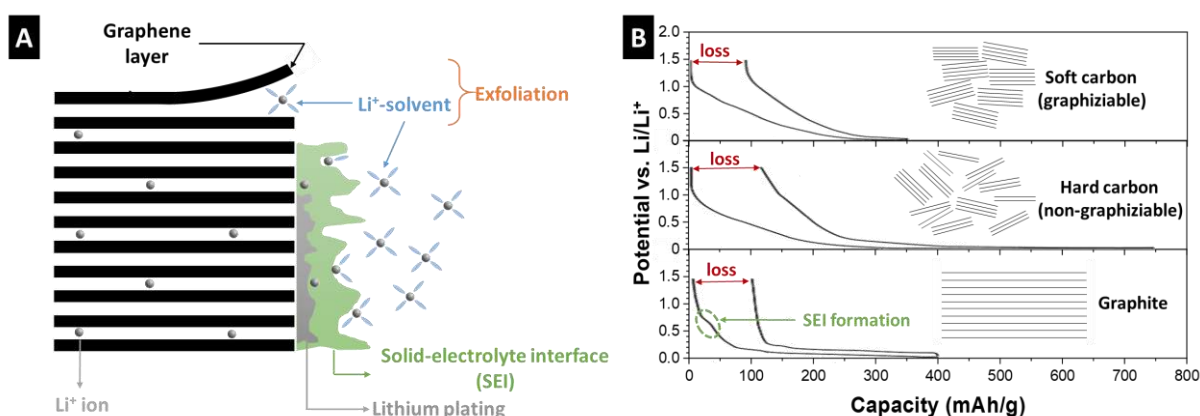


Figure 10. A) Schematic illustration of exfoliation of a graphene layer and SEI formation on the graphite (inspired by [139]). B) Typical voltage profiles for soft and hard carbon and graphite with their schematic illustrations (inset) (inspired by [194]).

The research interest has been dragged to the direction of insertion type metal oxides (e.g., TiO_2 , $\text{Li}_4\text{Ti}_5\text{O}_{12}$, etc.) to overcome graphite anode safety concerns. One of the insertion type metal oxides is TiO_2 as an alternative anode material for LIBs. Its polymorphs, such as anatase, rutile, brookite, and bronze, have been widely reported.[195] While all polymorphs have the same theoretical capacity of ca. 335 mAh/g for one mole lithium per formula, reaction mechanisms and Li insertion potentials vary.[196] For example, the insertion potential of the anatase phase is ca. 1.75 V vs. Li/Li^+ , while it is lower for the bronze phase, like 1.55 V vs. Li/Li^+ . Therefore, the bronze phase offers a higher energy density than the anatase phase. Moreover, the anatase phase exhibits a multi-step insertion mechanism, starting with a solid-solution reaction followed by a two-phase reaction. On the other hand, the bronze phase displays a simple two-phase insertion mechanism. However, TiO_2 phases are restricted by poor electrical conductivity, low Li diffusion coefficient (e.g., anatase: $10^{-17} \text{ cm}^2/\text{s}$), and practical capacity of about 150 mAh/g due to that 0.5 mole of lithium-ion is reversibly cyclable.[196, 197]

Another up-and-coming alternative candidate for graphite is lithium titanate ($\text{Li}_4\text{Ti}_5\text{O}_{12}$, LTO) due to its intrinsic properties, such as high insertion potential (ca. 1.5 V vs. Li/Li^+) and zero-strain insertion property during the electrochemical cyclic process.[198] The crystal structure of LTO is a spinel structure under the space group of $Fd\bar{3}m$, where tetrahedral $8a$ sites are occupied by lithium and the octahedral $16d$ sites are shared by titanium and lithium with an atomic ratio of 5:1, respectively (**Figure 11A**).[199] The lithium insertion causes the phase transformation from spinel LTO to rock salt $\text{Li}_7\text{Ti}_5\text{O}_{12}$ phase with a minor lattice contraction from 8.3595 Å to 8.3538 Å, respectively, resulting in the unit cell volume change of only 0.2%.[200] This small volume change, as called zero strain, provides superior structural stability to the LTO anode and prevents the LTO particles from microcrack issue, unlike the other insertion materials.[98] On the other hand, the high insertion potential of LTO at about 1.5 V vs. Li/Li^+ with a flat plateau (**Figure 11B**) prohibits the SEI formation, thereby supplying better safety than graphite anode but lowering the nominal cell voltage of 2.4 V than that of conventional LIBs (3.7 V).[98, 199] Moreover, one of the drawbacks of LTO is its low theoretical capacity of 175 mAh/g for three mole lithium per formula compared to graphite. Another drawback of LTO is its low electrical conductivity (10^{-8} - 10^{-13} S/cm) and low lithium diffusion coefficient (10^{-13} - 10^{-9} cm^2/s), which results in poor rate handling ability.[98, 201-205] Lattice doping, surface coating, forming a composite or hybrid with carbon, and reduction of particle size can be counted as the way of improvement of the ionic and electronic conductivity.[206-209] For example, hollow microsphere $\text{Li}_4\text{Ti}_5\text{O}_{12}$ coated with N-doped carbon particles showed a specific capacity of 141 mAh/g at a high C-rate of 20C.[206] However, even the improved performance of LTO still cannot meet the demand for desired high power LIBs. Therefore, the research on the better insertion-type of metal oxide anodes for LIBs has been going on.

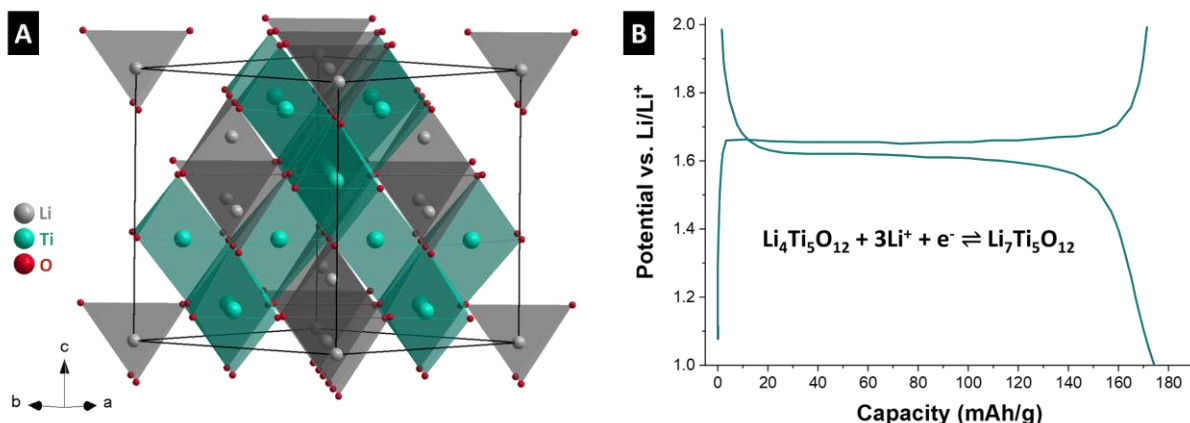


Figure 11. A) Structural illustration of $\text{Li}_4\text{Ti}_5\text{O}_{12}$. B) Typical voltage profile of $\text{Li}_4\text{Ti}_5\text{O}_{12}$ anode (inspired by [194]).

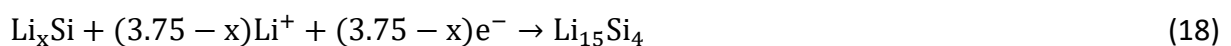
Vanadium and niobium-based oxides, such as V_2O_3 , Nb_2O_5 , $\text{Ti}_2\text{Nb}_{10}\text{O}_{29}$, etc., have been started investigating because of their wide range of oxidation states. Among vanadium-based oxides, few studies on vanadium trioxide (V_2O_3) assumes that it can be an insertion or conversion anode for LIBs. According to the insertion mechanism, the theoretical capacity of V_2O_3 is 356 mAh/g or 179 mAh/g, which are the numbers higher than that of the LTO anode.[210, 211] Although the high theoretical capacity of V_2O_3 and low voltage applicability (lower 1 V vs. Li/Li^+) makes it a possible promising candidate as an anode, the poor cycling stability and rate handling ability is its obstacles.[212] In the niobium-based oxides family, Nb_2O_5 has been shown as an alternative anode due to its high theoretical capacity of 200 mAh/g and SEI formation avoidable operation potential (above 1 V vs. Li/Li^+). In addition to that, Nb_2O_5 can be formed with different crystal structures, such as tetragonal, hexagonal, orthorhombic, and monoclinic, which brings along the advantage of different electrochemical responses. Another niobium-based anode family member is $\text{Ti}_2\text{Nb}_{10}\text{O}_{29}$, which possesses a higher theoretical capacity of 396 mAh/g than commercially in use insertion type metal oxide anodes, such as TiO_2 , LTO. However, low electronic conductivity (ca. 5×10^{-9} S/cm) leads to poor rate handling ability. Although each of those metal oxide anodes can be a great candidate for replacing commercial anodes, their electrochemical performances need to be improved by new approaches like the hybrid material approach, which will be further discussed in the later sections.

2.6.2. Formation type anodes

As aforementioned, formation is the reaction mechanism resulting in a new phase within the electrode materials. Usually, such a mechanism provides a higher capacity than the insertion mechanism. Among other anode materials, formation type anode materials result in high energy density and relatively low cost.[213] However, there are some handicaps regarding durability and life cycle due to their large volume expansion/contraction during the charging/discharging processes. The group IVA elements, silicon (Si), germanium (Ge), tin (Sn), and lead (Pb) can be given as examples, which can form alloys with lithium by following the route of the formation reaction. The obtained alloy exhibits different physical properties than either from lithium or the group IVA elements. In addition to the group IVA elements, various other elements have been investigated, such as Al, [214] Sb, [215] Zn, In, Cd [216], Mg, Bi, [217, 218] etc. In the following subsections, the most promising materials for real applications will be briefly discussed.

Silicon

Reasons for silicon as a promising anode candidate for LIBs are their extremely high theoretical capacity (4200 mAh/g, **Figure 12A**), high abundancy, low costs, and non-toxicity.[219, 220] At the elevated temperature (415 °C), Wen et al. presented that silicon and lithium undergo the formation of $\text{Li}_{12}\text{Si}_7$, Li_7Si_3 , $\text{Li}_{13}\text{Si}_4$, and $\text{Li}_{22}\text{Si}_5$ ($\text{Li}_{4.4}\text{Si}$).[221] The theoretical capacity calculation of silicon is based on the $\text{Li}_{4.4}\text{Si}$ alloy phase, where one silicon atom can accommodate a maximum of 4.4 lithium. However, room temperature experiments have shown that the voltage profile of silicon exhibits a relatively flat voltage plateau around 0.1 V vs. Li/Li^+ , and the metastable $\text{Li}_{15}\text{Si}_4$ ($\text{Li}_{3.75}\text{Si}$) phase instead of $\text{Li}_{4.4}\text{Si}$ occurs at the end of the lithiation.[222] The first lithiation mechanism of crystalline Si can be given as the following **Equation 17** and **18**:



Equation 17 represents the amorphization of crystalline Si by the formation of the amorphous Li_xSi phase until the potential reaches 50 mV vs. Li/Li^+ . On the other hand, further dropping of the voltage leads to the crystallization of the amorphous Li_xSi phase to crystalline $\text{Li}_{15}\text{Si}_4$ (**Equation 18**). The well-known amorphization of silicon anode occurs at the first delithiation process (**Equation 19**), where the crystalline $\text{Li}_{15}\text{Si}_4$ phase partially transforms into amorphous silicon instead of crystalline Si.[222, 223]



The lithiation process of silicon causes large volume expansion of ca. 280%, followed by pulverization, electrode delamination from the current collector, and instability of SEI on the silicon particles (**Figure 12B**), therefore, poor cyclic stability.[224] Moreover, the electronic conductivity (ca. 10^{-3} S/cm) and the lithium diffusion coefficient (10^{-14} - 10^{-13} cm²/s) in Si is relatively low, which hinders the performance of a silicon anode for high currents.[225] Nano-sized silicon particles can compensate for the volume change and shorten the lithium path, which eventuates in improved cyclic stability and rate handling performance. Another approach to further improve the performance of the silicon anode can be made by synthesizing silicon together with conductive carbon (e.g., carbon nanotubes (CNTs), graphite, etc.) to decrease the electrode resistance and advance rate handling performance. Although nanosized hybrid silicon/carbon can increase the cyclic stability performance of ca. 35%, there is still room for further improvement. Therefore, tremendous effort has been recently devoted to silicon nanowires due to their large strain, volume accommodation properties, and 1D electronic pathways for efficient charge transport.[225, 226]

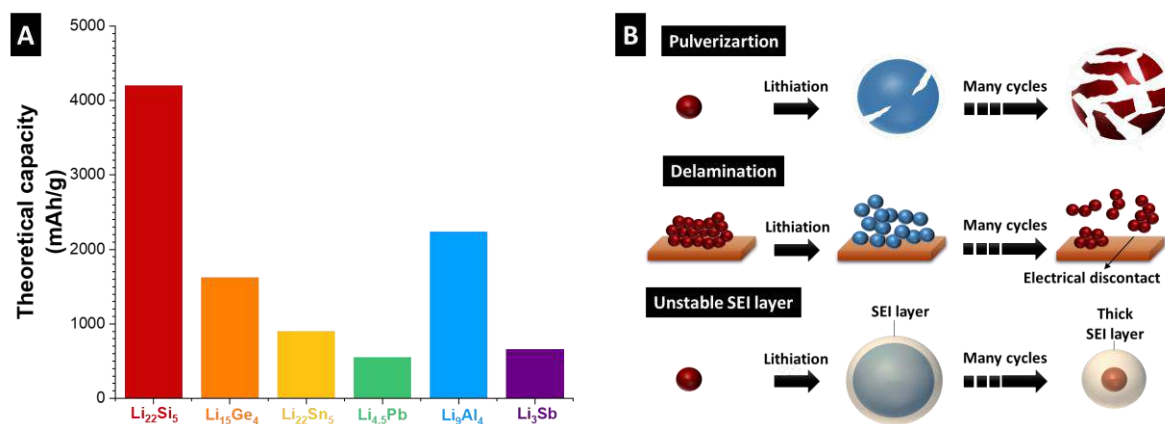


Figure 12. A) Theoretical capacities of some of the formation type anodes. B) Failure mechanism of silicon anode (inspired by [227]).

Aluminum

Aluminum is an attractive anode material for LIBs due to its low cost, high abundance, and excellent electronic conductivity, on top of its relatively low atomic weight compared to Si anode.[228] According to the Al-Li binary phase diagram, AlLi, Al₂Li₃, and Al₄Li₉ are the possible intermetallic compounds.[229] The theoretical capacity of Al₄Li₉ is 2235 mAh/g (**Figure 12A**),

while the theoretical capacity is 993 mAh/g for AlLi alloy.[214] However, as in the case of the silicon anode, the major challenge of an Al anode is its poor cyclic stability, which can be explained by two main reasons. First, the unit cell volume expansion of Al (ca. 96% for AlLi formation) during lithiation leads to instability of the SEI layer on the surface of Al particles, resulting in low coulombic efficiency.[230, 231] Second, Li-Al alloying leads to the pulverization of active material because of volume expansion/compaction, thus losing the electrical contact between the active material and current collector.[228] Recently, a carefully designed Al-TiO₂ yolk-shell approach has been suggested, where the TiO₂ shell faces with electrolyte and prevents the inner aluminum particles from SEI formation on them. In such a scenario, the yolk-shell-designed particles showed robust cyclic stability with a specific capacity of ca. 1100 mAh/g.[228]

The other elements

Germanium has gained attention due to the relatively higher lithium diffusion coefficient (10^{-12} - 10^{-10} cm²/s) and electronic conductivity (ca. 1.45×10^{-2} S/cm) compared to silicon, despite its discouraging cost and a lower theoretical capacity (1623 mAh/g for Li₁₅Ge₄, **Figure 12A**) than that of silicon.[218, 222, 232] Unlike silicon anode, the rate handling performance of Ge is superior compared to silicon anode because the diffusivity of lithium in Ge is 400 times higher than that of lithium in Si at room temperature. Hence, the particle size of Ge is not necessary to be smaller than Si to achieve superior performance.[233] In addition, the isotropic lithiation process prevents its particles from the cracking issue differently than silicon. However, similar to Si anodes, Ge also suffers from volume expansion (>300%) during the electrochemical process, where crystalline Ge particles transform to highly porous amorphous materials resulting in rapid capacity decay.[222] Therefore, the more advanced design of Ge anodes is still necessary.

Tin possesses the theoretical capacity of 900 mAh/g for Li₂₂Sn₅, which is similar to the capacity of Si and Ge (**Figure 12A**).[218] Another attractive property of Sn is its high electronic conductivity of 9.1×10^4 S/cm.[234] However, the brittle Li₁₇Sn₄ phase forms on the particles instead of the Li₂₂Sn₅ phase.[235] Like the other formation type anode materials, tin also exhibits poor cyclic stability. Unlike others, reducing the particle size of tin does not favor improving the lifespan. The studies showed that Sn particles undergo microcracking formation during lithiation and become porous after delithiation, which one can explain by less mechanical stability of Sn compared to Si.[218, 222]

Antimony (Sb) exhibits a high electronic conductivity (2.5×10^4 S/cm) and relatively high theoretical capacity (660 mAh/g for Li_3Sb , **Figure 12A**). The two-dimensional puckered layer structure of antimony makes Sb a promising anode candidate for LIB applications.[234] During lithiation, rhombohedral Sb transforms into the hexagonal Li_2Sb phase and finally reaches to cubic Li_3Sb phase.[215] The volume change of 135% during the lithiation process and thus poor cycle life are its drawbacks like the other formation type anodes.[236] Different design nanostructured Sb particles have been applied for LIBs to decrease the strain and thus enhance the cycle life performance.[237] Nanoparticles agglomeration has been pointed at as another reason for the short cycle life of Sb. Therefore, the synthesis of hybrid nanostructured Sb/carbon particles is offered as a solution since carbon can buffer the volume expansion/compaction during the electrochemical cyclic process. For example, rod-like Sb/carbon kept its specific capacity of 500 mAh/g even after 100 cycles.[238] Although there has been significant improvement in the Sb anode's performance, it is still far from practical applications.

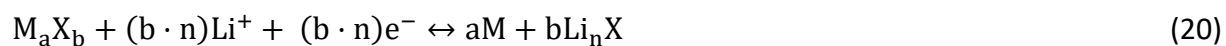
In short, employing formation reaction by mean of alloying reaction shares one issue in common: the large volume change. The nature of this mechanism is that after lithiation, new phases form, resulting in large strain and stress in the materials. Although alloying materials can deliver very high capacity, cyclic stability is very crucial. Hence, well-engineered materials are very important. Nanoparticles can lower the volume expansion during lithiation, but one should keep in mind that nanoparticles have high surface energy and high surface area. A large surface area means a large SEI layer, consuming more electrolytes and high-capacity loss for the first cycle. The well-designed morphology of materials could significantly prolong cycle life as the volume expansion is limit in one direction (e.g., nanowire). Surface engineering of alloying materials seems to be an elegant and effective method for enhancing cycle life. The formation type anodes could replace commercial anode like graphite, but the most important factor is the cost. Surface engineering or nanowire synthesis requires a multistep of processing and thus manufacturing process is difficult by this time.

2.6.3. Displacement type anodes

A wide range of transition metal oxides, sulfides, selenides, fluorides, nitrides, phosphides, and recently hydrides have been investigated as a high capacity anode to meet the demand for high energy density LIB systems.[239, 240] If the molecular formula of the displacement

type anodes is described as M_aX_b (M: transition metal, X: O, S, Se, F, N, P, and H, etc.), the reaction mechanism of lithiation/delithiation process can be written in the following

Equation 20:



The first lithiation of M_aX_b particles leads to structural change and amorphization, which results in a nanoscale transition metal cluster surrounded by an electrochemically inactive Li_nX phase. The determination of cyclic stability performance of the displacement anode materials is based on the decomposition reversibility of Li_nX matrix under the SEI layer by the highly electroactive transition metal particles (**Figure 13A**). Like formation type anodes, displacement type anodes are also known as severe volume change materials during lithiation/delithiation cycles.[241] Furthermore, displacement type anodes generally display tunable reaction potentials, depending on the durability of the ionic bond between cationic (transition metal) and anionic (e.g., O^{2-} , F^-) species. In other words, the weaker the ionic bonding, the larger potential for the full cell applications are. For example, $CoS_{0.89}$, CoO , CoF_2 , where the Co possesses the oxidation state of 2+, the displacement reaction occurs at 1.73 V, 1.79 V, and 2.74 V vs. Li^+/Li with the Gibbs free energy of -266, -347, and -499 kJ/mol, respectively.[242] In addition to that, there is a direct correlation between the oxidation state of transition metal and capacity. For instance, CoF_2 with Co^{2+} has a theoretical capacity of 600 mAh/g, while CoF_3 with Co^{3+} possesses the theoretical capacity of 694 mAh/g; however, CoF_3 with a high working potential 3.54 V vs. Li/Li^+ can be a cathode candidate instead of an anode.[242-244] Despite the high theoretical capacity, one of the drawbacks of the displacement anodes is the voltage hysteresis between charge and discharge profiles (**Figure 13B**) that one can explain by compressive stress in the surface layer of active materials, resulting in the prevention of lithium intercalation, and thus an extra electrical overpotential requirement.[179, 245] The voltage hysteresis and anionic species of the displacement anode are correlated. The voltage hysteresis from lower to higher for displacement type materials can be given in order like fluorides, oxides, sulfides, nitrides, and phosphides.[239] Pulverization problems during the electrochemical process and poor conductivity are responsible for poor rate capability and rapid capacity fading of displacement type anode materials.[246] Moreover, the formation of partially reversible electrolyte decomposition has been proven to be an additional challenge, which has an impact on cyclic stability.[247] Transition metal oxides have been chosen to discuss in the following section.

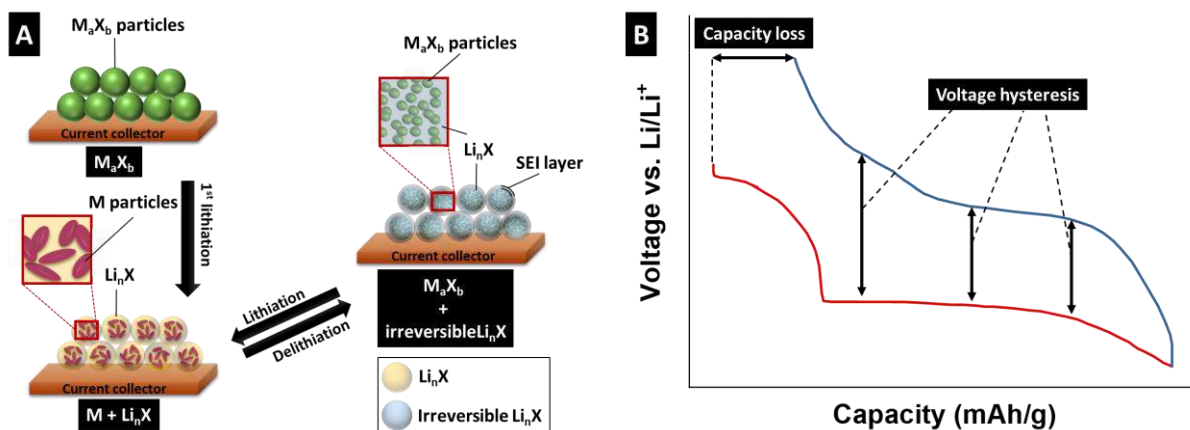


Figure 13. A) Schematic illustration of displacement type anodes (inspired by [239]). B) Voltage profile for showing the voltage hysteresis in displacement type anodes (inspired by [248]).

Transition metal oxides

Iron oxides, with their natural forms of hematite ($\alpha\text{-Fe}_2\text{O}_3$) and magnetite (Fe_3O_4), have been drawing attention due to their high theoretical capacities of 1007 and 924 mAh/g, respectively.[179] During the lithiation process at around 0.8 V vs. Li/Li^+ , the structural reorganization leads to the volume change of ca. 100% for hematite.[249] The voltage hysteresis occurs for the delithiation process by shifting the voltage between 1.2 V and 2.0 V vs. Li/Li^+ . [250] Both hematite and magnetite exhibit volume expansion and low coulombic efficiency; therefore, downsizing of the particles with the different morphological approaches and hybrid particles with carbonaceous materials have been tried to enhance the lifespan.[251-254] For example, neat Fe_2O_3 particles display fast capacity decay right after the first 40 cycles and reach the specific capacity of 300 mAh/g, Fe_2O_3 /carbon hybrid particles show a stable cyclic performance with the specific capacity of about 750 mAh/g.[255] FeO , with its cubic rock salt structure, has been investigated; however, it draws less interest than the other iron oxides due to its lower theoretical capacity of 744 mAh/g than that of the other iron oxides.[256]

The manganese oxide family has several suitable forms like MnO , Mn_2O_3 , MnO_2 , and Mn_3O_4 , with the theoretical capacities of 756, 1019, 1223, and 937 mAh/g, respectively, for lithium-ion battery applications.[257] As the iron oxide family, downsizing of the particles and hybridization with conductive carbon particles are used for the manganese family. For instance, nanosized MnO/C exhibit robust cyclic stability with a specific capacity of

1000 mAh/g at the specific current of 0.5 A/g, while hybrid Mn_3O_4 nanoparticles on reduced graphene oxide sheets show a specific capacity of ca. 800 mAh/g at 0.4 A/g.[258, 259]

CoO and Co_3O_4 phases possess the theoretical capacities of 715 and 890 mAh/g, respectively. The lithiation/delithiation of CoO takes place at 0.7 V and 2.1 V vs. Li/Li^+ , respectively, while the voltage plateaus of the Co_3O_4 phase appears between 0.8 V and 2.2 V vs. Li/Li^+ . [179] The electrochemical results of CoO and Co_3O_4 with carbonaceous materials show improved performances.[260, 261]

Molybdenum trioxide (MoO_3) and molybdenum dioxide (MoO_2) can be given as examples of molybdenum oxide displacement anodes for LIBs with the theoretical capacities of 1117 and 838 mAh/g, respectively. After the MnO_2 phase, the MoO_3 takes the second-highest capacity in the displacement reaction-based transition metal oxides.[179] For instance, MoO_3/C hybrid micro-balls kept its specific capacity at 800 mAh/g at the specific current of 2 A/g even after 300 cycles. [22]

There are many more transition metal oxide candidates for LIBs, such as CuO , Cu_2O , WO_3 , Cr_2O_3 , RuO_2 , NiO , SnO_2 , etc., with the theoretical capacities of 674, 375, 693, 1058, 806, 718, and 711 mAh/g, respectively.[179, 241, 262] Despite different capacities and voltage hysteresis, the common issues of transition metal oxides are poor coulombic efficiency, cyclic stability, and rate handling ability. Particle size reduction and hybridization techniques seem promising; however, further enhancement and enriching methods are still required.

3. Hybrid materials for lithium-ion battery

Hybrid materials (HMs) were developed a long time ago; however, their recognition starts at the end of the 20th and the beginning of the 21st century with having new physicochemical characterization techniques.[263] Hybrid materials are assembled from two moieties (organic and inorganic) on the molecular scale, provide new superior properties than their individual constituents.[263, 264] However, there can be great confusion between nanocomposites and the HMs due to the fact that both materials consist of two moieties; organic and inorganic. Although the definition borderline of these materials is unsharp, one can explain that nanocomposites contain discrete structural units within the particle size range of 1-100 nm. On the other hand, the HMs are the materials that are co-synthesized by both organic and inorganic moieties from molecular precursors.[263, 265] The co-synthesizing of the organic and inorganic components brings along the possibilities of a weak (e.g., van der Waals, electrostatic interactions) or strong (e.g., covalent bonding) interfacial interaction between building blocks of the HMs. While the former hybrid material is called *class I* hybrid, the latter is called *class II* hybrid. The properties of the obtained HMs are highly correlated with these interactions, which dependent on the co-synthesis conditions. The co-synthesis can be carried out either by a building blocks approach or *in situ* formation of the components. The building blocks approach can be used in the case of the requirement of keeping the original properties of one of the components, while *in situ* formation of the components approaches provides the possibility of totally different properties possessor HMs than its individual components.[263]

Conventional electrodes for LIBs are based on the physical admixture of electrochemically active material, conductive carbon, and a polymeric binder. In the resulted composite electrode, the active material and carbon display particle-to-particle junction, which can lead to electrochemical performance loss. The particle-to-particle junction can cause an increase of interfacial impedance, which decreases the charge percolation by way of disrupting the electron hopping process in the electrode.[266-268] The capacity loss during electrochemical cycling and the poor electrochemical performance of the composite electrodes can be explained by the absence of the continuous electronic and/or ionic network.[269, 270] The limitation of the composite electrode approach on the electrochemical performance was the driven force for the researcher to visit the hybrid electrode approach (**Figure 14**).

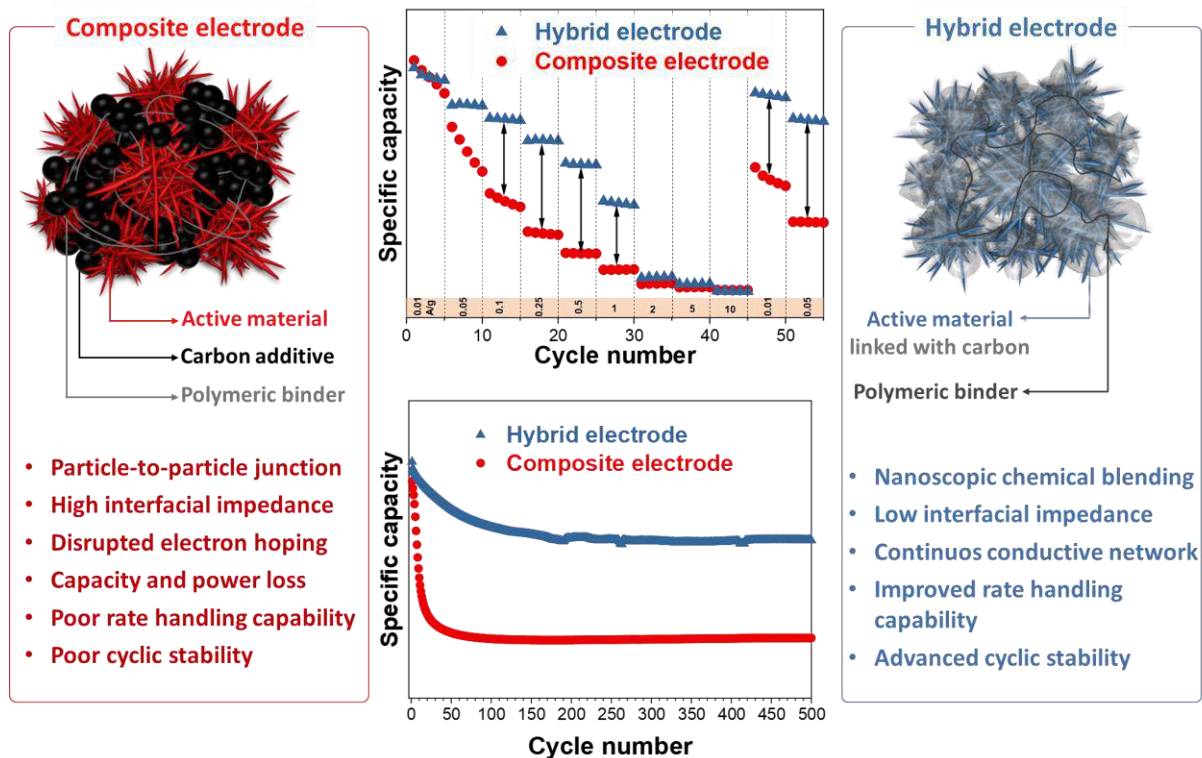


Figure 14. Overview of composite and hybrid electrode comparison.

Hybrid materials are the inspiration of the hybrid electrode approach, which bases on the co-production of electrochemically active and conductive carbon concurrently. The possible interfacial interactions between the electrochemically active inorganic material and carbon, and better homogeneity of the component distribution in the hybrid electrode compared to the composite electrode approach opens the door for better charge percolation. Consequently, hybrid electrodes show a better rate handling performance without sacrificing capacity.[265, 271] It is worth noting that the hybrid materials in the LIBs application are most likely class II materials. As reviewed by Wei-De Zhang et al., the preparation of hybrid material involves the combination of metal oxide and carbon (CNTs: carbon nanotubes). The CNTs or other carbon was found to facilitate the dispersion of the oxides. It, thus, provides a continuous conducting pathway.[272] However, the attachment of carbon and oxide materials have been under investigation. Depending on the different synthesis techniques applied, including impregnation, sol-gel, hydrothermal, and so on, the resulting hybrid materials exhibit rather different interactions between redox-active materials and carbon. If the carbon precursor has oxygen functional groups like oxidized-CNT and graphene oxide, such functional groups provide the chemically active sites for the growth of metal oxide.[271] Yet, defining the classes of metal oxide-carbon hybrid materials require thorough

characterization techniques, such as XANES (X-ray absorption near-edge spectroscopy). The XANES is a good candidate due to its sensitivity to the chemical bonding, electronic structure, and interactions in the materials, which can serve for realizing the interaction of such carbon and metal oxide hybrid material. For example, Liang et al. conducted XANES of Co_3O_4 -carbon hybrid material and observed from C, O, and N K-edge spectra that Co-O-C and Co-N-C are formed. Hence, it is the class II hybrid material because there is the phase that links between Co_3O_4 and reduced graphene oxide via covalent bonding.[273] Other studies were performed on CoO/NCNT (N-doped carbon nanotube) and $\text{MnCo}_2\text{O}_4/\text{N-rmGO}$ (N-doped reduced graphene oxide), which showed the formation of covalent interfacial metal-O-C and metal-N-C bonds.[274, 275] In addition to that, the interfacial interactions can provide some level of control over the morphology and size of the electrochemically active inorganic particles in the HMs, which has an impact on the electrochemical performance.[271] Downsizing the particles has an effect on the physical properties of the materials, the so-called quantum size effect. For example, every atom becomes a surface atom when the particle size is smaller than 10 nm, which means that every atom has the potential to interact with its surrounding environment.[263] The smaller particle size decreases the charge transfer resistance, and hence the smaller particle provides better rate handling ability and better cyclic stability with even higher specific capacity compared to its larger counterparts.[276] For example, Wang et al. revealed that $\text{LiMn}_{1-x}\text{Fe}_x\text{PO}_4/\text{reduced mildly oxidized graphene oxide (rmGO)}$ hybrid material for LIBs displays nanorod morphology while non-hybrid $\text{LiMn}_{1-x}\text{Fe}_x\text{PO}_4$ presents irregularly shaped morphology with larger particle size compared to hybrid particles. Furthermore, the non-hybrid $\text{LiMn}_{1-x}\text{Fe}_x\text{PO}_4$ exhibits a specific capacity of about 45 mAh/g at the low C-rate of C/2 (ca. 0.02 A/g), the hybrid $\text{LiMn}_{1-x}\text{Fe}_x\text{PO}_4/\text{rmGO}$ can supply a specific capacity of 150 mAh/g even at the high C-rate of 2C (ca. 0.3 A/g).[277] Also, Li et al. revealed that non-hybrid bare- Mn_3O_4 particles with the spherical morphology in size range of 40-100 nm show poor cyclic stability, like losing their capacity by half in the first 50 cycles. On the other hand, hybrid $\text{Mn}_3\text{O}_4/\text{graphene sheets}$ with a smaller particle size of ca. 20 nm exhibit stable cycle stability and better rate handling ability than that of its non-hybrid counterpart.[278] Another advantage of the hybrid electrode approach is that the synergetic effect of carbon can serve as a protective barrier towards the volume change during the electrochemical process.[279] For instance, composite pure silicon anode display poor cyclic stability and rate handling capability, where hybrid Si nanoparticles embedded in porous

carbon/graphene electrode shows improved cyclic stability and rate handling performance due to that its carbon scaffold can accommodate the huge volume expansion of Si particles during lithiation/delithiation process.[280] Hence, apart from seeking alternative anode/cathode materials, hybridization of the existing materials with carbon is seen as a driving force that will take the LIBs development one step further.

4. Overview of the conducted investigations

The current state-of-art for electrode designs for LIBs has been moving its direction to the hybrid electrode architecture due to its synergetic effects on carbon and electrochemically active material resulting in advanced electrochemical performance. However, the most common synthesizing methods for HMs require several complex steps. Although achieving hybrid materials are relatively new in the field of lithium-ion batteries, it has been proven that their performances are impressive compared to composite ones. The remaining question is which synthesis route could lead us to superior performance and commercially applicable. Additionally, understanding the underlining mechanism on why hybrid material has shown greater performance is essential. Does it depend on the synthesis method? How does the carbon in hybrid materials improve the ability of the Faradaic phase? Throughout this study, three types of metal oxide were selected as the anode materials (**Figure 15**), namely, V_2O_3 , Nb_2O_5 , and $Ti_2Nb_{10}O_{29}$. Instead of multi-steps wet chemical synthesis, the noble and simple solid-state reaction by the use of relatively cost-effective metal carbides precursors was selected to obtain metal oxide/carbon hybrid materials. This reaction is called the chloroxidation process and CO_2 oxidation process. The resulting materials in chapter 5.1, 5.2, and 5.3 are shown and proved the underlining hypothesis that hybrid materials can deliver much better performance in terms of fast charging/discharging and, most importantly, cyclic stability.

Vanadium oxides have been taken attention in the field of lithium-ion batteries due to their different oxidation states, such as V_2O_5 , VO_2 , etc. Although the V_2O_3 phase has great potential as an anode material for LIBs, only very few studies have been explored and showed that it suffers from the volume change during the lithiation/delithiation process. The studies revealed that carbon in the hybrid materials could suppress the volume change during the electrochemical process, resulting in advanced performance. Therefore, as a first material, V_2O_3 has been chosen to explore the new synthesis approach for hybrid materials in this dissertation (**chapter 5.1**).

Another promising anode candidate for LIBs is Nb_2O_5 due to its obtainable different crystal structures and its safe operating potential, above 1 V vs. Li/Li^+ . The fast charging ability of orthorhombic Nb_2O_5 , whereas monoclinic Nb_2O_5 exhibits the highest specific capacity among all structures. Thus, the orthorhombic and monoclinic phases are more attractive among all Nb_2O_5 phases (**chapter 5.2**).

Following up work from **chapter 5.1** and **5.2**, one can further improve the charge capacity toward binary metal oxide. The multiple redox couples of $\text{Ti}_2\text{Nb}_{10}\text{O}_{29}$ (TNO) provide a high theoretical capacity of about 400 mAh/g, which gives great potential to TNO for LIB applications. However, the poor conductivity of TNO leads to poor rate handling performance. The hybrid material approach has been proved to be useful to overcome the limitations of the composite approach. Therefore, TNO was selected to explore in **chapter 5.3**.

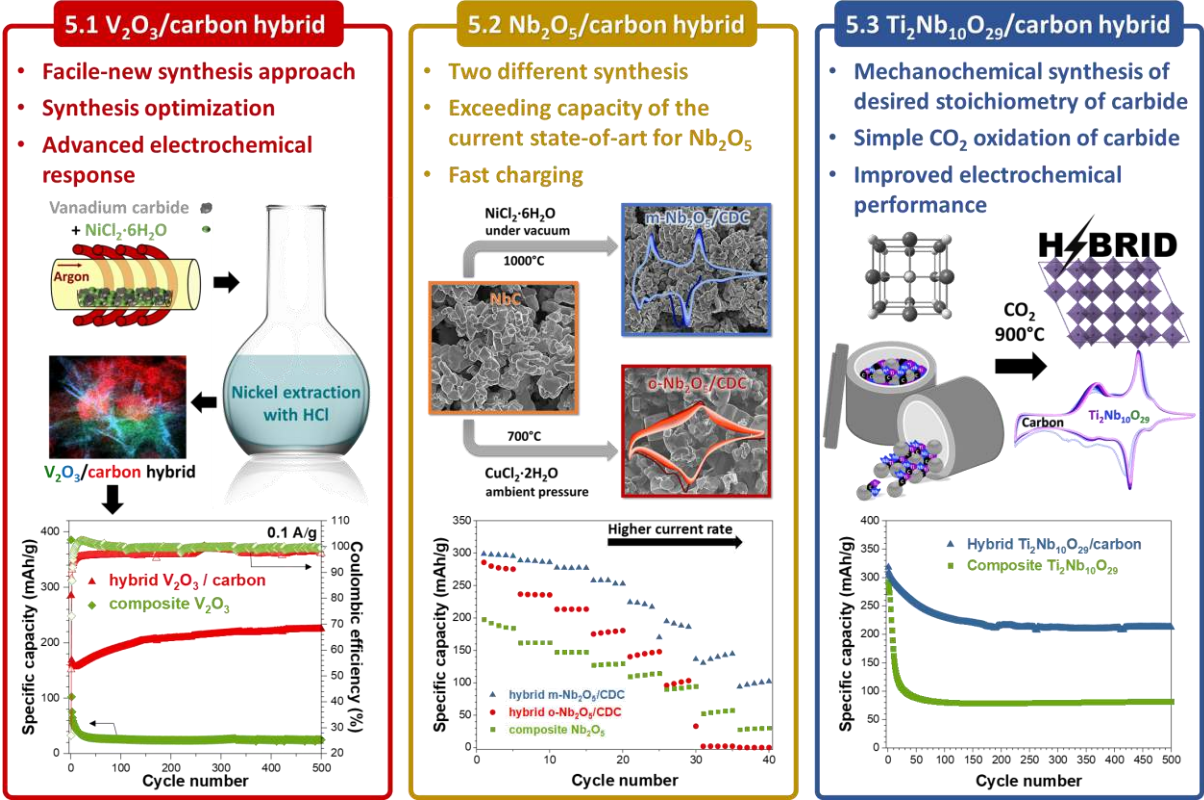


Figure 15. Overview of the different chapters of this dissertation.

5. Results and discussion

5.1. Vanadium (III) oxide/carbon core/shell hybrids as an anode for lithium-ion batteries

Öznil Budak,^{1,2} Pattarachai Srimuk,^{1,2} Aura Tolosa,^{1,2} Simon Fleischmann,^{1,2}
Juhan Lee,^{1,2} Stefan W. Hieke,³ Anna Frank,³ Christina Scheu,^{3,4} Volker Presser^{1,2}

¹ *INM - Leibniz Institute for New Materials, Campus D2 2, 66123 Saarbrücken, Germany*

² *Saarland University, Campus D2 2, 66123 Saarbrücken, Germany*

³ *Max-Planck-Institut für Eisenforschung GmbH, Nanoanalytics and Interfaces, Max-Planck-Straße 1, 40237 Düsseldorf, Germany*

⁴ *Materials Analytics, RWTH, Aachen University, Kopernikusstraße 10, 52074 Aachen, Germany*

Citation:

Ö. Budak, P. Srimuk, A. Tolosa, S. Fleischmann, J. Lee, S. W. Hieke, A. Frank, C. Scheu, V. Presser, VANADIUM (III) OXIDE/CARBON CORE/SHELL HYBRIDS AS AN ANODE FOR LITHIUM-ION BATTERIES, *Batteries & Supercaps* 2(1) (2019) 74-82.

Own contribution:

Material synthesis, measurements, data analysis, writing, plotting, discussion

The first study provides a facile new synthesis method (so-called chloroxidation), which involves the one-step conversion of vanadium carbide into a hybrid V₂O₃/nanoporous carbon using solid-state reactions. The chloroxidation process was performed under an Ar atmosphere with the vanadium carbide and NiCl₂·6H₂O as precursors by using different stoichiometric amounts between the precursors to obtain optimized conditions for the resulting hybrid material. The acquired hybrid materials were washed with HCl to remove residual elemental nickel. The optimized hybrid material showed improved rate handling capability than that of its composite counterpart. Furthermore, the composite electrode was losing its initial capacity even in the first ten cycles; the capacity of optimized hybrid material was increasing cycle by cycle.

Vanadium (III) Oxide/Carbon Core/Shell Hybrids as an Anode for Lithium-Ion Batteries

Öznil Budak,^[a, b] Pattarachai Srimuk,^[a, b] Aura Tolosa,^[a, b] Simon Fleischmann,^[a, b] Juhan Lee,^[a, b] Stefan W. Hieke,^[c] Anna Frank,^[c] Christina Scheu,^[c, d] and Volker Presser^{*,[a, b]}

We present a facile two-step synthesis of vanadium (III) oxide/carbon core/shell hybrid material for application as lithium-ion battery electrode. The first step is a thermal treatment of a mixture of vanadium carbide (VC) and $\text{NiCl}_2 \cdot 6\text{H}_2\text{O}$ at 700 °C in an inert gas atmosphere. Elemental nickel obtained from decomposing $\text{NiCl}_2 \cdot 6\text{H}_2\text{O}$ served as a catalyst to trigger the local formation of graphitic carbon. In a second step, residual nickel was removed by washing the material in aqueous HCl. By replacing $\text{NiCl}_2 \cdot 6\text{H}_2\text{O}$ with anhydrous NiCl_2 , we obtained a hybrid material of vanadium carbide-derived carbon and a

vanadium carbide core. Material characterization revealed a needle-like morphology of the rhombohedral V_2O_3 along with two carbon species with a different degree of graphitic ordering. We varied the $\text{NiCl}_2 \cdot 6\text{H}_2\text{O}$ -to-VC ratio, and the optimized material yielded a capacity of $110 \text{ mAh} \cdot \text{g}^{-1}$ at $2.5 \text{ A} \cdot \text{g}^{-1}$ which increased to $225 \text{ mAh} \cdot \text{g}^{-1}$ at $0.1 \text{ A} \cdot \text{g}^{-1}$ after 500 cycles in the potential range of 0.01–3.00 V vs. Li/Li^+ . This enhanced performance is in stark contrast to the loss of lithium uptake capacity when using commercially available V_2O_3 mixed with carbon black, where 93% of the initial capacity was lost after 50 cycles.

1. Introduction

Lithium-ion batteries (LIBs) are attractive for electrochemical energy storage due to their high energy density and efficiency.^[1,2] The continuous research and development on LIBs not only consider the storage capacity and the ability to handle high charge/discharge rates, but also safety, cost, and cycle life.^[3–5] As a critical component of LIBs, the structural and electrochemical properties of the electrode materials strongly influence the overall device performance.^[2,6,7] Graphite, silicon, titanium dioxide, and lithium titanate have been thoroughly investigated for LIBs anodes.^[8–11] With a specific capacity of $372 \text{ mAh} \cdot \text{g}^{-1}$, graphite anodes have been employed in commercial LIB devices.^[1] However, graphite anodes suffer from safety hazards because metallic lithium can be easily electroplated during charging, particularly at a high current rate and low temperatures.^[7,12] Silicon anodes have a much higher theoretical capacity of about $4200 \text{ mAh} \cdot \text{g}^{-1}$ but provide at present only poor capacity retention due to substantial

volumetric changes during cycling.^[13] Anodes composed of TiO_2 (rutile or anatase) and $\text{Li}_4\text{Ti}_5\text{O}_{12}$ exhibit higher rate capability and structure stability but their use remains restricted by their lower theoretical capacity of 168–175 $\text{mAh} \cdot \text{g}^{-1}$.^[9,14,15]

Capitalizing on different vanadium oxidation states, V_2O_5 , VO_2 , and V_2O_3 , have been explored as LIB cathodes and anodes.^[16–19] Among these, V_2O_5 is an attractive LIB cathode material due to the high theoretical capacity of $294 \text{ mAh} \cdot \text{g}^{-1}$ in the range of 4.0–2.0 V vs. Li/Li^+ .^[20,21] A slightly higher capacity of $323 \text{ mAh} \cdot \text{g}^{-1}$ has been reported for VO_2 in the range of 1.8–3.8 V vs. Li/Li^+ .^[22] V_2O_3 is a promising anode candidate for LIBs but there have been only very few studies exploring V_2O_3 as an anode material for LIBs so far.^[23–26] The current state of the art assumes that V_2O_3 undergoes structural volume change during galvanostatic charge/discharge cycling; this effect and the low electronic conductivity explain the poor cycling stability.^[25] For example, there is a 50–60% capacity loss of bulk V_2O_3 after 50–100 charge/discharge cycles.^[23,25] Additionally, it remains unclear from the literature if it is intercalation or conversion by which mechanism V_2O_3 operates as an anode in LIBs. For example, Shi et al. (Ref.^[24]) assumed that V_2O_3 is a typical conversion type anode material for LIBs with a theoretical capacity of $1070 \text{ mAh} \cdot \text{g}^{-1}$. Another mechanism is intercalation reported by Sun et al. (Ref.^[25]) and McNulty et al. (Ref.^[27]) as the theoretical capacity of $356 \text{ mAh} \cdot \text{g}^{-1}$ and $179 \text{ mAh} \cdot \text{g}^{-1}$ for $\text{Li}_1\text{V}_2\text{O}_3$, respectively.

To overcome the limited performance of bulk V_2O_3 mixed with a conductive additive, recent studies have explored hybrid electrodes.^[18] In composite electrodes, mechanically admixed carbon serves as an electrically conducting agent between the metal oxide and the current collector. Alternatively, the hybrid electrode architecture employs a nanoscopic chemical blending of the metal oxide phase with carbon, and the resulting materials provide improved electrochemical performance.^[18,28,29]

[a] Ö. Budak, P. Srimuk, A. Tolosa, S. Fleischmann, Dr. J. Lee, Prof. Dr. V. Presser
INM – Leibniz Institute for New Materials
Campus D2 2, 66123 Saarbrücken, Germany
E-mail: volker.presser@leibniz-inm.de

[b] Ö. Budak, P. Srimuk, A. Tolosa, S. Fleischmann, Dr. J. Lee, Prof. Dr. V. Presser
Department of Materials Science and Engineering
Saarland University
Campus D2 2, 66123 Saarbrücken, Germany

[c] Dr. S. W. Hieke, Dr. A. Frank, Prof. Dr. C. Scheu
Max-Planck-Institut für Eisenforschung GmbH
Nanoanalytics and Interfaces
Max-Planck-Straße 1, 40237 Düsseldorf, Germany

[d] Prof. Dr. C. Scheu
Materials Analytics
RWTH Aachen University
Kopernikusstraße 10, 52074 Aachen, Germany

Supporting information for this article is available on the WWW under <https://doi.org/10.1002/batt.201800115>

Studies on V_2O_3 /carbon hybrids have reported a range of capacity values, and while some works used the material as a cathode, others used it as a LIB anode. For example, Odani et al. investigated carbon-coated V_2O_3 as a LIB cathode with a low capacity of $25 \text{ mAh} \cdot \text{g}^{-1}$ in the voltage range of 2.0–4.0 V vs. Li/Li^+ .^[30] As found by Sun et al.,^[25] ordered lamellar V_2O_3 provides a capacity of about $120 \text{ mAh} \cdot \text{g}^{-1}$ with the cutoff voltage of 0.3 V and 1.5 V vs. Li/Li^+ , and Jiang et al. (Ref.^[23]) reported carbon-coated yolk-shell V_2O_3 microspheres as an anode material with the capacity of $437 \text{ mAh} \cdot \text{g}^{-1}$ at the specific current of $0.1 \text{ mA} \cdot \text{g}^{-1}$ in the voltage window of 0.1–3.0 V vs. Li/Li^+ . The porous V_2O_3/C composite material was reported with a discharge capacity of $283 \text{ mAh} \cdot \text{g}^{-1}$ in the voltage range of 0–3 V vs. Li/Li^+ by Shi et al. (Ref.^[24]). The reversible capacity of $536 \text{ mAh} \cdot \text{g}^{-1}$ from composite V_2O_3 -ordered mesoporous carbon at a current density of $1 \text{ A} \cdot \text{g}^{-1}$ in the voltage range of 0.02–3 V was achieved by Zeng et al. (Ref.^[31]).

Considering the promising performance of hybrid materials, we have previously developed the top-down synthesis of V_2O_3 /carbide-derived carbon core/shell particles.^[20] In our earlier work, we used a three-step synthesis: first, a mixture of vanadium carbide and $\text{NiCl}_2 \cdot 6\text{H}_2\text{O}$ was heated in a vacuum, and the evolving chlorine gas extracted vanadium from the outer regions of the carbide grains; this leads to the formation of a carbide-derived carbon shell. The latter is sufficiently nanoporous so that ion transport across the carbon shell is accomplished. Second, residual nickel from the thermal decomposition of $\text{NiCl}_2 \cdot 6\text{H}_2\text{O}$ was removed by washing in aqueous HCl. Third, the residual carbide core was transformed to V_2O_5 by thermal oxidation at 450–600 °C while the carbide-derived carbon shell was maintained. In our present work, we significantly simplify the synthesis by using only one thermal treatment step that, concurrently, yields a carbide-derived carbon shell and a vanadium oxide core. The produced material is freed from residual nickel by simple washing with aqueous HCl and can be used as a LIB anode with promising cycling performance.

Experimental

Material Synthesis

$V_2O_3/\text{VC-CDC}$ and $\text{VC}/\text{VC-CDC}$ core/shell materials were synthesized by using a solid mixture of VC powder (purity 99.9%, $< 2 \mu\text{m}$, Sigma Aldrich) and two different precursors, $\text{NiCl}_2 \cdot 6\text{H}_2\text{O}$ (purity 99.5%, Alfa Aesar) and NiCl_2 (purity 99.99%, Sigma Aldrich), respectively.

The stoichiometric amounts of 2.0 mol, 2.5 mol, and 3.0 mol of $\text{NiCl}_2 \cdot 6\text{H}_2\text{O}$ per 1 mol of VC were mixed and ground in a mortar. The mixtures were transferred into quartz glass crucible and placed in a quartz tube furnace (HTRH, Gero) which was continuously flushed with Ar gas with a flow rate of $50 \text{ cm}^3 \cdot \text{min}^{-1}$. The furnace was heated from room temperature to 700 °C with a heating rate of $2.5 \text{ }^\circ\text{C} \cdot \text{min}^{-1}$ and held at the annealing temperature for 3 h. Afterward, the samples were cooled to room temperature. The outlet of the tube was fed through a reservoir filled with aqueous 5 M NaOH to neutralize the gaseous reaction products (esp. CO_2 and HCl, see Supporting Information, Figure S1). The resulting

material was washed with 200 mL of aqueous 3 M HCl to remove the residual elemental nickel. The solution was stirred overnight and washed with an excess amount of distilled water until the pH of the discarded water was neutral. The filtered product was dried at 80 °C overnight. The final products of the $V_2O_3/\text{VC-CDC}$ syntheses are labeled $V_2O_3/\text{VC-CDC-1:2}$, $V_2O_3/\text{VC-CDC-1:2.5}$, and $V_2O_3/\text{VC-CDC-1:3}$.

For the synthesis of the $\text{VC}/\text{VC-CDC}$ core/shell material, we modified the procedure used for the synthesis of $V_2O_3/\text{VC-CDC}$ core/shell material by using a stoichiometric ratio of NiCl_2 and VC of 2:1 and a synthesis temperature of 1000 °C.

Structural Characterization

X-ray powder diffraction (XRD) patterns were recorded using a D8 Discover diffractometer (Bruker AXS) with $\text{Cu-K}\alpha$ radiation ($\lambda = 1.5406 \text{ \AA}$) and a Goebel mirror in point focus (0.5 mm). The system was calibrated with LaB_6 (purity 99%, Sigma Aldrich), and the samples were placed on a single sapphire crystal. A VANTEC-500 (Bruker AXS) 2D detector was positioned at 20°, 40°, 60°, 80°, and 100° 2θ with a measurement time of 7 min per step. Rietveld refinement analyses were performed by using the software TOPAS from Bruker.

Raman spectra were recorded with a Renishaw inVia Raman Microscope equipped with an Nd-YAG laser with an excitation wavelength of 532 nm and a power of 0.05 mW at the surface of the sample, using an objective lens with a numeric aperture of 0.75. The spectra of the samples were recorded with 20 accumulations and 30 s acquisition time. All spectra were normalized to 100%, and fitting was achieved assuming Voigt peak profiles for the D-mode, G-mode, and amorphous carbon.

Gas sorption analysis (GSA) was conducted to obtain a specific surface area (SSA), and pore volume of the samples. We carried out the measurements with an Autosorb-6B system (Quantachrome) using nitrogen gas at $-196 \text{ }^\circ\text{C}$ in a relative pressure range from 0.008 to 1.0 in 76 steps. Prior to the measurements, the powder samples were degassed at 250 °C and 10^2 Pa for 12 h. The SSA was calculated using the Brunauer-Emmett-Teller (BET) equation^[32] in the linear pressure range (ca. 0.01–0.1) with the ASiQwin-software. The values for the total pore volume were obtained at a relative pressure of $P/P_0 = 0.95$. Since the materials were hybrids of either VC-CDC and VC or VC-CDC and V_2O_3 , the direct use of density functional theory kernels designed for pure carbon samples prohibited the further porosity analysis regarding the pore size distribution.^[33] Instead, we limited the porosity analysis to the quantification of the BET surface area and the total pore volume.

The sample morphology was characterized by scanning electron microscopy (SEM) using a JEOL JSM 7500F at an acceleration voltage of 3 kV. The samples were fixed on a steel sample holder by using sticky carbon tape. The chemical compositions of the samples were quantified by energy dispersive X-ray (EDX) spectroscopy with an X-Max-150 detector (Oxford Instruments) attached to the SEM chamber. The spectra of fifty spots were measured with an acceleration voltage of 14 kV and averaged.

Transmission electron microscopy (TEM) investigations were carried out by using a JEOL JEM-2100F instrument operated at 200 kV. Scanning TEM (STEM) was performed on a probe-corrected FEI Titan Themis 60-300 X-FEG S/TEM instrument operated at 300 kV equipped with an FEI Super-X windowless EDX system with 4 synchronized silicon drift detectors from Bruker. The samples were dispersed in isopropanol or ethanol through sonication for 2 min and drop-casted onto a copper grid with a lacey carbon film.

Thermogravimetric analysis coupled with mass spectrometry (TGA-MS) was carried out up to 1000 °C with a heating rate of 2.5 °C·min⁻¹ in argon with a STA449F3 Jupiter and QMS 403 C Aeolos from Netzsch for a mixture of 1 mol VC per 2 mol of NiCl₂·6H₂O.

Electrochemical Characterization

To prepare electrodes, 90 mass% of the active material was blended in a mortar with 10 mass% polyvinylidene fluoride (PVdF, Alfa Aesar) as a binder. N-methyl-2-pyrrolidone (NMP, Sigma Aldrich) was added to the solid mixture until the slurry reached a sufficient viscosity; the slurry was then coated on a Cu foil at a wet thickness of 150 μm. The coated slurry was dried in a vacuum oven at 110 °C overnight. The packing density of the electrode was adjusted by dry-pressing in the rolling machine (HR01 hot rolling machine, MTI) and cut to circular shape with a diameter of 12 mm. The average mass loading was 2.6 mg·cm⁻² with a dry thickness of 96 μm.

For comparison, we also made electrodes using commercially available V₂O₃ (Sigma Aldrich) which consisted of 80 mass% V₂O₃, 10 mass% carbon black (C65 from Imerys Graphite & Carbon), and 10 mass% PVdF following the same preparation procedure as for the other materials. These electrodes are labeled “com-V₂O₃” to reflect the commercial source of V₂O₃ and the composite nature of these electrodes (i.e., a physical mixture of the metal oxide and the conductive additive).

For electrochemical measurements, 2032-type coin cells were assembled in an argon-filled glove box (O₂, H₂O < 1 ppm). We used lithium foil (diameter of 12 mm) as a reference and counter electrode, 1 M lithium hexafluorophosphate (LiPF₆) in an ethylene carbonate (EC) and dimethyl carbonate (DMC) mixture in the ratio EC:DMC (1:1 by volume) as electrolyte (LP 30, BASF), and two layers of Celgard 2325 as separator with a diameter of 18 mm.

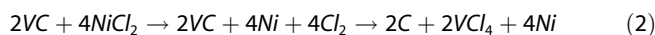
Cyclic voltammetry (CV) was carried out using a VMP300 system from Bio-Logic multichannel potentiostat in the potential range of 0.01–3.00 V vs. Li/Li⁺ at a scan rate of 0.05 mV·s⁻¹. An Arbin system was used for galvanostatic charge/discharge cycling with potential limitation (GCPL) in the range of 0.01–3.00 V vs. Li/Li⁺ at room temperature. The calculated specific capacity of the samples is based on the active mass of the electrode material including carbon mass of the hybrid materials. For the com-V₂O₃ electrode, the specific capacity was normalized by just the metal oxide mass. The capacity retention test was performed during galvanostatic charge/discharge cycling at 0.1 A·g⁻¹ from 0.01 V to 3.00 V vs. Li/Li⁺ in half-cell configuration.

To better understand the structural changes of the material during electrochemical benchmarking, post mortem XRD and Raman spectroscopy analyses were carried out for the electrodes by disassembling the cells after cycling stability testing. To understand the intermediate structural changes, the cells were charged/discharged at the specific current at 0.1 A·g⁻¹ for 40 cycles. Thereafter, the cycled cells were held at 1.5 V, 0.75 V, and 0.01 V vs. Li/Li⁺ for the lithiation and at 0.75 V, 1.5 V, and 3.0 V for the delithiation. Those six cells were disassembled and gently cleaned by using propylene carbonate (PC). The washed electrodes were subjected to XRD measurements.

2. Results and Discussion

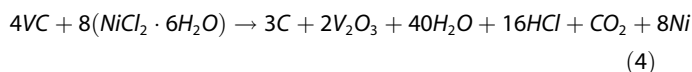
2.1. Material Synthesis Concept

Thermal annealing of nickel chloride leads to its decomposition and the evolution of chlorine gas.^[20] In the presence of a metal carbide like vanadium carbide, the evolving chlorine selectively reacts with the metal ions, producing gaseous vanadium chloride. This process leaves behind nanoporous carbide-derived carbon (CDC) as the solid reaction product.^[20,34, 35] For example, the mixture of vanadium carbide and NiCl₂·6H₂O leads to the formation of VC-CDC when the annealing is carried out in a vacuum furnace.^[20] As seen from Equation (1–3), this reaction considers the decomposition of NiCl₂ which is obtained via the dehydration of NiCl₂·6H₂O during the thermal treatment (700 °C). Nickel is a by-product of the process and can be removed from the material by aqueous HCl washing because the resulting NiCl₂ phase is water soluble. Adjusting the molar ratio of chlorine to carbide, a VC core can be maintained while a shell of nanoporous CDC is being produced. In a subsequent step, the vanadium carbide core is then transformed to vanadium oxide, while maintaining largely the CDC shell. The combination of a metal oxide core for lithium-ion intercalation and an electrically conductive outer carbon shell make this core/shell hybrid material attractive for electrochemical energy storage.^[18]



The need for two separate thermal treatment steps, one for the CDC-process and a subsequent one for the carbide oxidation, complicates the fabrication of this core/shell hybrid material. This applies in particular because the two thermal treatment steps are separated by washing the carbide/carbon core/shell material in aqueous HCl.

The present work uses the same precursor as our previous work (i.e., VC and NiCl₂·6H₂O) but carries out the annealing process in an inert gas atmosphere (argon) instead of a low vacuum. By this way, we avoid the rapid removal of desorbing water and enable a reaction per Equation (4).



In addition, we also carried out experiments with anhydrous nickel chloride (NiCl₂), which should only result in CDC formation via Equation (2).

To understand the mechanism of V₂O₃ formation, we carried out a thermogravimetric analysis with a coupled mass spectrometer (Figure S1). The mass loss below 100 °C aligns with the desorption of surface water, as indicated by the increase of the H₂O signal. As the temperature was increased to 200 °C, a significant amount of water was produced by the

release of crystal water from NiCl_2 . Additionally, gaseous HCl was detected at 100–200 °C suggesting the loss of chloride, which possibly reacts with the as-produced water to form hydroxyl radicals. The absence of OH^- in our measurements indicates that resulting hydroxyl radicals react on the surface of vanadium carbide yielding O_2 gas as the final product. Apparently, the loss of chloride and crystal water continued as the temperature was further increased. Oxygen leads to the formation of vanadium (III) oxide at around 700 °C, which aligns with a decrease of the O_2 signal at this temperature.

2.2. Material Characterization

We first analyzed the VC/VC-CDC sample synthesized from the mixture of anhydrous NiCl_2 and vanadium carbide by XRD. The synthesis mechanism of VC/VC-CDC follows Equation (2), and we obtained residual cubic vanadium carbide (PDF 01-089-2608, Figure 1A and Table S1) with a unit cell of $a = 8.34 \text{ \AA}$ with characteristic Bragg reflections at 37.4°, 63.0°, and 43.4° 2 θ . In addition, the Bragg reflection at 26.2° indicates carbon (hexagonal graphite: PDF 01-089-7213) and the presence of vanadium carbide-derived carbon (VC-CDC) was also confirmed by Raman spectroscopy (Figure 1B and Table 1).^[34] The Raman

Table 1. Raman spectra analysis of the D and G-modes. FWHM = full-width at half-maximum.

Sample	Mode	Position [cm^{-1}]	FWHM [cm^{-1}]	I_D/I_G
com- V_2O_3	D-mode	1354	109	2.02
	G-mode	1606	77	
VC/VC-CDC	D-mode	1349	61	0.9
	G-mode	1587	50	
$\text{V}_2\text{O}_3/\text{VC-CDC-1:2}$	D-mode	1351	63	1.1
	G-mode	1593	66	
$\text{V}_2\text{O}_3/\text{VC-CDC-1:2.5}$	D-mode	1349	73	1.1
	G-mode	1591	61	
$\text{V}_2\text{O}_3/\text{VC-CDC-1:3}$	D-mode	1348	109	2.1
	G-mode	1603	68	

spectra present two distinct peaks between 1200–2000 cm^{-1} , namely the D-mode and G-mode characteristic of incompletely graphitic carbon.^[36] The G-mode corresponds to the stretching vibration of pairs of sp^2 atoms in rings and chains, and the D-mode corresponds to the breathing mode of sp^2 -hybridized carbon rings, which is active in the presence of defects.^[37] Peak fitting of the Raman spectra (Table 1 and Figure S2A) yielded the D-mode position at 1349 cm^{-1} and the G-mode position at 1587 cm^{-1} . In addition to that, carbon of the VC/VC-CDC sample presents a low I_D/I_G ratio of 0.9 and a full-width at half-

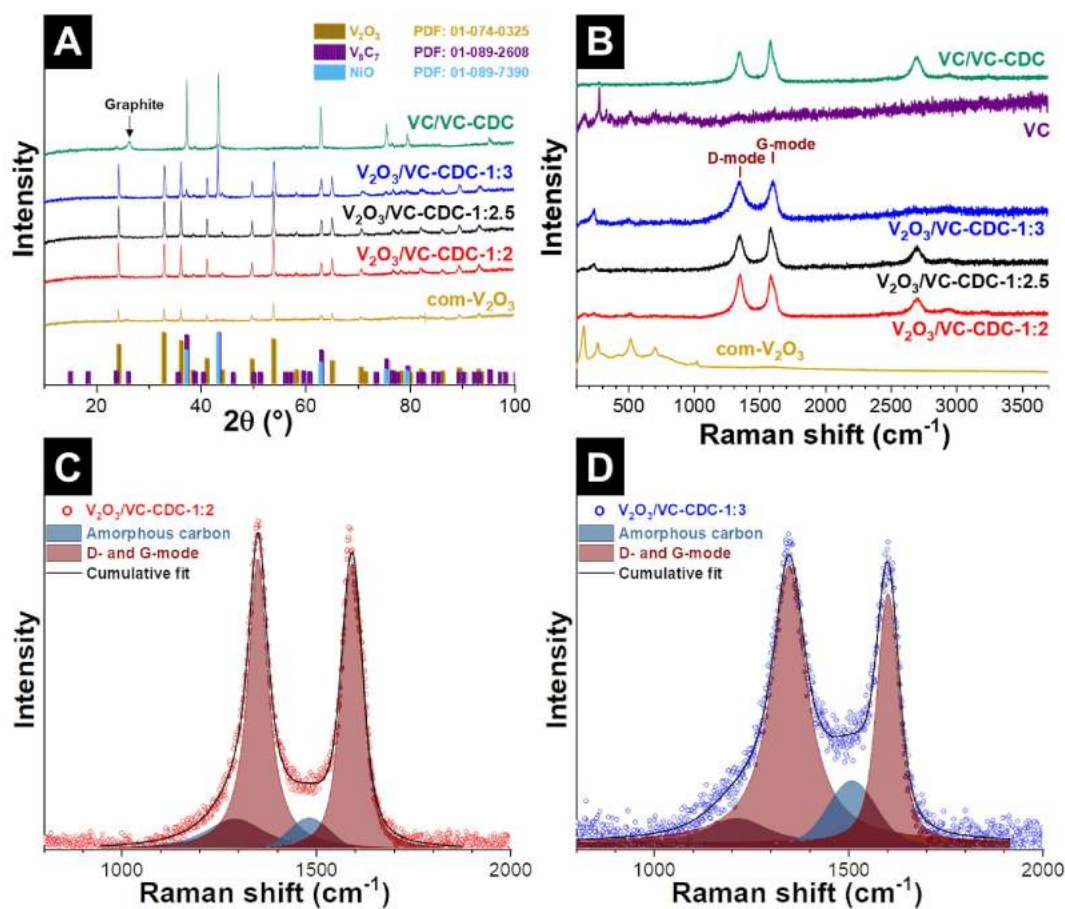


Figure 1. A) X-ray diffraction (XRD) pattern of the samples and the matched reflection position phases from the literature. B) Raman overview spectra of the samples. Fitted Raman spectra of $\text{V}_2\text{O}_3/\text{VC-CDC-1:2}$ (C) and $\text{V}_2\text{O}_3/\text{VC-CDC-1:3}$ (D).

maximum (FWHM) for the D- and G-mode with 61 cm^{-1} and 50 cm^{-1} , respectively.

In contrast to the use of anhydrous NiCl_2 , there is a different reaction outcome when mixing vanadium carbide with $\text{NiCl}_2 \cdot 6\text{H}_2\text{O}$. We used stoichiometric ratios of 1:2, 1:2.5, and 1:3 of VC to $\text{NiCl}_2 \cdot 6\text{H}_2\text{O}$ to investigate the influence of the amount of Ni on the degree of the graphitization of the carbon phase. As seen from the X-ray diffraction pattern (Figure 1A), we obtained vanadium oxide instead of VC-CDC. The sharp X-ray reflections at 24.3° , 33.1° , 41.2° , 43.3° , and 54.1° 2θ relate to karelianite-type rhombohedral V_2O_3 (PDF 01-074-0325). The higher energy barrier of the oxidation of nickel, compared to vanadium, prevented the formation of nickel oxide^[38] and no reflections related to NiO (PDF 01-089-7390) were identified by XRD (Figure 1A and Table S1). The only exception was $\text{V}_2\text{O}_3/\text{VC-CDC-1:3}$ where 21 mass % of NiO was found in the sample (as determined by Rietveld analysis).

Beside vanadium oxide, we also obtained carbon (VC-CDC) when using $\text{NiCl}_2 \cdot 6\text{H}_2\text{O}$. The Raman spectra of all $\text{V}_2\text{O}_3/\text{VC-CDC}$ samples (Figure 1B) show the characteristic broad peaks of incompletely graphitic carbon at around 1350 cm^{-1} (D-mode) and 1597 cm^{-1} (G-mode). Table 1 lists the positions of D- and G-mode, the full-width at half-maximum (FWHM), and the integral I_D/I_G intensity ratio of these peaks. Figure 1C–D presents the peak fitting of the Raman spectrum of $\text{V}_2\text{O}_3/\text{VC-CDC-1:2}$ and $\text{V}_2\text{O}_3/\text{VC-CDC-1:3}$. The $\text{V}_2\text{O}_3/\text{VC-CDC-1:3}$ sample has the highest I_D/I_G ratio of 2.1 and the widest FWHM for the D- and G-mode with 109 cm^{-1} and 68 cm^{-1} , respectively. In the case of $\text{V}_2\text{O}_3/\text{VC-CDC}$ samples, the higher degree of carbon disorder than that of

VC/VC-CDC aligns with the partial oxidation of carbon by oxygen during the in-situ synthesis (Figure S1B). Yet, the spatial resolution of Raman measurements of about $1\text{ }\mu\text{m}$ only provides us with an average quantitative assessment of all carbon present within the sampling volume. Therefore, we used transmission electron microscopy to better characterize carbon on a nanoscale.

When anhydrous nickel chloride thermally decomposed, we see that vanadium carbide particles (Figure 2A) were transformed to carbide cores engulfed by two carbon species: one with a lower degree of ordering (as typical for CDC obtained at 1000°C)^[39] and layered ribbons of graphitic carbon (Figure 2B–C). The overall structural ordering of VC-CDC is low, but graphitic layers and ribbons are seen throughout the VC/VC-CDC sample. The latter possibly impeded the diffusion of in-situ produced chlorine gas and kinetically slowed the carbide-to-carbon transformation.^[40] In our case, this is beneficial since we wanted to maintain a carbide core for the carbide-to-oxide formation. We explain the formation of two carbon phases with a very different degree of ordering by the catalytic properties of elemental nickel which is produced as a by-product of decomposing nickel chloride.^[41,42] Transmission electron micrographs confirm the presence of both carbon phases for all $\text{V}_2\text{O}_3/\text{VC-CDC}$ samples (Figure 2D–I). For these oxide/carbon hybrid materials, we find needle-like V_2O_3 surrounded by carbon, as evidenced by elemental mapping performed in STEM mode (Figure S4). Among the $\text{V}_2\text{O}_3/\text{VC-CDC}$ samples, a higher stoichiometric ratio of VC to $\text{NiCl}_2 \cdot 6\text{H}_2\text{O}$ yielded fewer needle-like V_2O_3 (Figure 2D–I).

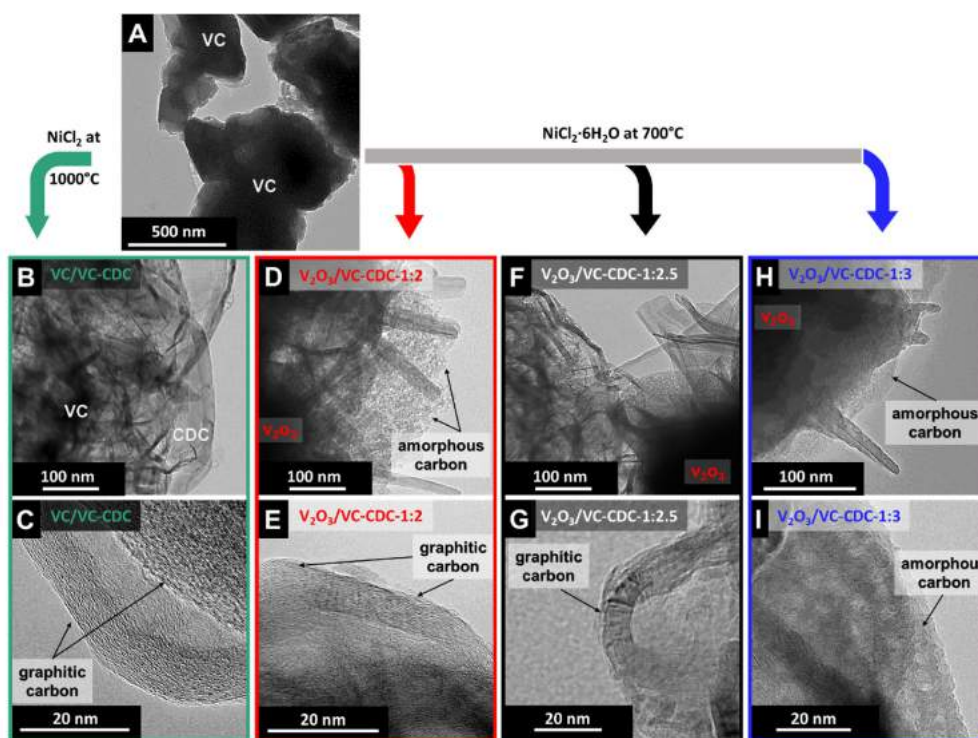


Figure 2. Bright field transmission electron micrographs of the initial vanadium carbide(A), of VC/VC-CDC (B–C), of $\text{V}_2\text{O}_3/\text{VC-CDC-1:2}$ (D–E), of $\text{V}_2\text{O}_3/\text{VC-CDC-1:2.5}$ (F–G), and of $\text{V}_2\text{O}_3/\text{VC-CDC-1:3}$ (H–I).

Elemental analysis of the samples on a more global scale was performed by EDX measurements in the SEM (Table 3). The highest carbon content (ca. 33 mass%) was found for VC/VC-CDC, and the amount of carbon decreased for V₂O₃/VC-CDC with the increasing amount of NiCl₂·6H₂O. The lowest value of carbon was found for V₂O₃/VC-CDC-1:3 with ca. 8 mass%. The decreased carbon content aligns with an increased amount of oxidizing species being mobilized during the decomposition of NiCl₂·6H₂O.

We carried out nitrogen gas sorption to characterize the porosity of the synthesized materials, and the data are presented in Table 2. As seen from the sorption isotherm

Sample	SSA _{BET} [m ² ·g ⁻¹]	Total pore volume [cm ³ ·g ⁻¹]
VC/VC-CDC	125	0.21
V ₂ O ₃ /VC-CDC-1:2	71	0.08
V ₂ O ₃ /VC-CDC-1:2.5	24	0.03
V ₂ O ₃ /VC-CDC-1:3	16	0.02

Sample	Carbon [mass%]	Oxygen [mass%]	Vanadium [mass%]	Nickel [mass%]
VC/VC-CDC	32.5 ± 14.2	11.8 ± 6.7	53.7 ± 14.8	0.5 ± 0.4
V ₂ O ₃ /VC-CDC-1:2	15.8 ± 6.2	30.7 ± 7.3	52.1 ± 10.2	0.9 ± 1.0
V ₂ O ₃ /VC-CDC-1:2.5	13.3 ± 7.0	21.6 ± 6.9	63.2 ± 9.4	2 ± 1.1
V ₂ O ₃ /VC-CDC-1:3	7.6 ± 4.3	22.3 ± 8.1	60.6 ± 16.2	9.4 ± 5.0

(Figure S5), all samples showed a type II isotherm which is indicative of macroporous materials with some mesopores.^[43] VC/VC-CDC had a total pore volume of 0.21 cm³·g⁻¹ with an SSA_{BET} of 125 m²·g⁻¹. Among the metal oxide/carbon hybrids, the V₂O₃/VC-CDC-1:2 sample had the largest SSA_{BET} of 71 m²·g⁻¹ and the smallest surface area was found for V₂O₃/VC-CDC-1:3 (16 m²·g⁻¹). This trend aligns with the amount of

carbon and shows that the porosity is mostly accomplished by nanoporous carbon, whereas a small specific surface area is associated with the metal oxide domains.

2.3. Electrochemical Analysis

For the electrochemical characterization, we used electrodes made from the as-synthesized VC/VC-CDC and V₂O₃/VC-CDC materials and added 10 mass% of PVdF binder but no conductive additive. The latter was possible because the presence of VC-CDC by itself was sufficient to provide a conductive pathway for electron transport in the samples. For comparison, we also cast electrodes of a mixture of 80 mass% commercial V₂O₃, 10 mass% of carbon black, and 10 mass% of PVdF; these electrodes are labeled com-V₂O₃. Using 1 M LiPF₆ in an EC/DMC as the electrolyte, we tested all materials in a half-cell configuration with an oversized lithium counter electrode.

The initial cycle performance was analyzed by cyclic voltammetry (CV) in the range of 0.01–3.00 V vs. Li/Li⁺ at a scan rate of 0.05 mV·s⁻¹ to characterize the reduction and oxidation potentials of the samples (Figure 3). The largest amount of charge was passed for V₂O₃/VC-CDC-1:2, and the cyclic voltammograms of all samples exhibit broad cathodic and anodic peaks. Near 0.01 V vs. Li/Li⁺, the increased current of all samples results from intercalation and deintercalation of lithium-ions into graphitic carbon.^[44] The other possible current peaks relate to the multistep reduction of V³⁺ to lower valence states.^[23] The cathodic peak at 0.70 V may be associated with the formation of Li₂O, and the complex solid electrolyte interface (SEI);^[45] its disappearance after the first cycle aligns with the formation of a stable SEI (Figure 3B). In addition, the V₂O₃/VC-CDC-1:3 sample shows a cathodic peak at 0.40 V (Figure 3A), and it is possible that the presence of NiO leads to a shift in the potential for SEI formation.

With contributions from the lithiation/delithiation of the V₂O₃ domains and a small contribution from carbon lithiation/

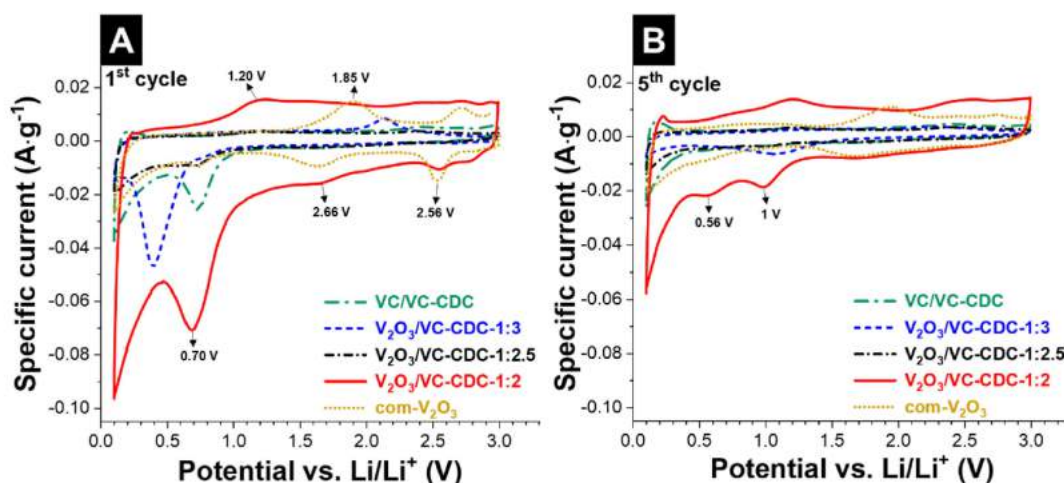


Figure 3. Cyclic voltammograms of the samples from the 1st cycle (A) and the 5th cycle (B) in the range of 0.01–3.00 V vs. Li/Li⁺ at a scan rate of 0.05 mV·s⁻¹.

delithiation (Table 3), we can express the Li intercalation/deintercalation process by Equations (5) and (6).^[25]



We further characterized the electrochemical performance with galvanostatic charge/discharge cycling at a specific current of $0.1 \text{ A} \cdot \text{g}^{-1}$ in the voltage range from 0.01 V to 3.00 V vs. Li/Li⁺. The voltage profiles of the 10th cycle are found in Figure 4A. The results agree with the electrochemical behavior seen with cyclic voltammetry: the highest charge storage capacity is seen for V₂O₃/VC-CDC-1:2 ($157 \text{ mAh} \cdot \text{g}^{-1}$), followed by VC-CDC ($76 \text{ mAh} \cdot \text{g}^{-1}$), com-V₂O₃ ($44 \text{ mAh} \cdot \text{g}^{-1}$), V₂O₃/VC-CDC-1:2.5 ($39 \text{ mAh} \cdot \text{g}^{-1}$), and V₂O₃/VC-CDC-1:3 ($20 \text{ mAh} \cdot \text{g}^{-1}$). In general, we see the combination of (multistep) lithiation of V₂O₃. Below 0.1 V vs. Li/Li⁺, there is an additional charge contribution related to lithiation of carbon.

The rate handling performance of all samples was characterized by galvanostatic charge/discharge cycling at specific currents in the range of 0.01–10 $\text{A} \cdot \text{g}^{-1}$ in the voltage window of 0.01–3.00 vs. Li/Li⁺ (Figure 4B). After the first cycle at the specific current of $0.01 \text{ A} \cdot \text{g}^{-1}$, V₂O₃/VC-CDC-1:2 demonstrates the highest capacity of about $187 \text{ mAh} \cdot \text{g}^{-1}$, which is higher than the capacity of the com-V₂O₃ composite electrode ($126 \text{ mAh} \cdot \text{g}^{-1}$), and V₂O₃/VC-CDC-1:2.5 preserves the lowest reversible capacity of $51 \text{ mAh} \cdot \text{g}^{-1}$. The initial capacity of V₂O₃/VC-CDC-1:3 sample drops from $234 \text{ mAh} \cdot \text{g}^{-1}$ to $66 \text{ mAh} \cdot \text{g}^{-1}$ at the 5th cycle, which can be explained by the presence of bunsenite-type cubic NiO (Figure 1A): NiO is known to cause poor capacity retention for lithium-ion batteries due to its low electrical conductivity and substantial volume change during the conversion reaction.^[46] Accordingly, we confirm a rapid and complete loss of the reversible capacity of V₂O₃/VC-CDC-1:3 at higher rates.

As the specific current is increased, V₂O₃/VC-CDC-1:2 shows a good rate handling by maintaining values of about

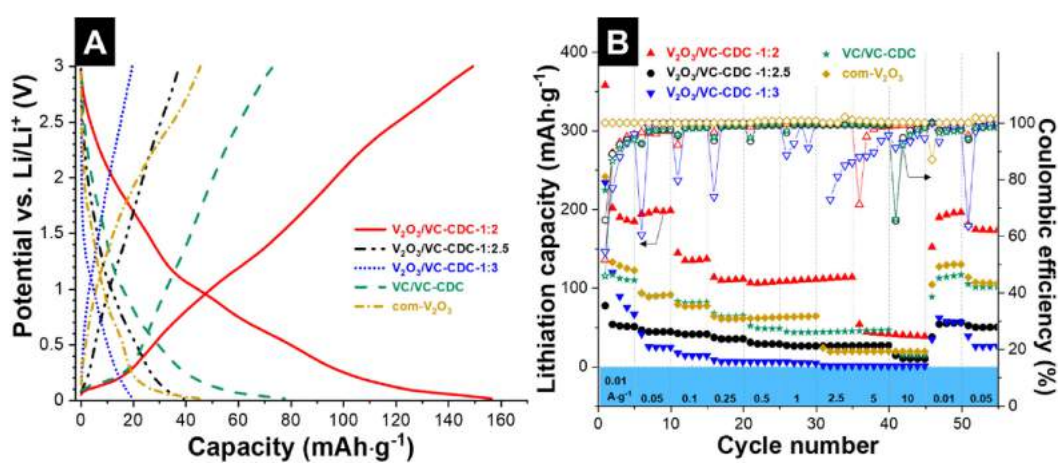


Figure 4. A) The 10th cycle voltage profiles of the samples measured with galvanostatic charge/discharge cycling at a specific current of $0.1 \text{ A} \cdot \text{g}^{-1}$ from 0.01–3.00 V vs. Li/Li⁺. B) Rate handling performance of the samples in the voltage range of 0.01–3.00 V vs. Li/Li⁺.

$110 \text{ mAh} \cdot \text{g}^{-1}$ at $2.5 \text{ A} \cdot \text{g}^{-1}$ and about $40 \text{ mAh} \cdot \text{g}^{-1}$ at $10 \text{ A} \cdot \text{g}^{-1}$ (Figure 4B). This performance is significantly better than com-V₂O₃ electrodes where only $18 \text{ mAh} \cdot \text{g}^{-1}$ was maintained at $2.5 \text{ A} \cdot \text{g}^{-1}$; the latter corresponds with a capacity loss of 71% compared to the low-rate capacity. Electrodes of VC/VC-CDC showed a low initial capacity at $0.01 \text{ A} \cdot \text{g}^{-1}$ of $224 \text{ mAh} \cdot \text{g}^{-1}$ during the first cycle and $117 \text{ mAh} \cdot \text{g}^{-1}$ during the second cycle. Yet, this material maintained about 52% ($40 \text{ mAh} \cdot \text{g}^{-1}$) of the capacity at $0.5 \text{ A} \cdot \text{g}^{-1}$. In the absence of V₂O₃ domains, the charge storage capacity of VC/VC-CDC is limited to ion electro-sorption of lithium on the surface area, and below 0.1 V vs. Li/Li⁺ to lithium intercalation within graphitic domains of the carbon phase. With the presence of significant amounts of residual vanadium carbide acting as dead mass, the overall charge storage capacity is limited, but the short diffusion pathways for lithium to intercalate in the graphitic domains explain the high rate handling ability. The first-cycle performance of about $112 \text{ mAh} \cdot \text{g}^{-1}$ of VC/VC-CDC is also fully restored after returning to the low rate of $0.01 \text{ A} \cdot \text{g}^{-1}$ after 45 cycles.

The cycling stability was tested in the voltage range of 0.01–3.00 V vs. Li/Li⁺ at a specific current of $0.1 \text{ A} \cdot \text{g}^{-1}$ (Figure 5). For

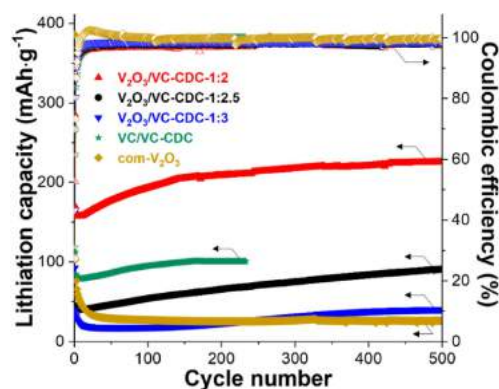


Figure 5. Cycling stability of the samples at $0.1 \text{ A} \cdot \text{g}^{-1}$.

the second cycle, the highest capacity is obtained for $V_2O_3/VC-CDC-1:2$ ($168 \text{ mAh}\cdot\text{g}^{-1}$), followed by $VC-CDC$ ($111 \text{ mAh}\cdot\text{g}^{-1}$), $com-V_2O_3$ ($102 \text{ mAh}\cdot\text{g}^{-1}$), $V_2O_3/VC-CDC-1:2.5$ ($57 \text{ mAh}\cdot\text{g}^{-1}$), and $V_2O_3/VC-CDC-1:3$ ($38 \text{ mAh}\cdot\text{g}^{-1}$). The capacity of $com-V_2O_3$ decreased to $27 \text{ mAh}\cdot\text{g}^{-1}$ after 50 cycles, while the capacity of the all other samples increases after the first ten cycles. The capacity increase of $VC/VC-CDC$ electrode proceeded even until the 165th cycle. Afterward, the $VC/VC-CDC$ electrode exhibited a constant capacity of $100 \text{ mAh}\cdot\text{g}^{-1}$. The 500th charge/discharge cycle of $V_2O_3/VC-CDC-1:2.5$ yielded a specific capacity of $90 \text{ mAh}\cdot\text{g}^{-1}$, of $V_2O_3/VC-CDC-1:3$ a value of $40 \text{ mAh}\cdot\text{g}^{-1}$, and of $com-V_2O_3$ only $25 \text{ mAh}\cdot\text{g}^{-1}$. The best material $V_2O_3/VC-CDC-1:2$ yielded a capacity of $225 \text{ mAh}\cdot\text{g}^{-1}$ after 500 cycles.

To better understand the cycling performance, we carried out post mortem XRD and Raman analyses (Figure 6A–B) of the electrodes. By this way, we explored possible changes to the structure of V_2O_3 and/or carbon as the possible reason for the improved performance during cycling testing. Considering the metal oxide, we see that the rhombohedral crystal structure of V_2O_3 was maintained in all samples after 500 cycles (Figure 6A). From this finding, we conclude that rhombohedral V_2O_3 is sufficiently stable for lithium intercalation and deintercalation under the conditions we applied for electrochemical cycling. In addition, the XRD results at different lithiation/delithiation states indicate no significant volume changes (Figure S5–6, and Table S3). This contrasts with previous reports that the significant volume change of V_2O_3 during cycling leads to poor capacity retention.^[23,25,47] The comparison of XRD data from the pristine samples and the post mortem analysis of the discharged electrodes after 500 cycles shows no significant residual volume changes of V_2O_3 (Table S1–S2).

As a next step, we investigated possible changes to the structure of carbon in the hybrid materials. Structural changes of carbon can best be studied for the $VC/VC-CDC$ sample. The latter showed an increase of the specific capacity during continuous charge/discharge cycling (Figure 5). While pristine $VC/VC-CDC$ showed a Bragg reflection indicative of hexagonal graphitic carbon at 26.3° 2θ (Figure 1A), this peak has weakened after cycling (Figure 6A). Correspondingly, post mortem Raman analysis (Figure 6B) shows an increased disorder

of carbon per the increased I_D/I_G intensity ratios from 0.9 to 1.2 (Table 1, 4). Similarly, we confirmed an increased I_D/I_G intensity

Table 4. Post mortem Raman spectra analysis of the D and G-modes of the electrodes. FWHM = full-width at half-maximum.

Sample	Mode	Position [cm^{-1}]	FWHM [cm^{-1}]	I_D/I_G
com- V_2O_3	D-mode	1345	122	0.9
	G-mode	1589	81	
VC/VC-CDC	D-mode	1353	123	1.2
	G-mode	1590	67	
$V_2O_3/VC-CDC-1:2$	D-mode	1349	140	2.7
	G-mode	1599	74	
$V_2O_3/VC-CDC-1:2.5$	D-mode	1351	161	2.3
	G-mode	1599	76	
$V_2O_3/VC-CDC-1:3$	D-mode	1350	99	2.2
	G-mode	1602	64	

ratio of carbon in $V_2O_3/VC-CDC-1:2$ (from 1.1 to 2.7), $V_2O_3/VC-CDC-1:2.5$ (from 1.1 to 2.3), and $V_2O_3/VC-CDC-1:3$ (from 2.1 to 2.2). The latter shows the smallest change of the carbon phase and the lowest electrochemical performance.

With evident structural changes of the carbon phase and small changes of V_2O_3 , we can now explain the enhanced performance of $VC/VC-CDC$ and all three $V_2O_3/VC-CDC$ samples: Seemingly, the ability of carbon in the hybrid material electrodes to reversibly store and release lithium is improved over the course of continued charge/discharge cycling. This ability benefits the overall performance because the low minimum voltage limit of 0.01 V vs. Li/Li^+ allows lithium intercalation into (graphitic) carbon.

3. Conclusions

We present a simplified synthesis for V_2O_3 /carbon hybrid materials. In the first step, $\text{NiCl}_2\cdot 6\text{H}_2\text{O}$ reacts with vanadium carbide to concurrently produce rhombohedral V_2O_3 and carbon. During the decomposition of $\text{NiCl}_2\cdot 6\text{H}_2\text{O}$, vanadium is selectively etched, leaving behind nanoporous carbide-derived carbon with a disordered structure. Locally, the residual nickel

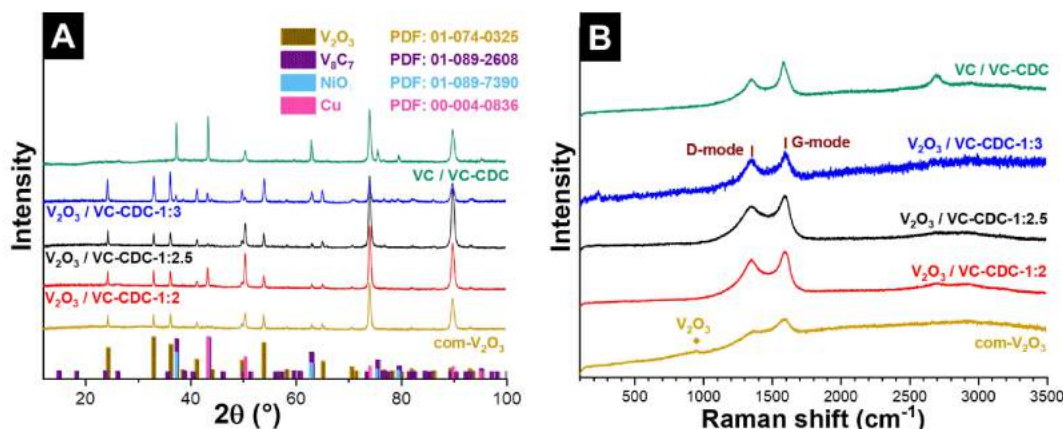


Figure 6. A) XRD pattern and B) Raman spectra of the samples after 500 cycles.

leads to the formation of carbon with a much higher degree of graphitic ordering. After the one-step thermal annealing, the remaining metallic nickel can easily be removed from the sample by washing in aqueous HCl. We tested the electrochemical performance in the broad voltage window of 0.01–3.0 V vs. Li/Li⁺. The best electrochemical performance of V₂O₃/VC-CDC hybrid material as an anode for LIBs with a half-cell configuration was 187 mAh·g⁻¹ at a low rate of 0.01 A·g⁻¹ and still 105 mAh·g⁻¹ at the high specific current of 2.5 A·g⁻¹. This performance was much better compared to commercially available V₂O₃ mixed with the same amount of carbon as present in our hybrid system; the composite electrode only had an initial specific capacity of 18 mAh·g⁻¹ at the specific current of 2.5 A·g⁻¹. With the very low potential of 0.01 V vs. Li/Li⁺, the adaptation of the materials presented in our study may also carefully consider the possible issue of electroplating.

Supporting Information

Thermogravimetric data with coupled mass spectra, scanning electron micrographs, nitrogen gas sorption isotherms, Raman peak fitting analysis, scanning transmission electron micrographs, and results from the Rietveld analysis.

Acknowledgments

The authors thank Eduard Arzt (INM) for his continuing support. The INM team acknowledges the funding of the COSH-CDC project (PR-1173/5-1) by the German Research Foundation (DFG). This work was part of the Carbon Metal Oxide Nanohybrid project (CarMON) supported by the Leibniz Association (SAW-2017). The authors thank Mesut Aslan, Jaehoon Choi, Robert Drumm, Ingrid Grobelsek, Benjamin Krüner, Eunho Lim, and Rafael Linzmeyer Zornitta (all at INM) for technical support and helpful discussions.

Conflict of Interest

The authors declare no conflict of interest.

Keywords: anode materials · carbide-derived carbon · hybrid materials · lithium-ion batteries · vanadia

- [1] N. Nitta, F. Wu, J. T. Lee, G. Yushin *Mater. Today*. **2015**, *18*, 252–264.
- [2] Z. Yang, J. Zhang, M. C. Kintner-Meyer, X. Lu, D. Choi, J. P. Lemmon, J. Liu *Chem. Rev.* **2011**, *111*, 3577–3613.
- [3] M. Armand, J. M. Tarascon *Nature*. **2008**, *451*, 652.
- [4] M. Broussely, G. Archdale *J. Power Sources*. **2004**, *136*, 386–394.
- [5] P. Geng, S. Zheng, H. Tang, R. Zhu, L. Zhang, S. Cao, H. Xue, H. Pang *Adv. Energy Mater.* **2018**, *8*, 1703259.
- [6] J. M. Tarascon, M. Armand *Nature*. **2001**, *414*, 359.
- [7] Z. Zhang, S. S. Zhang, *Rechargeable Batteries*, Springer International Publishing Cham, **2015**.
- [8] N. A. Kaskhedikar, J. Maier *Adv. Mater.* **2009**, *21*, 2664–2680.
- [9] G. N. Zhu, Y. G. Wang, Y. Y. Xia *Energy Environ. Sci.* **2012**, *5*, 6652–6667.

- [10] F. Joho, B. Rykart, R. Imhof, P. Novak, M. E. Spahr, A. Monnier *J. Power Sources*. **1999**, *81–82*, 243–247.
- [11] S. Goriparti, E. Miele, F. De Angelis, E. Di Fabrizio, R. P. Zaccaria, C. Capiglia *J. Power Sources*. **2014**, *257*, 421–443.
- [12] J. R. Dahn, T. Zheng, Y. Liu, J. S. Xue *Science*. **1995**, *270*, 590–593.
- [13] T. Song, J. Xia, J. H. Lee, D. H. Lee, M. S. Kwon, J. M. Choi, J. Wu, S. K. Doo, H. Chang, W. I. Park, D. S. Zang, H. Kim, Y. Huang, K. C. Hwang, J. A. Rogers, U. Paik *Nano Lett.* **2010**, *10*, 1710–1716.
- [14] M. Widmaier, K. Pfeifer, L. Bommer, V. Presser *Batteries & Supercaps*. **2018**, *1*, 11–26.
- [15] E. Lim, H. Shim, S. Fleischmann, V. Presser *J. Mater. Chem. A*. **2018**, *6*, 9480–9488.
- [16] C. Z. Wu, Y. Xie *Energy Environ. Sci.* **2010**, *3*, 1191–1206.
- [17] G. Silversmit, D. Depla, H. Poelman, G. B. Marin, R. De Gryse *J. Electron Spectrosc. Relat. Phenom.* **2004**, *135*, 167–175.
- [18] S. Fleischmann, A. Tolosa, V. Presser *Chem. Eur. J.* **2018**, *24*, 12143–12153.
- [19] N. A. Chernova, M. Roppolo, A. C. Dillon, M. S. Whittingham *J. Mater. Chem.* **2009**, *19*, 2526–2552.
- [20] M. Zeiger, T. Ariyanto, B. Krüner, N. J. Peter, S. Fleischmann, B. J. M. Etzold, V. Presser *J. Mater. Chem. A*. **2016**, *4*, 18899–18909.
- [21] T. Kudo, Y. Ikeda, T. Watanabe, M. Hibino, M. Miyayama, H. Abe, K. Kajita *Solid State Ionics*. **2002**, *152–153*, 833–841.
- [22] T. E. Ashton, D. Hevia Borrás, A. Iadecola, K. M. Wiaderek, P. J. Chupas, K. W. Chapman, S. A. Corr *Acta Crystallogr. Sect. B* **2015**, *71*, 722–726.
- [23] L. Jiang, Y. Qu, Z. Ren, P. Yu, D. Zhao, W. Zhou, L. Wang, H. Fu *ACS Appl. Mater. Interfaces*. **2015**, *7*, 1595–1601.
- [24] Y. Shi, Z. J. Zhang, D. Wexler, S. L. Chou, J. Gao, H. D. Abruna, H. J. Li, H. K. Liu, Y. P. Wu, J. Z. Wang *J. Power Sources*. **2015**, *275*, 392–398.
- [25] Y. F. Sun, S. S. Jiang, W. T. Bi, C. Z. Wu, Y. Xie *J. Power Sources*. **2011**, *196*, 8644–8650.
- [26] Y. Yan, B. Li, W. Guo, H. Pang, H. Xue *J. Power Sources*. **2016**, *329*, 148–169.
- [27] D. McNulty, D. N. Buckley, C. O'Dwyer *ChemElectroChem*. **2017**, *4*, 2037–2044.
- [28] M. R. Lukatskaya, B. Dunn, Y. Gogotsi *Nat. Commun.* **2016**, *7*, 12647.
- [29] M. Widmaier, N. Jäckel, M. Zeiger, M. Abuzarli, C. Engel, L. Bommer, V. Presser *Electrochim. Acta*. **2017**, *247*, 1006–1018.
- [30] A. Odani, V. G. Pol, S. V. Pol, M. Kolytyn, A. Gedanken, D. Aurbach, *Adv. Mater.* **2006**, *18*, 1431–1436.
- [31] L. Zeng, C. Zheng, J. Xi, H. Fei, M. Wei *Carbon*. **2013**, *62*, 382–388.
- [32] S. Brunauer, P. H. Emmett, E. Teller *J. Am. Chem. Soc.* **1938**, *60*, 309–319.
- [33] G. Y. Gor, M. Thommes, K. A. Cychosz, A. V. Neimark *Carbon*. **2012**, *50*, 1583–1590.
- [34] V. Presser, M. Heon, Y. Gogotsi *Adv. Funct. Mater.* **2011**, *21*, 810–833.
- [35] T. Ariyanto, A. M. Kern, B. J. M. Etzold, G. R. Zhang *Electrochem. Commun.* **2017**, *82*, 12–15.
- [36] A. C. Ferrari, D. M. Basko *Nat. Nanotechnol.* **2013**, *8*, 235.
- [37] A. C. Ferrari *Solid State Commun.* **2007**, *143*, 47–57.
- [38] H. J. T. Ellingham *J. Soc. Chem. Ind.* **1944**, *63*, 125–133.
- [39] R. Dash, J. Chmiola, G. Yushin, Y. Gogotsi, G. Laudisio, J. Singer, J. Fischer, S. Kucheyev *Carbon*. **2006**, *44*, 2489–2497.
- [40] C. R. Perez, S.-H. Yeon, J. Segalini, V. Presser, P.-L. Taberna, P. Simon, Y. Gogotsi *Adv. Funct. Mater.* **2013**, *23*, 1081–1089.
- [41] M. Zeiger, N. Jäckel, V. N. Mochalin, V. Presser *J. Mater. Chem. A*. **2016**, *4*, 3172–3196.
- [42] R. Fu, T. F. Baumann, S. Cronin, G. Dresselhaus, M. S. Dresselhaus, J. H. Satcher, Jr. *Langmuir*. **2005**, *21*, 2647–2651.
- [43] M. Thommes, K. Kaneko, A. V. Neimark, J. P. Olivier, F. Rodriguez-Reinoso, J. Rouquerol, K. S. W. Sing *Pure Appl. Chem.* **2015**, *87*, 1051–1069.
- [44] A. P. Cohn, L. Oakes, R. Carter, S. Chatterjee, A. S. Westover, K. Share, C. L. Pint *Nanoscale*. **2014**, *6*, 4669–4675.
- [45] S. J. An, J. L. Li, C. Daniel, D. Mohanty, S. Nagpure, D. L. Wood *Carbon*. **2016**, *105*, 52–76.
- [46] A. Iturrondobeitia, A. Goni, I. Gil de Muro, L. Lezama, T. Rojo *Nanomaterials*. **2017**, *7*, 423.
- [47] B. Xiao, B. Zhang, L. B. Tang, C. S. An, Z. J. He, H. Tong, W. J. Yu, J. C. Zheng *Ceram. Int.* **2018**, *44*, 15044–15049.

Manuscript received: October 27, 2018
Version of record online: December 7, 2018

Supporting Information

© Copyright Wiley-VCH Verlag GmbH & Co. KGaA, 69451 Weinheim, 2018

Vanadium (III) Oxide/Carbon Core/Shell Hybrids as an Anode for Lithium-Ion Batteries

Öznil Budak, Pattarachai Srimuk, Aura Tolosa, Simon Fleischmann, Juhan Lee, Stefan W. Hieke, Anna Frank, Christina Scheu, and Volker Presser*

Table S1. Results from the Rietveld analysis from X-ray diffraction pattern of the samples (pristine).

Sample	Phase	Space group	Powder diffraction file (PDF) number	Cell parameter (Å)	Volume (Å ³)	Content (%)
com-V ₂ O ₃	V ₂ O ₃	$R\bar{3}c$	01-074-0325	$a = 4.96$ $c = 14.00$	298	100
	V ₈ C ₇	$P4_332$	01-089-2608	$a = 8.34$	580	96
VC/VC-CDC	Graphite	$P6_3mc$	01-089-7213	$a = 2.48$ $c = 6.78$	36	4
	V ₂ O ₃	$R\bar{3}c$	01-074-0325	$a = 4.96$ $c = 13.99$	298	100
V ₂ O ₃ /VC-CDC-1:2	V ₂ O ₃	$R\bar{3}c$	01-074-0325	$a = 4.96$ $c = 13.99$	298	100
V ₂ O ₃ /VC-CDC-1:2.5	V ₂ O ₃	$R\bar{3}c$	01-074-0325	$a = 4.96$ $c = 13.99$	298	100
V ₂ O ₃ /VC-CDC-1:3	V ₂ O ₃	$R\bar{3}c$	01-074-0325	$a = 4.96$ $c = 13.96$	263	79
	NiO	$R\bar{3}m$	01-089-7390	$a = 2.95$	18	21

Table S2. Results from the Rietveld analysis from the X-ray diffraction pattern of the post mortem samples (after 500 galvanostatic charge/discharge cycles).

Sample	Phase	Space group	Powder diffraction file (PDF) number	Cell parameter (Å)	Volume (Å ³)
com-V ₂ O ₃	V ₂ O ₃	$R\bar{3}c$	01-074-0325	$a = 4.96$ $c = 14.00$	298
	Cu	$Fm\bar{3}m$	00-004-0836	$a = 3.62$	47
VC/VC-CDC	V ₈ C ₇	$P4_332$	01-089-2608	$a = 8.34$	579
	Cu	$Fm\bar{3}m$	00-004-0836	$a = 3.62$	47
V ₂ O ₃ /VC-CDC-1:2	V ₂ O ₃	$R\bar{3}c$	01-074-0325	$a = 4.95$ $c = 13.99$	297
	Cu	$Fm\bar{3}m$	00-004-0836	$a = 3.62$	47
V ₂ O ₃ /VC-CDC-1:2.5	V ₂ O ₃	$R\bar{3}c$	01-074-0325	$a = 4.96$ $c = 13.99$	298
	Cu	$Fm\bar{3}m$	00-004-0836	$a = 3.62$	47
V ₂ O ₃ /VC-CDC-1:3	V ₂ O ₃	$R\bar{3}c$	01-074-0325	$a = 4.96$ $c = 13.94$	296
	NiO	$R\bar{3}m$	01-089-7390	$a = 2.95$	18
	Cu	$Fm\bar{3}m$	00-004-0836	$a = 3.62$	47

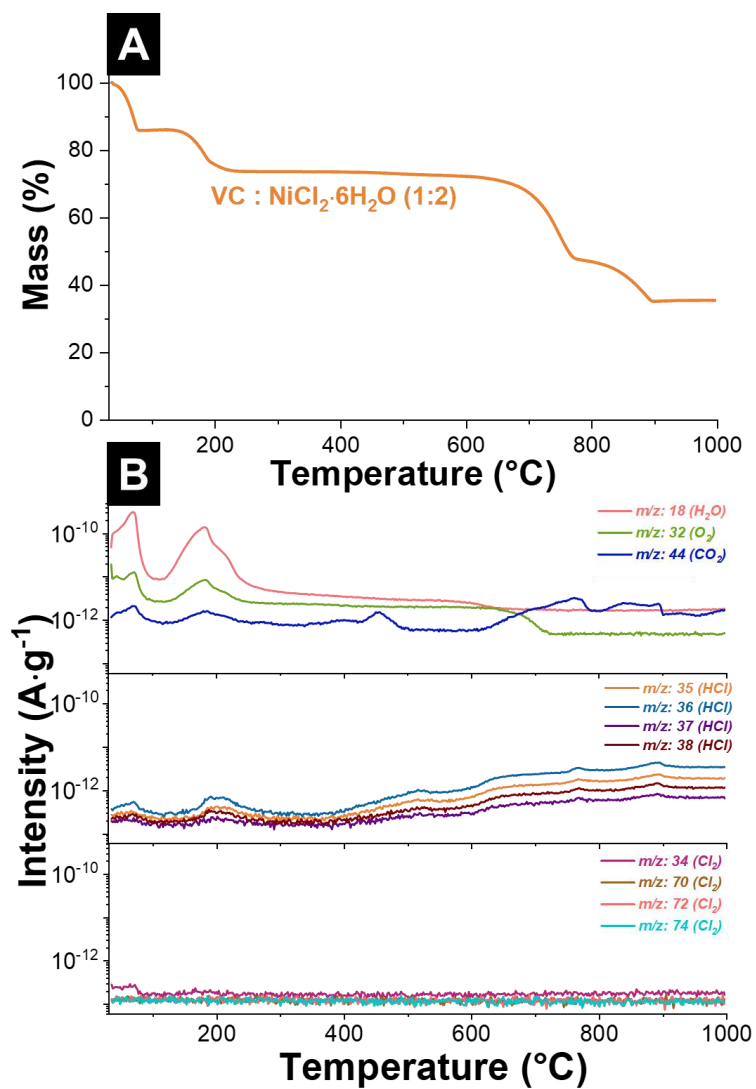


Figure S1. (A) Thermogram and (B) corresponding mass spectra of the TGA-MS measurements of the mixture with the stoichiometric ratios of 1 mol of VC and 2 mol of NiCl₂·6H₂O.

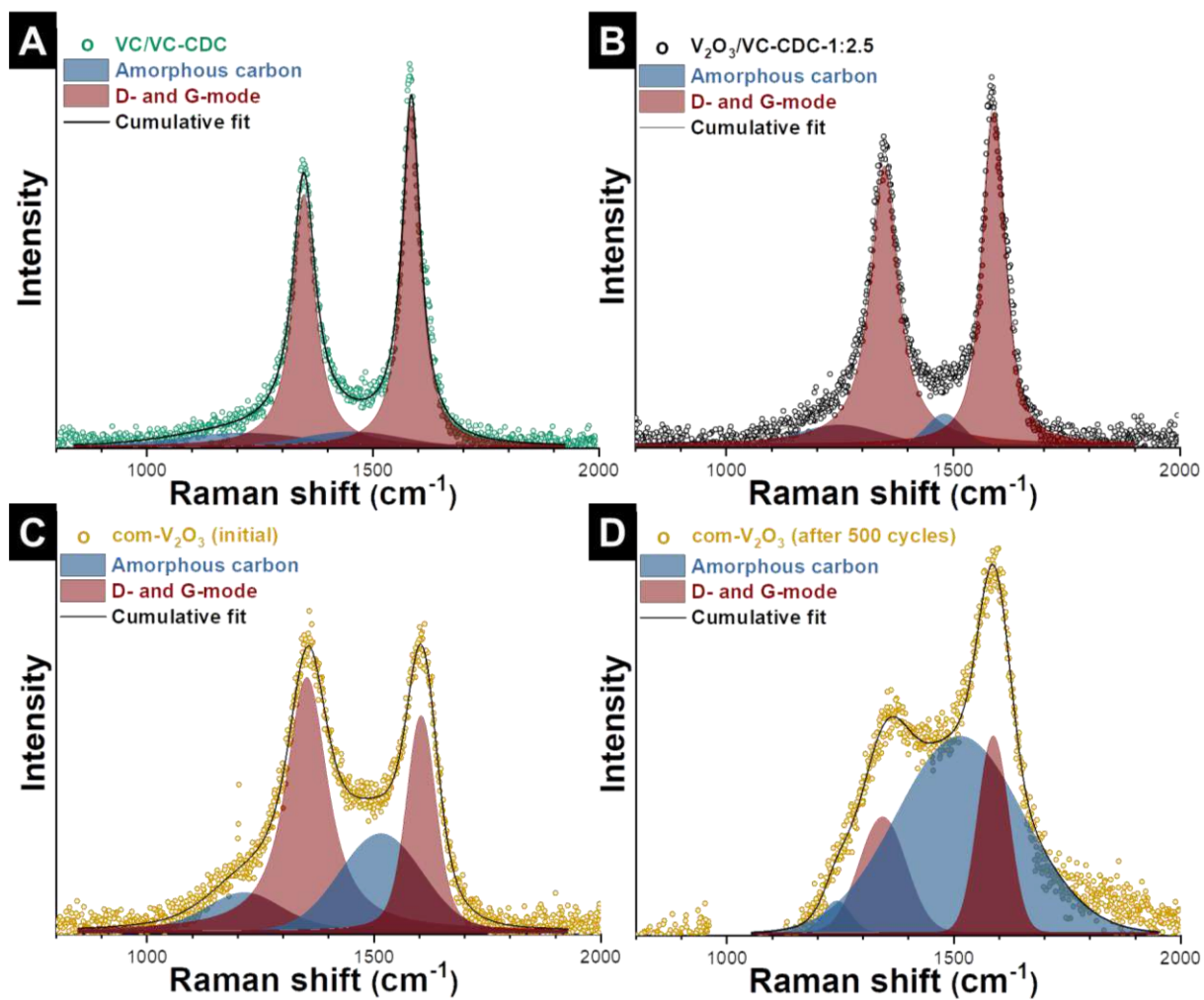


Figure S2. Measured and fitted Raman spectra of (A) VC/VC-CDC, (B) $\text{V}_2\text{O}_3/\text{VC-CDC-1:2.5}$, (C) com- V_2O_3 before electrochemical cycling, and (D) com- V_2O_3 after 500 charge/discharge cycles.

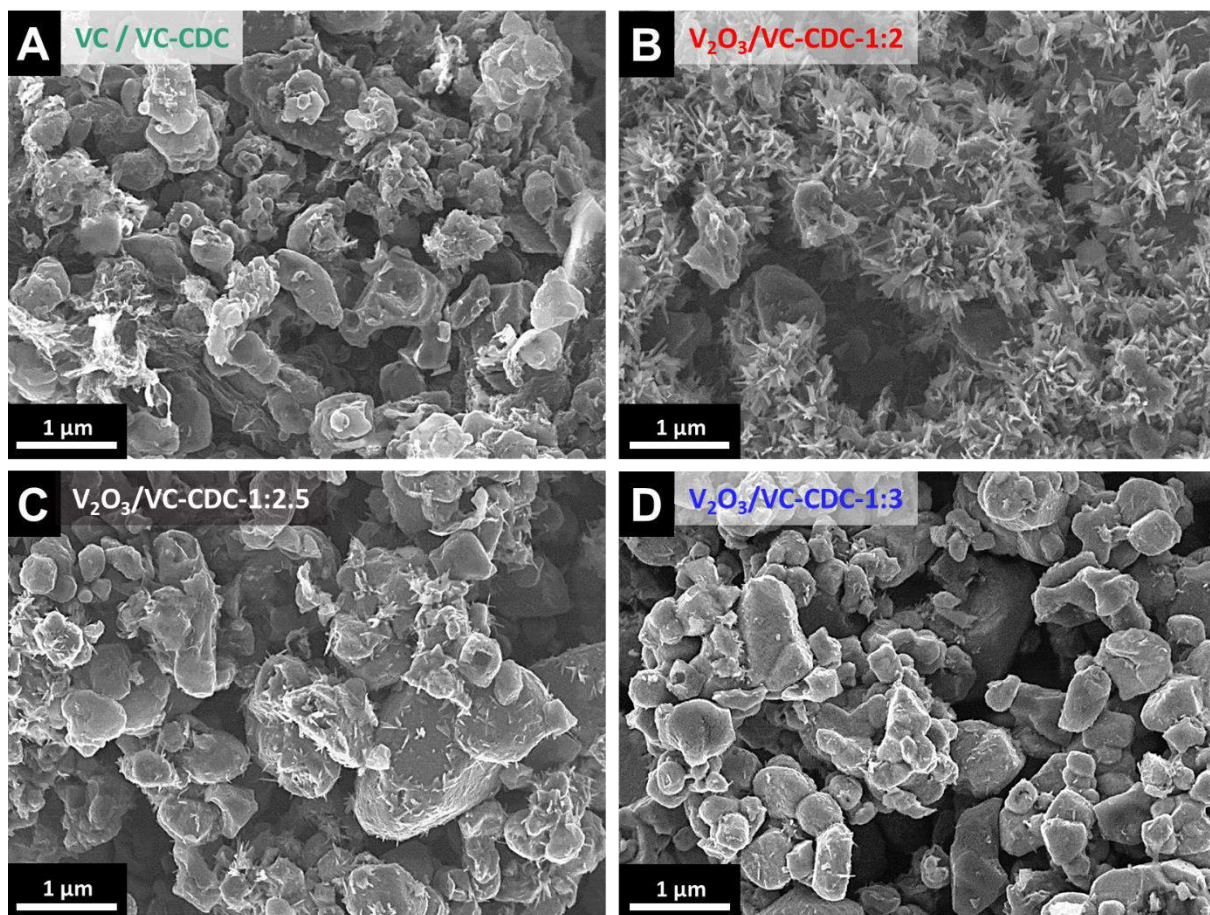


Figure S3. Scanning electron micrographs of (A) VC/VC-CDC, (B) V₂O₃/VC-CDC-1:2, (C) V₂O₃/VC-CDC-1:2.5, and (D) V₂O₃/VC-CDC-1:3.

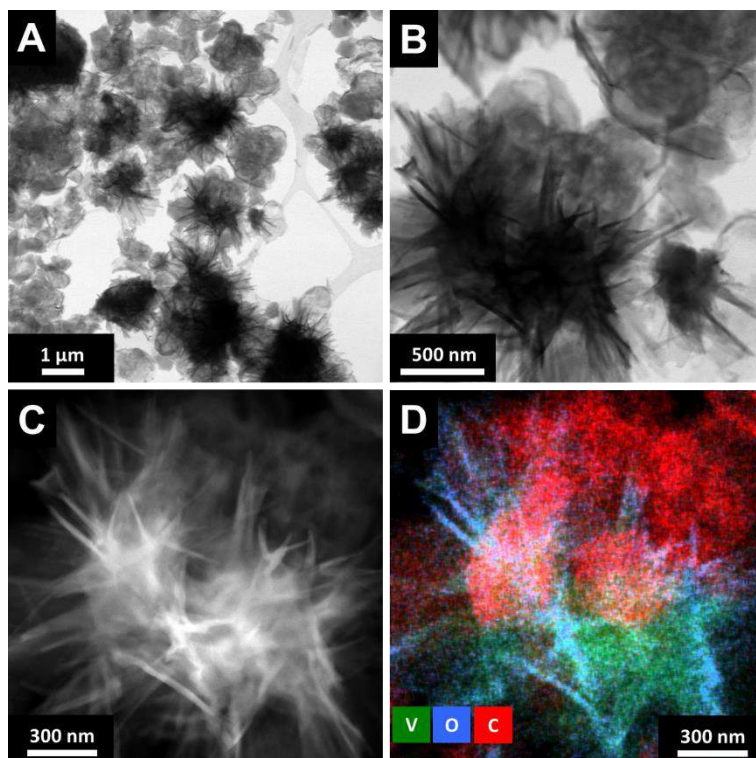


Figure S4. Panel A and B show bright field STEM images of $V_2O_3/VC-CDC-1:2$. Panel D displays the elemental map for vanadium (green), carbon (red), and oxygen (blue) of the corresponding HAADF STEM image shown in panel C.

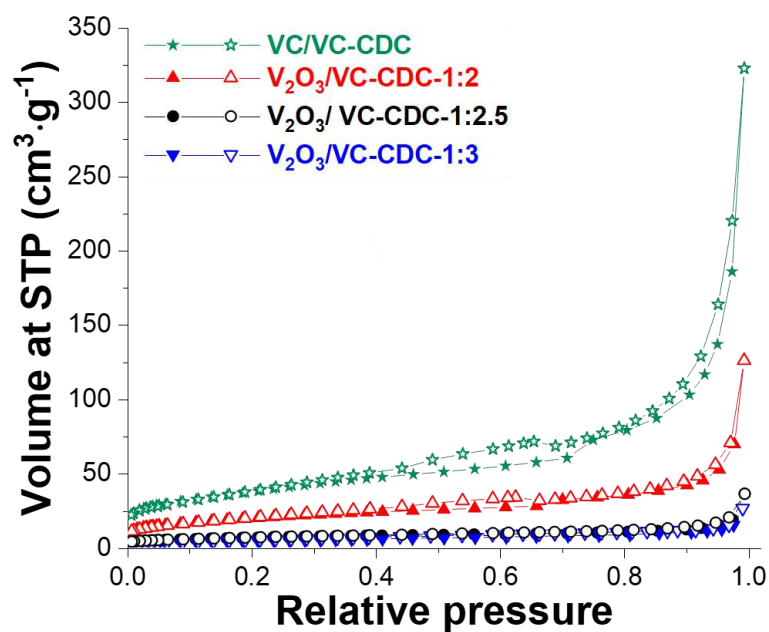


Figure S5. Nitrogen sorption isotherms of all samples (STP: standard temperature and pressure). Closed symbols: adsorption branch; open symbols: desorption branch.

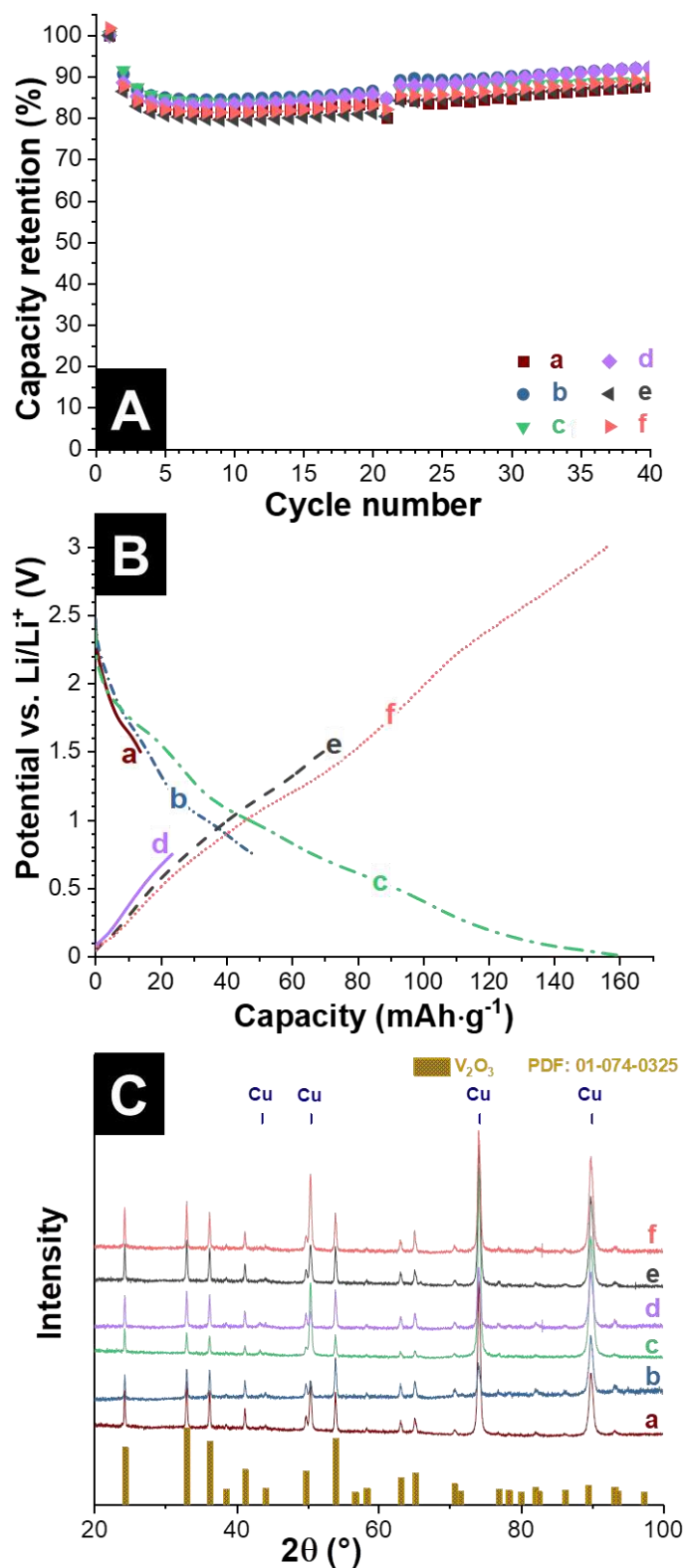


Figure S6. (A) Cycling stability of V₂O₃/VC-CDC-1:2 measured at a specific current of 0.1 A·g⁻¹ for 40 cycles, (B) The 41st cycle voltage profiles of V₂O₃/VC-CDC-1:2 stopped at certain potentials where a, b, and c refer to lithiation at 1.5 V, 0.75 V, and 0.01 V vs. Li/Li⁺, d, e, and f refer to delithiation at 0.75 V, 1.5 V, and 3.0 V vs. Li/Li⁺, respectively. (C) Post mortem XRD pattern of the V₂O₃/VC-CDC-1:2 of the corresponding potential in B.

Table S3. Results from the Rietveld analysis from the post mortem X-ray diffraction pattern of the V₂O₃/VC-CDC-1:2 (at different lithiation/delithiation states).

Sample	Phase	Space group	Powder diffraction file (PDF) number	Cell parameter (Å)	Volume (Å ³)
Lithiation at 1.5 V (a)	V ₂ O ₃	<i>R</i> $\bar{3}$ <i>c</i>	01-074-0325	<i>a</i> = 4.96 <i>c</i> = 13.99	298
	Cu	<i>Fm</i> $\bar{3}$ <i>m</i>	00-004-0836	<i>a</i> = 3.62	47
Lithiation at 0.75 V (b)	V ₂ O ₃	<i>R</i> $\bar{3}$ <i>c</i>	01-074-0325	<i>a</i> = 4.96 <i>c</i> = 13.99	298
	Cu	<i>Fm</i> $\bar{3}$ <i>m</i>	00-004-0836	<i>a</i> = 3.62	47
Lithiation at 0.01 V (c)	V ₂ O ₃	<i>R</i> $\bar{3}$ <i>c</i>	01-074-0325	<i>a</i> = 4.95 <i>c</i> = 13.99	297
	Cu	<i>Fm</i> $\bar{3}$ <i>m</i>	00-004-0836	<i>a</i> = 3.62	47
Delithiation at 0.75 V (d)	V ₂ O ₃	<i>R</i> $\bar{3}$ <i>c</i>	01-074-0325	<i>a</i> = 4.96 <i>c</i> = 13.99	297
	Cu	<i>Fm</i> $\bar{3}$ <i>m</i>	00-004-0836	<i>a</i> = 3.62	47
Delithiation at 1.5 V (e)	V ₂ O ₃	<i>R</i> $\bar{3}$ <i>c</i>	01-074-0325	<i>a</i> = 4.95 <i>c</i> = 13.98	297
	Cu	<i>Fm</i> $\bar{3}$ <i>m</i>	00-004-0836	<i>a</i> = 3.62	47
Delithiation at 3 V (f)	V ₂ O ₃	<i>R</i> $\bar{3}$ <i>c</i>	01-074-0325	<i>a</i> = 4.95 <i>c</i> = 13.98	297
	Cu	<i>Fm</i> $\bar{3}$ <i>m</i>	00-004-0836	<i>a</i> = 3.62	47

5.2. Carbide-derived niobium pentoxide with an enhanced charge storage capacity for use as a lithium-ion battery electrode

Öznil Budak^{1,2} Miriam Geißler,³ Dennis Becker,⁴ Angela Kruth,⁵
Antje Quade,⁵ Robert Haberkorn,⁴ Guido Kickelbick,⁴ Bastian J. M. Etzold,³ Volker Presser^{1,2}

¹ *INM - Leibniz Institute for New Materials, Campus D2 2, 66123 Saarbrücken, Germany*

² *Saarland University, Campus D2 2, 66123 Saarbrücken, Germany*

³ *Ernst-Berl-Institut für Technische und Makromolekulare Chemie, Technische Universität Darmstadt, 64287 Darmstadt, Germany*

⁴ *Inorganic Solid-State-Chemistry, Saarland University, 66123 Saarbrücken, Germany*

⁵ *Leibniz Institute for Plasma Science and Technology, 17489 Greifswald, Germany*

Citation:

Ö. Budak, M. Geißler, D. Becker, A. Kruth, A. Quade, R. Haberkorn, G. Kickelbick, B.J.M. Etzold, V. Presser, CARBIDE-DERIVED NIOBIUM PENTOXIDE WITH AN ENHANCED CHARGE STORAGE CAPACITY FOR USE AS A LITHIUM-ION BATTERY ELECTRODE, ACS Applied Energy Materials 10.1021/acsaem.9b02549 (2020).

Own contribution:

Material synthesis, measurements, data analysis, writing, plotting, discussion

This study explores two different synthesis approaches for Nb₂O₅/carbon hybrid materials. The first synthesis was conducted via two thermal treatment; the first thermal treatment was the partial conversion of NbC particles to NbC/carbon under vacuum using NiCl₂·6H₂O, while the second thermal treatment was targeting the conversion of NbC particles to Nb₂O₅ via CO₂ oxidation atmosphere to keep carbon in the hybrid structure. The second synthesis was performed via the chloroxidation method with only one thermal treatment step. Two different structures possessor Nb₂O₅/carbon hybrid were observed, namely *m*-Nb₂O₅/carbon and *o*-Nb₂O₅/CDC. Both hybrid materials display a specific capacity of about 300 mAh/g, which is significantly the highest capacity obtained until now from Nb₂O₅ electrodes. Moreover, the hybrid *m*-Nb₂O₅/carbon can provide a higher capacity for high current rates compared to the composite counterpart.

Carbide-Derived Niobium Pentoxide with Enhanced Charge Storage Capacity for Use as a Lithium-Ion Battery Electrode

Ö. Budak, M. Geißler, D. Becker, A. Kruth, A. Quade, R. Haberkorn, G. Kickelbick, B. J. M. Etzold, and V. Presser*



Cite This: *ACS Appl. Energy Mater.* 2020, 3, 4275–4285



Read Online

ACCESS |



Metrics & More



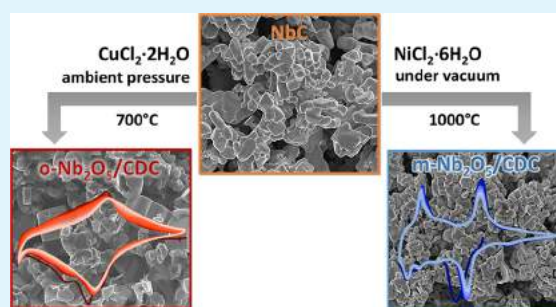
Article Recommendations



Supporting Information

ABSTRACT: Nb_2O_5 has been explored as a promising anode material for use as lithium-ion batteries (LIBs), but depending on the crystal structure, the specific capacity was always reported to be usually around or below 200 mAh/g. For the first time, we present coarse-grained Nb_2O_5 materials that significantly overcome this capacity limitation with the promise of enabling high power applications. Our work introduces coarse-grained carbide-derived Nb_2O_5 phases obtained either by a one-step or a two-step bulk conversion process. By in situ production of chlorine gas from metal chloride salt at ambient pressure, we obtain in just one step directly orthorhombic Nb_2O_5 alongside carbide-derived carbon (o- $\text{Nb}_2\text{O}_5/\text{CDC}$). In situ formation of chlorine gas from metal chloride salt under vacuum conditions yields CDC covering the remaining carbide core, which can be transformed into metal oxides covered by a carbon shell upon thermal treatment in CO_2 gas. The two-step process yielded a mixed-phase tetragonal and monoclinic Nb_2O_5 with CDC (m- $\text{Nb}_2\text{O}_5/\text{CDC}$). Our combined diffraction and spectroscopic data confirm that carbide-derived Nb_2O_5 materials show disordering of the crystallographic planes caused by oxygen deficiency in the structural units and, in the case of m- $\text{Nb}_2\text{O}_5/\text{CDC}$, severe stacking faults. This defect engineering allows access to a very high specific capacity exceeding the two-electron transfer process of conventional Nb_2O_5 . The charge storage capacities of the resulting m- $\text{Nb}_2\text{O}_5/\text{CDC}$ and o- $\text{Nb}_2\text{O}_5/\text{CDC}$ are, in both cases, around 300 mAh/g at a specific current of 10 mA/g, thereby, the values are significantly higher than that of the state-of-the-art for Nb_2O_5 as a LIB anode. Carbide-derived Nb_2O_5 materials also show robust cycling stability over 500 cycles with capacity fading only 24% for the sample m- $\text{Nb}_2\text{O}_5/\text{CDC}$ and 28% for o- $\text{Nb}_2\text{O}_5/\text{CDC}$, suggesting low degree of expansion/compaction during lithiation and delithiation.

KEYWORDS: lithium-ion battery, electrochemical energy storage, hybrid material, carbide-derived oxide, niobium pentoxide



1. INTRODUCTION

Electrochemical energy storage (EES) with high specific energy and power is essential for the successful transition of combustion engine vehicles to electric cars, advanced mobile communication devices, and energy harvesting technologies.^{1,2} The most advanced and widespread type of EES is the lithium-ion battery (LIB)³ because of its long cycle life, high energy density, and efficiency.⁴ To meet the growing demands in energy and power ratings, there is a constant need for the development of improved and optimized LIB electrode materials. Metallic lithium offers a high theoretical capacity of 3860 mAh/g with a low redox potential of -3.04 V vs. standard hydrogen electrode (SHE) but is plagued by dendrite formation and safety concerns; therefore, lithium insertion compounds are preferred for rechargeable LIBs.^{4,5} Graphite, for example, provides a high specific capacity of 372 mAh/g and a low insertion potential of $+0.2$ V vs. Li/Li^+ , which translates to a high energy and power density.¹ However, graphite suffers from large stress during Li insertion/desertion, resulting in reduced cycling stability.⁶ As an alternative, researchers have explored TiO_2 and $\text{Li}_4\text{Ti}_5\text{O}_{12}$

(LTO), which have a high operating voltage of 1.7 and 1.5 V vs. Li/Li^+ , respectively. While there is the benefit of a low volume change for TiO_2 (4%) and LTO (<1%), these two materials provide only a limited theoretical capacity of about 170 mAh/g.^{7,8}

Niobium pentoxide (Nb_2O_5) is an alternative insertion-type anode to LIBs due to its various superior features.⁹ The operating redox potential of Nb_2O_5 is above 1 V vs. Li/Li^+ .¹⁰ At this voltage, electroplating is prevented, and a safer device operation is enabled.¹¹ Nb_2O_5 can be obtained in different crystal structures, including hexagonal, orthorhombic, tetragonal, and monoclinic, which have different electrochemical properties.^{12,13} For example, Viet et al. measured for the

Received: December 30, 2019

Accepted: April 15, 2020

Published: April 15, 2020



pseudohexagonal Nb₂O₅ electrode a specific capacity of 150 mAh/g at redox couple peaks of 1.84 V vs. Li/Li⁺, while Li et al. showed for polymorph Nb₂O₅ a specific capacity of 190 mAh/g within the voltage window of 1.2–3.0 V vs. Li/Li⁺.^{14,15} Hollow nanospheres of hexagonal Nb₂O₅ exhibit a specific capacity of 172 mAh/g at a C-rate of 0.5.¹⁶ Pseudohexagonal and orthorhombic Nb₂O₅/amorphous carbon core/shell materials provide about 200 mAh/g at 0.1 C in the voltage range of 1.0–3.0 V vs. Li/Li⁺.¹⁷ 3D holey-graphene/orthorhombic Nb₂O₅ has been found to exhibit a capacity of 139 mAh/g at a high C-rate of 10.¹⁸ Nanobelts composed of orthorhombic Nb₂O₅ found by Wei et al. presented an initial specific capacity of 250 mAh/g in the voltage range of 1.2–3.0 V vs. Li/Li⁺.¹⁹ Tetragonal Nb₂O₅ was described as a transformation phase in orthorhombic and monoclinic phases, where the initial specific capacity was ca. 230 mAh/g in the voltage window of 1.2–3 V vs. Li/Li⁺.¹³ Using electrospinning, our team reported reversible capacities of 160 and 240 mAh/g, respectively, for tetragonal and monoclinic Nb₂O₅/carbon fiber mats at a specific current of 0.025 A/g in the voltage window of 0.8–3.0 V vs. Li/Li⁺.²⁰ In all these structures, orthorhombic and tetragonal Nb₂O₅ are highly promising candidates due to the fact that they are capable of maintaining their original structures even after lithium insertion, resulting in better electrochemical cycling performance.^{13,21} The orthorhombic Nb₂O₅ phase shows suppressed lithiation/delithiation peaks in the electrochemical signature with more pseudocapacitive resemblance as a result of ion insertion into the large interstitial sites.^{22,23} Monoclinic Nb₂O₅ was reported to have the highest capacity among them of 242 mAh/g.¹⁴

Until now, different crystal structures of Nb₂O₅ have been mostly reported to yield a lithiation capacity of about 200 mAh/g, which aligns with a two-electron transport process via the transition between Nb⁵⁺ and Nb⁴⁺ and the formation of Li₂Nb₂O₅.^{24,25} Kumagai et al.²¹ have mentioned already in 1983 that Nb₂O₅ should allow insertion of “at least” two lithium ions. Furthermore, Shi et al.²⁴ speculated about the concurrence of Nb⁵⁺ to Nb⁴⁺ and the Nb³⁺ oxidation state changes during lithiation/delithiation. This uncertainty about the upper limit for reversible Li-insertion into Nb₂O₅ host structures for LIBs has inspired our work. There have also been two recent studies, where an excess value of 200 mAh/g was enabled by utilization of nanoscaled Nb₂O₅ and the added surface area may play a key role in enhancing the energy storage metrics.^{26,27} Our work, however, targets to unlock the high charge storage domain not by nanoscale material design but by defect engineering and crystal structure optimization of bulk materials (starting with coarse-grained carbide particles as the precursor). Controlling the structural defects (stacking faults and oxygen vacancies) not only significantly boosts the conductivity of materials but also enables a higher intrinsic charge storage capacity.^{28,29}

Our work uses the unique tool of carbide-derived oxide synthesis to design Nb₂O₅ with tailored defect structures and implement carbon at the nanoscale level to make it an advanced hybrid electrode material. We introduce, for the first time, cyclic stable bulk Nb₂O₅ with a reversible high specific capacity of 300 mAh/g. This high performance is observed for carbide-derived Nb₂O₅/carbon hybrid materials with a disordered crystal structure. We present data with this high charge storage capacity for two Nb₂O₅ crystal structures, namely orthorhombic Nb₂O₅, and mixed monoclinic and tetragonal Nb₂O₅. Carbides are a convenient and versatile precursor for the synthesis of metal oxides and metal oxide/carbon hybrids. We used two synthesis routes: a two-step and a one-step method. Facile carbide

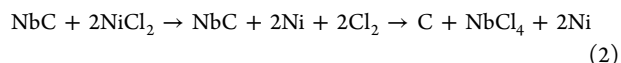
conversion can be obtained by the two-step process of chlorination (to create carbon) followed by oxidation (to create the metal oxide phase but without removing all formerly formed carbon).³⁰ Alternatively, one-step processing of metal carbide via chloroxidation triggered by the decomposition of a chloride hydrate (e.g., NiCl₂·6H₂O) directly leads to the coexistence of metal oxide and carbide.³¹

2. EXPERIMENTAL

2.1. Material Synthesis. 2.1.1. Nb₂O₅ Material Nomenclature.

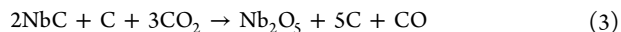
Considering the specific crystal structures of m-Nb₂O₅/CDC and o-Nb₂O₅/CDC, our nomenclature deviates from previous studies.³² For example, the conventional name for orthorhombic Nb₂O₅ would be Tief-Nb₂O₅ (T-Nb₂O₅).³³ We prefer to address our material as o-Nb₂O₅ as a more suitable name considering the differences in the crystal structure compared to actual Tief-Nb₂O₅. Also, we chose m-Nb₂O₅ with *m* standing for *mixed* because it contains tetragonal Mittel-Nb₂O₅ (M-Nb₂O₅) and monoclinic Nadel-Nb₂O₅ (N-Nb₂O₅). We also used commercially available Nb₂O₅, which contains tetragonal and monoclinic phase contents and is labeled com-Nb₂O₅.

2.1.2. Synthesis of m-Nb₂O₅/CDC. The synthesis of m-Nb₂O₅/CDC was performed by two thermal treatment steps. In the first step, for the synthesis of NbC/CDC particles, in situ production of chlorine under vacuum conditions was used for the reactive extraction of niobium from NbC using NiCl₂·6H₂O as the chlorine source.³⁴ At this step, the decomposition of NiCl₂·6H₂O under vacuum conditions leads to incomplete conversion of NbC (eqs 1 and 2). The following step is to oxidize the residual NbC with CO₂ instead of using O₂ to avoid complete carbon burn-off.

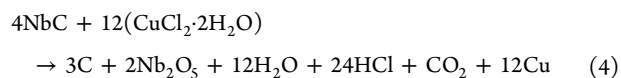


For the incomplete conversion of NbC to carbide-derived carbon (CDC), NbC (H.C. Starck, purity ≥98%) and NiCl₂·6H₂O (Alfa Aesar, purity 98%) were homogenized using a mortar with a stoichiometric ratio of 1.0 mol NbC per 0.8 mol NiCl₂·6H₂O. Then, the solid mixture was transferred into a graphite crucible, and the latter was placed in the isothermal zone of a tubular furnace (Gero, type: DZF 100–750/13, diameter: 34 cm, and length: 1.5 m). Afterward, the furnace was evacuated until a pressure of about 1 mbar was achieved, heated to 1000 °C at a rate of 3.3 °C/min, and held at 1000 °C for 3 h. The furnace was then cooled to room temperature. The sample from the furnace was washed with 200 mL of aqueous 3 M HCl to eliminate elemental Ni. After stirring the solution overnight, the particles were filtered by using an excessive amount of distilled water. The filtered particles were dried at 75 °C overnight. The obtained sample was labeled as NbC/CDC.

In the second step of the synthesis, the NbC/CDC particles were subjected to carbide-to-oxide conversion. The thermal treatment was carried out using a VG Scienta GP-CVD tube furnace in a gas mixture of Ar (flow rate: 100 cm³/min) and CO₂ (flow rate: 50 cm³/min) at 900 °C for 1 h. During the heating and cooling process, the CO₂ gas flow was excluded. The sample was labeled m-Nb₂O₅/CDC. The process can be expressed by eq3.



2.1.3. Synthesis of o-Nb₂O₅/CDC. The synthesis of o-Nb₂O₅/CDC involved the one-step chloroxidation of niobium carbide (NbC, H. C. Starck, purity ≥98%) and CuCl₂·2H₂O (Sigma Aldrich, purity ≥98%) with a stoichiometric amount of 1.0 mol NbC per 4.0 mol CuCl₂·2H₂O under ambient pressure.³¹ The process can be expressed by eq4.



NbC and CuCl₂·2H₂O were ground using a mortar until a homogeneous mixture was obtained. The obtained mixture was transferred to a quartz glass crucible and placed in an isothermal

zone of a quartz tube furnace (HTRH, Gero). After sealing the furnace, Ar gas was flushed at a flow rate of 50 cm³/min during the whole process. As a first step, the furnace was held at room temperature for 5 h to equilibrate the Ar gas atmosphere. Then, the furnace was heated to 700 °C at a rate of 2.5 °C/min and held at 700 °C for 3 h. Afterward, the furnace was cooled to room temperature. The obtained material was then poured into 200 mL of 3 M HCl solution and stirred overnight to remove elemental Cu. The acquired solution was filtered by using the vacuum filtration method with an excess amount of distilled water until the pH of the filtrate reached a value of 7. The filtrated product was dried at 75 °C overnight. The resulting sample was labeled o-Nb₂O₅/CDC.

2.2. Material Characterization. Scanning electron microscopy (SEM) images were obtained using a JEOL JSM 7500F field emission scanning electron microscope at an accelerating voltage of 3 kV. All samples were placed on a steel sample holder by using carbon tape. Transmission electron microscope (TEM) images were recorded using a JEOL JEM-2100F system operating at 200 kV in a vacuum. The samples were prepared by dispersing and sonicating in isopropanol and drop-cast onto a copper grid with a lacey carbon film. In addition, the elemental composition mapping of m-Nb₂O₅/CDC and o-Nb₂O₅/CDC was performed by energy-dispersive X-ray analysis (EDX) using an X-Max-150 detector from Oxford Instruments coupled with a JEOL JEM-2100F system.

Elemental analysis (CHNS) was carried out using a Vario Micro Cube System with sulfanilamide as the calibrant and a reduction temperature of 850 °C. Quantitative analysis of elemental oxygen was performed by using an OXY cube oxygen analyzer at 1450 °C.

X-ray photoelectron spectroscopy (XPS) was conducted using an Axis Ultra DLD spectrometer (Kratos Analytical) with monochromatic Al-K α as the photoelectron excitation source. At an X-ray radiation power of 150 W (15 kV, 10 mA) with a spot size of about 250 μ m, we used pass energies of 160 eV (wide scan) and 80 eV (elemental scan). For high-resolution scans, we used an X-ray radiation power of 225 W and a pass energy of 10 eV.

Powder X-ray diffraction (XRD) was performed using a Bruker AXS D8 Advance diffractometer with Ni-filtered Cu-K α radiation (wavelength: 0.15406 nm, voltage: 40 kV, current: 40 mA) for the powder samples of o-Nb₂O₅/CDC, m-Nb₂O₅/CDC, and com-Nb₂O₅. A variable diverge slit was used at the primary beam side and a Bruker AXS LYNXEYE detector at the secondary beam side. The background was reduced by discriminating against the detector. Air scattering was reduced by a knife edge. Measurements were carried out with standard powder sample holders in the 2 θ range between 7 and 150° with a step size of 0.013° and a total scan time of 4 h.

X-ray powder diffraction of NbC/CDC was carried out using a Bruker AXS D8 Discover diffractometer with Cu-K α radiation (wavelength: 0.15406 nm, voltage: 40 kV, current: 40 mA), a Goebel mirror (point focus: 0.5 mm), and a Bruker AXS VANTEC 500 area detector. The measurement was performed by positioning the detector from 20 to 100° 2 θ with an increment of 20° 2 θ . The total measurement time was chosen as 55 min. The Bruker AXS software TOPAS 5 was used for Rietveld refinements for all the powder samples. Instrumental line broadening was included in a fundamental parameter approach.³⁵

Raman spectra were recorded using a Renishaw inVia system equipped with an Nd-YAG laser (532 nm) and a power of 0.5 mW at the surface of the samples. From each of the samples, 10 different spots were recorded with five accumulations and 30 s acquisition time in the range of 100–3200 cm⁻¹. Peak analysis was performed by baseline corrections, assuming Voigt peak profiles for D-mode, G-mode, D'-mode, and amorphous carbon.

To obtain values for the specific surface area (SSA) and pore volume of the samples, nitrogen gas sorption analysis (GSA) at -196 °C was performed using a Quantachrome Quadrasorb system. The samples were degassed at 300 °C under vacuum conditions for 24 h. The total pore volume was obtained at a relative pressure value of 0.95. The SSA values were calculated using the Brunauer–Emmett–Teller (BET) equation (Ref.³⁶) in the linear pressure range of 0.01–0.1 (Ref.³⁷) using the ASiQwin software package.

Thermogravimetric analysis (TGA) using a TG 209 F1 Libra system (Netzsch) was performed to characterize oxidation vacancies of the m-Nb₂O₅/CDC and o-Nb₂O₅/CDC samples. TGA of the samples was carried out in a mixture of synthetic air (80 cm³/min) and Ar (20 cm³/min) with a heating rate of 5 °C/min.

2.3. Electrochemical Characterization. A slurry of the electrodes was prepared using a mixture of 80 mass % of active materials (o-Nb₂O₅/CDC, m-Nb₂O₅/CDC, and com-Nb₂O₅), 10 mass % of polyvinylidene fluoride (PVdF, Alfa Aesar) as a binder, and 10 mass % of carbon black (C65, Imerys Graphite & Carbon) as a conductive additive. The required amount of active materials and carbon black was mixed using a mortar. The mixtures were added into a solution of PVdF and *N*-methyl-2-pyrrolidone (NMP, Sigma-Aldrich). An excess amount of NMP was added to the slurry to adjust the viscosity, and the resulting slurry was stirred overnight, and then coated on Cu foil with a wet thickness of 125 μ m. The coated electrodes were dried at 110 °C in a vacuum for 10 h. After that, the coated electrodes were gently pressed in a rolling machine (HR01 hot rolling machine, MTI) and cut into a circle shape with a diameter of 12 mm. The average mass loading values of o-Nb₂O₅/CDC and m-Nb₂O₅/CDC were 2.1 and 1.4 mg/cm², respectively.

Coin cells (2032-type) were assembled in an argon-filled glove box (O₂, H₂O < 1 ppm) with lithium foil (diameter of 12 mm) as the counter and reference electrode, two pieces of Celgard 2325 (diameter of 18 mm) as a separator, and 1 M lithium hexafluorophosphate (LiPF₆) in an ethylene carbonate (EC) and dimethyl carbonate (DMC) mixture in the volumetric ratio of 1:1-EC:DMC (Sigma-Aldrich) as the electrolyte.

A VMP300 system connected to a Bio-Logic multichannel potentiostat was used to record the cyclic voltammetry (CV) results in the potential range of 1.0–2.5 V vs. Li/Li⁺ at a scan rate of 0.05 mV/s. For galvanostatic charge/discharge cycling with potential limitation, GCPL measurements were carried out using an Arbin Battery Cycler in the range of 1.0–2.5 V vs. Li/Li⁺ using 0.01–10 A/g to observe the rate capability and specific current of 1 A/g to examine cyclic stability. The specific capacity was calculated based on the mass of the active material of the electrodes.

To quantify the strain of the electrodes during charging and discharging, electrochemical dilatometry measurements were carried out using an ECD-2-nanosystem from EL-CELL connected to a VSP300 Bio-Logic multichannel potentiostat.³⁸ The dilatometer cell was assembled in an Argon-filled glove box (O₂, H₂O < 1 ppm) with metallic lithium (diameter of 11 mm) as the counter and reference electrode, one piece of glass microfiber filters (GF/F, Whatman) with a diameter of 13 mm as an additional separator, and 1 M lithium hexafluorophosphate (LiPF₆) in an ethylene carbonate (EC) and dimethyl carbonate (DMC) mixture in the volumetric ratio of 1:1-EC:DMC (Sigma Aldrich) as the electrolyte. The measurements were performed at a scan rate of 0.5 mV/s at 25 \pm 1 °C.

3. RESULTS AND DISCUSSION

3.1. Material Characterization. To better capitalize on the charge storage capacity intrinsic to ion insertion into the host matrix of crystalline niobium pentoxide, we designed a synthesis strategy to implement electrically conductive carbon at the nanoscale level within the metal oxide matrix.³⁹ Such hybrids are attractive electrode materials for combined high power and high energy applications.^{39–41} For our work, we used two different synthesis routes: (1) a two-step process first incompletely converted NbC to CDC at 1000 °C yielding NbC/CDC; then, the residual core was subjected to thermal treatment in CO₂ at 900 °C to oxidize the carbide core without completely removing the CDC phase, yielding mixed monoclinic and tetragonal niobium pentoxide/carbide-derived carbon (m-Nb₂O₅/CDC). (2) The one-step chloroxidation of NbC at 700 °C yielded orthorhombic niobium pentoxide/carbide-derived carbon (o-Nb₂O₅/CDC). To better understand the influence of the structural defect on the electrochemical properties of m-Nb₂O₅/

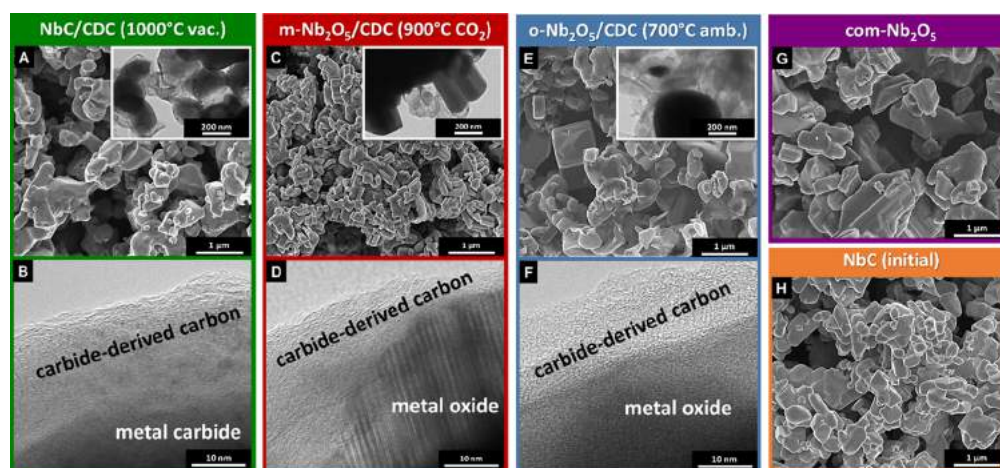


Figure 1. Scanning electron micrographs and TEM micrographs (inset, upper right corner) (A, B) of the NbC/CDC, (C, D) of m-Nb₂O₅/CDC, and (E, F) of o-Nb₂O₅/CDC. Scanning electron micrograph of (G) com-Nb₂O₅ and (H) the initial NbC powder.

CDC, we further investigated commercial niobium pentoxide (com-Nb₂O₅), which also contains a monoclinic and tetragonal Nb₂O₅ phase mixture with a lower degree of defect.

In our two-step synthesis, scanning electron micrographs show that the NbC/CDC material is composed of particles in the range of ca. 0.5–1 μm (Figure 1A). This value aligns with the initial particle size of the NbC material (Figure 1H) as the carbide-to-CDC transformation is known to be largely conformal, that is, preserves the size and shape of the initial ceramic.^{42,43} Transmission electron micrographs (Figure 1A,B) reveal the presence of carbon (CDC) predominantly at the outer regions of the NbC granules. The CDC domains are partially removed but not completely lost after oxidation at 900 °C in CO₂, as indicated by the decreased particle size with a rod-like morphology (Figure 1C,D). Thereby, the m-Nb₂O₅/CDC sample qualifies as a hybrid material of carbon (2.6 mass %) and niobium oxide (97.4 mass %), as confirmed by chemical analysis (Table 1).

Table 1. Elemental Composition Analysis by XPS and Carbon Content Measured by Elemental CHNS-O Analysis

sample	XPS		CHNS-O	
	Nb:O atomic ratio	Nb (at%)	C (mass %)	O (mass %)
m-Nb ₂ O ₅ /CDC	0.36	15.2	2.6 ± 0.1	12.5 ± 0.7
o-Nb ₂ O ₅ /CDC	0.24	5.2	5.7 ± 0.3	29.6 ± 1.6
stoichiometric Nb ₂ O ₅	0.40	28.6	0	30.1

As seen in Figure 1E, the particle morphology and the size of o-Nb₂O₅/CDC are very close to the initial NbC material (Figure 1H). In comparison to m-Nb₂O₅/CDC, o-Nb₂O₅/CDC shows a much more disordered carbon phase as a result of the lower synthesis temperature.⁴² Chemical analysis shows 5.7 mass % of carbon and 94.3 mass % of niobium pentoxide (Table 1), yielding, like for m-Nb₂O₅/CDC, a hybrid material of carbon and metal oxide.

The structure of the NbC/CDC particles was further analyzed by XRD. The diffraction pattern was refined using Rietveld refinement (Supplementary Information, Figure S1 and Table S1). We determined residual cubic (*Fm*3*m*) NbC with a lattice parameter of *a* = 0.45 nm with the characteristic Bragg positions at 34.7, 40.3, 58.3, and 69.6° 2θ. After oxidation in CO₂, NbC/

CDC was converted to m-Nb₂O₅/CDC, and the corresponding diffractogram did not match with common Nb₂O₅ phases (Figure 2A).

Based on X-ray diffraction, the most likely explanation for the measured intensities found for m-Nb₂O₅/CDC (Figure 2A) and com-Nb₂O₅/CDC (Figure 2D) was to assume the co-existence of the two different crystal phases of Nb₂O₅. To this end, we calculated the diffraction patterns of monoclinic Nb₂O_{4.91} (space group *P2*/*m*, ICSD 160156; Figure 2B)⁴⁴ and tetragonal Nb₂O₅ (space group *I4*/*mmm*, ICSD 17027; Figure 2C).⁴⁵ By comparing the calculated and measured intensities in Figure 2A and Figure 2D, we see a fair and partial matching to the powder pattern; no reasonable agreement between the calculated and observed patterns was achieved when assuming only one crystal structure (i.e., either only tetragonal or only monoclinic).

The calculated position of the (330) reflection of the tetragonal phase at 18.6° 2θ was shifted to higher angles compared to the observed one. In contrast, the calculated (440) reflection at 24.8° 2θ was shifted to lower angles. This may not be compensated by variations of the lattice parameters. Either another structure type of lower symmetry or special properties of the microstructure of the tetragonal phase might cause this phenomenon. A similar problem was encountered in the case of the monoclinic phase. The reflection groups around 18 and 25° 2θ would have to move toward another, which was not possible in the given symmetry.

As seen in Figure 2B,C, tetragonal Nb₂O₅ (M-Nb₂O₅) and monoclinic Nb₂O₅ (N-Nb₂O₅) are structurally closely related. These structures are composed of blocks of linked NbO₆ octahedra with different block sizes and shearing of these blocks.^{45–47} The defects of oxygen in Nb₂O_{4.91} are compensated by forming a shear structure of the tetragonal Nb₂O₅. An even more drastic splitting of the reflections may be found in the pattern of orthorhombic Nb₂O_{4.83} (space group *Cmcm*, ICSD 160157, Ref.⁴⁴). The reflection splitting of Nb₂O₅ correlates with the oxygen content.⁴⁴ This means that a smaller number of oxygen deficiencies translate to a lower reflection splitting.

Severe anisotropic reflection broadening is present in the diffraction patterns of the sample m-Nb₂O₅/CDC (Figure 2A). The (00*L*) reflections show only minor broadening, while (*hk*0) reflections show major broadening. A lattice parameter very similar to *c* in tetragonal Nb₂O₅ is also given by both other

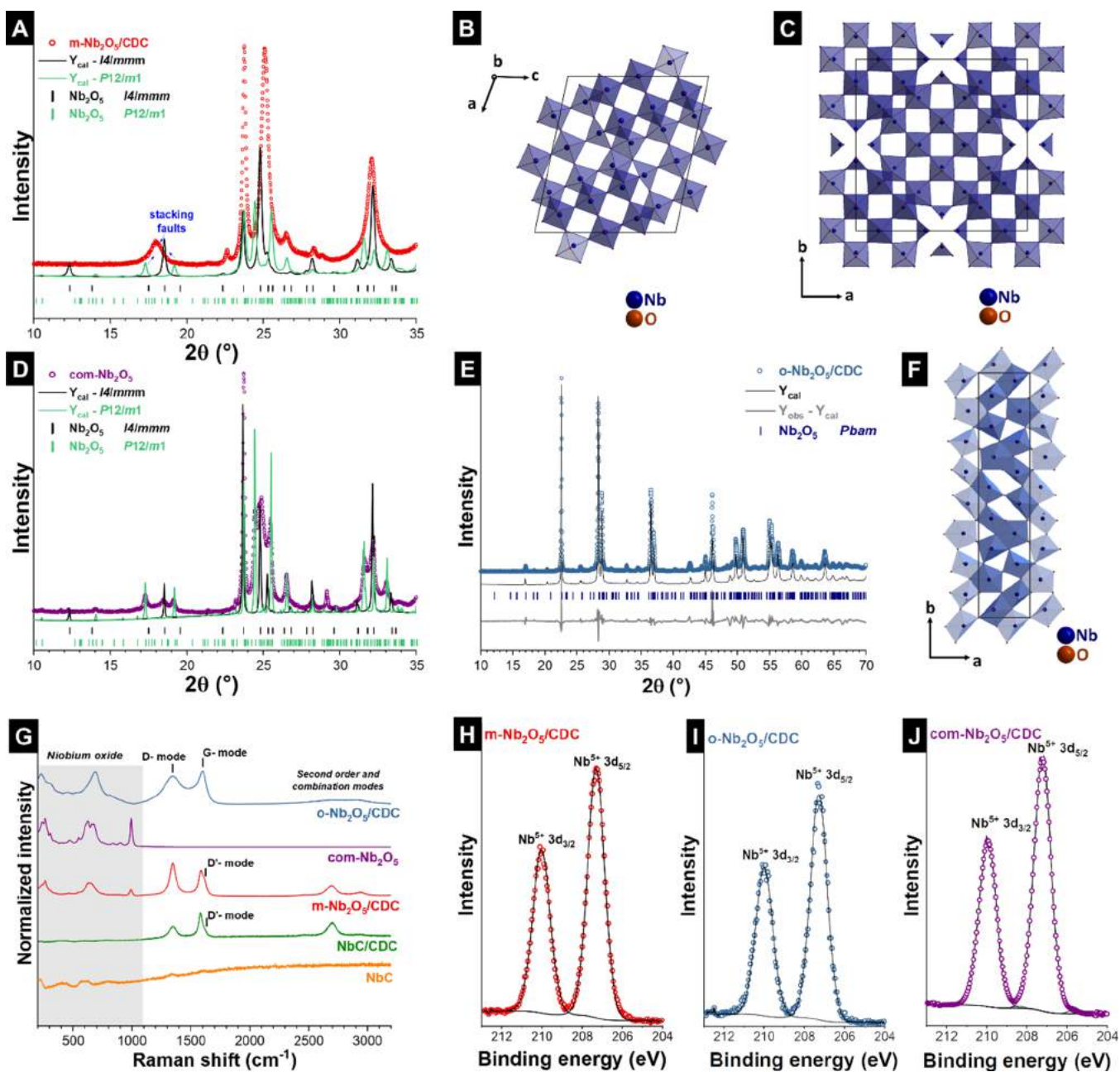


Figure 2. (A) Measured X-ray diffraction pattern of m-Nb₂O₅/CDC with the calculated pattern of monoclinic Nb₂O_{4.91} (*P12/m1*) and tetragonal Nb₂O₅ (*I4/mmm*). (B) Calculated crystal structure of monoclinic Nb₂O_{4.91} (*P12/m1*) and (C) tetragonal Nb₂O₅ (*I4/mmm*). (D) Measured X-ray diffraction pattern of com-Nb₂O₅ with the calculated pattern of monoclinic Nb₂O_{4.91} (*P12/m1*) and tetragonal Nb₂O₅ (*I4/mmm*). (E) Rietveld refinement of the X-ray diffraction pattern of o-Nb₂O₅/CDC. (F) Calculated crystal structure of orthorhombic Nb₂O₅ (*Pbam*). (G) Raman spectra and (H–J) XPS Nb 3d spectra of the samples.

structures (ca. 0.382 nm), while the other lattice parameters are different and range from 2.03 nm in the tetragonal structure to 1.57 and 1.79 nm in the monoclinic structure. Different arrangements of the shearing structures may coexist within small domains, without disrupting the mean symmetry of the host lattice completely. This leads to diffuse broadening instead of distinct sharp reflections. Also, stacking faults have been reported to exist within Nb₂O₅ samples.⁴⁷ Stacking faults may cause symmetry contradictory shifting of reflections and isotropic or anisotropic or even asymmetric broadening.^{48–50} Therefore, the observed pattern is consistent with tetragonal Nb₂O₅ as the host lattice with different types of domain defects, a combination of different shear structures and stacking faults.

Therefore, the overall structure may be described as defect-rich tetragonal.

We included in our study also commercially available Nb₂O₅ (com-Nb₂O₅). The analysis of com-Nb₂O₅ (Figure 2D) showed partial fitting with fixed microstructural parameters using the phases of Nb₂O_{4.91} (space group *P2/m*) and tetragonal Nb₂O₅ (space group *I4/mmm*). The reflections of com-Nb₂O₅ (especially at 17.5/18.5/19.1 °2θ) display a lower degree of broadening and less shifting in comparison with the reflections of m-Nb₂O₅/CDC (Figure 2A). A lower reflection splitting correlates with oxygen vacancies in the structures. The reflection splitting of m-Nb₂O₅/CDC is much higher than that of com-Nb₂O₅. Hence, the m-Nb₂O₅/CDC material possesses higher

oxygen deficiency than com-Nb₂O₅. Therefore, the com-Nb₂O₅ can be characterized as a lower-degree-defected mixed monoclinic and tetragonal state structure.

The X-ray diffractogram of o-Nb₂O₅/CDC (Figure 2E) can be well fitted using the orthorhombic structure of Nb₂O₅ proposed by Kato et al. (space group *Pbam*, ICSD 1840).³³ Four of the seven sites of Nb were originally described with *x,y,z* sites (Wyckoff position 8i, multiplicity 8) with *z* being close to 1/2, leading to a split position with a site occupancy factor (SOF) of 0.5. The additional three 4g Nb sites with SOF < 0.1 were defined to fit the residual electron density. An R-value R_{wp} of 8.27% was achieved using this model in Rietveld refinement. To simplify the model, the three 4g Nb sites were removed, and the former 8i Nb sites were substituted by *x,y,1/2* sites (Wyckoff position 4h, multiplicity 4) with a value of SOF = 1. Using the simplified model, we obtained a value for R_{wp} of 8.64%. Since the difference in the residuals was small and the simplified model provided an adequate description of the pattern, we used it in our work, and the corresponding crystal structure is shown in Figure 2F and Supporting Information, Table S1. The reflection profile of o-Nb₂O₅/CDC also reveals a minor but slightly anisotropic broadening of the reflections. Especially the (001) reflection at 22.6° 2θ and the (002) reflection at 46.1° 2θ show a sharper reflection profile compared to other reflections. Such is consistent with the lattice strain, and additional weak reflections may relate to a small amount of the secondary phase, like a different structure of niobium with lower symmetry.

For further characterization, we employed Raman spectroscopy (Figure 2G). The Raman spectra of NbC/CDC, m-Nb₂O₅/CDC, and o-Nb₂O₅/CDC show the characteristic peaks of incomplete graphitic carbon for sp²-hybridized carbon, D- and G-modes at around 1346 and 1588 cm⁻¹, and carbon-related combination and overtone modes between 2500 and 3200 cm⁻¹.⁵¹ The samples NbC/CDC and m-Nb₂O₅/CDC present also a D'-mode at 1632 cm⁻¹, which is related to a disorder-induced splitting of the carbon E_{2g} mode.⁵² The presence of a discernable D'-mode aligns with edge-defects in a carbon network with a higher degree of graphitic ordering compared to m-Nb₂O₅/CDC. In the latter case, we see much broader D- and G-mode bands.

The peak deconvolution of the Raman spectra is outlined in Table 2 and Supplementary Information, Figure S2. The full-

Table 2. Raman Spectra Analysis of the Carbon D- and G-Modes^a

sample	mode	position (cm ⁻¹)	FWHM (cm ⁻¹)	I _D /I _G
NbC/CDC	D-mode	1346	73 ± 7	0.9 ± 0.2
	G-mode	1580	37 ± 5	
m-Nb ₂ O ₅ /CDC	D-mode	1348	63 ± 4	1.4 ± 0.2
	G-mode	1584	56 ± 2	
o-Nb ₂ O ₅ /CDC	D-mode	1344	164 ± 7	2.7 ± 0.5
	G-mode	1601	68 ± 3	

^aFWHM = full-width at half-maximum.

width at half maximum (FWHM) of the D- and G-mode of o-Nb₂O₅/CDC was 164 ± 7 and 68 ± 3 cm⁻¹, respectively. For comparison, for NbC/CDC, the D-mode FWHM was 73 ± 7 cm⁻¹ and the G-mode FWHM was 37 ± 5 cm⁻¹. The narrower D- and G-modes align with the lower I_D/I_G ratio of NbC/CDC (0.9 ± 0.2) compared to o-Nb₂O₅/CDC (1.4 ± 0.2). This can be explained by the partial oxidation of the CDC when

transforming NbC/CDC into m-Nb₂O₅/CDC. Even broader D-mode (164 ± 07 cm⁻¹) and G-mode (68 ± 3 cm⁻¹) along with a larger I_D/I_G ratio (2.7 ± 0.5) were seen for o-Nb₂O₅/CDC. The more disordered nature of the carbon in o-Nb₂O₅/CDC was a result of the lower processing temperature (700 °C) compared to m-Nb₂O₅/CDC (900–1000 °C) as well known from conventional CDC synthesis.^{53–55} In addition to the disordered structure, the CDC present in m-Nb₂O₅/CDC and o-Nb₂O₅/CDC is also nanoporous, as seen from the enhanced specific surface area of 19 and 57 m²/g, respectively (Supplementary Information, Table S2; sorption isotherm are displayed in Supplementary Information, Figure S3).

Raman spectra of m-Nb₂O₅/CDC and o-Nb₂O₅/CDC also show vibrational modes related to Nb–O–Nb in the low wavenumber region of 100–300 cm⁻¹ and the Nb–O stretching mode in the range of 500–800 cm⁻¹.⁵⁶ While the edge-shared octahedral NbO₆ stretching mode of o-Nb₂O₅/CDC displays the Raman peak at 688 cm⁻¹, m-Nb₂O₅/CDC shows the Raman peak at 628 cm⁻¹.⁵⁷ The latter peak indicates distorted NbO₆ octahedra in the structure of o-Nb₂O₅/CDC, while the Raman peak of m-Nb₂O₅/CDC located at 688 cm⁻¹ aligns with the more ordered NbO₆ octahedra.^{56,58} We also find the spectral feature of the Nb=O terminal double bond in the region of 850–1000 cm⁻¹ for m-Nb₂O₅/CDC and o-Nb₂O₅/CDC samples.⁵⁶ In addition to that, the Raman spectrum of com-Nb₂O₅ (Figure 2G) shows only niobium oxide peaks in the region of 100–1000 cm⁻¹.

X-ray photoelectron spectroscopy (XPS) was performed to further analyze the Nb-valence states of o-Nb₂O₅/CDC, m-Nb₂O₅/CDC, and com-Nb₂O₅. The XPS spectra of Nb 3d of the samples are shown in Figure 2H–J. The identical binding energy for Nb 3d (Nb⁵⁺) in Nb₂O₅ was detected at 210.1 and 207.3 eV for Nb 3d_{3/2} and Nb 3d_{5/2}, respectively.⁵⁹ The O 1s-signal was fitted to three subpeaks located at 530.3, 531.7, and 532.9 eV, which were attributed to the Nb–O bond, C–O bond/hydroxyl groups, and H₂O/C=O, respectively (Supplementary Information, Figure S4A–C).¹⁴ As seen from Table 1, the measured Nb:O atomic ratio of m-Nb₂O₅/CDC (0.36) and o-Nb₂O₅/CDC (0.24) was both lower than what was expected for stoichiometric Nb₂O₅ (0.4). The closest value to the stoichiometrically ideal ratio was found for com-Nb₂O₅ (0.39), as seen in Supplementary Information, Table S3. In addition, we further performed thermogravimetric analysis of m-Nb₂O₅/CDC and o-Nb₂O₅/CDC using a mixture of synthetic air and argon (Supporting Information, Figure S5). The observed mass gain (Table 1) aligns with oxygen deficiency in m-Nb₂O₅/CDC (~4%) and o-Nb₂O₅/CDC (~1%). Carbon is mostly present in the sp²-hybridization, but we also find sp³-carbon, C–O bonds, and COO groups with the XPS peaks at 284.1, 285.1, 286.6, and 288.7 eV, respectively (Supplementary Information, Figure S4D,E).^{60,61}

3.2. Electrochemical Analysis. Initial electrochemical testing showed the need to add a conductive additive (carbon black; 10 mass %) to the Nb₂O₅/carbon hybrid material to fully capitalize on the intrinsic charge storage capacity of the samples. The intrinsically present carbon (CDC) provides better charge transport in the samples; however, an insufficient amount of carbon is present in the samples as the sole charge carrier conductor. We first carried out cyclic voltammetry at a scan rate of 0.05 mV/s, and the cut-off potential was between 1.0 and 2.5 V vs. Li/Li⁺ (Figure 3A–C). The cyclic voltammogram of m-Nb₂O₅/CDC shows sharp reduction peaks at 1.6 and 1.1 V vs. Li/Li⁺ and oxidation peaks at 1.2 and 1.7 V vs. Li/Li⁺. The

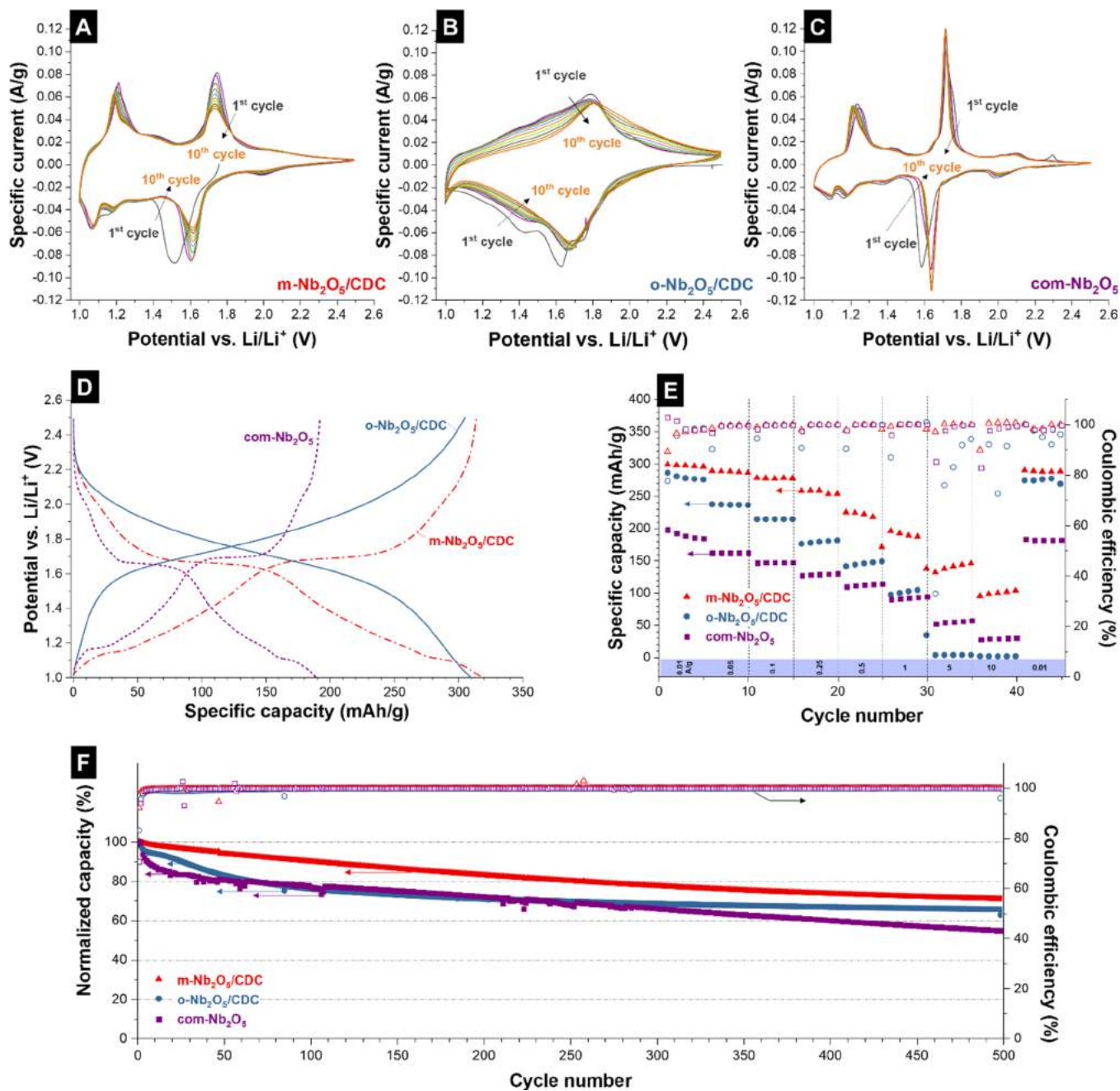


Figure 3. Cyclic voltammograms of (A) $m\text{-Nb}_2\text{O}_5/\text{CDC}$, (B) $o\text{-Nb}_2\text{O}_5/\text{CDC}$, and (C) $\text{com-Nb}_2\text{O}_5$. GCPL charge/discharge profiles of (D) $m\text{-Nb}_2\text{O}_5/\text{CDC}$, $o\text{-Nb}_2\text{O}_5/\text{CDC}$, and $\text{com-Nb}_2\text{O}_5$ samples at a specific current of 0.01 A/g. Rate handling performance of (E) $m\text{-Nb}_2\text{O}_5/\text{CDC}$, and $o\text{-Nb}_2\text{O}_5/\text{CDC}$. Cyclic stability performance of (F) $m\text{-Nb}_2\text{O}_5/\text{CDC}$, $o\text{-Nb}_2\text{O}_5/\text{CDC}$, and $\text{com-Nb}_2\text{O}_5$ at a specific current of 0.1 A/g.

amplitude of the redox peak pair at 1.6 V vs. Li/Li^+ and 1.7 V vs. Li/Li^+ seen in the cyclic voltammograms is decreased as the number of cycles is increased, while the oxidation peak at 1.2 V vs. Li/Li^+ is increased (Figure 3A). The cyclic voltammogram of $o\text{-Nb}_2\text{O}_5/\text{CDC}$ shows just one broad lithiation/delithiation peak pair at 1.6–1.8 V vs. Li/Li^+ (Figure 3B). This electrochemical signature is typical for orthorhombic Nb_2O_5 .^{9,14} Similar to what we have observed in the $m\text{-Nb}_2\text{O}_5/\text{CDC}$, $o\text{-Nb}_2\text{O}_5/\text{CDC}$ also showed a broad peak. The broadening becomes stronger as the cycle number increased.

To better understand the impact of the different degree defected structures of monoclinic and tetragonal phases of Nb_2O_5 on the electrochemical performance, we further

compared commercially available Nb_2O_5 ($\text{com-Nb}_2\text{O}_5$) and $m\text{-Nb}_2\text{O}_5/\text{CDC}$. As seen in Figure 3C, $\text{com-Nb}_2\text{O}_5$ depicts a much sharper lithiation and delithiation peak than that of $m\text{-Nb}_2\text{O}_5/\text{CDC}$, suggesting that lithium ions are hosted in the specific site in the structure of $\text{com-Nb}_2\text{O}_5$, whereas lithium ions are randomly diffused through the vacancies caused by stacking fault in the structure. The $\text{com-Nb}_2\text{O}_5$ also consists of vacancies caused by the stacking fault in the structure; however, $m\text{-Nb}_2\text{O}_5/\text{CDC}$ reveals a higher degree of stacking fault (Figure 2A,D). Thus, the broadening redox peaks in $m\text{-Nb}_2\text{O}_5/\text{CDC}$ are most likely caused by random diffusion of lithium in the structure.

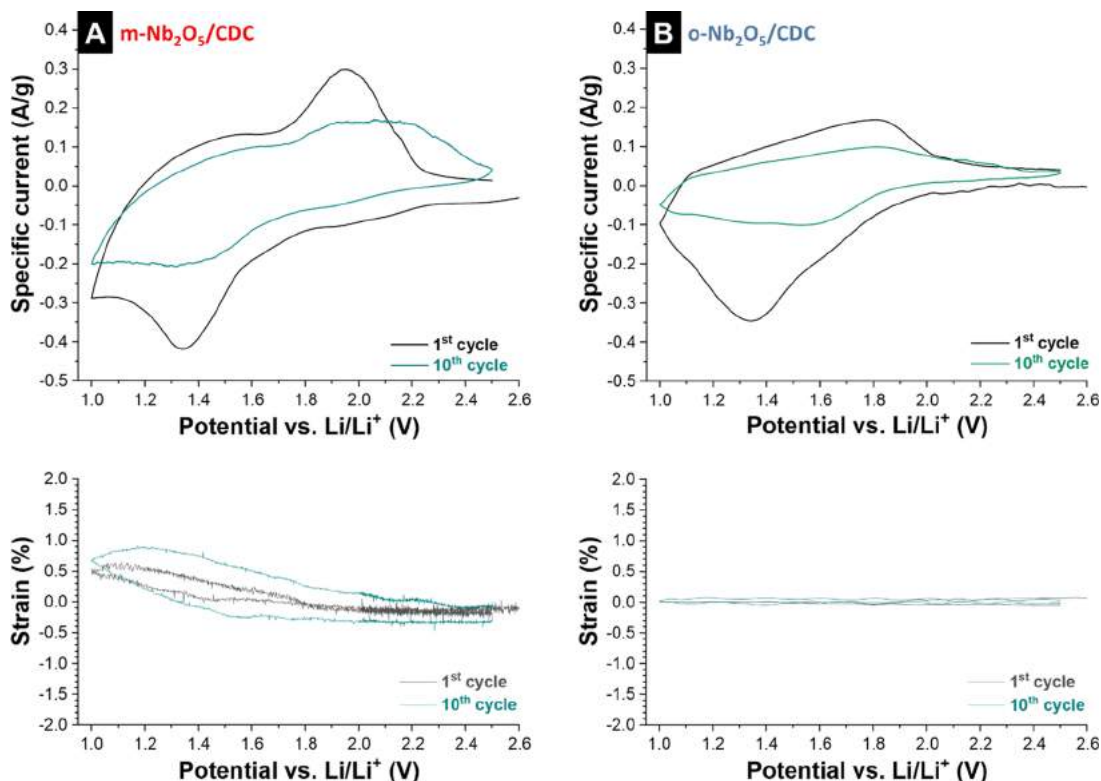


Figure 4. Electrochemical expansion curve (bottom) and the corresponding cyclic voltammogram (top) at 0.5 mV/s sweep rate of (A) m-Nb₂O₅/CDC and (B) o-Nb₂O₅/CDC recorded for the 1st and 10th cycle.

The galvanostatic charge/discharge operation at 0.01 A/g shows the ability of m-Nb₂O₅/CDC and o-Nb₂O₅/CDC to yield a charge storage capacity of about 300 mAh/g (Figure 3D). The profile shape aligns with the presence of several (m-Nb₂O₅/CDC and com-Nb₂O₅) or just one diffuse (o-Nb₂O₅/CDC) redox peak. The calculated capacity is normalized to the full mass of Nb₂O₅/CDC, that is, excluding the binder and carbon black but including the mass of CDC. This result is in contrast to the state-of-the-art in the Nb₂O₅ for use as a lithium-ion battery, where maximum insertion capacity was reported about 200 mAh/g (Supporting Information, Table S4).^{9,14} An excess of 200 mAh/g must also relate to a charge transfer process that involves three instead of two electrons in the voltage window (≥ 1 V vs. Li/Li⁺) of Li insertion to Nb₂O₅. For example, nanostructured monoclinic Nb₂O₅ also shows 242 mAh/g at a specific current of 0.05 A/g in the voltage window of 1.0–2.6 vs. Li/Li⁺, while box-implanted orthorhombic Nb₂O₅ nanorods provide a capacity of 247 mAh/g at 0.04 A/g in the voltage window of 1.1 to 3.0 V vs. Li/Li⁺ (Supporting Information, Table S4). The low amount of CDC and the limited charge storage via ion electrosorption of a material with <100 m²/g rule out the active role of carbon. Instead, the enhanced energy storage ability must relate to the intrinsic features of m-Nb₂O₅ and o-Nb₂O₅ instead, which are aided by the carbide-derive oxide-formation route and the presence of residual carbon. Oxygen deficiencies, as confirmed by the TGA results of m-Nb₂O₅/CDC and o-Nb₂O₅/CDC, are known to provide an increased specific capacity of lithium-insertion materials.^{62,63}

Table S4 in the Supporting Information shows that the high performance of Nb₂O₅ has been limited to nanoscaled materials, such as nanobelts, nanorods, or nanosheets.^{26,27} In contrast, our results demonstrate that it is possible for micrometer-scaled (bulk) materials to achieve high performance by careful design

of crystal structure defects as well. This approach is possibly adaptable to other bulk materials and may open new design concepts for advanced electrode material development.

Considering the interstitial sites for lithium accommodation, m-Nb₂O₅/CDC provides rather constrained space as compared with o-Nb₂O₅/CDC, which results in a higher barrier energy. However, the ion transport path within the structure of m-Nb₂O₅/CDC seems to be faster than that of o-Nb₂O₅/CDC. However, the charge transfer kinetics may also play a role because m-Nb₂O₅/CDC has a higher degree of graphitic carbon than that of carbon in the m-Nb₂O₅/CDC (Table 2). Based on the structures shown in Figure 2B,C,F, m-Nb₂O₅ may provide fast lithium diffusion due to its shorter mean free path per structure and small grain boundary. The material o-Nb₂O₅/CDC shows a zig-zag diffusion path resulting in higher kinetic energy. With the added effect of the large grain boundary, the electrochemical performance of o-Nb₂O₅/CDC is either limited by diffusion or charge transfer kinetics.

To this end, we conducted kinetic analysis by plotting the current at a specific potential versus the scan rate (Supplementary Information, Figure S6). Within such a current-vs.-scan rate plot, a slope of 0.5 (b value) corresponds to a diffusion-limited process, while a slope of 1.0 would be found for an ideal ion electrosorption process.^{64–68} When fitting data obtained for rates between 0.05 and 3 mV/s, we obtain for m-Nb₂O₅/CDC peak currents at 1.6 and 1.7 V vs. Li/Li⁺ and broad peaks for o-Nb₂O₅/CDC a b-value of ca. 0.5. This value is slightly smaller (i.e., more diffusion limited) compared to the com-Nb₂O₅ material with b values of 0.59–0.65. We further analyzed the cyclic voltammograms by using the method described by Ardizzone et al. (Supplementary Information, Figure S7).⁶⁷ The total charge scales well with the inverse of the square root of the

scan rate, which indicates the solid-state diffusion-limited process.

From Figure 3E, we see that m-Nb₂O₅/CDC is capable of performing faster charge/discharge as compared to the sample o-Nb₂O₅/CDC. From the kinetic analysis of the cyclic voltammograms (Supplementary Information, Figures S6 and S7), both materials are under diffusion control; thus, the superior rate handling of m-Nb₂O₅/CDC can be explained as follows: (1) o-Nb₂O₅/CDC possess a lower degree of graphitic carbon than that of m-Nb₂O₅/CDC, (2) o-Nb₂O₅/CDC has lower oxygen deficiency than m-Nb₂O₅/CDC, which causes lower conductivity, resulting in poorer rate handling performance,⁶⁹ (3) the particle size of m-Nb₂O₅/CDC (Figure 1C) is smaller than that of o-Nb₂O₅/CDC (Figure 1E), (4) the specific surface area of the o-Nb₂O₅/CDC (57 m²/g) is larger than that of m-Nb₂O₅/CDC (19 m²/g), while the microporous contribution as seen from the isotherm of o-Nb₂O₅/CDC is higher than that of m-Nb₂O₅/CDC (Supporting Information, Figure S3); thus, the combination of surface area and mesoporosity enables the electrolyte penetration throughout the material, resulting in higher capacity and better rate handling, (5) CDC distribution in the o-Nb₂O₅/CDC is poorer than that of m-Nb₂O₅/CDC (Supporting Information, Figure S8). At 10 A/g charge/discharge rate, m-Nb₂O₅/CDC possesses a specific capacity of 100 mAh/g, while o-Nb₂O₅/CDC completely loses the charge storage ability (Figure 3E). After 40 cycles of rate handling, both Nb₂O₅ largely recover their specific capacity at 0.01 A/g (288 mAh/g for m-Nb₂O₅/CDC and 274 mAh/g for o-Nb₂O₅/CDC). This different capacity between our m-Nb₂O₅/CDC and com-Nb₂O₅ might be explained by three main reasons: (1) the lower degree of deflection in the structures of com-Nb₂O₅ compared to m-Nb₂O₅/CDC, (2) the significant larger particle size of com-Nb₂O₅ (Figure 1G) compared to m-Nb₂O₅/CDC (Figure 1C), and (3) the absence of the nanoscopic blending of Nb₂O₅ with carbon.

Performance stability was tested at a specific current of 0.1 A/g (Figure 3F). After 500 galvanostatic charge/discharge cycles, m-Nb₂O₅/CDC has maintained 72% of the specific capacity, while o-Nb₂O₅/CDC and com-Nb₂O₅ can maintained 66 and 55%, respectively. This obtained lower cyclic stability of com-Nb₂O₅ compared to m-Nb₂O₅/CDC and o-Nb₂O₅/CDC might be explained by the Coulombic efficiency ranges during the entire charge/discharge operation at values above 98% for all samples.

The performance stability of m-Nb₂O₅/CDC and o-Nb₂O₅/CDC is also aided by being virtually zero-strain materials during lithiation and delithiation. This absence of microstrain translates also to a zero-macrostrain as revealed by electrochemical dilatometry (Figure 4). The m-Nb₂O₅/CDC and o-Nb₂O₅/CDC materials display no significant compaction/expansion during Li⁺ insertion at the range of 1.3 and 1.9 V vs. Li/Li⁺. A slightly larger initial amplitude of strain is seen for m-Nb₂O₅/CDC of up to 1%, which increases for continued cycling (Figure 4A). The height change of o-Nb₂O₅/CDC remains stable at an amplitude below ±2% (Figure 4B).

Based on the half-cell data from galvanostatic charge–discharge, it is possible to construct a Ragone plot. While it is not suitable to compare the half-cell Ragone plot data with device-normalized performance, it still allows us to obtain a robust relative comparison between the three types of materials tested in our work. As seen in Figure 5, the performance of half-cells of m-Nb₂O₅/CDC and o-Nb₂O₅/CDC is very comparable,

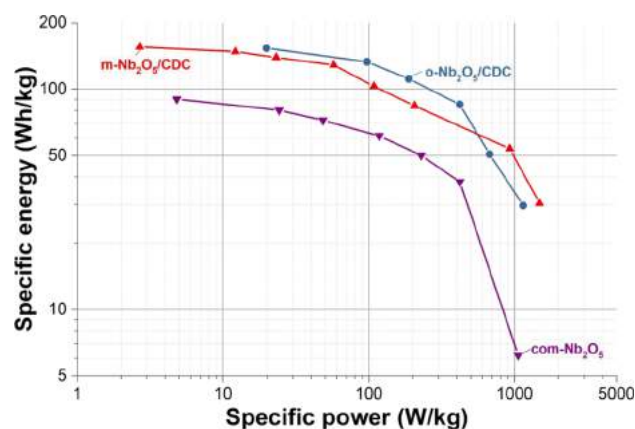


Figure 5. Ragone plot for half-cells of m-Nb₂O₅/CDC, o-Nb₂O₅/CDC, and com-Nb₂O₅.

while both samples are superior compared with com-Nb₂O₅. For example, the m-Nb₂O₅/CDC exhibits specific energies of 156 and 31 Wh/kg at specific power values of 3 W/kg and 1 kW/kg, respectively. In comparison, com-Nb₂O₅ delivers 90 Wh/kg at 5 W/kg and 6 Wh/kg at 1 kW/kg.

4. CONCLUSIONS

Niobium carbide is an attractive precursor for the synthesis of niobium pentoxide with enhanced electrochemical performance for use as a LIB anode material. Either by a two-step process of chlorination followed by oxidation in CO₂ or via one-step chloroxidation, we obtained Nb₂O₅/CDC hybrid materials with about 4 mass % of carbon. Carbide-derived o-Nb₂O₅/CDC and m-Nb₂O₅/CDC materials show a maximum capacity of about 300 mAh/g, which significantly exceeds the current state-of-the-art performance for Nb₂O₅ of about 200 mAh/g. Based on our results, we believe that the oxygen deficiency and the stacking faults in the Nb₂O₅ structures result in a superior capacity performance of Nb₂O₅/CDC as an anode for LIBs. Kinetically, o-Nb₂O₅/CDC exhibits slower charge/discharge performance compared to m-Nb₂O₅/CDC; the latter affords even 100 mAh/g at a high rate of 10 A/g. We also show evidence of robust cyclic stability over 500 cycles, suggesting a highly reversible lithiation/delithiation process, in alignment with a virtual zero strain material, as confirmed by electrochemical dilatometry.

■ ASSOCIATED CONTENT

Supporting Information

The Supporting Information is available free of charge at <https://pubs.acs.org/doi/10.1021/acsaem.9b02549>.

Results from the Rietveld refinement analysis, elemental composition analysis by XPS, scanning electron micrographs, transmission electron micrographs, Raman spectra and peak fitting analysis, nitrogen gas sorption isotherms, and electrochemical results (PDF).

■ AUTHOR INFORMATION

Corresponding Author

V. Presser – INM - Leibniz Institute for New Materials, 66123 Saarbrücken, Germany; Department of Materials Science and Engineering, Saarland University, 66123 Saarbrücken, Germany; orcid.org/0000-0003-2181-0590; Email: volker.presser@leibniz-inm.de

Authors

- Ö. Budak** – INM - Leibniz Institute for New Materials, 66123 Saarbrücken, Germany; Department of Materials Science and Engineering, Saarland University, 66123 Saarbrücken, Germany
- M. Geißler** – Ernst-Berl-Institut für Technische und Makromolekulare Chemie, Technische Universität Darmstadt, 64287 Darmstadt, Germany
- D. Becker** – Inorganic Solid-State Chemistry, Saarland University, 66123 Saarbrücken, Germany
- A. Kruth** – Leibniz Institute for Plasma Science and Technology, 17489 Greifswald, Germany
- A. Quade** – Leibniz Institute for Plasma Science and Technology, 17489 Greifswald, Germany
- R. Haberkorn** – Inorganic Solid-State Chemistry, Saarland University, 66123 Saarbrücken, Germany
- G. Kickelbick** – Inorganic Solid-State Chemistry, Saarland University, 66123 Saarbrücken, Germany
- B. J. M. Etzold** – Ernst-Berl-Institut für Technische und Makromolekulare Chemie, Technische Universität Darmstadt, 64287 Darmstadt, Germany; orcid.org/0000-0001-6530-4978

Complete contact information is available at:
<https://pubs.acs.org/10.1021/acsaem.9b02549>

Notes

The authors declare no competing financial interest.

ACKNOWLEDGMENTS

The authors acknowledge funding of the COSH-CDC project (PR-1173/5 & ET 101/14) by the German Research Foundation (DFG, Deutsche Forschungsgemeinschaft). This work was part of the Carbon Metal Oxide Nanohybrid project (CarMON) supported by the Leibniz Association (SAW-2017). The INM authors thank Eduard Arzt (INM) for his continuing support.

REFERENCES

- (1) Nitta, N.; Wu, F.; Lee, J. T.; Yushin, G. Li-ion battery materials: present and future. *Mater. Today* **2015**, *18*, 252–264.
- (2) Lukatskaya, M. R.; Dunn, B.; Gogotsi, Y. Multidimensional materials and device architectures for future hybrid energy storage. *Nat. Commun.* **2016**, *7*, 12647.
- (3) Brandt, K. Historical development of secondary lithium batteries. *Solid State Ionics* **1994**, *69*, 173–183.
- (4) Dunn, B.; Kamath, H.; Tarascon, J.-M. Electrical energy storage for the grid: A battery of choices. *Science* **2011**, *334*, 928–935.
- (5) Kim, H.; Jeong, G.; Kim, Y.-U.; Kim, J.-H.; Park, C.-M.; Sohn, H.-J. Metallic anodes for next generation secondary batteries. *Chem. Soc. Rev.* **2013**, *42*, 9011–9034.
- (6) Zhao, K.; Pharr, M.; Vlassak, J. J.; Suo, Z. Fracture of electrodes in lithium-ion batteries caused by fast charging. *J. Appl. Phys.* **2010**, *108*, No. 073517.
- (7) Lim, E.; Shim, H.; Fleischmann, S.; Presser, V. Fast and stable lithium-ion storage kinetics of anatase titanium dioxide/carbon onion hybrid electrodes. *J. Mater. Chem. A* **2018**, *6*, 9480–9488.
- (8) Scrosati, B.; Garche, J. Lithium batteries: Status, prospects and future. *J. Power Sources* **2010**, *195*, 2419–2430.
- (9) Augustyn, V.; Come, J.; Lowe, M. A.; Kim, J. W.; Taberna, P.-L.; Tolbert, S. H.; Abruña, H. D.; Simon, P.; Dunn, B. High-rate electrochemical energy storage through Li⁺ intercalation pseudocapacitance. *Nat. Mater.* **2013**, *12*, 518–522.
- (10) Han, J.-T.; Goodenough, J. B. 3-V Full cell performance of anode framework TiNb₂O₇/spinel LiNi_{0.5}Mn_{1.5}O₄. *Chem. Mater.* **2011**, *23*, 3404–3407.
- (11) Uhlmann, C.; Illig, J.; Ender, M.; Schuster, R.; Ivers-Tiffée, E. In situ detection of lithium metal plating on graphite in experimental cells. *J. Power Sources* **2015**, *279*, 428–438.
- (12) Kumagai, N.; Koishikawa, Y.; Komaba, S.; Koshiba, N. Thermodynamics and kinetics of lithium intercalation into Nb₂O₅ electrodes for a 2 V rechargeable lithium battery. *J. Electrochem. Soc.* **1999**, *146*, 3203–3210.
- (13) Kodama, R.; Terada, Y.; Nakai, I.; Komaba, S.; Kumagai, N. Electrochemical and in situ XAFS-XRD investigation of Nb₂O₅ for rechargeable lithium batteries. *J. Electrochem. Soc.* **2006**, *153*, A583–A588.
- (14) Viet, A. L.; Reddy, M. V.; Jose, R.; Chowdari, B. V. R.; Ramakrishna, S. Nanostructured Nb₂O₅ polymorphs by electrospinning for rechargeable lithium batteries. *J. Phys. Chem. C* **2009**, *114*, 664–671.
- (15) Li, S.; Xu, Q.; Uchaker, E.; Cao, X.; Cao, G. Comparison of amorphous, pseudo-hexagonal and orthorhombic Nb₂O₅ for high-rate lithium ion insertion. *Cryst Eng Comm* **2016**, *18*, 2532–2540.
- (16) Sasidharan, M.; Gunawardhana, N.; Yoshio, M.; Nakashima, K. Nb₂O₅ hollow nanospheres as anode material for enhanced performance in lithium ion batteries. *Mater. Res. Bull.* **2012**, *47*, 2161–2164.
- (17) Kim, K.; Woo, S.-G.; Jo, Y. N.; Lee, J.; Kim, J.-H. Niobium oxide nanoparticle core-amorphous carbon shell structure for fast reversible lithium storage. *Electrochim. Acta* **2017**, *240*, 316–322.
- (18) Sun, H.; Mei, L.; Liang, J.; Zhao, Z.; Lee, C.; Fei, H.; Ding, M.; Lau, J.; Li, M.; Wang, C.; Xu, X.; Hao, G.; Papandrea, B.; Shakir, I.; Dunn, B.; Huang, Y.; Duan, X. Three-dimensional holey-graphene/niobia composite architectures for ultrahigh-rate energy storage. *Science* **2017**, *356*, 599–604.
- (19) Wei, M.; Wei, K.; Ichihara, M.; Zhou, H. Nb₂O₅ nanobelts: A lithium intercalation host with large capacity and high rate capability. *Electrochem. Commun.* **2008**, *10*, 980–983.
- (20) Tolosa, A.; Fleischmann, S.; Grobelsek, I.; Quade, A.; Lim, E.; Presser, V. Binder-free hybrid titanium-niobium oxide/carbon nanofiber mats for lithium-ion battery electrodes. *Chem Sus Chem* **2018**, *11*, 159–170.
- (21) Kumagai, N.; Tanno, K.; Nakajima, T.; Watanabe, N. Structural changes of Nb₂O₅ and V₂O₅ as rechargeable cathodes for lithium battery. *Electrochim. Acta* **1983**, *28*, 17–22.
- (22) Come, J.; Augustyn, V.; Kim, J. W.; Rozier, P.; Taberna, P.-L.; Gogotsi, P.; Long, J. W.; Dunn, B.; Simon, P. Electrochemical kinetics of nanostructured Nb₂O₅ electrodes. *J. Electrochem. Soc.* **2014**, *161*, A718–A725.
- (23) Kong, L.; Liu, X.; Wei, J.; Wang, S.; Xu, B. B.; Long, D.; Chen, F. T-Nb₂O₅ nanoparticle enabled pseudocapacitance with fast Li-ion intercalation. *Nanoscale* **2018**, *10*, 14165–14170.
- (24) Shi, C.; Xiang, K.; Zhu, Y.; Zhou, W.; Chen, X.; Chen, H. Box-implanted Nb₂O₅ nanorods as superior anode materials in lithium ion batteries. *Ceram. Int.* **2017**, *43*, 12388–12395.
- (25) Li, G.; Wang, X.; Ma, X. Nb₂O₅-carbon core-shell nanocomposite as anode material for lithium ion battery. *J. Energy Chem.* **2013**, *22*, 357–362.
- (26) Lin, J.; Yuan, Y.; Su, Q.; Pan, A.; Dinesh, S.; Peng, C.; Cao, G.; Liang, S. Facile synthesis of Nb₂O₅/carbon nanocomposites as advanced anode materials for lithium-ion batteries. *Electrochim. Acta* **2018**, *292*, 63–71.
- (27) Lu, H.; Xiang, K.; Bai, N.; Zhou, W.; Wang, S.; Chen, H. Urchin-shaped Nb₂O₅ microspheres synthesized by the facile hydrothermal method and their lithium storage performance. *Mater. Lett.* **2016**, *167*, 106–108.
- (28) Wu, L.; Zheng, J.; Wang, L.; Xiong, X.; Shao, Y.; Wang, G.; Wang, J.-H.; Zhong, S.; Wu, M. PPy-encapsulated SnS₂ nanosheets stabilized by defects on a TiO₂ support as a durable anode material for lithium-ion batteries. *Angew. Chem., Int. Ed.* **2019**, *58*, 811–815.
- (29) Liu, J.; Hou, M.; Yi, J.; Guo, S.; Wang, C.; Xia, Y. Improving the electrochemical performance of layered lithium-rich transition-metal oxides by controlling the structural defects. *Energy Environ. Sci.* **2014**, *7*, 705–714.

- (30) Zeiger, M.; Ariyanto, T.; Krüner, B.; Peter, N. J.; Fleischmann, S.; Etzold, B. J. M.; Presser, V. Vanadium pentoxide/carbide-derived carbon core-shell hybrid particles for high performance electrochemical energy storage. *J. Mater. Chem. A* **2016**, *4*, 18899–18909.
- (31) Budak, Ö.; Srimuk, P.; Tolosa, A.; Fleischmann, S.; Lee, J.; Hieke, S. W.; Frank, A.; Scheu, C.; Presser, V. Vanadium (III) oxide/carbon core/shell hybrids as an anode for lithium-ion batteries. *Batteries Supercaps* **2019**, *2*, 74–82.
- (32) Schäfer, H.; Gruehn, R.; Schulte, F. The modifications of niobium pentoxide. *Angew. Chem., Int. Ed.* **1966**, *5*, 40–52.
- (33) Kato, K.; Tamura, S. Die Kristallstruktur von T-Nb₂O₅. *Acta Crystallogr., Sect. B* **1975**, *31*, 673–677.
- (34) Ariyanto, T.; Zhang, G.-R.; Riyahi, F.; Gläsel, J.; Etzold, B. J. M. Controlled synthesis of core-shell carbide-derived carbons through in situ generated chlorine. *Carbon* **2017**, *115*, 422–429.
- (35) Cheary, R. W.; Coelho, A. A.; Cline, J. P. Fundamental Parameters Line Profile Fitting in Laboratory Diffractometers. *J. Res. Natl. Bur. Stand.* **2004**, *109*, 1–25.
- (36) Brunauer, S.; Emmett, P. H.; Teller, E. Adsorption of gases in multimolecular layers. *J. Am. Chem. Soc.* **1938**, *60*, 309–319.
- (37) Thommes, M.; Kaneko, K.; Neimark, A. V.; Olivier, J. P.; Rodriguez-Reinoso, F.; Rouquerol, J.; Sing, K. S. W. Physisorption of gases, with special reference to the evaluation of surface area and pore size distribution (IUPAC Technical Report). *Pure Appl. Chem.* **2015**, *87*, 1051–1069.
- (38) Jäckel, N.; Emge, S. P.; Krüner, B.; Roling, B.; Presser, V. Quantitative information about electrosorption of ionic liquids in carbon nanopores from electrochemical dilatometry and quartz crystal microbalance measurements. *J. Phys. Chem. C* **2017**, *121*, 19120–19128.
- (39) Salanne, M.; Rotenberg, B.; Naoi, K.; Kaneko, K.; Taberna, P. L.; Grey, C. P.; Dunn, B.; Simon, P. Efficient storage mechanisms for building better supercapacitors. *Nat. Energy* **2016**, *1*, 16070.
- (40) Fleischmann, S.; Tolosa, A.; Presser, V. Design of carbon/metal oxide hybrids for electrochemical energy storage. *Chem. - Eur J.* **2018**, *24*, 12143–12153.
- (41) Widmaier, M.; Jäckel, N.; Zeiger, M.; Abuzarli, M.; Engel, C.; Bommer, L.; Presser, V. Influence of carbon distribution on the electrochemical performance and stability of lithium titanate based energy storage devices. *Electrochim. Acta* **2017**, *247*, 1006–1018.
- (42) Presser, V.; Heon, M.; Gogotsi, Y. Carbide-derived carbons - from porous networks to nanotubes and graphene. *Adv. Funct. Mater.* **2011**, *21*, 810–833.
- (43) Cambaz, Z. G.; Yushin, G. N.; Gogotsi, Y.; Vyshnyakova, K. L.; Peresentseva, L. N. Formation of carbide-derived carbon on beta-silicon carbide whiskers. *J. Am. Ceram. Soc.* **2006**, *89*, 509–514.
- (44) McQueen, T.; Xu, Q.; Andersen, E. N.; Zandbergen, H. W.; Cava, R. J. Structures of the reduced niobium oxides Nb₁₂O₂₉ and Nb₂₂O₅₄. *J. Solid State Chem.* **2007**, *180*, 2864–2870.
- (45) Mertin, W.; Andersson, S.; Gruehn, R. Über die Kristallstruktur von M-Nb₂O₅. *J. Solid State Chem.* **1970**, *1*, 419–424.
- (46) Anderson, J. S.; Browne, J. M.; Hutchison, J. L. Electron microscopy of the niobium oxides. I. Twinning and defects in H-Nb₂O₅. *J. Solid State Chem.* **1972**, *5*, 419–431.
- (47) Rohrer, F. E.; Larsson, A. K. Twinning and defects in N-Nb₂O₅. *Acta Crystallogr., Sect. B* **2000**, *56*, 780–784.
- (48) Makinson, J. D.; Lee, J. S. H.; Magner, S. H.; De Angelis, R. J.; Weins, W. N.; Hieronymus, A. S. X-ray diffraction signatures of defects in nanocrystalline materials. *Adv. X-ray Anal.* **2000**, *42*, 407–411.
- (49) Balogh, L.; Ribárik, G.; Ungár, T. Stacking faults and twin boundaries in fcc crystals determined by X-ray diffraction profile analysis. *J. Appl. Phys.* **2006**, *100*, No. 023512.
- (50) Lu, Z.; Dahn, J. R. Effects of stacking fault defects on the X-ray diffraction patterns of T₂, O₂, and O₆ structure Li_{2/3}[Co_xNi_{1/3-x}Mn_{2/3}]₂O₇. *Chem. Mater.* **2001**, *13*, 2078–2083.
- (51) Ferrari, A. C.; Basko, D. M. Raman spectroscopy as a versatile tool for studying the properties of graphene. *Nat. Nanotechnol.* **2013**, *8*, 235–246.
- (52) Tsu, R.; González, H. J.; Hernández, C. I. Observation of splitting of the E_{2g} mode and two-phonon spectrum in graphites. *Solid State Commun.* **1978**, *27*, 507–510.
- (53) Dash, R.; Chmiola, J.; Yushin, G.; Gogotsi, Y.; Laudisio, G.; Singer, J.; Fischer, J.; Kucheyev, S. Titanium carbide derived nanoporous carbon for energy-related applications. *Carbon* **2006**, *44*, 2489–2497.
- (54) He, L.; Chathoth, S. M.; Melnichenko, Y. B.; Presser, V.; McDonough, J.; Gogotsi, Y. Small-angle neutron scattering characterization of the structure of nanoporous carbons for energy-related applications. *Microporous Mesoporous Mater.* **2012**, *149*, 46–54.
- (55) Becker, P.; Glenk, F.; Kormann, M.; Popovska, N.; Etzold, B. J. M. Chlorination of titanium carbide for the processing of nanoporous carbon: A kinetic study. *Chem. Eng. J.* **2010**, *159*, 236–241.
- (56) Jehng, J. M.; Wachs, I. E. Structural chemistry and Raman spectra of niobium oxides. *Chem. Mater.* **1991**, *3*, 100–107.
- (57) Pittman, R. M.; Bell, A. T. Raman studies of the structure of niobium oxide/titanium oxide (Nb₂O₅/TiO₂). *J. Phys. Chem.* **1993**, *97*, 12178–12185.
- (58) Kulkarni, A. K.; Praveen, C. S.; Sethi, Y. A.; Panmand, R. P.; Arbu, S. S.; Naik, S. D.; Ghule, A. V.; Kale, B. B. Nanostructured N-doped orthorhombic Nb₂O₅ as an efficient stable photocatalyst for hydrogen generation under visible light. *Dalton Trans.* **2017**, *46*, 14859–14868.
- (59) Özer, N.; Barreto, T.; Büyüklımanlı, T.; Lampert, C. M. Characterization of sol-gel deposited niobium pentoxide films for electrochromic devices. *Sol. Energy Mater. Sol. Cells* **1995**, *36*, 433–443.
- (60) Mérel, P.; Tabbal, M.; Chaker, M.; Moisa, S.; Margot, J. Direct evaluation of the sp³ content in diamond-like-carbon films by XPS. *Appl. Surf. Sci.* **1998**, *136*, 105–110.
- (61) Chilkoti, A.; Ratner, B. D.; Briggs, D. Plasma-deposited polymeric films prepared from carbonyl-containing volatile precursors: XPS chemical derivatization and static SIMS surface characterization. *Chem. Mater.* **1991**, *3*, 51–61.
- (62) Widmaier, M.; Pfeifer, K.; Bommer, L.; Presser, V. Valence-tuned lithium titanate nanopowder for high-rate electrochemical energy storage. *Batteries Supercaps* **2018**, *1*, 11–26.
- (63) Yabuuchi, N.; Takeuchi, M.; Nakayama, M.; Shiiba, H.; Ogawa, M.; Nakayama, K.; Ohta, T.; Endo, D.; Ozaki, T.; Inamasu, T.; Sato, K.; Komaba, S. High-capacity electrode materials for rechargeable lithium batteries: Li₃NbO₄-based system with cation-disordered rocksalt structure. *Proc. Natl. Acad. Sci. U. S. A.* **2015**, *112*, 7650.
- (64) Anjos, D. M.; McDonough, J. K.; Perre, E.; Brown, G. M.; Overbury, S. H.; Gogotsi, Y.; Presser, V. Pseudocapacitance and performance stability of quinone-coated carbon onions. *Nano Energy* **2013**, *2*, 702–712.
- (65) Opitz, M.; Yue, J.; Wallauer, J.; Smarsly, B.; Roling, B. mechanisms of charge storage in nanoparticulate TiO₂ and Li₄Ti₅O₁₂ anodes: new insights from scan rate-dependent cyclic voltammetry. *Electrochim. Acta* **2015**, *168*, 125–132.
- (66) Brezesinski, T.; Wang, J.; Tolbert, S. H.; Dunn, B. Ordered mesoporous α-MoO₃ with iso-oriented nanocrystalline walls for thin-film pseudocapacitors. *Nat. Mater.* **2010**, *9*, 146–151.
- (67) Ardizzone, S.; Fregonara, G.; Trasatti, S. "Inner" and "outer" active surface of RuO₂ electrodes. *Electrochim. Acta* **1990**, *35*, 263–267.
- (68) Mathis, T. S.; Kurra, N.; Wang, X.; Pinto, D.; Simon, P.; Gogotsi, Y. Energy storage data reporting in perspective - guidelines for interpreting the performance of electrochemical energy storage systems. *Adv. Energy Mater.* **2019**, *9*, 1902007.
- (69) Janninck, R. F.; Whitmore, D. H. Electrical conduction in nonstoichiometric α-Nb₂O₅. *J. Chem. Phys.* **1962**, *37*, 2750–2754.

Supporting Information

Carbide-derived niobium pentoxide with an enhanced charge storage capacity for use as a lithium-ion battery electrode

Ö. Budak,^{a,b} M. Geißler,^c D. Becker,^d A. Kruth,^e A. Quade,^e
R. Haberkorn,^d G. Kickelbick,^d B. J. M. Etzold,^c and V. Presser^{a,b,*}

^a INM - Leibniz Institute for New Materials, 66123 Saarbrücken, Germany

^b Department of Materials Science and Engineering, Saarland University, 66123 Saarbrücken, Germany

^c Ernst-Berl-Institut für Technische und Makromolekulare Chemie, Technische Universität Darmstadt,
64287 Darmstadt, Germany

^d Inorganic Solid State Chemistry, Saarland University, 66123 Saarbrücken, Germany

^e Leibniz Institute for Plasma Science and Technology, 17489 Greifswald, Germany

* Corresponding author's eMail: volker.presser@leibniz-inm.de

Table S1. Rietveld analysis results of the samples.

Sample	Phase	Space group	Lattice parameter (Å)	Interaxial angle (°)	Volume (Å ³)	Content (%)
NbC/CDC	NbC	$Fm\bar{3}m$	$a = 4.5(2)$	-	89.6(3)	100
m-Nb ₂ O ₅ /CDC	Nb ₂ O _{4.91}	$P2/m$	$a = 20.3(1)$ $c = 3.8(2)$	-	1573.8(5)	50.9
	Nb ₂ O ₅	$I4/mmm$	$a = 21.2(3)$ $b = 3.8(4)$ $c = 19.3(2)$	$\beta = 119.8(2)$	1359.3(2)	49.1
o-Nb ₂ O ₅ /CDC	Nb ₂ O ₅	$Pbam$	$a = 6.2(2)$ $b = 29.3(7)$ $c = 3.93(9)$	-	710.6(3)	100
com-Nb ₂ O ₅	Nb ₂ O _{4.91}	$P2/m$	$a = 20.3(1)$ $c = 3.8(2)$	-	1573.8(1)	40.2
	Nb ₂ O ₅	$I4/mmm$	$a = 21.2(1)$ $b = 3.8(2)$ $c = 19.3(4)$	$\beta = 119.8(2)$	1359.3(9)	59.8

Table S2. Porosity data obtained from nitrogen gas sorption analysis at -196 °C.

Sample	SSA _{BET} (m ² ·g ⁻¹)	Total pore volume (cm ³ ·g ⁻¹)
NbC	≤5	0.02
NbC/CDC	9	0.01
m-Nb ₂ O ₅ /CDC	19	0.03
o-Nb ₂ O ₅ /CDC	57	0.04

Table S3. Elemental surface composition analysis of com-Nb₂O₅ by XPS.

Sample	XPS	
	Nb:O atomic ratio	Nb (at%)
com-Nb ₂ O ₅	0.39	20.6

Table S4. Electrochemical performance comparison of different crystal structures of Nb₂O₅. Not available data from literature references are denoted as “n.a.”. CDC: carbide-derived carbon. rGO: reduced graphene oxide. EMC: ethyl methyl carbonate. DEC: diethylene carbonate. PC: propylene carbonate.

Materials	Phase(s)	Capacity at low rate (mAh/g, A/g)	Capacity at high rate (mAh/g, A/g)	Potential range (V vs. Li/Li ⁺)	Capacity retention (% , cycle number)	Electrolyte	Reference
T-Nb ₂ O ₅	orthorhombic	159, 0.2	113, 2	1.0-3.0	n.a.	1 M LiPF ₆ in EC:DMC	[1]
Yolk-shell Nb ₂ O ₅	orthorhombic	171, 0.5	127, 10	1.0-3.0	n.a.	n.a.	[2]
Nanostructured Nb ₂ O ₅	pseudohexagonal	152, 0.05	n.a.		n.a.	n.a.	
	orthorhombic	189, 0.05	n.a.	1.0-2.6	n.a.	n.a.	[3]
	monoclinic	242, 0.05	n.a.		96, 100	n.a.	
Nb ₂ O ₅ /carbon nanodots	orthorhombic	385*, 0.1	134, 5	0.01-3.0	n.a.	1 M LiPF ₆ in EC:DMC:EMC	[4]
Nanoparticle Nb ₂ O ₅	amorphous	125, 0.05	50, 0.5				
	pseudohexagonal	191, 0.05	114, 0.5	1.2-3.0	n.a.	1 M LiPF ₆ in EC:DMC	[5]
	orthorhombic	150, 0.05	75, 0.5				
Nb ₂ O ₅ hollow nanospheres	hexagonal	200, 0.6	144, 2.5	1.0-3.0	90, 250	1 M LiPF ₆ in EC:DMC	[6]
Nb ₂ O ₅ urchins	monoclinic	407*, 0.05	n.a.	0.01-3.0	96, 200	1 M LiPF ₆ in EC:DMC	[7]
Box-implanted Nb ₂ O ₅ nanorods	orthorhombic	247, 0.04	76, 5	1.1-3.0	92, 200	1 M LiPF ₆ in EC:DMC	[8]
Nb ₂ O ₅ -nanobelts	orthorhombic	225, 0.1	77, 10	1.2-3.0	n.a.	1 M LiClO ₄ in EC:DMC	[9]
T-Nb ₂ O ₅ a+rGO+ CDC	orthorhombic	100, 0.1	60, 1.5	1.2-3.0	n.a.	1 M LiClO ₄ in EC:DMC	[10]
Layered Nb ₂ O ₅	orthorhombic	204, 0.05	125, 1	1.0-3.0	94, 400	1 M LiClO ₄ in EC:DMC	[11]
Nb ₂ O ₅ /NbO ₂ composite	monoclinic	150, 0.2	50, 5	1.0-3.0	62, 900	1 M LiPF ₆ in EC:DEC	[12]
Nb ₂ O ₅ -carbon	pseudohexagonal	170, 0.05	80, 1	1.2-3.0	70, 300	1 M LiClO ₄ in PC	[13]
Nb ₂ O ₅ nanorods	orthorhombic	225, 0.225	170, 3.4	1.0-3.0	93, 2500	1 M LiPF ₆ in EC:DMC	[14]
Nb ₂ O ₅ nanosheet	orthorhombic	200, 0.02	150, 0.4	1.0-3.0	80, 100	1 M LiPF ₆ in EC:DMC	[15]
o-Nb₂O₅/CDC	orthorhombic	277, 0.01	0.5, 10	1.0-3.0	66, 500	1 M LiPF ₆ in EC:DMC	This work
m-Nb₂O₅/CDC	monoclinic-tetragonal	297, 0.01	100, 10	1.0-3.0	72, 500	1 M LiPF ₆ in EC:DMC	This work

*: the charge storage capacity also includes contributions from conversion reactions because of the use of very low potentials below 1 V vs. Li/Li⁺.

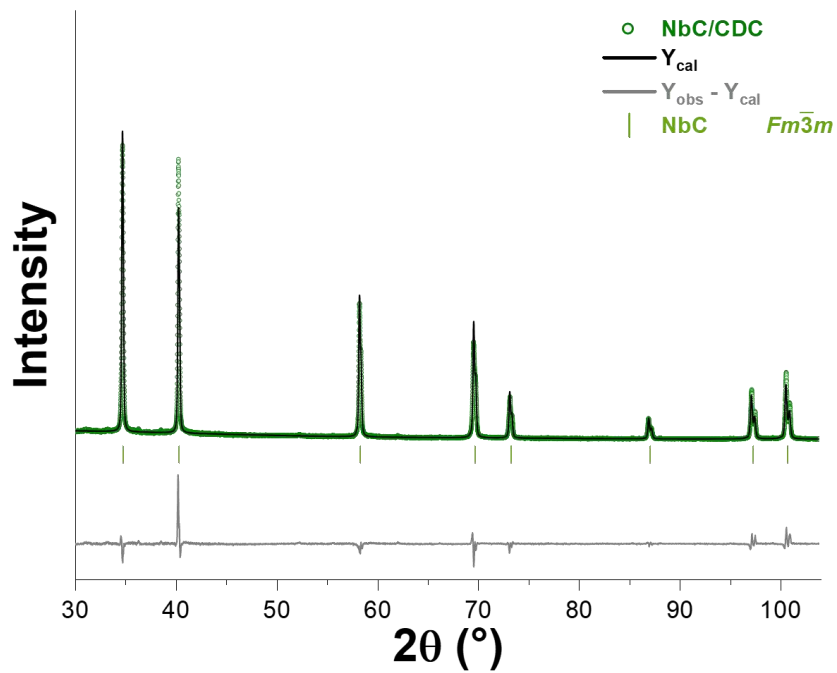


Figure S1. Rietveld refinement of the XRD pattern of NbC/CDC.

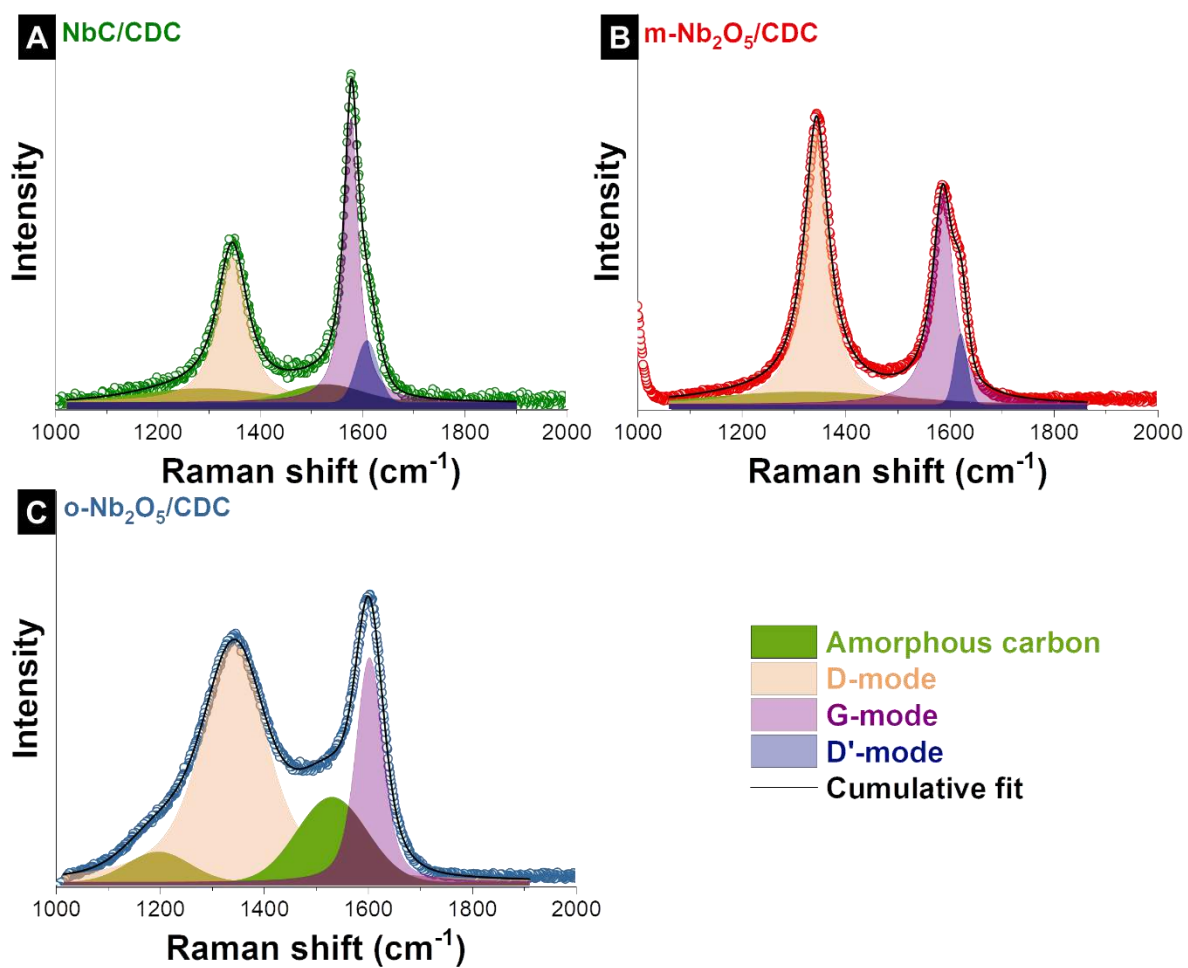


Figure S2. Raman spectra deconvolution of NbC/CDC (A), m-Nb₂O₅/CDC (B) and o-Nb₂O₅/CDC (C).

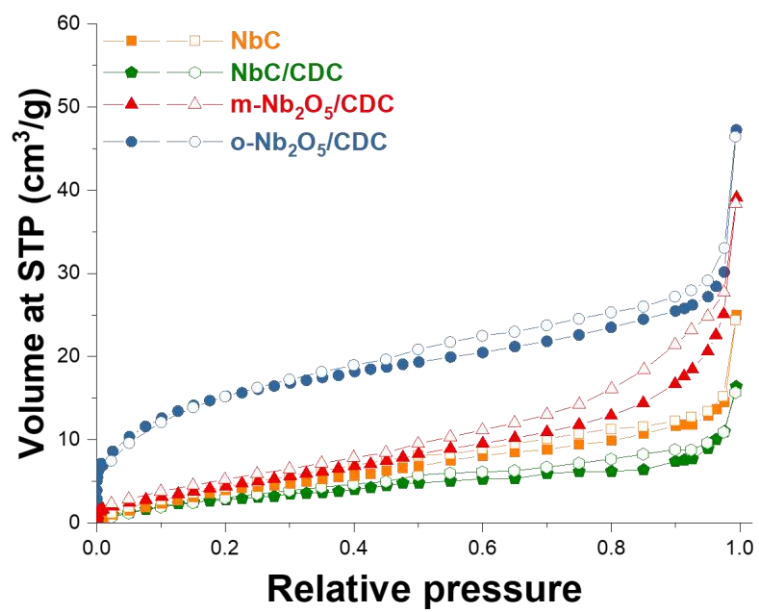


Figure S3. Nitrogen sorption isotherms recorded at -196 °C of all samples.

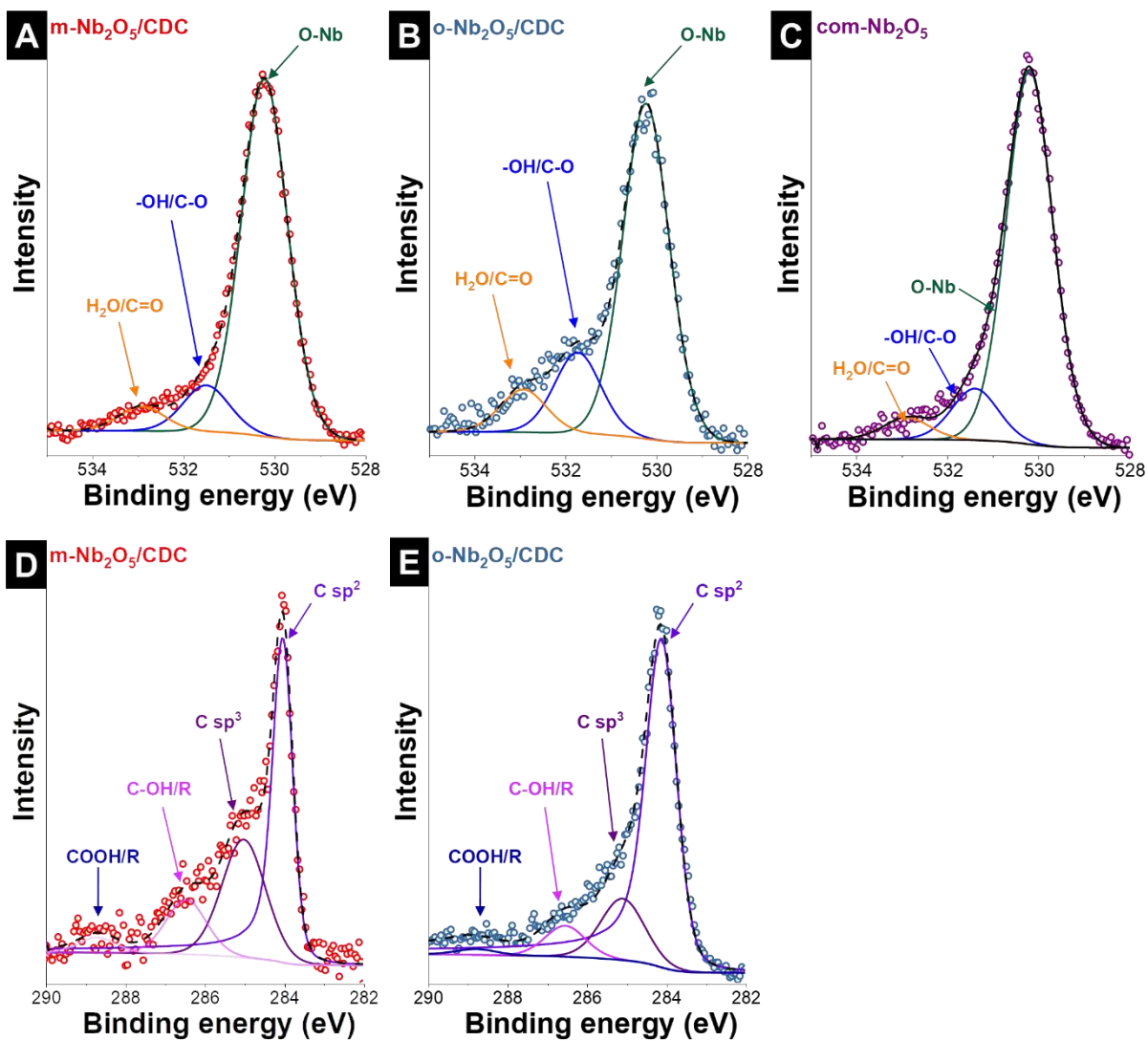


Figure S4. XPS O 1s spectra of $m\text{-Nb}_2\text{O}_5/\text{CDC}$ (A), $o\text{-Nb}_2\text{O}_5/\text{CDC}$ (B) and $com\text{-Nb}_2\text{O}_5$ (C). XPS C 1s spectrum of $m\text{-Nb}_2\text{O}_5/\text{CDC}$ (D), $o\text{-Nb}_2\text{O}_5/\text{CDC}$ (E).

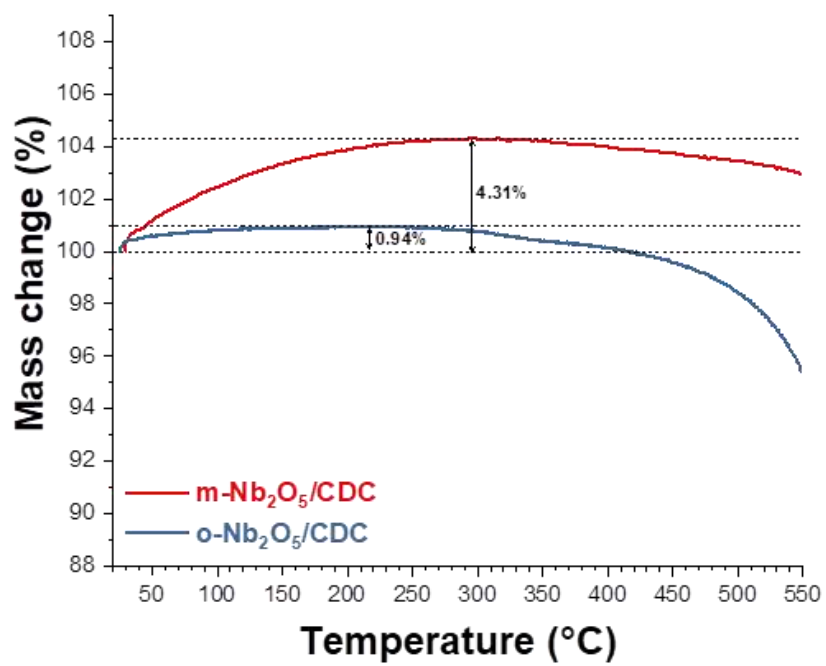


Figure S5. Thermogravimetric analysis of m-Nb₂O₅/CDC, and o-Nb₂O₅/CDC.

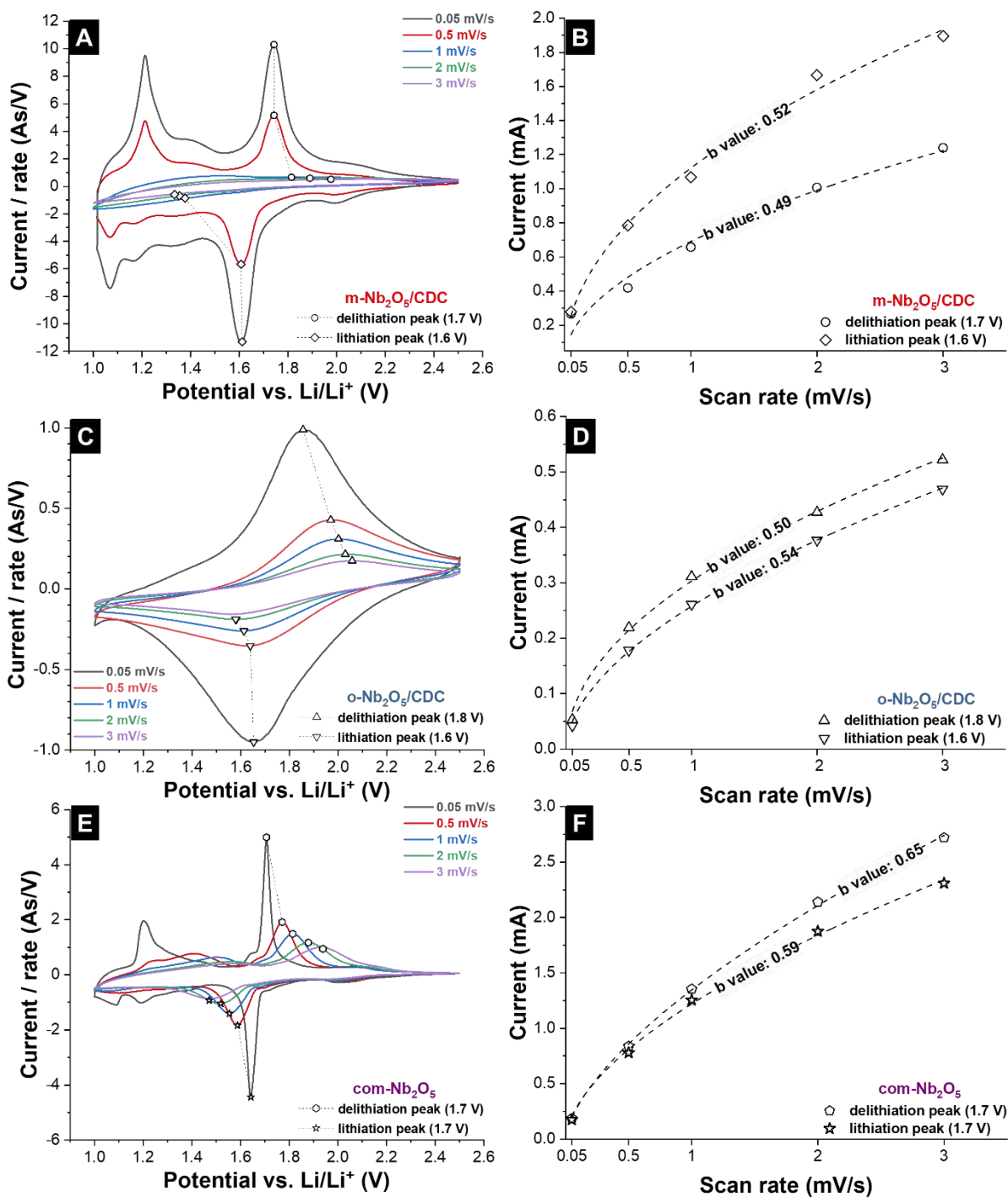


Figure S6. (A, C, E) Cyclic voltammograms of m-Nb₂O₅/CDC, o-Nb₂O₅/CDC, and com-Nb₂O₅, at different scan rates, respectively. (B, D, F) Kinetic analysis of m-Nb₂O₅/CDC, o-Nb₂O₅/CDC, and com-Nb₂O₅.

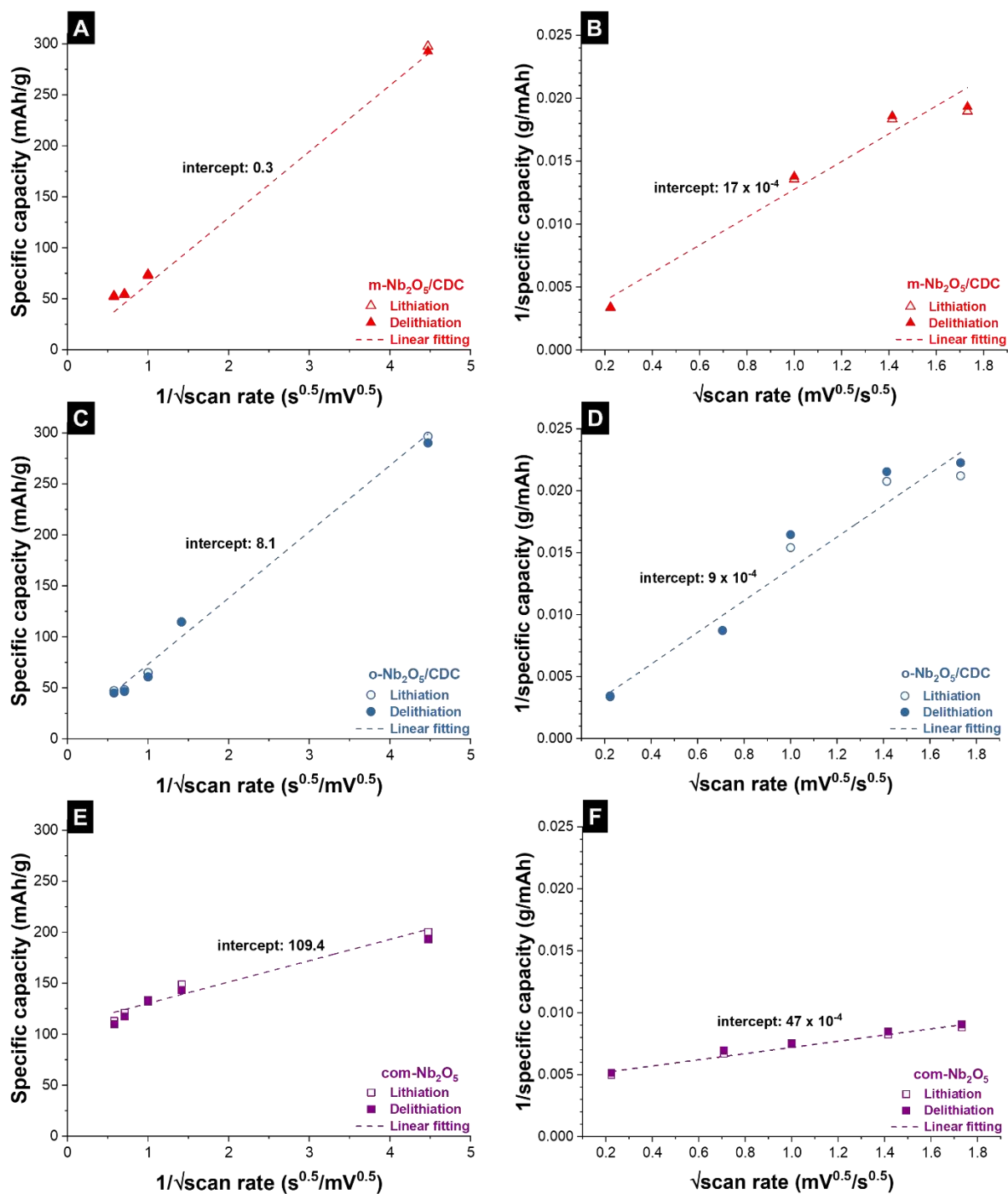


Figure S7. (A, C, E) Charge plot as a function of $1/\text{scan rate}$ ($\vartheta^{-0.5}$) of m-Nb₂O₅/CDC, o-Nb₂O₅/CDC, and com-Nb₂O₅, respectively. (B, D, F) Inverted charge plot as a function of scan rate ($\vartheta^{0.5}$) of m-Nb₂O₅/CDC, o-Nb₂O₅/CDC, and com-Nb₂O₅.

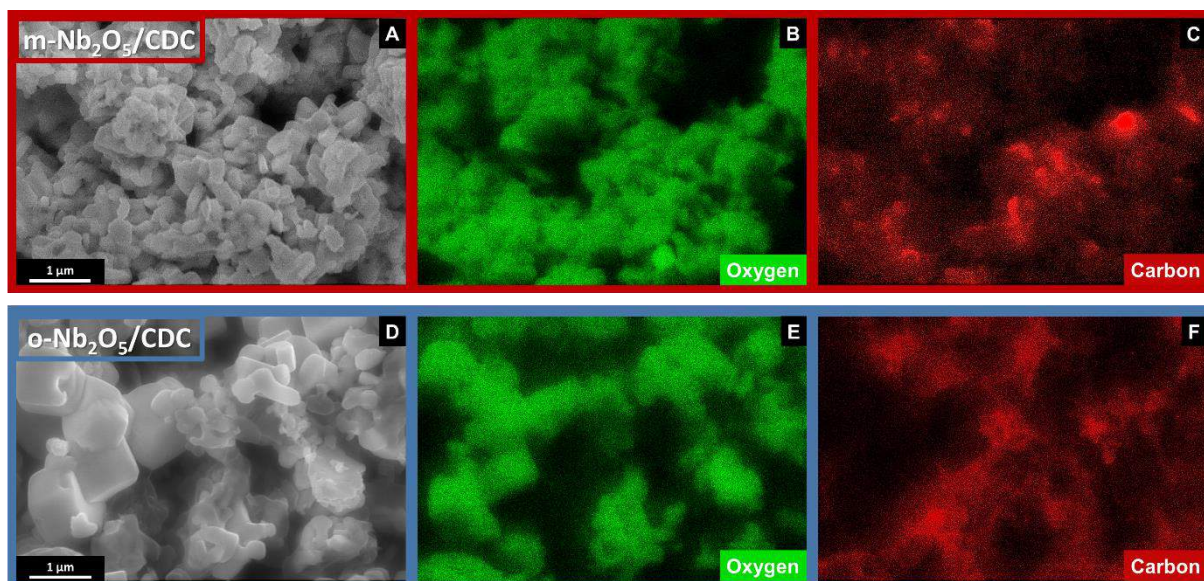


Figure S8. SEM image of (A), and the elemental composition mapping by EDX of (B,C) m-Nb₂O₅/CDC, and SEM image of (D), and the elemental composition mapping by EDX of (E,F) o-Nb₂O₅/CDC.

References

- [1] G. Liu, B. Jin, K. Bao, H. Xie, J. Guo, X. Ji, R. Zhang, Q. Jiang, Facile synthesis of porous Nb₂O₅ microspheres as anodes for lithium-ion batteries, *International Journal of Hydrogen Energy* 42(9) (2017) 6065-6071.
- [2] Y. Yoo, Y.C. Kang, Mesoporous Nb₂O₅ microspheres with filled and yolk-shell structure as anode materials for lithium-ion batteries, *Journal of Alloys and Compounds* 776 (2019) 722-730.
- [3] A.L. Viet, M.V. Reddy, R. Jose, B.V.R. Chowdari, S. Ramakrishna, Nanostructured Nb₂O₅ Polymorphs by Electrospinning for Rechargeable Lithium Batteries, *The Journal of Physical Chemistry C* 114(1) (2010) 664-671.
- [4] J. Lin, Y. Yuan, Q. Su, A. Pan, S. Dinesh, C. Peng, G. Cao, S. Liang, Facile synthesis of Nb₂O₅/carbon nanocomposites as advanced anode materials for lithium-ion batteries, *Electrochimica Acta* 292 (2018) 63-71.
- [5] S. Li, Q. Xu, E. Uchaker, X. Cao, G. Cao, Comparison of amorphous, pseudohexagonal and orthorhombic Nb₂O₅ for high-rate lithium ion insertion, *CrystEngComm* 18(14) (2016) 2532-2540.
- [6] M. Sasidharan, N. Gunawardhana, M. Yoshio, K. Nakashima, Nb₂O₅ hollow nanospheres as anode material for enhanced performance in lithium ion batteries, *Materials Research Bulletin* 47(9) (2012) 2161-2164.
- [7] H. Lu, K. Xiang, N. Bai, W. Zhou, S. Wang, H. Chen, Urchin-shaped Nb₂O₅ microspheres synthesized by the facile hydrothermal method and their lithium storage performance, *Materials Letters* 167 (2016) 106-108.
- [8] C. Shi, K. Xiang, Y. Zhu, W. Zhou, X. Chen, H. Chen, Box-implanted Nb₂O₅ nanorods as superior anode materials in lithium ion batteries, *Ceramics International* 43(15) (2017) 12388-12395.
- [9] M. Wei, K. Wei, M. Ichihara, H. Zhou, Nb₂O₅ nanobelts: A lithium intercalation host with large capacity and high rate capability, *Electrochemistry Communications* 10(7) (2008) 980-983.
- [10] C.-H. Lai, D. Ashby, M. Moz, Y. Gogotsi, L. Pilon, B. Dunn, Designing Pseudocapacitance for Nb₂O₅/Carbide-Derived Carbon Electrodes and Hybrid Devices, *Langmuir* 33(37) (2017) 9407-9415.
- [11] C. Zhang, S.J. Kim, M. Ghidui, M.-Q. Zhao, M.W. Barsoum, V. Nicolosi, Y. Gogotsi, Layered Orthorhombic Nb₂O₅@Nb₄C₃T_x and TiO₂@Ti₃C₂T_x Hierarchical Composites for High Performance Li-ion Batteries, *Advanced Functional Materials* 26(23) (2016) 4143-4151.
- [12] H. Park, D. Lee, T. Song, High capacity monoclinic Nb₂O₅ and semiconducting NbO₂ composite as high-power anode material for Li-Ion batteries, *Journal of Power Sources* 414 (2019) 377-382.
- [13] G. Li, X. Wang, X. Ma, Nb₂O₅-carbon core-shell nanocomposite as anode material for lithium ion battery, *Journal of Energy Chemistry* 22(3) (2013) 357-362.
- [14] B. Deng, T. Lei, W. Zhu, L. Xiao, J. Liu, In-Plane Assembled Orthorhombic Nb₂O₅ Nanorod Films with High-Rate Li⁺ Intercalation for High-Performance Flexible Li-Ion Capacitors, *Advanced Functional Materials* 28(1) (2018) 1704330.
- [15] J. Chen, H. Wang, X. Zhang, B. Liu, L. Xu, Z. Zhang, Y. Zhang, 2D ultrathin nanosheet-assembled Nb₂O₅ microflowers for lithium ion batteries, *Materials Letters* 227 (2018) 112-115.

5.3. Titanium niobium oxide $Ti_2Nb_{10}O_{29}$ /carbon hybrid electrodes derived by mechanochemically synthesized carbide for high-performance lithium-ion batteries

Öznil Budak^{1,2} Pattarachai Srimuk,¹ Mesut Aslan,¹ Hwirim Shim,^{1,2}
Lars Borchardt,³ Volker Presser^{1,2}

¹ *INM - Leibniz Institute for New Materials, Campus D2 2, 66123 Saarbrücken, Germany*

² *Saarland University, Campus D2 2, 66123 Saarbrücken, Germany*

³ *Inorganic Chemistry I, Ruhr-University Bochum, 44780 Bochum, Germany*

Citation:

Ö. Budak, P. Srimuk, M. Aslan, H. Shim, L. Borchardt, V. Presser, TITANIUM NIOBIUM OXIDE $Ti_2Nb_{10}O_{29}$ /CARBON HYBRID ELECTRODES DERIVED BY MECHANOCHEMICALLY SYNTHESIZED CARBIDE FOR HIGH-PERFORMANCE LITHIUM-ION BATTERIES, *ChemSusChem* 10.1002/cssc.202002229 (2020).

Own contribution:

Material synthesis, measurements, data analysis, writing, plotting, discussion

The study focuses on $Ti_2Nb_{10}O_{29}$ /carbon hybrid anode material for LIB applications. The $Ti_2Nb_{10}O_{29}$ is a desired electrochemically active material due to its high theoretical capacity of about 400 mAh/g. The desired titanium niobium phase possesses the stoichiometric ratio of Ti and Nb of 1 to 5. To be able to reach the pure $Ti_2Nb_{10}O_{29}$ phase, the first step of the synthesis involves the mechanochemical synthesis of titanium niobium carbide at room temperature by the use of elemental titanium, elemental niobium, and carbon; where two different carbon sources were chosen to explore the influence on the resulting hybrid material performance. The obtained mechanochemically synthesized carbides were converted to $Ti_2Nb_{10}O_{29}$ /carbon hybrid under CO_2 atmosphere, while non-hybrid $Ti_2Nb_{10}O_{29}$ particles were achieved via heat treatment under synthetic air. The hybrid $Ti_2Nb_{10}O_{29}$ /carbon electrodes show better rate handling and improved cyclic stability compared to their composite counterparts.

Titanium Niobium Oxide $\text{Ti}_2\text{Nb}_{10}\text{O}_{29}$ /Carbon Hybrid Electrodes Derived by Mechanochemically Synthesized Carbide for High-Performance Lithium-Ion Batteries

Öznil Budak,^[a, b] Pattarachai Srimuk,^[a] Mesut Aslan,^[a] Hwirim Shim,^[a, b] Lars Borchardt,^[c] and Volker Presser^{*[a, b]}

This work introduces the facile and scalable two-step synthesis of $\text{Ti}_2\text{Nb}_{10}\text{O}_{29}$ (TNO)/carbon hybrid material as a promising anode for lithium-ion batteries (LIBs). The first step consisted of a mechanically induced self-sustaining reaction via ball-milling at room temperature to produce titanium niobium carbide with a Ti and Nb stoichiometric ratio of 1 to 5. The second step involved the oxidation of as-synthesized titanium niobium carbide to produce TNO. Synthetic air yielded fully oxidized TNO, while annealing in CO_2 resulted in TNO/carbon hybrids. The electrochemical performance for the hybrid and non-hybrid electrodes was surveyed in a narrow potential window (1.0–2.5 V vs. Li/Li^+) and a large potential window (0.05–2.5 V vs. Li/Li^+). The best hybrid material displayed a specific capacity of

350 mAh g^{-1} at a rate of 0.01 A g^{-1} (144 mAh g^{-1} at 1 A g^{-1}) in the large potential window regime. The electrochemical performance of hybrid materials was superior compared to non-hybrid materials for operation within the large potential window. Due to the advantage of carbon in hybrid material, the rate handling was faster than that of the non-hybrid one. The hybrid materials displayed robust cycling stability and maintained ca. 70% of their initial capacities after 500 cycles. In contrast, only ca. 26% of the initial capacity was maintained after the first 40 cycles for non-hybrid materials. We also applied our hybrid material as an anode in a full-cell lithium-ion battery by coupling it with commercial LiMn_2O_4 .

Introduction

Electrochemical energy storage (EES) has become an integral part of the large-scale implementation of renewable energy sources into the power grid, mobile computing/communication, and the transition of our fleet of internal-combustion-engine cars towards electric vehicles. One important EES technology, the lithium-ion battery (LIB; featuring long cycle life, high energy density, and energy efficiency), capitalizes on the reversible charge storage intrinsic to lithiation/delithiation.^[1] Recent research focused on developing electrode materials with high charge-storage capacity, cycling stable, and low production costs. Among different phases of titanium niobium oxide,^[2] $\text{Ti}_2\text{Nb}_{10}\text{O}_{29}$ (TNO) draws considerable interest as an

anode for LIBs.^[3] This is due to the theoretical capacity of TNO (396 mAh g^{-1}) being comparable to or higher than that of commercially used lithium-insertion materials such as graphite, TiO_2 , and $\text{Li}_4\text{Ti}_5\text{O}_{12}$ (LTO).^[4] The enhanced energy-storage capacity of TNO relates to its multiple redox couples of $\text{Ti}^{4+/3+}$, $\text{Nb}^{5+/4+}$, and $\text{Nb}^{4+/3+}$.^[5]

TNO suffers from a low electronic conductivity of about $5 \cdot 10^{-9} \text{ S cm}^{-1}$ and a poor rate capability.^[5c,6] To overcome this issue, Takashima et al. demonstrated an enhanced electronic conductivity of TNO with oxygen deficiencies ($8 \cdot 10^{-6} \text{ S cm}^{-1}$) when reducing Ti^{4+} to Ti^{3+} .^[6] Alternatively to modifying the electronic band structure of TNO, one can also employ conductive carbon in TNO electrodes.^[5e,7] Combining neat metal oxides with carbon may either be accomplished by mechanical mixing (composite electrodes) or by nanoscopic blending of the two components (hybrid materials) in the electrode.^[7b] The resulting electrochemical properties strongly depend on the synthesis approach and resulting carbon distribution. For example, TNO/reduced graphene oxide composites showed a specific capacity of 100 mAh g^{-1} at 1 A g^{-1} ,^[8] whereas electrospun TNO/carbon hybrid fiber materials showed a specific capacity of 140 mAh g^{-1} at a high specific current of 5 A g^{-1} .^[7a] TNO/carbon composite electrodes prepared with 20 wt% acetylene black as a conductive additive delivered a specific capacity of 145 mAh g^{-1} at 4 A g^{-1} (30 °C),^[5b] while hybrid nanosized TNO/carbon onion electrodes delivered a specific capacity of 170 mAh g^{-1} at 5 A g^{-1} .^[5e] Recently, Luo et al. reported that TNO/holey reduced graphene oxide can provide 175 mAh g^{-1} at 7 A g^{-1} (40 °C) while neat TNO can only deliver 120 mAh g^{-1} .^[9] Carbon nanofiber/TNO displays fast charge-

[a] Ö. Budak, Dr. P. Srimuk, Dr. M. Aslan, H. Shim, V. Presser
INM – Leibniz Institute for New Materials
66123 Saarbrücken (Germany)
E-mail: volker.presser@leibniz-inm.de

[b] Ö. Budak, H. Shim, V. Presser
Department of Materials Science and Engineering
Saarland University
66123 Saarbrücken (Germany)

[c] Prof. L. Borchardt
Inorganic Chemistry I
Ruhr-University Bochum
44780 Bochum (Germany)

Supporting information for this article is available on the WWW under <https://doi.org/10.1002/cssc.202002229>

© 2020 The Authors. ChemSusChem published by Wiley-VCH GmbH. This is an open access article under the terms of the Creative Commons Attribution License, which permits use, distribution and reproduction in any medium, provided the original work is properly cited.

transfer kinetics with a specific capacity of ca. 200 mAh g⁻¹ at 8 Ag⁻¹ (60 °C),^[10] while N-doped TNO/C core-branch arrays exhibit a specific capacity of about 150 mAh g⁻¹ at a high scan rate of 15 Ag⁻¹ (100 °C).^[11] In addition to those, TNO microspheres coated with N-doped carbon shows a specific capacity of 200 mAh g⁻¹ at 8 Ag (40 °C), which is 50 mAh g⁻¹ higher compared to that of neat TNO.^[12] Clearly, TNO hybrid materials can utilize the redox activity of the material better and deliver a faster charge/discharge rate than non-hybrid materials.^[2a]

Previous works have only explored the complex wet-chemical synthesis of nanosized TNO particles and carbon hybrid electrodes for lithium-ion batteries (LIBs). Our work introduces a new two-step synthesis for producing carbide-derived, nanosized TNO and carbon hybrid materials. The process involves first a mechanically induced self-sustaining reaction (MSR) to obtain titanium niobium carbide (TNC) and a thermal annealing step to convert the material to TNO. The incomplete oxidation of carbides allows for the controlled design of metal oxide/carbon hybrids^[7c,13] and the adjustment of crystal structure defects (oxygen vacancies).^[14] To the best of our knowledge, our present work is the first to demonstrate a mixed metal oxide derived from a mixed metal carbide for battery applications. As a feature of the carbide-derived oxide synthesis, it is possible to adjust the titanium-to-niobium molar ratio of the carbide to a value of 1:5 so that the resulting mixed metal oxide phase would be Ti₂Nb₁₀O₂₉. The resulting TNO and carbon hybrid electrodes were tested as an anode material for LIBs using two different potential windows, namely, a narrow (1.0–2.5 V vs. Li/Li⁺) and a wide window (0.05–2.5 V vs. Li/Li⁺).

Experimental Section

Material synthesis

Synthesis of (Ti,Nb)C

Titanium niobium carbide (TNC) was synthesized by MSR at room temperature using niobium powder (99.9%, < 65 μm, chemPUR), titanium powder (325 mesh, abcr), and carbon. Two different types of carbon sources were used for the synthesis of TNC to evaluate their impact on the electrochemical performance. One of the carbons was commercially available carbon black type Super C45 (Timcal Graphite & Carbon), named as CB in this study. We also used carbon onions (abbreviated as OLC in this study),^[15] which were synthesized by annealing high-purity detonation nanodiamond powder (NaBond) at 1300 °C under vacuum.^[16] The titanium powder, niobium powder, and carbon were first mixed with a Ti/Nb/C molar ratio of ca. 1:5:5^[17] by using a Turbula shaker mixer for 15 min to acquire a homogenous powder mixture. Ten hard metal balls (96 wt% WC, 4 wt% Co) with a diameter of 10 mm and a mass of 7.6 g per ball were mixed with the obtained solid mixture into a 125 mL hard metal vial. Then, the vial was filled with Ar gas (H₂O, O₂ < 1 ppm) for 30 min. We kept the ball-to-powder mass ratio at 15. The vial was placed in one of the holders of the ball-milling machine (Retsch PM400), and the same mass of the vial was also put on the opposite side of the vial holders to balance the system. The ball milling was carried out at a spinning rate of 300 rpm for 6 h by pausing every 15 min to avoid an escalating heat build-up. The synthesized TNC samples were named based on the carbon

sources. For instance, TNC-OLC was synthesized by using carbon onions, whereas TNC-CB was produced using carbon black.

Synthesis of Ti₂Nb₁₀O₂₉

TNC-CB and TNC-OLC were used as precursors to synthesize Ti₂Nb₁₀O₂₉ (TNO) by using the gas-solid reaction. A quartz crucible with TNC powder was placed in the isothermal zone of the tube furnace (VG Scienta GP-CVD), then the furnace was flushed with Ar gas at a flow rate of 100 cm³ min⁻¹ for 2 h to ensure that an inert gas atmosphere was generated in the furnace before starting the thermal treatment. After that, the furnace was heated to 900 °C at a heating rate of 5 °C min⁻¹ with an Ar flow rate of 50 cm³ min⁻¹. The Ar atmosphere was chosen to avoid carbon burning during the heating. To obtain TNO-CB-CO₂ and TNO-OLC-CO₂, CO₂ gas was also fed to the furnace with a flow rate of 50 cm³ min⁻¹ right after reaching 900 °C; the furnace was then kept at 900 °C for 1 h.

We also studied TNO produced by thermal annealing in synthetic air instead of CO₂. To produce TNO-CB-Air, and TNO-OLC-Air, only synthetic air was flushed at a flow rate of 50 cm³ min⁻¹ during the holding temperature of 900 °C for 1 h. Afterwards, the sample was cooled to room temperature naturally using only Ar gas at a flow rate of 50 cm³ min⁻¹.

Material characterization

Scanning electron microscopy (SEM) images were obtained with a JEOL JSM 7500F field emission scanning electron microscope at an acceleration voltage of 3 kV. The samples were fixed on a stainless-steel sample holder by using sticky carbon tape. The chemical compositions of the samples were quantified by energy-dispersive X-ray (EDX) spectroscopy with an X-MAX-150 detector (Oxford Instruments) attached to the SEM chamber. The samples were placed on a copper tape in the case of EDX analysis. The spectra of thirty spots were measured with an acceleration voltage of 15 kV and averaged.

The carbon content was quantified by chemical analysis using a MICRO Cube (Elementar Analysensysteme GmbH). The latter system was heated to reach a temperature of +1150 °C at the combustion tube and +850 °C at the reduction tube.

X-ray powder diffraction (XRD) measurements were conducted with a D8 Discover diffractometer (Bruker AXS) with Cu_{Kα} radiation (wavelength: 0.15406 nm; voltage: 40 kV; current: 40 mA), a Goebel mirror in point focus (1 mm), and a VANTEC-500 2D detector. The patterns were recorded at the positioned 2D detector from 17° to 97° 2θ with the increment of 20° 2θ; the total XRD measurement time was 60 min. The Rietveld refinement for TNC-CB and TNC-OLC, and Le Bail fitting analysis of TNO-CB-CO₂, TNO-OLC-CO₂, TNO-CB-Air, and TNO-OLC-Air were carried out by using the Bruker AXS software TOPAS 6.

Raman spectra were recorded with a Renishaw inVia system equipped with an Nd-YAG laser of 532 nm, an excitation power of 0.5 mW at the surface of the samples, and an objective lens with a numeric aperture of 0.75. Spectra of 10 points were recorded for each sample, with 30 s acquisition time for three accumulations in the range of 100–3200 cm⁻¹. Peak analysis was made by starting with baseline corrections and assuming Voigt peak profiles for the D mode, D* mode, G mode, and D** mode.^[18]

Electrochemical characterization

Electrodes were prepared from a slurry of samples (TNO-CB-CO₂, TNO-OLC-CO₂, TNO-CB-Air, and TNO-OLC-Air), polyvinylidene fluoride (PVDF, Alfa Aesar) as a binder, and carbon black (Super C65, Imerys Graphite & Carbon) as a conductive additive with a composition of 80:10:10 wt%, respectively. After mixing the required amount of sample and carbon black in a mortar with isopropanol for 10 min, the mortar was placed in an oven at 60 °C for 1 h to evaporate the isopropanol from the mixture. The obtained mixture was added to the prefabricated solution of PVDF and *N*-methyl-2-pyrrolidone (NMP, Sigma-Aldrich). The viscosity of the slurry was adjusted by an excess amount of NMP, and the resulting slurry was stirred overnight. The obtained slurry was coated on Cu foil at a wet thickness of 200 μm by using a doctor blade. The coated electrodes were dried in an oven at 110 °C under vacuum conditions overnight. The dry electrode sheets were cold pressed by using a rolling machine (HR01, MTI). The resulting electrode sheets were cut into a circle shape with a diameter of 10 mm. The average mass loadings of TNO-CB-CO₂ and TNO-OLC-CO₂ were 1.5 and 1.7 mg cm⁻², respectively; for TNO-CB-Air and TNO-OLC-Air the mass loadings were 1.8 and 1.9 mg cm⁻², respectively.

Coin cells (2032-type) were assembled in an Ar-filled glove box (O₂, H₂O < 1 ppm) using a lithium chip (diameter: 12 mm) as a counter and reference electrode, 1 M lithium hexafluorophosphate (LiPF₆) in an ethylene carbonate (EC) and dimethyl carbonate (DMC) mixture in the volumetric ratio of 1:1-EC/DMC (Sigma-Aldrich) as an electrolyte, and two pieces of Celgard 2325 (diameter: 18 mm) as separator. This setup is referred to as half-cell.

All half-cell electrochemical measurements were performed for the hybrid and non-hybrid materials using two different potential window ranges, namely, 1.0–2.5 and 0.05–2.5 V vs. Li/Li⁺ at a scan rate of 0.05 mVs⁻¹. Galvanostatic charge/discharge with potential limitation (GCPL) measurements were performed in an Arbin Battery Cycler by using the specific current range from 0.01 to 10 Ag⁻¹ to examine the rate capability; 0.1 Ag⁻¹ was used to observe cycling stability. Cyclic voltammetry (CV) results were carried out with a VMP300 system from Bio-Logic multichannel potentiostat at scan rates of 0.05–2 mVs⁻¹. The specific capacities were calculated based on the active material mass of the electrodes (excluding the mass of polymer binder) for the potential window of 0.05–2.5 V vs. Li/Li⁺, while the specific capacity of the electrochemical results in the potential window of 1.0–2.5 V vs. Li/Li⁺ was obtained by excluding the mass of carbon and polymer binder amount from TNO-CB-CO₂ and TNO-OLC-CO₂ electrodes. This capacity calculation method was preferred to obtain more reliable values due to the possible capacity contributions of carbon at low voltages.

Electrochemical impedance spectroscopy (EIS) measurements were carried out by using a VMP300 Bio-Logic multichannel potentiostat at an applied AC voltage amplitude of 10 mV in the frequency range of 200 kHz to 10 mHz after 1 h resting of the half-cells.

To better understand the structural changes of the materials at different lithiation/delithiation states, half-cells were assembled for each of the materials. The cells were charged/discharged at the specific current of 0.1 Ag⁻¹ for 10 cycles in the potential range of 0.05–2.5 V vs. Li/Li⁺. Afterwards, the cells were held at 1.35 and 0.05 V vs. Li/Li⁺ for lithiation and at 1.35 and 2.5 V vs. Li/Li⁺ for delithiation until reaching an equilibrium current. Then the tested cells were disassembled in an Ar-filled glove box (O₂, H₂O < 1 ppm), and the electrodes were gently cleaned using DMC. Lastly, post-mortem XRD measurements were performed on the cycled electrodes.

LiMn₂O₄ (LMO, < 0.5 μm, > 99%, Sigma-Aldrich) was chosen as a cathode for the full-cell testing. The electrode was prepared by using LMO, carbon black (Super C65, Imerys Graphite & Carbon), and PVDF at a ratio of 80:10:10 (w/w), respectively. The LMO slurry preparation was carried out as aforementioned for the electrode preparation of hybrid and non-hybrid materials, apart that the slurry was coated on Al foil at a wet thickness of 400 μm. The average mass loading of the obtained LMO electrode was 11.3 mg cm⁻² with a diameter of 12 mm. Before conducting full-cell experiments, an as-prepared LMO electrode was tested for rate capability in half-cell configuration using a potential window of 3.0–4.5 V vs. Li/Li⁺ following the procedures mentioned before.

For further evaluating the performance of the hybrid material (TNO-OLC-CO₂), we assembled full-cells by using custom-built poly-ether ether ketone cells described in elsewhere.^[19] The TNO-OLC-CO₂ electrode was employed as a negative electrode (anode), LMO electrode as a positive electrode (cathode), and metallic lithium chip as a reference electrode. We used two pieces of Whatman GF/F glass fiber (diameter: 13 mm) as a separator and 1 M LiPF₆ in EC/DMC (1:1 v/v, Sigma-Aldrich) as the electrolyte. The built full-cell was cycled at C-rates of 0.1C, 0.2C, 0.5C, 1C, 2C, and 5C in the potential range of 0.5–4.5 V vs. Li/Li⁺ to obtain the Ragone plot. The specific energies of the full cell were calculated by integrating the voltage profile over the discharge time as in Equation (1):

$$E_{sp} = \frac{I \int_{t_0}^t U(t) dt}{m} \quad (1)$$

where I is applied current, U is the time-dependent cell voltage, t is the time, and m is the mass of both electrodes (TNO-OLC-CO₂, and LMO), separator, and current collectors (total dead-mass: 20.1 mg), excluding the mass of the polymer binder.

The specific power of the full cell was calculated by dividing the specific energy by discharging time. The entire mass of the negative and positive electrodes was used for the calculation of the specific capacities, specific energies, and specific powers. The obtained full-cell results were labeled as "TNO-OLC-CO₂/LMO".

Results and Discussion

Materials characterization

The formation of TNC occurs in the Ti-Nb-C system at 1600 °C (Figure 1A).^[17,20] To convert TNC to Ti₂Nb₁₀O₂₉, we chose a Ti/Nb molar ratio of 1:5. Accordingly, the atomic carbon percentage was 45% and those of Ti and Nb were 9.2% and 45.8%, respectively. The phase diagram shows an isothermal cut at 1600 °C and is not directly translatable to mechanochemical synthesis conditions. Our synthesis employs MSR, which offers a solvent-free direct reaction route at ambient temperature and product uniformity.^[21] After the MSR of Ti, Nb, and C, we confirmed the formation of carbides by using X-ray diffraction (Figure 1B). The diffraction pattern of TNC-CB and TNC-OLC were analyzed by using Rietveld refinement, assuming that the occupancy of Nb atoms in the carbide structure is five times higher than that of Ti atoms (Supporting Information, Table S1). We identified cubic ($Fm\bar{3}m$) titanium niobium carbide as a main phase and hexagonal ($P\bar{6}m2$) WC as an impurity phase (less than 2 wt% as determined by Rietveld analysis) related to the

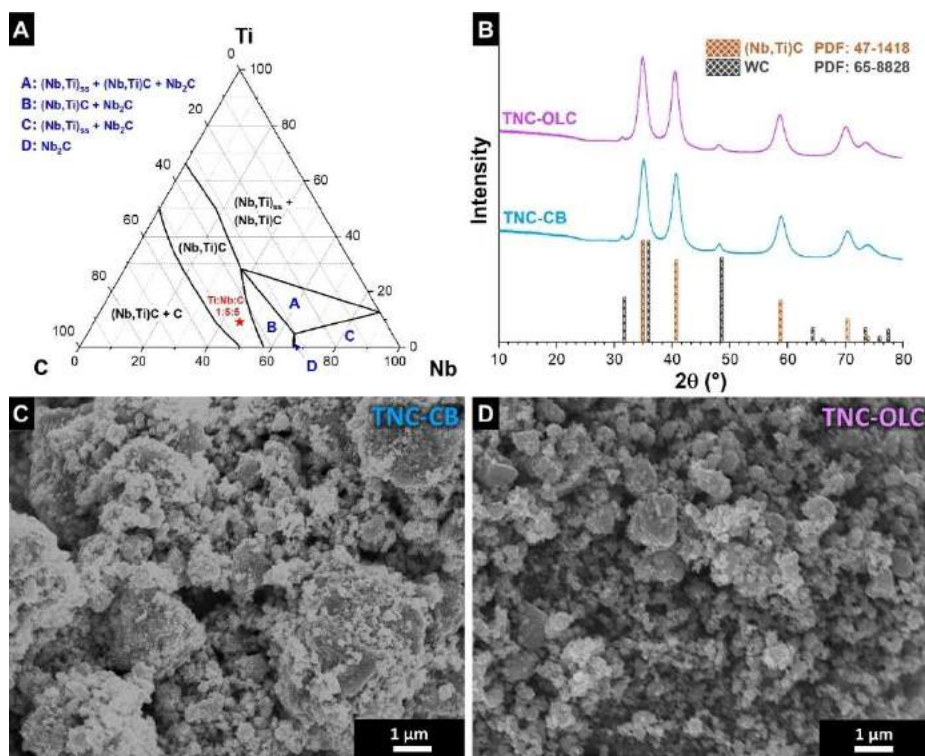


Figure 1. (A) Ternary phase diagram of Ti-Nb-C at 1600 °C (adapted from Ref. [17]). The red star marks the chemical composition used for the carbide synthesis in this work. “ss” stands for a solid solution. (B) XRD pattern of the titanium niobium carbide samples and the matched Bragg positions. SEM images of (C) TNC-CB and (D) TNC-OLC obtained after ball-milling.

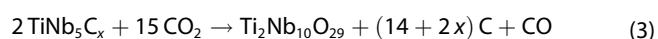
use of WC balls. The value of the a -lattice parameter of 4.43 Å also confirms the presence of Ti within the (Ti,Nb)C lattice; for comparison, pure NbC would yield an a -constant of 4.45 Å and pure TiC of 4.32 Å.^[17] The associated Ti/Nb ratio would be, based on the work of Ono and Moriyama, about 1:5.^[17] In comparison to TNC-CB, TNC-OLC has a similar lattice parameter and cell volume; however, the domain size of TNC-CB (20 nm) is slightly larger than that of TNC-OLC (15 nm). The SEM images of TNC-CB and TNC-OLC display irregular particles and agglomerates (Figure 1C and D). SEM images of CB and OLC are provided in the Supporting Information (Figure S1A and B).

For both TNC-CB and TNC-OLC, a Ti/Nb ratio of 1:5 was chosen to obtain pure $Ti_2Nb_{10}O_{29}$ as the final product. The synthesis of TNO samples was carried out using two different atmospheric conditions: synthetic air and CO_2 . Synthetic air was used to produce the non-hybrid materials (TNO-CB-Air, TNO-OLC-Air). This was accomplished by the complete volatilization of residual carbon from the carbide precursors and the full conversion of the carbide to oxide. The CO_2 atmosphere allowed, via the Boudouard reaction, the preservation of some carbon from the carbide precursor, which has a dramatic influence on the electrochemical performance of the hybrid materials (TNO-CB- CO_2 , and TNO-OLC- CO_2). To enable a better understanding of TNO formation by the CO_2 oxidation method, thermogravimetric analysis coupled with mass spectroscopy (TGA-MS) was conducted under the same synthesis conditions of the hybrid materials (Supporting Information, Figure S2).

During heating under only Ar, CO was detected at around 800 °C for both hybrid material syntheses. Until reaching the synthesis holding temperature of 900 °C, the mass loss was higher for the TNO-CB- CO_2 synthesis (3.6%) than that of TNO-OLC- CO_2 synthesis (1.2%). While the heating process was performed under inert gas, the CO outgassing and the mass loss can only be explained by oxidation of free carbon caused by the possible surface functional groups of the free carbon. After the start of the holding temperature 900 °C under the gas mixture of Ar and CO_2 , the mass change showed an observable increase of CO outgassing, which is in good agreement with the Boudouard reaction [Eq. (2)].



As a parallel reaction to the Boudouard reaction, the transformation of carbide to TNO might be described by Equation (3):



As a result, the synthesis in a CO_2 -containing atmosphere yielded a hybrid material (TNO-CB- CO_2 , TNO-OLC- CO_2). The obtained hybrid and non-hybrid materials display a Ti/Nb ratio of 1:5, with the hybrid materials TNO-CB- CO_2 and TNO-OLC- CO_2 having a carbon content of 1.2 wt% and 6.4 wt%, respectively (Table 1). The carbon-content difference in the hybrid materials

Table 1. Elemental composition analysis by energy-dispersive X-ray spectroscopy attached to a scanning electron microscope (SEM-EDX) and carbon content measured by elemental analysis.

Sample	SEM-EDX Ti [at%]	Nb [at%]	O [at%]	Elemental C [wt%]
TNO-CB-CO ₂	3.8 ± 0.6	19.6 ± 1.5	67.4 ± 3.5	1.2 ± 0.1
TNO-OLC-CO ₂	3.6 ± 1.2	18.9 ± 5.3	60.8 ± 6.2	6.4 ± 0.1
TNO-CB-Air	4.0 ± 1.0	21.7 ± 5.0	73.1 ± 6.8	0.1 ± 0.1
TNO-OLC-Air	3.7 ± 0.6	19.2 ± 2.9	76.6 ± 3.5	0.1 ± 0.1

can be explained by the difference in morphology difference between the TNC-CB and TNC-OLC precursors. The smaller grain size and less degree of agglomeration of TNC-OLC compared to TNC-CB might lead to different reaction kinetics for Equations (2) and (3), resulting in a higher amount of carbon for TNO-OLC-CO₂. Hence, the electrochemical performance of TNO-OLC-CO₂ could be better than that of TNO-CB-CO₂, as will be discussed later.

The resulting nanomaterial after CO₂ oxidation of titanium niobium carbide at 900 °C, TNO-OLC-CO₂, exhibits an agglomerated morphology (Figure 2B). Also, non-hybrid samples TNO-CB-Air and TNO-OLC-Air, and hybrid TNO-CB-CO₂ sample show particles with an irregular agglomerated morphology (Figure 2A, and Supporting Information, Figure S3). The crystal structure characterization of TNO samples was further performed by Le Bail fitting of X-ray diffractograms (Supporting Information, Table S2). The Le Bail fitting method was chosen since the obtained patterns exhibit only monoclinic (A12/m1) dititanium decaniobium oxide (Ti₂Nb₁₀O₂₉, PDF 40-0039; Wadsley-Roth shear structure)^[22] with characteristic Bragg reflections

at 23.8°, 25.0°, and 32.1 2θ (Figure 2C). The TNO-CB-CO₂ and TNO-CB-Air samples show an average domain size of about 55 nm, whereas the domain size of TNO-OLC-CO₂ and TNO-OLC-Air samples were slightly larger (63 and 88 nm, respectively; Supporting Information, Table S2). This can be explained by possible different surface reactivity resulting from different domain sizes of the TNC-CB and TNC-OLC precursors.

The Raman spectra of TNO-CB-CO₂, TNO-OLC-CO₂, TNO-CB-Air, and TNO-OLC-Air are in alignment with the X-ray diffraction results and confirm the presence of Ti₂Nb₁₀O₂₉ (Figure 2D). The Raman bands located at 543, 648, 894, and 1000 cm⁻¹ correspond to corner- and edge-shared TiO₆ octahedra and corner- and edge-shared NbO₆ octahedra, respectively.^[23] Apart from TNO-CB-Air and TNO-OLC-Air, all hybrid materials show the characteristic peaks of incomplete graphitic sp²-hybridized carbon, namely, the D mode and the G mode at around 1358 and 1600 cm⁻¹, respectively.^[24] As seen in Table 2, the full-width at half-maximum (FWHM) of the carbon-related G mode and the I_D/I_G ratio of TNO-CB-CO₂ and TNO-OLC-CO₂ are similar, namely, 73 and 70 cm⁻¹ and 2.6 and 2.7, respectively. However,

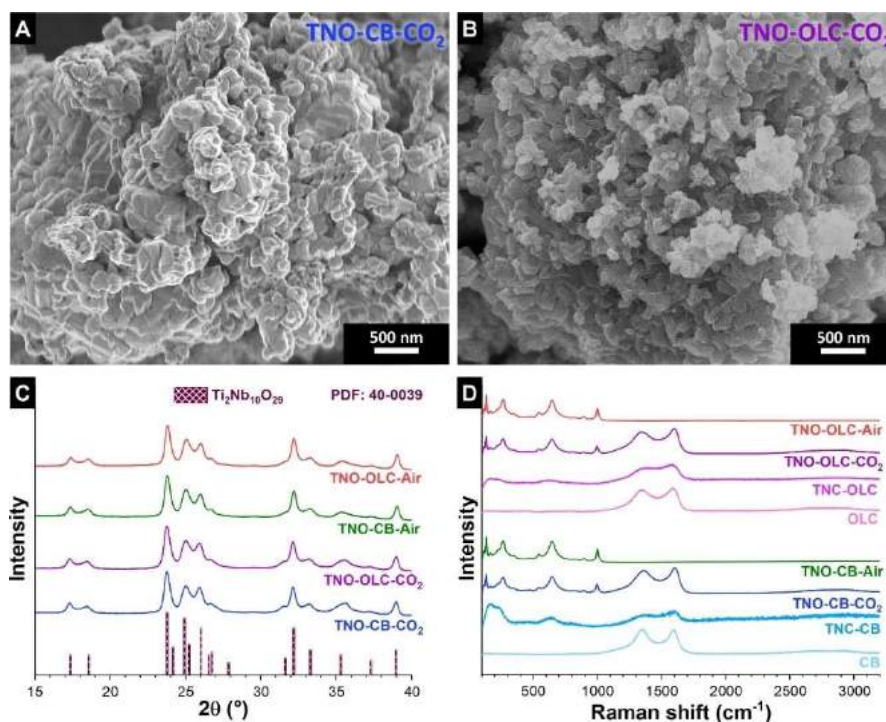


Figure 2. Material characterization of the TNO-carbon hybrid materials, carbon onions (OLC) and carbon black (CB). SEM images of (A) TNO-CB-CO₂ and (B) TNO-OLC-CO₂. (C) X-ray diffraction patterns of the TNO samples and the matched phase Bragg reflections. (D) Raman spectra of all samples.

Sample	Mode	Position [cm ⁻¹]	FWHM [cm ⁻¹]	I _D /I _G
CB	D mode	1351 ± 2	128 ± 6	2.5 ± 0.3
	G mode	1598 ± 1	76 ± 2	
TNC-CB	D mode	1365 ± 4	210 ± 9	2.4 ± 0.5
	G mode	1604 ± 3	101 ± 6	
TNO-CB-CO ₂	D mode	1363 ± 3	154 ± 8	2.6 ± 0.5
	G mode	1607 ± 2	73 ± 3	
OLC	D mode	1347 ± 2	160 ± 4	3.3 ± 0.4
	G mode	1604 ± 2	84 ± 2	
TNC-OLC	D mode	1374 ± 7	199 ± 9	1.3 ± 0.2
	G mode	1583 ± 9	130 ± 9	
TNO-OLC-CO ₂	D mode	1347 ± 6	167 ± 4	2.7 ± 0.5
	G mode	1604 ± 1	70 ± 4	

the FWHM of the D mode of TNO-CB-CO₂ (154 cm⁻¹) and TNO-OLC-CO₂ (167 cm⁻¹) are slightly different. Due to the fact that the D mode corresponds to the breathing mode of sp²-hybridized carbon rings and is active in the presence of defects, TNO-CB-CO₂ may exhibit a slightly higher degree of graphitic ordering compared to TNO-OLC-CO₂. We suspect that the higher degree of graphitic carbon could lead to better rate capability of the materials, but the distribution of the carbon phase is also of vital importance for the electrochemical performance. Hence, we will discuss the influence of different carbon precursors based on electrochemical performance later.

Electrochemical analysis

The electrochemical performance of the as-synthesized materials was tested by using two different operational potential windows: the typical potential range of 1.0–2.5 V vs. Li/Li⁺, which most previous works have explored, and additionally within a widened range of 0.05–2.5 V vs. Li/Li⁺. The latter was included to further study TNO as an anode material and to specifically address performance stability.

First, the non-hybrid (TNO-CB-Air and TNO-OLC-Air) and hybrid materials (TNO-CB-CO₂, and TNO-OLC-CO₂) were anodically scanned from open-circuit potential to 1.0 V vs. Li/Li⁺ using CV. Figure 3 shows that there are multiple redox couples during lithium intercalation into the TNO structure. The peak at 1.8–1.9 V vs. Li/Li⁺ indicates the redox couple of Ti⁴⁺/Ti³⁺,

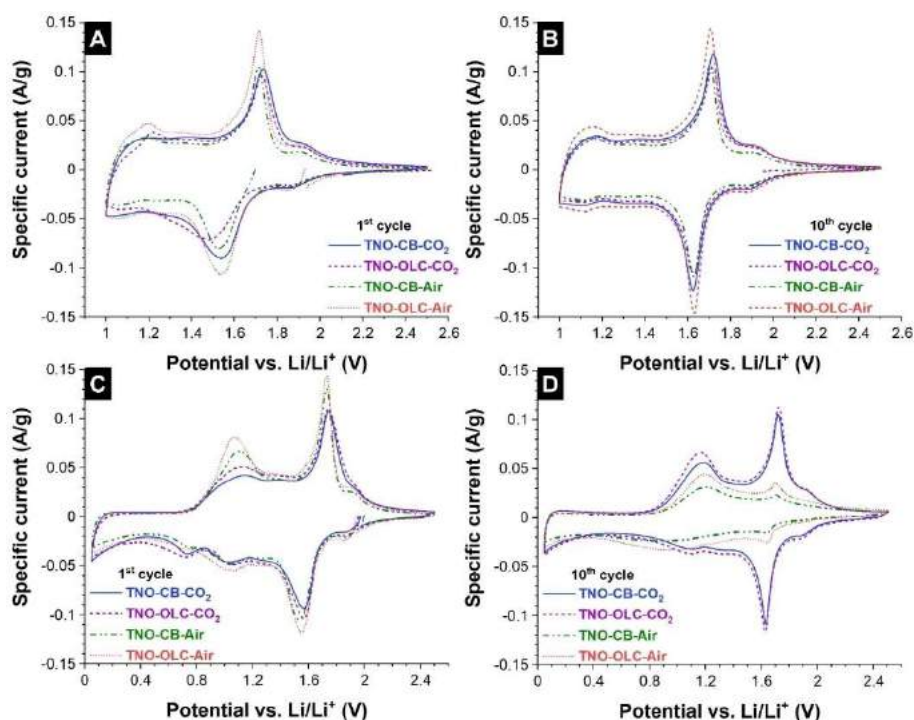


Figure 3. CVs at a scan rate of 0.05 mVs⁻¹ of the first cycle (A,C) and the 10th cycle (B,D) of the samples for the potential window of 1.0–2.5 V vs. Li/Li⁺ (A,B) and 0.05–2.5 V vs. Li/Li⁺ (C,D).

whereas the sharp peak at 1.4–1.6 V vs. Li/Li⁺ represents the Nb⁵⁺/Nb⁴⁺ transition. We also observed a broad peak at around 1.0–1.1 V vs. Li/Li⁺, suggesting another redox couple of Nb (Nb⁴⁺/Nb³⁺).^[25] When the electrode was cathodically scanned from 1.0 to 2.5 V vs. Li/Li⁺, we see three redox peaks that indicate the delithiation process. The 10th CV cycle is shown in Figure 3B. For all four electrodes, the CV areas are almost identical for TNO-CB-CO₂, TNO-OLC-CO₂, TNO-CB-Air, and TNO-OLC-Air. This observation indicates that there is no significant change in the specific capacity. In good agreement with the galvanostatic charge/discharge results (Supporting Information, Figure S4A), TNO-CB-CO₂, TNO-CB-Air, and TNO-OLC-Air exhibit a specific capacity of ca. 275 mAh g⁻¹ at a specific current of 0.01 Ag⁻¹. Compared to the other materials, TNO-OLC-CO₂ delivers a slightly lower capacity (250 mAh g⁻¹). Considering a theoretical capacity of Ti₂Nb₁₀O₂₉ is 396 mAh g⁻¹ (22 Li⁺ per unit formula), our materials deliver only 70% of the theoretical value within the potential of 1.0–2.5 V vs. Li/Li⁺. Possibly, the operational potential of 1.0–2.5 V vs. Li/Li⁺ does not allow the full insertion/de-insertion of lithium. Thus, we also explored an extended potential regime to further quantify the maximum lithium storage capacity and life cycle of the TNO.

To understand the improved rate capability, a kinetics analysis (*b*-value) was applied by using the peak current obtained from CVs at different scan rates (Supporting Information, Figure S5). The data was fitted using Equation (4):

$$i = a\dot{v}^b \quad (4)$$

where *a* and *b* are fitting variables. For a *b*-value of 0.5, a process would be limited by diffusion, whereas a *b*-value of 1 is typical for a surface-controlled mechanism.^[26] At the potential range of 1.0–2.5 V vs. Li/Li⁺, the analyzed data indicate that the lithiation/delithiation process is diffusion controlled (Supporting Information, Figure S5).

The cycling stability was also tested at 0.1 Ag⁻¹, and the results are shown in the Supporting Information, Figure S4B. The non-hybrid materials, TNO-CB-Air and TNO-OLC-Air, have an initial capacity of 203 and 238 mAh g⁻¹, while the initial capacity values are 217 and 225 mAh g⁻¹ for TNO-CB-CO₂ and TNO-OLC-CO₂ hybrid materials, respectively. Compared to hybrids, the performance decays faster for the non-hybrid materials during the first 50–100 charge/discharge cycles, remaining at a rather constant performance level thereafter. For example, the capacity loss after 150 cycles of hybrid TNO-CB-CO₂ is only 7.2% whereas the loss in initial capacity for the non-hybrid TNO-CB-Air is more than two times as high (16.0%). Specifically, TNO-CB-Air and TNO-OLC-Air have a 29.2% and 29.4% capacity decrease after 500 cycles, while TNO-CB-CO₂ and TNO-OLC-CO₂ only lose 20.6% and 24.9%, respectively, of their initial capacities after 500 cycles. The better cycling performance of the hybrid material may result from the better charge percolation/conductivity via carbon in the hybrid materials; carbon might also protect the active material from deterioration of the electrochemical properties.^[5d,27] The rate capability results within the narrow operating potential range did not indicate universally superior charge percolation of the

hybrid materials; therefore, the lower cycling stability of non-hybrid TNO may be caused by the dynamic volume change during the charge/discharge process.^[5a]

CVs of carbon-hybrid TNO materials (TNO-CB-CO₂, TNO-OLC-CO₂) performed within the wider potential window of 0.05–2.5 V vs. Li/Li⁺ (Figure 3C and D) show a different behavior compared to the non-hybrid materials (TNO-CB-Air, TNO-OLC-Air). In the first cycle, three reduction peaks between 0.8 and 2.1 V vs. Li/Li⁺ indicate the transitions of Ti⁴⁺/Ti³⁺, Nb⁵⁺/Nb⁴⁺, and Nb⁴⁺/Nb³⁺ (Figure 3C). When scanning to lower potentials, we observed a peak at 0.7 V vs. Li/Li⁺, which could be related to the SEI (solid-electrolyte interface) formation. During the cathodic scan, the oxidation peak at 1.1 V vs. Li/Li⁺ is much more pronounced compared to the potential range 1.0–2.5 V vs. Li/Li⁺. This means that when applying a potential lower than 1.0 V vs. Li/Li⁺, it might trigger full lithium intercalation into the TNO structure, especially for the redox couple of Nb⁴⁺/Nb³⁺. Subsequently, the electrochemical behavior completely changes in the 10th cycle (Figure 3D). Hybrid materials (TNO-CB-CO₂ and TNO-OLC-CO₂) can maintain the peak at 1.9 V vs. Li/Li⁺ (Ti⁴⁺/Ti³⁺), 1.6 V vs. Li/Li⁺ (Nb⁵⁺/Nb⁴⁺), and 1.1 V vs. Li/Li⁺ (Nb⁴⁺/Nb³⁺) while the non-hybrid materials (TNO-CB-Air, and TNO-OLC-Air) lose the activity of Ti⁴⁺/Ti³⁺ and Nb⁵⁺/Nb⁴⁺.

The galvanostatic charge/discharge cycling was carried out for a potential range of 0.05–2.5 V vs. Li/Li⁺, as shown in Figure 4A. Except for TNO-CB-CO₂, all samples exhibit an initial capacity of about 350 mAh g⁻¹. The latter value corresponds to 88% of the theoretical capacity of TNO. These high values are, to the best of our knowledge, the highest ones obtained for Ti₂Nb₁₀O₂₉/carbon materials (either composite or hybrid), as shown in Supporting Information, Table S3. The only higher value was reported for another type of TNO, namely TiNb₂O₇/C nanoporous microspheres (393 mAh g⁻¹ at 0.1 Ag⁻¹).^[28]

Some differences can be seen between the hybrid and non-hybrid materials for continuous cycling. Specifically, the non-hybrid materials (TNO-CB-Air and TNO-OLC-Air) show a more rapid loss of capacity, while the performance of hybrid samples is more stable within each specific current level. The hybrid materials (TNO-CB-CO₂, TNO-OLC-CO₂) can still provide ca. 150 mAh g⁻¹ at a high specific current of 1 Ag⁻¹. This might be explained by the delithiation at 1.1 and 1.7 V vs. Li/Li⁺ changing to more surface-controlled reactions for the hybrid materials (*b*-value: 0.7) in comparison to the non-hybrid materials (*b*-value: 0.6) as revealed by kinetics analysis (Supporting Information, Figure S6). In addition, the amount of conductive carbon in the electrodes and a uniform carbon distribution to generate an electron conduction path will affect the rate handling ability.^[29] Therefore, the better rate capability of TNO-OLC-CO₂ compared to TNO-CB-CO₂ might be correlated with the higher amount of carbon and better carbon distribution (Table 1, and Supporting Information, Figure S7).

To further understand the better rate capability of hybrid materials than that of non-hybrid materials, EIS of the half-cells was performed, and the corresponding Nyquist plot is shown in the Supporting Information, Figure S8, with the equivalent circuit being shown as an inset (R₁ + (Q/(R₂ + W)) + C). The electrical impedance spectra are composed of one semicircle

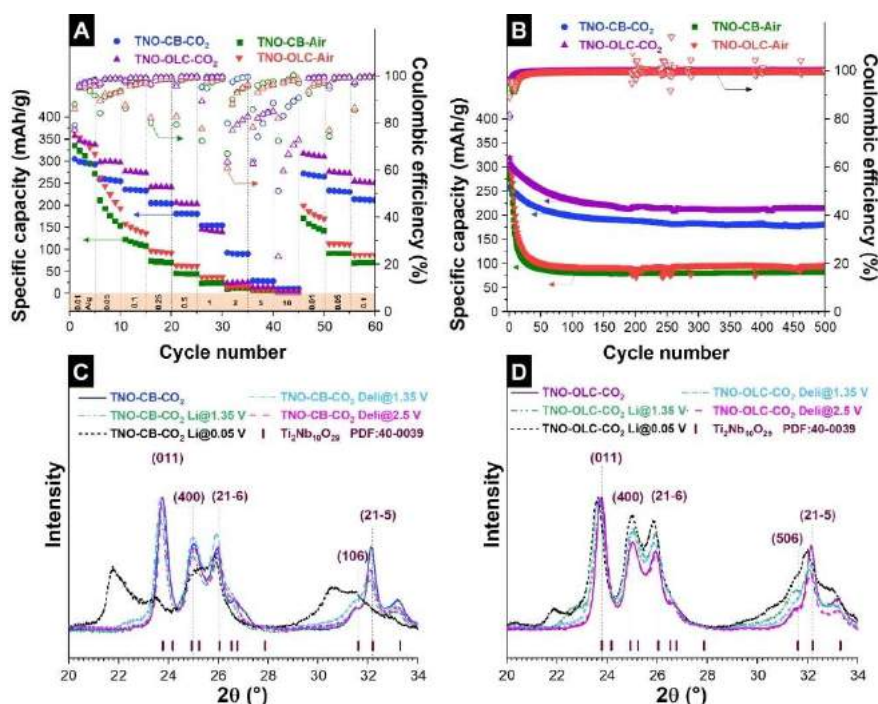


Figure 4. (A) Rate capability of the hybrid and non-hybrid materials in the potential window of 0.05–2.5 V vs. Li/Li⁺. (B) Cycling stability of the hybrid and non-hybrid materials in the potential window of 0.05–2.5 V vs. Li/Li⁺ at a specific current of 0.1 Ag⁻¹. XRD patterns of (C) TNO-CB-CO₂ and (D) TNO-OLC-CO₂ electrodes at different lithiated (“Li”: values at different potentials vs. Li/Li⁺) and delithiated states (“Deli”: values at different potentials vs. Li/Li⁺), respectively.

and one linear regime. These features are indicative of a charge-transfer element and a mass-transport element. In the equivalent circuit, R_1 , R_2 , Q , W , and C stand for electrolyte and cell component resistance, charge-transfer resistance, constant phase element, the Warburg impedance, and constant phase element based on an ideal capacitor, respectively. The fitted charge-transfer resistance values of the hybrids TNO-CB-CO₂ and TNO-OLC-CO₂ are 168.8 Ω and 138.7 Ω , respectively, which are significantly lower than the charge-transfer resistance of the non-hybrid materials TNO-CB-Air and TNO-OLC-Air (Supporting Information, Table S4). The lower charge-transfer resistance indicates faster charge-transfer kinetics in the hybrid materials due to improved electronic conductivity. Also, the higher carbon content in TNO-OLC-CO₂ compared to TNO-CB-CO₂ may align with both a lower charge-transfer resistance and an improved rate capability.

When returning to a low rate (0.01 Ag⁻¹) after 45 cycles, hybrid materials can largely recover their initial capacities while non-hybrid materials can only provide ca. 44% of their initial capacities. The cycling stability of the samples within the potential window of 0.05–2.5 V vs. Li/Li⁺ is depicted in Figure 4B. In this enlarged potential window, the cycling stabilities of the hybrid and non-hybrid materials show a significant difference. The initial capacities of the hybrid material (TNO-OLC-CO₂) and non-hybrid materials (TNO-CB-Air and TNO-OLC-Air) are very similar at a level of about 300 mAh g⁻¹. In contrast, the hybrid electrode (TNO-CB-CO₂) exhibits a specific capacity of ca. 250 mAh g⁻¹. The hybrid materials, TNO-CB-CO₂ and TNO-OLC-CO₂, preserve 70% and 67%, respectively, of their initial

capacities after 500 cycles. For comparison, the non-hybrid materials retain only 27% of their initial capacities after the first 50 cycles.

To further understand why the hybrid materials outperform their non-hybrid counterparts, we conducted half-cell experiments of all samples by holding them at certain voltages for different lithiation/delithiation states after the first 10 cycles for the potential window of 0.05–2.5 V vs. Li/Li⁺. After the cells reached an equilibrium current, the cells were disassembled; we used X-ray diffraction to analyze the structural changes of TNO (Figure 4C and D). While the Bragg reflections (011) and (21-5) in the lithiated state at 1.35 V vs. Li/Li⁺ of TNO-CB-CO₂ shift to lower angles, differences become more visible after reaching the fully lithiated state at 0.05 V vs. Li/Li⁺ (Figure 4C). Further, the Bragg reflections of (011) and (21-5) proceeded to shift towards larger d spacings (lower angles), and the new reflections at ca. 21.8°2 θ , and 30.5°2 θ appears when reaching the fully lithiated state. These data suggest that as TNO is fully lithiated, a new crystal phase emerges.^[5a] For TNO-OLC-CO₂, the new phase reflections become visible even for the lithiation state of 1.35 V vs. Li/Li⁺ at 22.6° and 30.7°2 θ (namely: TNO-OLC-CO₂ Li@1.35 V), then they move to lower angles 21.8° and 30.5°2 θ after reaching the full lithiation state at 0.05 V vs. Li/Li⁺ (Figure 4D). In both hybrid materials, two phases coexist after reaching the full lithiation state at 0.05 V vs. Li/Li⁺.^[5a] At the deepest lithiation state (0.05 V vs. Li/Li⁺), TNO-CB-CO₂ exhibits broader and higher intensity reflections for the aforementioned new phase positions (ca. 21.8° and 30.5°2 θ) than that of TNO-OLC-CO₂. We suspect that the higher amount of carbon in the

TNO-OLC-CO₂ than that of TNO-CB-CO₂ (Table 1) might suppress a volume change as well as an anisotropic lattice change. The reflections of the hybrid materials regain their initial Bragg positions after returning to the fully delithiated state at 2.5 V vs. Li/Li⁺ (Figure 4C and D). In contrast, the X-ray diffractograms of the non-hybrid materials at different lithiation and delithiation states show neither new reflections nor significant shifting of the reflections (Supporting Information, Figure S9).

A possible explanation for the observed electrochemical degradation may be the formation of microcracks as a result of unit-cell expansion during deep lithiation at the potential of 0.05 V vs. Li/Li⁺.^[30] This process may be suppressed for the hybrid material because of the nanoscopic level blending of active material and conductive carbon.^[31] Although this explanation is in alignment with the literature and the observed electrochemical performance, further work is needed to verify this degradation mechanism for our materials.

To demonstrate our hybrid material as the anode in a full-cell lithium-ion battery, we paired our anodes with a commercially available LiMn₂O₄ (LMO) cathode (Figure 5). The charge/mass balance of the cell was based on the specific capacity of both anode and cathode. After careful analysis of the half-cell data, the mass ratio between anode and cathode was 0.3 for the full-cell measurement. We used a C rate of 0.1C in a cell voltage range of 0.5–4.5 V (Figure 5A). The voltage profile of the positive electrode displays a lithiation/delithiation plateau at 4.0 V vs. Li/Li⁺, which is attributed to the Mn³⁺/Mn⁴⁺ redox couple.^[32] The voltage profile of TNO-OLC-CO₂ exhibits three different slopes at around 1.9, 1.7, and 1.1 V vs. Li/Li⁺, which agree with the CVs shown in Figure 3C and D. The calculated energy efficiency from the voltage profile of the cell is 64% at 0.1C. The full-cell results of TNO-OLC-CO₂//LMO are compared with full-cell results of graphite and LTO coupled with LMO in a Ragone plot (Figure 5B).

At a low C rate of 0.1C, the TNO-OLC-CO₂//LMO full-cell delivers a maximum energy of 83 Wh kg⁻¹, which is lower than

the highest specific energy of graphite, whereas LTO can only provide 98 Wh kg⁻¹, and 44 Wh kg⁻¹, respectively. However, these preliminary results can be further optimized by eliminating the dead mass. In our results, without considering the package mass, only 42% is the active mass; hence, by decreasing the mass of the current collector, the performance of this cell could increase significantly. As noted, the specific power of TNO-OLC-CO₂//LMO (64.8 W kg⁻¹) is lower than that of graphite and LTO (161 and 1.8 kW kg⁻¹, respectively). This poorer power performance of the TNO-OLC-CO₂//LMO full cell might be explained by the reduced rate capability of commercial LMO (Supporting Information, Figure S10).

Conclusions

We present a facile two-step synthesis method for carbide-derived electrode materials for lithium-ion battery (LIB) applications based on Ti₂Nb₁₀O₂₉ (TNO) and carbon. The prepared TNO hybrid and non-hybrid electrodes were tested in two different potential windows: a narrow range (1.0–2.5 V vs. Li/Li⁺) and a wide range (0.05–2.5 V vs. Li/Li⁺). While the performance of the hybrid and non-hybrid electrodes for the narrow potential window show no significant differences, hybrid electrodes exhibit superior performance compared to the non-hybrid electrodes for the wider potential window. X-ray diffraction analysis of the electrodes held at certain lithiation/delithiation states after 10 cycles for the large potential window revealed that hybrid electrodes have a two-phase region after reaching the fully lithiated state while non-hybrid electrodes show no significant structural change. The initial capacities of all electrodes are similar (ca. 350 mAh g⁻¹), but there is a faster electrochemical performance decay of non-hybrid materials.

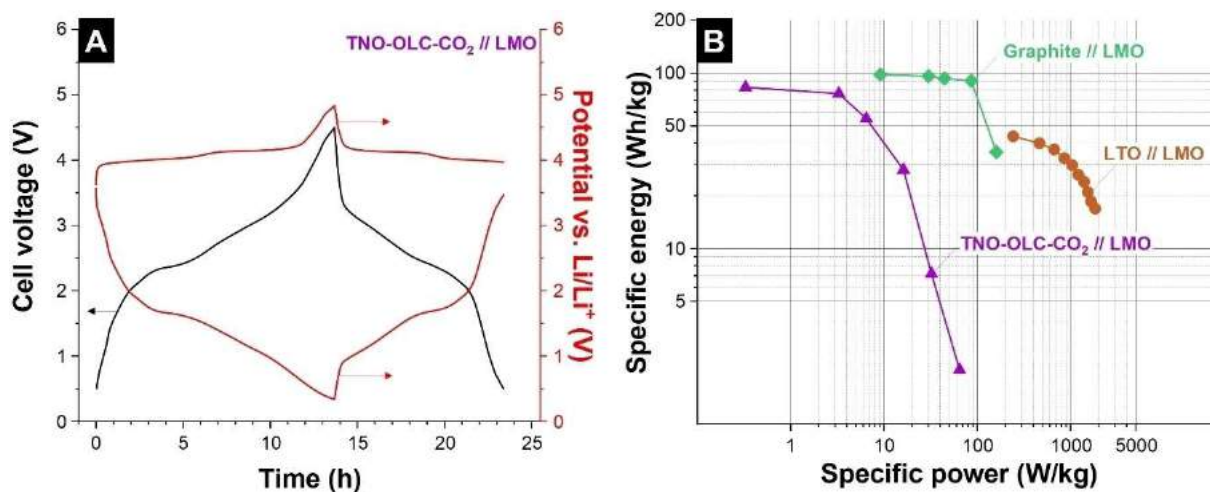


Figure 5. (A) Voltage profile of the full cell with TNO-OLC-CO₂ as negative electrode and LMO as positive electrode at 0.1C. The potentials are plotted as cell voltage and as the corresponding electrode potentials. (B) Ragone plot of the TNO-OLC-CO₂//LMO full cell, graphite//LMO (adapted from Ref. [33]) and LTO//LMO (adapted from Ref. [34]).

Supporting Information

Results from Rietveld refinement analysis, Le Bail analysis, scanning electron micrographs, X-ray diffractograms, illustrations of crystal structures, electrochemical results.

Acknowledgements

The INM-based authors acknowledge funding of the COSH-CDC project (PR-1173/5) by the German Research Foundation (DFG, Deutsche Forschungsgemeinschaft). L.B. acknowledges the Federal Ministry of Education and Research (Bundesministerium für Bildung und Forschung, BMBF) for support of the Mechanocarb project (award number 03SF0498). The INM-based authors thank Eduard Arzt (INM) for his continuing support and Robert Drumm & Bixian Ying (INM) for their technical support. Open access funding enabled and organized by Projekt DEAL.

Conflict of Interest

The authors declare no conflict of interest.

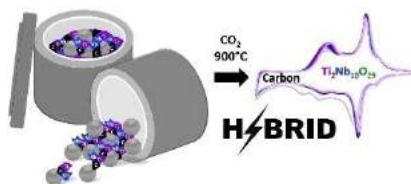
Keywords: batteries · lithium · hybrid material · mechanochemistry · titanium niobium oxide

- [1] A. Eftekhari, *ACS Sustainable Chem. Eng.* **2019**, *7*, 3684–3687.
- [2] a) H. Wang, R. Qian, Y. Cheng, H.-H. Wu, X. Wu, K. Pan, Q. Zhang, *J. Mater. Chem. A* **2020**, *8*, 18425–18463; b) H. Lyu, J. Li, T. Wang, B. P. Thapaliya, S. Men, C. J. Jafta, R. Tao, X.-G. Sun, S. Dai, *ACS Appl. Energy Mater.* **2020**, *3*, 5657–5665; c) Y.-G. Sun, T.-Q. Sun, X.-J. Lin, X.-S. Tao, D. Zhang, C. Zeng, A.-M. Cao, L.-J. Wan, *Sci. China Chem.* **2018**, *61*, 670–676.
- [3] N. Takami, K. Ise, Y. Harada, T. Iwasaki, T. Kishi, K. Hoshina, *J. Power Sources* **2018**, *396*, 429–436.
- [4] S. Lou, Y. Zhao, J. Wang, G. Yin, C. Du, X. Sun, *Small* **2019**, *15*, 1904740.
- [5] a) X. Wu, J. Miao, W. Han, Y.-S. Hu, D. Chen, J.-S. Lee, J. Kim, L. Chen, *Electrochem. Commun.* **2012**, *25*, 39–42; b) G. Liu, B. Jin, R. Zhang, K. Bao, H. Xie, J. Guo, M. Wei, Q. Jiang, *Int. J. Hydrogen Energy* **2016**, *41*, 14807–14812; c) S. Deng, Z. Luo, Y. Liu, X. Lou, C. Lin, C. Yang, H. Zhao, P. Zheng, Z. Sun, J. Li, N. Wang, H. Wu, *J. Power Sources* **2017**, *362*, 250–257; d) W. Mao, K. Liu, G. Guo, G. Liu, K. Bao, J. Guo, M. Hu, W. Wang, B. Li, K. Zhang, Y. Qian, *Electrochim. Acta* **2017**, *253*, 396–402; e) H. Shim, E. Lim, S. Fleischmann, A. Quade, A. Tolosa, V. Presser, *Sustainable Energy Fuels* **2019**, *3*, 1776–1789.
- [6] T. Takashima, T. Tojo, R. Inada, Y. Sakurai, *J. Power Sources* **2015**, *276*, 113–119.
- [7] a) A. Tolosa, S. Fleischmann, I. Grobelsek, A. Quade, E. Lim, V. Presser, *ChemSusChem* **2018**, *11*, 159–170; b) S. Fleischmann, A. Tolosa, V. Presser, *Chem. Eur. J.* **2018**, *24*, 12143–12153; c) Ö. Budak, P. Srimuk, A. Tolosa, S. Fleischmann, J. Lee, S. W. Hieke, A. Frank, C. Scheu, V. Presser, *Batt. Supercaps* **2019**, *2*, 74–82.
- [8] W. L. Wang, B.-Y. Oh, J.-Y. Park, H. Ki, J. Jang, G.-Y. Lee, H.-B. Gu, M.-H. Ham, *J. Power Sources* **2015**, *300*, 272–278.
- [9] N. Luo, G. Chen, Y. Shang, S. Lu, J. Mei, C. Tang, Z. He, W. Zeng, H. Zhan, *NANO* **2020**, *15*, 2050095.
- [10] Y. Tang, S. Deng, S. Shi, L. Wu, G. Wang, G. Pan, S. Lin, X. Xia, *Electrochim. Acta* **2020**, *332*, 135433.
- [11] Z. Yao, X. Xia, S. Zhang, C.-a. Zhou, G. Pan, Q. Xiong, Y. Wang, X. Wang, J. Tu, *Energy Storage Mater.* **2020**, *25*, 555–562.
- [12] G. Wan, L. Yang, S. Shi, Y. Tang, X. Xu, G. Wang, *Chem. Commun.* **2019**, *55*, 517–520.
- [13] M. Zeiger, T. Ariyanto, B. Krüner, N. J. Peter, S. Fleischmann, B. J. M. Etzold, V. Presser, *J. Mater. Chem. A* **2016**, *4*, 18899–18909.
- [14] Ö. Budak, M. Geißler, D. Becker, A. Kruth, A. Quade, R. Haberkorn, G. Kickelbick, B. J. M. Etzold, V. Presser, *ACS Appl. Energy Mater.* **2020**, *3*, 4275–4285.
- [15] M. Zeiger, N. Jäckel, V. N. Mochalin, V. Presser, *J. Mater. Chem. A* **2016**, *4*, 3172–3196.
- [16] M. Zeiger, D. Weingarh, V. Presser, *ChemElectroChem* **2015**, *2*, 1117–1127.
- [17] K. Ono, J. Moriyama, *J. Less-Common Met.* **1981**, *79*, 255–260.
- [18] A. Kaniyoor, S. Ramaprabhu, *AIP Adv.* **2012**, *2*, 032183.
- [19] D. Weingarh, M. Zeiger, N. Jäckel, M. Aslan, G. Feng, V. Presser, *Adv. Energy Mater.* **2014**, *4*, 1400316.
- [20] S. H. Choi, T. S. Kim, B. Ali, K. S. Choi, S. K. Hyun, J. J. Sim, W. J. Choi, W. Joo, J. H. Lim, T. H. Lee, K. T. Park, *Arch. Metall. Mater.* **2017**, *vol. 62*.
- [21] L. Takacs, *Prog. Mater. Sci.* **2002**, *47*, 355–414.
- [22] O. Yamaguchi, D. Tomihisa, N. Ogiso, K. Shimizu, *J. Am. Ceram. Soc.* **1986**, *69*, C-150–C-151.
- [23] a) N. G. Eror, U. Balachandran, *J. Solid State Chem.* **1982**, *45*, 276–279; b) Q. Cheng, J. Liang, Y. Zhu, L. Si, C. Guo, Y. Qian, *J. Mater. Chem. A* **2014**, *2*, 17258–17262.
- [24] A. C. Ferrari, D. M. Basko, *Nat. Nanotechnol.* **2013**, *8*, 235–246.
- [25] X. Lu, Z. Jian, Z. Fang, L. Gu, Y.-S. Hu, W. Chen, Z. Wang, L. Chen, *Energy Environ. Sci.* **2011**, *4*, 2638–2644.
- [26] a) S. Ardizzzone, G. Fregonara, S. Trasatti, *Electrochim. Acta* **1990**, *35*, 263–267; b) M. Opitz, J. P. Yue, J. Wallauer, B. Smarsly, B. Ruling, *Electrochim. Acta* **2015**, *168*, 125–132; c) S. Fleischmann, J. B. Mitchell, R. Wang, C. Zhan, D. E. Jiang, V. Presser, V. Augustyn, *Chem. Rev.* **2020**, *120*, 6738–6782.
- [27] M. R. Lukatskaya, B. Dunn, Y. Gogotsi, *Nat. Commun.* **2016**, *7*, 12647.
- [28] S. Shen, S. Deng, Y. Zhong, J. Wu, X. Wang, X. Xia, J. Tu, *Chin. Chem. Lett.* **2017**, *28*, 2219–2222.
- [29] M. Takeno, T. Fukutsuka, K. Miyazaki, T. Abe, *Carbon* **2017**, *122*, 202–206.
- [30] Y. Hu, X. Zhao, Z. Suo, *J. Mater. Res.* **2010**, *25*, 1007–1010.
- [31] T. Li, X.-Z. Yuan, L. Zhang, D. Song, K. Shi, C. Bock, *Electrochem. Energy Rev.* **2020**, *3*, 43–80.
- [32] N. Kiziltas-Yavuz, A. Bhaskar, D. Dixon, M. Yavuz, K. Nikolowski, L. Lu, R.-A. Eichel, H. Ehrenberg, *J. Power Sources* **2014**, *267*, 533–541.
- [33] G. B. Appetecchi, P. P. Prosini, *J. Power Sources* **2005**, *146*, 793–797.
- [34] A. Du Pasquier, I. Plietz, S. Menocal, G. Amatucci, *J. Power Sources* **2003**, *115*, 171–178.

Manuscript received: September 18, 2020
 Revised manuscript received: October 27, 2020
 Accepted manuscript online: October 30, 2020
 Version of record online: ■■■, ■■■■

FULL PAPERS

Nanoscale hybridization: mechanochemical carbide synthesis and subsequent thermal annealing yields unique nanohybrids of titanium niobium oxide and carbon. Capitalizing on the enhanced charge transport afforded by carbon and the lithium-ion intercalation of the metal oxide, the best hybrid material displayed a specific capacity of 350 mAh g^{-1} at a rate of 0.01 A g^{-1} (144 mAh g^{-1} at 1 A g^{-1}) within a potential range of $0.05\text{--}2.5 \text{ V}$ vs. Li/Li^+ .



Ö. Budak, Dr. P. Srimuk, Dr. M. Aslan,
H. Shim, Prof. L. Borchardt, V. Presser*

1 – 11

**Titanium Niobium Oxide $\text{Ti}_2\text{Nb}_{10}\text{O}_{29}$ /
Carbon Hybrid Electrodes Derived
by Mechanochemically Synthesized
Carbide for High-Performance
Lithium-Ion Batteries**



Supporting Information

Titanium niobium oxide $\text{Ti}_2\text{Nb}_{10}\text{O}_{29}$ /carbon hybrid electrodes derived by mechanochemically synthesized carbide for high-performance lithium-ion batteries

Ö. Budak,^{a,b} P. Srimuk,^a M. Aslan,^a H. Shim,^{a,b} L. Borchardt,^c and V. Presser^{a,b,*}

^a INM - Leibniz Institute for New Materials, 66123 Saarbrücken, Germany

^b Department of Materials Science and Engineering, Saarland University, 66123 Saarbrücken, Germany

^c Inorganic Chemistry I, Ruhr-University Bochum, 44780 Bochum, Germany

* Corresponding author's eMail: volker.presser@leibniz-inm.de

Table S1. Rietveld refinement results of TNC-CB and TNC-OLC.

Sample	Phase	Space group	Lattice parameter (Å)	Volume (Å ³)	Domain size (nm)	Amount (mass%)	R _{wp} (%)
TNC-CB	(Ti,Nb)C	<i>Fm</i> $\bar{3}$ <i>m</i>	<i>a</i> = 4.43(4)	87.09(4)	19.7(4)	98	2.3
	WC	<i>P</i> $\bar{6}$ <i>m</i> 2	<i>a</i> = 2.90(3) <i>c</i> = 2.85(3)	20.82(3)	9995.4(3)	2	
TNC-OLC	(Ti,Nb)C	<i>Fm</i> $\bar{3}$ <i>m</i>	<i>a</i> = 4.43(4)	88.12(4)	15.3(4)	98	2.5
	WC	<i>P</i> $\bar{6}$ <i>m</i> 2	<i>a</i> = 2.90(6) <i>c</i> = 2.85(6)	20.76(6)	9999.9(6)	2	

Table S2. Le Bail analysis results of the analysis of X-ray diffraction patterns of TNO-CB-CO₂, TNO-OLC-CO₂, TNO-CB-Air, and TNO-OLC-Air.

Sample	Phase	Space group	Lattice parameter (Å)	Interaxial angle (°)	Volume (Å ³)	Domain size (nm)	R _{wp} (%)
TNO-CB-CO ₂	Ti ₂ Nb ₁₀ O ₂₉	<i>A</i> 12/ <i>m</i> 1	<i>a</i> = 15.64 <i>b</i> = 3.82 <i>c</i> = 20.52	β = 113.4	1124.1	55	3.4
TNO-OLC-CO ₂	Ti ₂ Nb ₁₀ O ₂₉	<i>A</i> 12/ <i>m</i> 1	<i>a</i> = 15.62 <i>b</i> = 3.81 <i>c</i> = 20.52	β = 113.4	1122.4	63	3.7
TNO-CB-Air	Ti ₂ Nb ₁₀ O ₂₉	<i>A</i> 12/ <i>m</i> 1	<i>a</i> = 15.71 <i>b</i> = 3.85 <i>c</i> = 20.61	β = 113.4	1145.3	56	3.5
TNO-OLC-Air	Ti ₂ Nb ₁₀ O ₂₉	<i>A</i> 12/ <i>m</i> 1	<i>a</i> = 15.71 <i>b</i> = 3.85 <i>c</i> = 20.62	β = 113.4	1146.0	88	3.6

Table S3. Electrochemical performance comparison of titanium niobium oxides (TiNb_2O_7 , and $\text{Ti}_2\text{Nb}_{10}\text{O}_{29}$). CNTs: carbon nanotubes. CF: carbon fiber. rGO: reduced graphene oxide. CNFs: carbon nanofibers. CC: carbon cloth. DEC: diethylene carbonate. EMC: ethyl methyl carbonate. PC: propylene carbonate. MSR: Mechanically-induced self-sustaining reaction.

Materials	Synthesis	Capacity at a low rate (mAh/g, A/g)	Capacity at a high rate (mAh/g, A/g)	Voltage range (V vs. Li/Li ⁺)	Capacity retention (% cycle number)	Electrolyte	Reference
TiNb ₂ O ₇ /graphene hybrid	Solvothermal method	300, 0.03	150, 1.5	1.0-3.0	67, 300	1 M LiPF ₆ in EC:DMC	1
Nano-TiNb ₂ O ₇ /CNTs	Direct hydrolysis method	300, 0.03	150, 4.5	0.8-3.0	97, 100	1 M LiPF ₆ in EC:DMC:DEC	2
TiNb ₂ O ₇ /C nanoporous microspheres	Spray-drying method	393, 0.1	120, 3.6	1.0-2.6	75, 300	1 M LiPF ₆ in EC:DEC	3
CF/TiNb ₂ O ₇	Solvothermal method	250, 0.25	175, 1.75	1.0-2.5	88, 1000	1 M LiPF ₆ in EC:DMC	4
rGO-TiNb ₂ O ₇ microsphere	Solvothermal method	225, 0.23	25, 2.5	1.0-3.0	61, 500	1 M LiPF ₆ in EC:EMC	5
Ti ₂ Nb ₁₀ O ₂₉ /C composite	Solid-state reaction	296, 0.25	150, 4.5	1.0-2.5	87, 100	1 M LiPF ₆ in EC:DMC	6
Ti ₂ Nb ₁₀ O ₂₉ /rGO	Solid-state reaction, ball-milling	250, 0.03	100, 1	1.0-2.5	77, 50	1 M LiPF ₆ in EC:DMC	7
Ti ₂ Nb ₁₀ O ₂₉ /carbon onion nanohybrid	Sol-gel method	290, 0.01	169, 2	1.0-2.8	76, 800	1 M LiPF ₆ in EC:DMC	8
Ti ₂ Nb ₁₀ O ₂₉ /carbon hybrid fiber	Electro-spining	260, 0.025	180, 5	0.8-3.0	60, 500	1 M LiPF ₆ in EC:DMC	9
Ti ₂ Nb ₁₀ O ₂₉ /C microsphere	Solvothermal method	276, 0.27	215, 6.4	1.0-2.5	89, 200	1 M LiPF ₆ in EC:EMC:DEC	10
CNFs/Ti ₂ Nb ₁₀ O ₂₉ /CC	Electrophoretic deposition, solvothermal method	300, 0.03	200, 12	1.0-2.5	80, 1000	1 M LiPF ₆ in EC:DEC	11
TNO-CB-CO₂	MSR, CO₂ oxidation	272, 0.01	157, 1	1.0-2.5	82, 500	1 M LiPF ₆ in EC:DMC	This work
		304, 0.01	155, 1	0.05-2.5	70, 500		
TNO-OLC-CO₂	MSR, CO₂ oxidation	253, 0.01	151, 1	1.0-2.5	76, 500	1 M LiPF ₆ in EC:DMC	This work
		350, 0.01	144, 1	0.05-2.5	67, 500		

Table S4. Results of the R_1 and R_2 obtained by fitting the data from **Fig. S8**.

Material	R_1 (Ω)	R_2 (Ω)
TNO-CB-CO ₂	16.2	168.8
TNO-OLC-CO ₂	12.7	138.7
TNO-CB-Air	28.2	234.4
TNO-OLC-Air	7.3	184.4

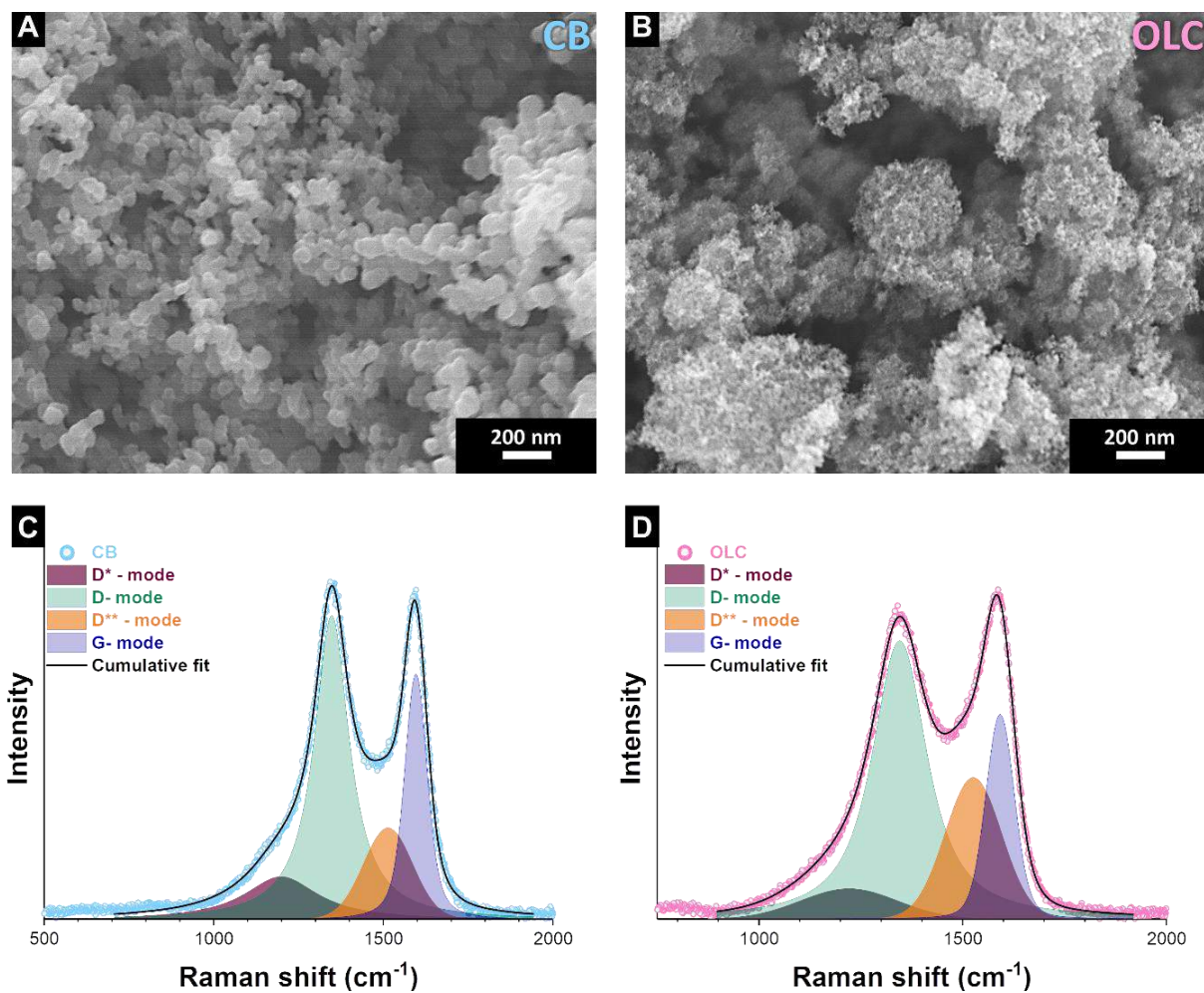


Fig. S1. Scanning electron micrographs of (A) CB, and (B) OLC. Fitted Raman spectra of (C) CB, and (D) OLC.

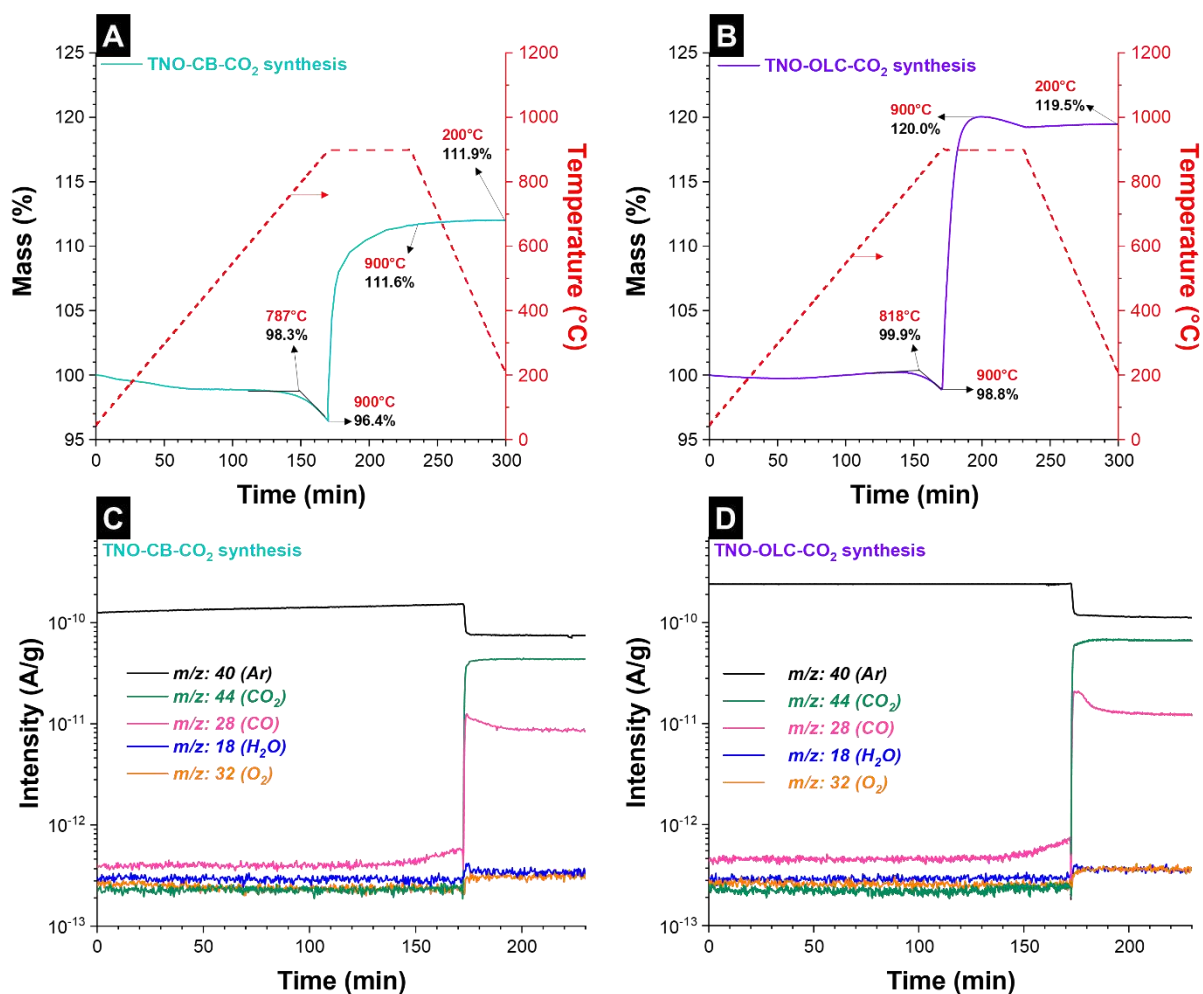


Fig. S2. Thermograms of (A) TNO-CB-CO₂, and (B) TNO-OLC-CO₂ synthesis following the synthesis protocol of hybrid materials. The corresponding mass spectra of TGA-MS measurements of (C) TNO-CB-CO₂, and (D) TNO-OLC-CO₂ synthesis.

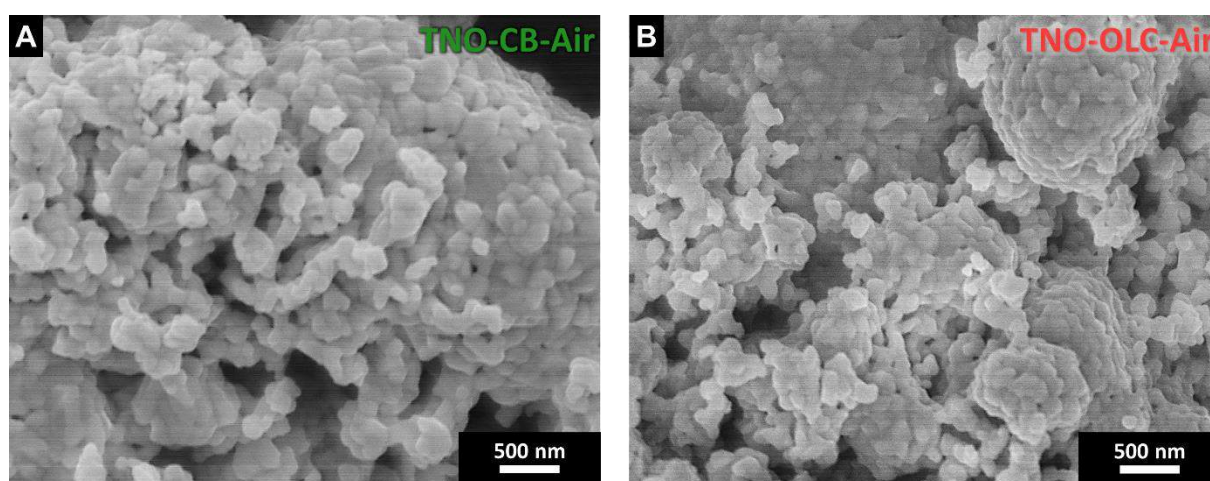


Fig. S3. Scanning electron micrographs of (A) TNO-CB-Air, and (B) TNO-OLC-Air.

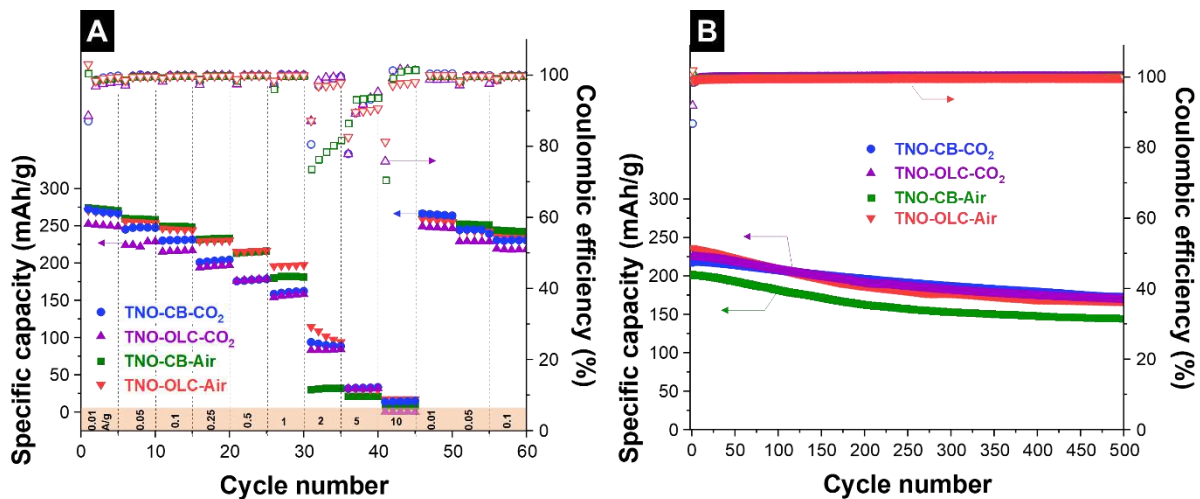


Fig. S4. (A) Rate handling performance of the hybrid and non-hybrid materials in the potential window of 1.0-2.5 V vs. Li/Li⁺. (B) Cyclic stability performance of the hybrid and non-hybrid materials in the potential window of 1.0-2.5 V vs. Li/Li⁺.

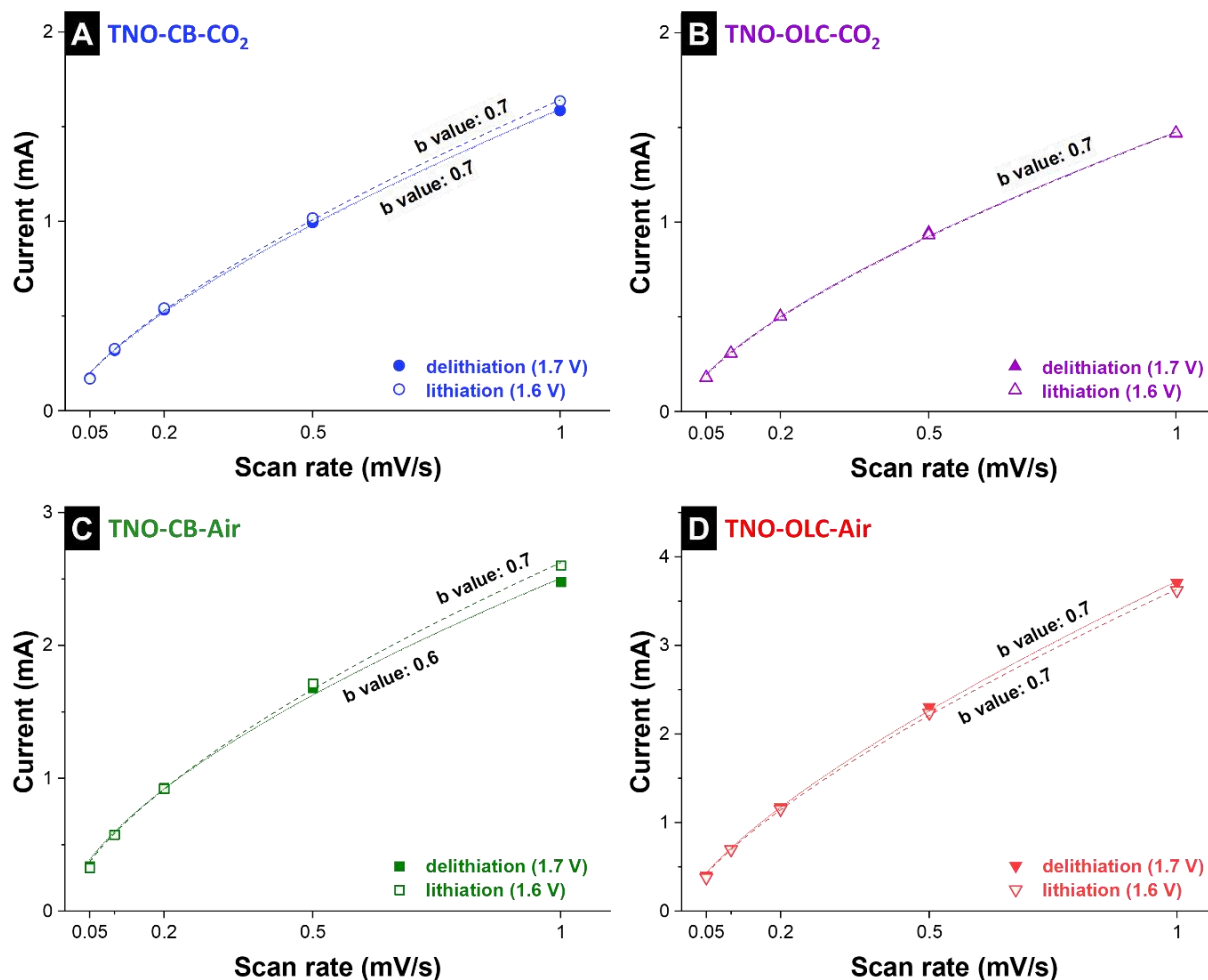


Fig. S5. Kinetic analysis of (A) TNO-CB-CO₂, (B) TNO-OLC-CO₂, (C) TNO-CB-Air, and (D) TNO-OLC-Air calculated from cyclic voltammograms at the different scan rates for the potential window of 1.0-2.5 V vs. Li/Li⁺.

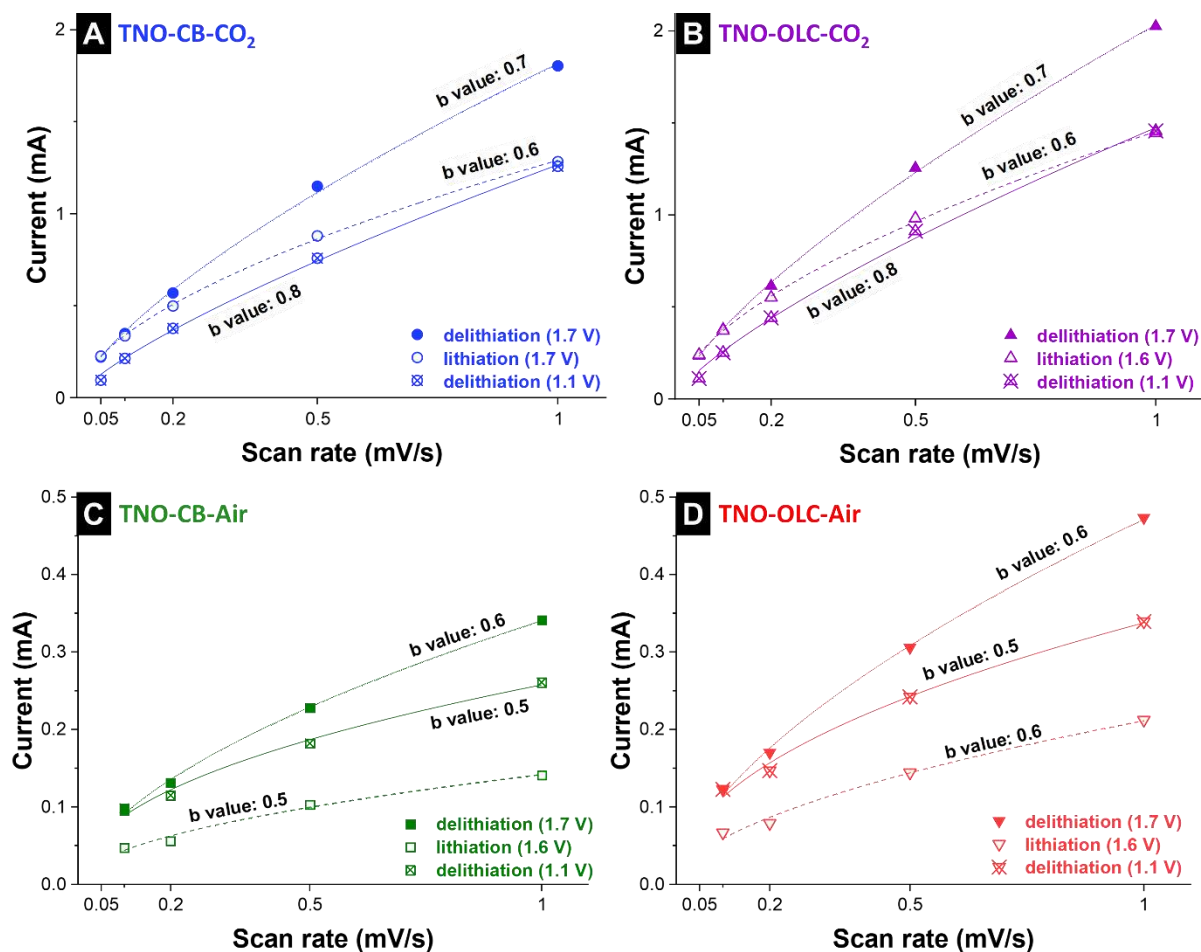


Fig. S6. Kinetic analysis of (A) TNO-CB-CO₂, (B) TNO-OLC-CO₂, (C) TNO-CB-Air, and (D) TNO-OLC-Air calculated from cyclic voltammograms at the different scan rates for the potential window of 0.05-2.5 V vs. Li/Li⁺.

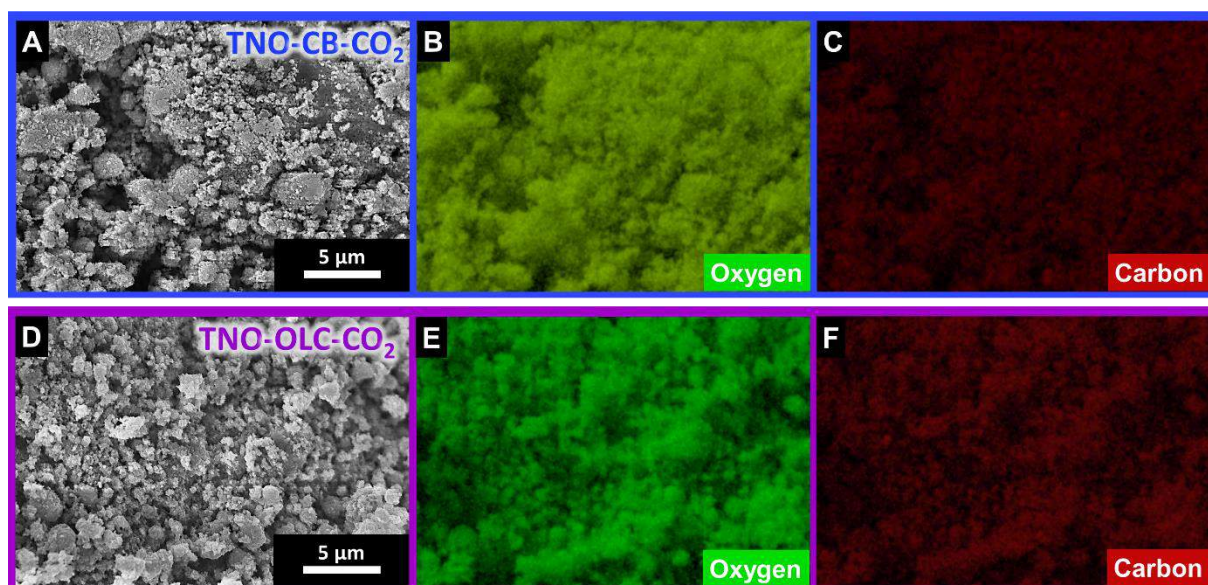


Fig. S7. (A-C) Analysis of the TNO-CB-CO₂ electrode: (A) Scanning electron micrographs, and (B-C) elemental mapping by EDX. (D-F) Analysis of the TNO-OLC-CO₂ electrode: (D) Scanning electron micrographs, and (E-F) elemental mapping by EDX.

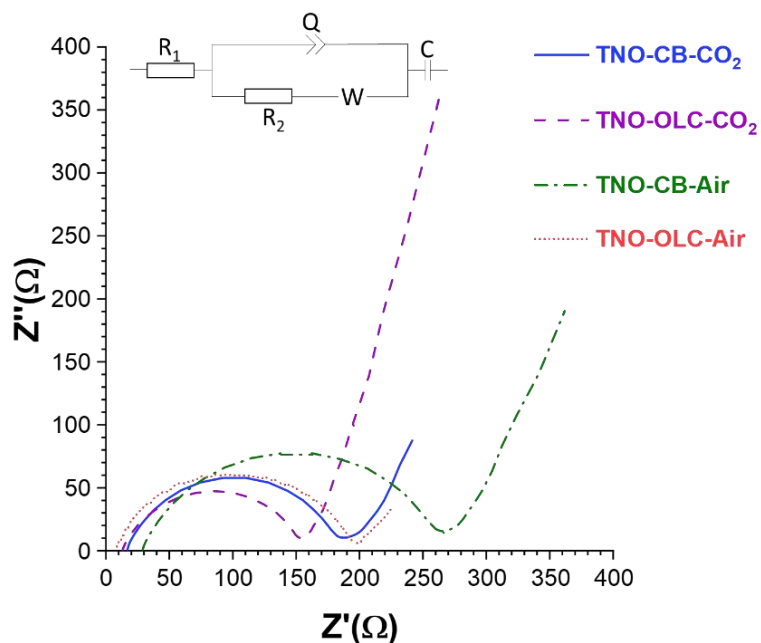


Fig. S8. Nyquist plot of hybrid and non-hybrid materials. The inset displays the equivalent circuit used for fitting of the electrochemical impedance spectra.

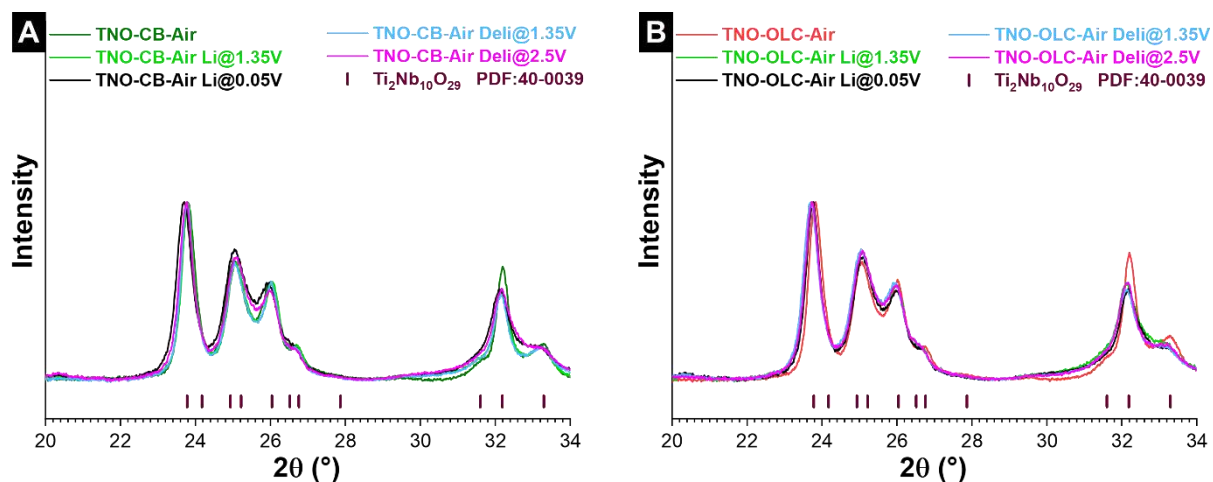


Fig. S9. X-ray diffraction patterns of (A) TNO-CB-Air, and (B) TNO-OLC-Air electrodes at the different lithiated/delithiated states (denoted as “Li” and “Deli”).

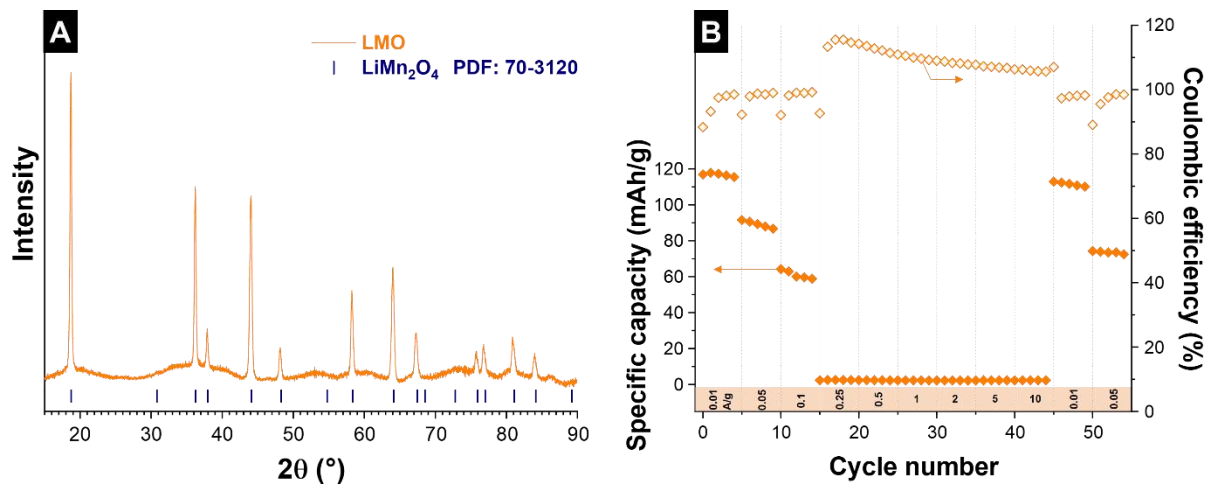


Fig. S10. (A) X-ray diffractogram of LiMn_2O_4 (LMO) with the reported Bragg positions from PDF 70-3120. (B) Rate handling performance of LMO.

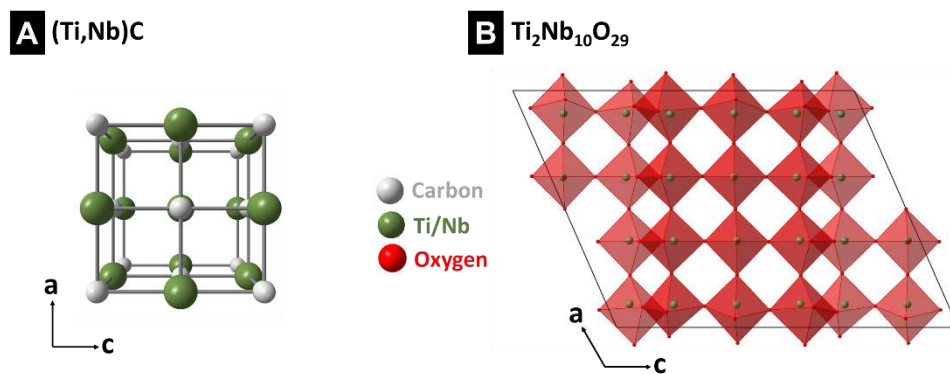


Fig. S11. Structural illustrations of the crystal lattice of (A) titanium niobium carbide $(\text{Ti,Nb})\text{C}$, and (B) $\text{Ti}_2\text{Nb}_{10}\text{O}_{29}$.

References

- [1] A. G. Ashish, P. Arunkumar, B. Babu, P. Manikandan, S. Sarang, M. M. Shaijumon *Electrochimica Acta*. **2015**, *176*, 285-292.
- [2] C. Lin, L. Hu, C. Cheng, K. Sun, X. Guo, Q. Shao, J. Li, N. Wang, Z. Guo *Electrochimica Acta*. **2018**, *260*, 65-72.
- [3] G. Zhu, Q. Li, Y. Zhao, R. Che *ACS Applied Materials & Interfaces*. **2017**, *9*, 41258-41264.
- [4] S. Shen, S. Deng, Y. Zhong, J. Wu, X. Wang, X. Xia, J. Tu *Chinese Chemical Letters*. **2017**, *28*, 2219-2222.
- [5] H. Noh, W. Choi *Journal of The Electrochemical Society*. **2016**, *163*, A1042-A1049.
- [6] G. Liu, B. Jin, R. Zhang, K. Bao, H. Xie, J. Guo, M. Wei, Q. Jiang *International Journal of Hydrogen Energy*. **2016**, *41*, 14807-14812.
- [7] W. L. Wang, B.-Y. Oh, J.-Y. Park, H. Ki, J. Jang, G.-Y. Lee, H.-B. Gu, M.-H. Ham *Journal of Power Sources*. **2015**, *300*, 272-278.
- [8] H. Shim, E. Lim, S. Fleischmann, A. Quade, A. Tolosa, V. Presser *Sustainable Energy & Fuels*. **2019**, *3*, 1776-1789.
- [9] A. Tolosa, S. Fleischmann, I. Grobelsek, A. Quade, E. Lim, V. Presser *ChemSusChem*. **2018**, *11*, 159-170.
- [10] X. Liu, H. Wang, S. Zhang, G. Liu, H. Xie, J. Ma *Electrochimica Acta*. **2018**, *292*, 759-768.
- [11] Y. Tang, S. Deng, S. Shi, L. Wu, G. Wang, G. Pan, S. Lin, X. Xia *Electrochimica Acta*. **2020**, *332*, 135433.

6. Summary, conclusions and outlook

New synthetic approaches for hybrid materials were developed to improve the performance of lithium-ion batteries. My work revealed that the bi-phase transformation of the metal carbides to the metal oxide/carbon hybrid via chloroxidation as a novel synthesis approach or even CO₂ oxidation enlightens the way of achieving advanced electrode materials for LIB energy storage applications. The most dominant synthesis for hybrid materials is based on wet-chemical syntheses, such as the sol-gel method, which provides good control of the particle size. However, it requires a controllable environment for the reproducibility point of view due to the precursors are highly sensitive to the environmental conditions. In addition, the sol-gel process requires thermal treatment or calcination process to form a high crystal for hosting lithium-ion in their structure. This makes the cost of materials even higher as it has a low yield compared to a simple solid-state reaction.

To obtain hybrid materials for the anode of LIBs, this thesis deals with the new approach solid-state reaction using metal carbides as precursors. Hence, this process brings many advantages:

- There is a various choice of materials as a precursor that results in metal oxide-carbon hybrid materials, which can be accomplished via the new synthesis approach, chloroxidation.
- Ternary metal carbide leads to ternary oxide-carbon hybrid materials, which can be easily controlled by variation of the atomic ratio of metal in carbides and accomplished via mechanochemical synthesis of ternary carbide at room temperature.
- Unlike traditional solid-state reaction that usually result in larger particles, the so-called chloroxidation provides much smaller particles and, thus, better electrochemical performance.

Following the as-mentioned advantages, three different metal oxide-carbon hybrid materials were explored, including V₂O₃, Nb₂O₅, and Ti₂Nb₁₀O₂₉. Three of these materials are derived from simple carbides (i.e., VC, NbC, and (Ti,Nb)C).

In **chapter 5.1**, V₂O₃/carbon hybrid material was synthesized via one thermal treatment step, so-called chloroxidation, where decomposition of hydrated metal chloride salt leads to the *in situ* generation of Cl₂ gas and oxidative atmosphere under atmospheric pressure conditions. The obtained material involves metallic Ni, which can easily be removed from the sample via

the acid washing process. This unique synthesis results in hybrid material with V_2O_3 as a core and nanoporous carbon as a shell. Compared with the V_2O_3 composite electrode, the optimized hybrid V_2O_3 /carbon electrode showed superior electrochemical performance, such as a specific capacity of 120 mAh/g at 2.5 A/g (5.2C, charging/discharging in 2.9 min). In addition to that, the unique carbon in the hybrid V_2O_3 /carbon electrode yielded capacity increase cycle by cycle, according to the post mortem results of the cycled electrodes.

In **chapter 5.2**, two different syntheses were used to obtain two different crystallographic phases of Nb_2O_5 /carbon hybrid materials. The first synthesis was accomplished via chloroxidation of NbC, resulting in an orthorhombic Nb_2O_5 /carbon hybrid material. The second synthesis involved two thermal treatment steps: first, the partial conversion of NbC to NbC/carbon core/shell by chlorine treatment, and second, conversion of NbC/carbon to Nb_2O_5 /carbon hybrid material via CO_2 gas. These two-thermal treatment steps result in a mixture of tetragonal and monoclinic phases containing the Nb_2O_5 /carbon hybrid material. The obtained hybrid materials exhibited a specific capacity of 300 mAh/g, which exceeds the current state-of-art performance of Nb_2O_5 of about 200 mAh/g. The outstanding performance of Nb_2O_5 /carbon hybrid materials was explained by oxygen deficiency and/or stacking faults in the Nb_2O_5 structures. Furthermore, the composite counterpart of the mixed-phase involving Nb_2O_5 /carbon hybrid showed a specific capacity of 100 mAh/g at 10 A/g (25C, charging/discharging in 0.6 min) and robust reversible cyclic stability.

In **chapter 5.3**, $Ti_2Nb_{10}O_{29}$ was chosen for hybrid electrode synthesis due to its high theoretical capacity for LIB applications. To be able to accomplish a pure $Ti_2Nb_{10}O_{29}$ phase in the $Ti_2Nb_{10}O_{29}$ /carbon hybrid electrode, the carbide precursor was obtained by using a mechanically induced self-sustaining reaction (MSR) via ball-milling at room temperature with a stoichiometric ratio of Ti and Nb of 1 to 5, and two different carbon sources (carbon black, and onion-like carbon). Then, the obtained titanium carbides were converted to hybrid $Ti_2Nb_{10}O_{29}$ /carbon using thermal treatment under CO_2 and Ar gases mixture, and non-hybrid $Ti_2Nb_{10}O_{29}$ by thermal oxidation via synthetic air. For the large voltage window (0.05 – 1.0 V vs. Li/Li⁺) applications, hybrid $Ti_2Nb_{10}O_{29}$ /carbon provides robust cyclic stability and maintain 70% of its initial specific capacity after 500 cycles, where the hybrid's counterpart non-hybrid $Ti_2Nb_{10}O_{29}$ losses 74% of its initial capacity even only after first 40 cycles.

When looking forward based on the finding of these works, we can see that hybrid materials have superior electrochemical performance in many aspects. First, the carbon in hybrid materials improves the electronic conductivity resulting in lower impedance at the interparticle compared to the traditional composite electrode. As seen from **chapter 5.1** to **5.3**, hybrid materials exhibit much faster charge/discharge performance than that of composite ones. Second, having carbon on the surface of metal oxide particle mitigate volume expansion and contraction during lithiation and delithiation process. As a result, we have observed throughout the work that hybrid materials show a robust cyclic performance. Finally, the synthesis method reported in this dissertation is by far very new and easy for large scale production. Naturally, the research trend in terms of materials development will evolve. New materials might be found to replace the-state-of-the-art; however, hybrid materials are one of the keys to achieve better electrochemical performance. The chloroxidation process of carbides has room to improve. It could lead to different metal oxides showing promising performance. The challenge is to apply this synthesis to produce high-performance cathode material. I believe that this process could reduce the cost of cathode materials significantly compared to the synthesis route used in the industry (precipitation process, followed by thermal treatment).

References

- [1] European Commission, Energy Roadmap 2050, Publication Office of the European Union (2012).
- [2] *Adoption of the Paris Agreement*, FCCC/CP/2015/L9/Rev.1 (UNFCCC, 2015).
- [3] A. Qazi, F. Hussain, N.A. Rahim, G. Hardaker, D. Alghazzawi, K. Shaban, K. Haruna, Towards Sustainable Energy: A Systematic Review of Renewable Energy Sources, Technologies, and Public Opinions, *IEEE Access* 7 (2019) 63837-63851.
- [4] M.A. Hannan, M. Faisal, P. Jern Ker, R.A. Begum, Z.Y. Dong, C. Zhang, Review of optimal methods and algorithms for sizing energy storage systems to achieve decarbonization in microgrid applications, *Renew. Sust. Energ. Rev.* 131 (2020) 110022.
- [5] M.R. Lukatskaya, B. Dunn, Y. Gogotsi, Multidimensional materials and device architectures for future hybrid energy storage, *Nat. Commun.* 7(1) (2016) 12647.
- [6] L. Guan, L. Yu, G.Z. Chen, Capacitive and non-capacitive faradaic charge storage, *Electrochim. Acta* 206 (2016) 464-478.
- [7] R. Korthauer, *Lithium-ion batteries: basics and applications*, Springer (2018).
- [8] I. Buchmann, *Batteries in a portable world*, Cadex Electronic Inc. (2016).
- [9] Q. Zhen, S. Bashir, J.L. Liu, *Nanostructured materials for next-generation energy storage and conversion*, Springer (2019).
- [10] J. Xie, Y.-C. Lu, A retrospective on lithium-ion batteries, *Nat. Commun.* 11(1) (2020) 2499.
- [11] M.S. Whittingham, Electrical energy storage and intercalation chemistry, *Science* 192(4244) (1976) 1126-1127.
- [12] K. Mizushima, P.C. Jones, P.J. Wiseman, J.B. Goodenough, Li_xCoO_2 ($0 < x < 1$): A new cathode material for batteries of high energy density, *Mater. Res. Bull.* 15(6) (1980) 783-789.
- [13] J.O. Besenhard, The electrochemical preparation and properties of ionic alkali metal-and NR_4 -graphite intercalation compounds in organic electrolytes, *Carbon* 14(2) (1976) 111-115.
- [14] A. Yoshino, K. Sanechika, T. Nakajima, Secondary battery. JP patent 1989293, (1985).
- [15] M. Winter, B. Barnett, K. Xu, Before Li Ion Batteries, *Chem. Rev.* 118(23) (2018) 11433-11456.
- [16] R. Fong, U. von Sacken, J.R. Dahn, Studies of Lithium Intercalation into Carbons Using Nonaqueous Electrochemical Cells, *J. Electrochem. Soc.* 137(7) (1990) 2009-2013.
- [17] M. Fujimoto, N. Yoshinaga, K. Ueno, N. Furukawa, T. Nohma, M. Takahashi, Lithium secondary battery. US Patent 5686138, (1994).
- [18] D. Guyomard, J.M. Tarascon, Rechargeable $\text{Li}_{1+x}\text{Mn}_2\text{O}_4$ /Carbon Cells with a New Electrolyte Composition: Potentiostatic Studies and Application to Practical Cells, *J. Electrochem. Soc.* 140(11) (1993) 3071-3081.
- [19] D. Linden, T.B. Reddy, *Handbook of batteries*, McGraw-Hill, New York 3rd edition (2002).
- [20] K. Xu, Nonaqueous Liquid Electrolytes for Lithium-Based Rechargeable Batteries, *Chem. Rev.* 104(10) (2004) 4303-4418.
- [21] G. Pistoia, M. De Rossi, B. Scrosati, Study of the behavior of ethylene carbonate as a nonaqueous battery solvent, *J. Electrochem. Soc.* 117(4) (1970) 500-502.
- [22] J.M. Tarascon, D. Guyomard, New electrolyte compositions stable over the 0 to 5 V voltage range and compatible with the $\text{Li}_{1+x}\text{Mn}_2\text{O}_4$ /carbon Li-ion cells, *Solid State Ion.* 69(3) (1994) 293-305.
- [23] Y. Ein-Eli, S.R. Thomas, V. Koch, D. Aurbach, B. Markovsky, A. Schechter, Ethylmethylcarbonate, a Promising Solvent for Li-Ion Rechargeable Batteries, *J. Electrochem. Soc.* 143(12) (1996) L273-L277.
- [24] C. Nanjundiah, J.L. Goldman, L.A. Dominey, V.R. Koch, Electrochemical Stability of LiMF_6 ($M = \text{P}, \text{As}, \text{Sb}$) in Tetrahydrofuran and Sulfolane, *J. Electrochem. Soc.* 135(12) (1988) 2914-2917.
- [25] G.H. Newman, R.W. Francis, L.H. Gaines, B.M.L. Rao, Hazard Investigations of LiClO_4 / Dioxolane Electrolyte, *J. Electrochem. Soc.* 127(9) (1980) 2025-2027.

- [26] H. Yang, G.V. Zhuang, P.N. Ross, Thermal stability of LiPF₆ salt and Li-ion battery electrolytes containing LiPF₆, *J. Power Sources* 161(1) (2006) 573-579.
- [27] S.K. Heiskanen, J. Kim, B.L. Lucht, Generation and Evolution of the Solid Electrolyte Interphase of Lithium-Ion Batteries, *Joule* 3(10) (2019) 2322-2333.
- [28] S.S. Zhang, A review on electrolyte additives for lithium-ion batteries, *J. Power Sources* 162(2) (2006) 1379-1394.
- [29] Q. Zhou, W.A. Henderson, G.B. Appetecchi, M. Montanino, S. Passerini, Physical and Electrochemical Properties of N-Alkyl-N-methylpyrrolidinium Bis(fluorosulfonyl)imide Ionic Liquids: PY₁₃FSI and PY₁₄FSI, *J. Phys. Chem. B* 112(43) (2008) 13577-13580.
- [30] A. Lewandowski, A. Świdarska-Mocek, Ionic liquids as electrolytes for Li-ion batteries—An overview of electrochemical studies, *J. Power Sources* 194(2) (2009) 601-609.
- [31] R. Jarosova, G.M. Swain, Rapid Preparation of Room Temperature Ionic Liquids with Low Water Content as Characterized with a ta-C:N Electrode, *J. Electrochem. Soc.* 162(8) (2015) H507-H511.
- [32] H. Liu, L. Jiang, Wettability by Ionic Liquids, *Small* 12(1) (2016) 9-15.
- [33] K. Ueno, J. Murai, K. Ikeda, S. Tsuzuki, M. Tsuchiya, R. Tatara, T. Mandai, Y. Umebayashi, K. Dokko, M. Watanabe, Li⁺ Solvation and Ionic Transport in Lithium Solvate Ionic Liquids Diluted by Molecular Solvents, *J. Phys. Chem. C* 120(29) (2016) 15792-15802.
- [34] M. Marcinek, J. Syzdek, M. Marczewski, M. Piszcz, L. Niedzicki, M. Kalita, A. Plewa-Marczewska, A. Bitner, P. Wieczorek, T. Trzeciak, M. Kasprzyk, P. Łęzak, Z. Zukowska, A. Zalewska, W. Wieczorek, Electrolytes for Li-ion transport – Review, *Solid State Ion.* 276 (2015) 107-126.
- [35] J.W. Fergus, Ceramic and polymeric solid electrolytes for lithium-ion batteries, *J. Power Sources* 195(15) (2010) 4554-4569.
- [36] Y. Tominaga, V. Nanthana, D. Tohyama, Ionic conduction in poly(ethylene carbonate)-based rubbery electrolytes including lithium salts, *Polym. J.* 44(12) (1973) 1155-1158.
- [37] Z. Xue, D. He, X. Xie, Poly(ethylene oxide)-based electrolytes for lithium-ion batteries, *J. Mater. Chem. A* 3(38) (2015) 19218-19253.
- [38] W.A. Henderson, Crystallization Kinetics of Glyme–LiX and PEO–LiX Polymer Electrolytes, *Macromolecules* 40(14) (2007) 4963-4971.
- [39] K.M. Abraham, Z. Jiang, PEO-Like Polymer Electrolytes with High Room Temperature Conductivity, *J. Electrochem. Soc.* 144(6) (1997) L136-L138.
- [40] S. Seki, K. Takei, H. Miyashiro, M. Watanabe, Physicochemical and Electrochemical Properties of Glyme–LiN(SO₂F)₂ Complex for Safe Lithium-ion Secondary Battery Electrolyte, *J. Electrochem. Soc.* 158(6) (2011) A769.
- [41] J.C. Bachman, S. Muy, A. Grimaud, H.-H. Chang, N. Pour, S.F. Lux, O. Paschos, F. Maglia, S. Lupart, P. Lamp, L. Giordano, Y. Shao-Horn, Inorganic Solid-State Electrolytes for Lithium Batteries: Mechanisms and Properties Governing Ion Conduction, *Chem. Rev.* 116(1) (2016) 140-162.
- [42] A. Manthiram, X. Yu, S. Wang, Lithium battery chemistries enabled by solid-state electrolytes, *Nat. Rev. Mater.* 2(4) (2017) 16103.
- [43] A. Banerjee, X. Wang, C. Fang, E.A. Wu, Y.S. Meng, Interfaces and Interphases in All-Solid-State Batteries with Inorganic Solid Electrolytes, *Chem. Rev.* 120(14) (2020) 6878-6933.
- [44] C. Cao, Z.-B. Li, X.-L. Wang, X.-B. Zhao, W.-Q. Han, Recent Advances in Inorganic Solid Electrolytes for Lithium Batteries, *Front. Energy Res.* 2(25) (2014).
- [45] Y. Harada, T. Ishigaki, H. Kawai, J. Kuwano, Lithium ion conductivity of polycrystalline perovskite La_{0.67-x}Li_{3x}TiO₃ with ordered and disordered arrangements of the A-site ions, *Solid State Ion.* 108(1) (1998) 407-413.
- [46] O. Bohnke, C. Bohnke, J.L. Fourquet, Mechanism of ionic conduction and electrochemical intercalation of lithium into the perovskite lanthanum lithium titanate, *Solid State Ion.* 91(1) (1996) 21-31.

- [47] S. Stramare, V. Thangadurai, W. Weppner, Lithium Lanthanum Titanates: A Review, *Chem. Mater.* 15(21) (2003) 3974-3990.
- [48] H. Aono, E. Sugimoto, Y. Sadaoka, N. Imanaka, G.y. Adachi, The Electrical Properties of Ceramic Electrolytes for $\text{LiM}_x\text{Ti}_{2-x}(\text{PO}_4)_3+y\text{Li}_2\text{O}$, $\text{M} = \text{Ge}, \text{Sn}, \text{Hf}$, and Zr Systems, *J. Electrochem. Soc.* 140(7) (1993) 1827-1833.
- [49] G.F. Ortiz, M.C. López, P. Lavela, C. Vidal-Abarca, J.L. Tirado, Improved lithium-ion transport in NASICON-type lithium titanium phosphate by calcium and iron doping, *Solid State Ion.* 262 (2014) 573-577.
- [50] M.A. Subramanian, R. Subramanian, A. Clearfield, Lithium ion conductors in the system $\text{AB(IV)}_2(\text{PO}_4)_3$ ($\text{B} = \text{Ti}, \text{Zr}$ and Hf), *Solid State Ion.* 18-19 (1986) 562-569.
- [51] A. Kubanska, L. Castro, L. Tortet, O. Schäf, M. Dollé, R. Bouchet, Elaboration of controlled size $\text{Li}_{1.5}\text{Al}_{0.5}\text{Ge}_{1.5}(\text{PO}_4)_3$ crystallites from glass-ceramics, *Solid State Ion.* 266 (2014) 44-50.
- [52] R. Norhaniza, R.H.Y. Subban, N.S. Mohamed, Cr and V substituted $\text{LiSn}_2\text{P}_3\text{O}_{12}$ solid electrolyte materials, *J. Power Sources* 244 (2013) 300-305.
- [53] K. Arbi, M. Hoelzel, A. Kuhn, F. García-Alvarado, J. Sanz, Structural Factors That Enhance Lithium Mobility in Fast-Ion $\text{Li}_{1+x}\text{Ti}_{2-x}\text{Al}_x(\text{PO}_4)_3$ ($0 \leq x \leq 0.4$) Conductors Investigated by Neutron Diffraction in the Temperature Range 100–500 K, *Inorg. Chem.* 52(16) (2013) 9290-9296.
- [54] K. Arbi, M. Tabellout, M.G. Lazarraga, J.M. Rojo, J. Sanz, Non-Arrhenius conductivity in the fast lithium conductor $\text{Li}_{1.2}\text{Ti}_{1.8}\text{Al}_{0.2}(\text{PO}_4)_3$: A ^7Li NMR and electric impedance study, *Phys. Rev. B* 72(9) (2005) 094302.
- [55] M. Cretin, P. Fabry, Comparative study of lithium ion conductors in the system $\text{Li}_{1+x}\text{Al}_x\text{Al}_{2-x}\text{V}(\text{PO}_4)_3$ with $\text{AlV}=\text{Ti}$ or Ge and $0 \leq x \leq 0.7$ for use as Li^+ sensitive membranes, *J. Eur. Ceram. Soc.* 19(16) (1999) 2931-2940.
- [56] H. Aono, E. Sugimoto, Y. Sadaoka, N. Imanaka, G.y. Adachi, Ionic Conductivity of Solid Electrolytes Based on Lithium Titanium Phosphate, *J. Electrochem. Soc.* 137(4) (1990) 1023-1027.
- [57] A. Ramzy, V. Thangadurai, Tailor-Made Development of Fast Li Ion Conducting Garnet-Like Solid Electrolytes, *ACS Appl. Mater. Interfaces* 2(2) (2010) 385-390.
- [58] V. Thangadurai, S. Narayanan, D. Pinzaru, Garnet-type solid-state fast Li ion conductors for Li batteries: critical review, *Chem. Soc. Rev.* 43(13) (2014) 4714-4727.
- [59] Y. Deng, C. Eames, J.-N. Chotard, F. Lalère, V. Seznec, S. Emge, O. Pecher, C.P. Grey, C. Masquelier, M.S. Islam, Structural and Mechanistic Insights into Fast Lithium-Ion Conduction in $\text{Li}_4\text{SiO}_4\text{--Li}_3\text{PO}_4$ Solid Electrolytes, *J. Am. Chem. Soc.* 137(28) (2015) 9136-9145.
- [60] S.P. Ong, Y. Mo, W.D. Richards, L. Miara, H.S. Lee, G. Ceder, Phase stability, electrochemical stability and ionic conductivity of the $\text{Li}_{10\pm 1}\text{MP}_2\text{X}_{12}$ ($\text{M} = \text{Ge}, \text{Si}, \text{Sn}, \text{Al}$ or P , and $\text{X} = \text{O}, \text{S}$ or Se) family of superionic conductors, *Energy Environ. Sci.* 6(1) (2013) 148-156.
- [61] S. Wenzel, S.J. Sedlmaier, C. Dietrich, W.G. Zeier, J. Janek, Interfacial reactivity and interphase growth of argyrodite solid electrolytes at lithium metal electrodes, *Solid State Ion.* 318 (2018) 102-112.
- [62] R.P. Rao, N. Sharma, V.K. Peterson, S. Adams, Formation and conductivity studies of lithium argyrodite solid electrolytes using in-situ neutron diffraction, *Solid State Ion.* 230 (2013) 72-76.
- [63] S. Randau, D.A. Weber, O. Kötz, R. Koerver, P. Braun, A. Weber, E. Ivers-Tiffée, T. Adermann, J. Kulisch, W.G. Zeier, F.H. Richter, J. Janek, Benchmarking the performance of all-solid-state lithium batteries, *Nat. Energy* 5(3) (2020) 259-270.
- [64] A. Manthiram, A reflection on lithium-ion battery cathode chemistry, *Nat. Commun.* 11(1) (2020) 1550.
- [65] M.S. Whittingham, Chemistry of intercalation compounds: Metal guests in chalcogenide hosts, *Prog. Solid State Chem.* 12(1) (1978) 41-99.
- [66] J.B. Goodenough, Metallic oxides, *Prog. Solid State Chem.* 5 (1971) 145-399.
- [67] C. Delmas, C. Fouassier, P. Hagemuller, Structural classification and properties of the layered oxides, *Physica B+C* 99(1) (1980) 81-85.

- [68] Y. Lyu, X. Wu, K. Wang, Z. Feng, T. Cheng, Y. Liu, M. Wang, R. Chen, L. Xu, J. Zhou, Y. Lu, B. Guo, An Overview on the Advances of LiCoO₂ Cathodes for Lithium-Ion Batteries, *Adv. Energy Mater.* n/a(n/a) (2020) 2000982.
- [69] J. Molenda, A. Stokłosa, T. Bąk, Modification in the electronic structure of cobalt bronze Li_xCoO₂ and the resulting electrochemical properties, *Solid State Ion.* 36(1) (1989) 53-58.
- [70] L. Sun, Z. Zhang, X. Hu, H. Tian, Y. Zhang, X. Yang, Realization of Ti Doping by Electrostatic Assembly to Improve the Stability of LiCoO₂ Cycled to 4.5 V, *J. Electrochem. Soc.* 166(10) (2019) A1793-A1798.
- [71] J. Zheng, S. Myeong, W. Cho, P. Yan, J. Xiao, C. Wang, J. Cho, J.-G. Zhang, Li- and Mn-Rich Cathode Materials: Challenges to Commercialization, *Adv. Energy Mater.* 7(6) (2017) 1601284.
- [72] G.G. Amatucci, J.M. Tarascon, L.C. Klein, CoO₂, The End Member of the Li_xCoO₂ Solid Solution, *J. Electrochem. Soc.* 143(3) (1996) 1114-1123.
- [73] J. Molenda, J. Marzec, Functional cathode materials for Li-ion batteries - Part III: Potential cathode materials Li_xNi_{1-y-z}Co_yMn_zO₂ and LiMn₂O₄, *Funct. Mater. Lett.* 02(01) (2009) 1-7.
- [74] G.G. Amatucci, J.M. Tarascon, L.C. Klein, Cobalt dissolution in LiCoO₂-based non-aqueous rechargeable batteries, *Solid State Ion.* 83(1) (1996) 167-173.
- [75] J.-N. Zhang, Q. Li, Y. Wang, J. Zheng, X. Yu, H. Li, Dynamic evolution of cathode electrolyte interphase (CEI) on high voltage LiCoO₂ cathode and its interaction with Li anode, *Energy Stor. Mater.* 14 (2018) 1-7.
- [76] A. Jena, P.-H. Lee, W.K. Pang, K.-C. Hsiao, V.K. Peterson, T. Darwish, N. Yepuri, S.-H. Wu, H. Chang, R.-S. Liu, Monitoring the phase evolution in LiCoO₂ electrodes during battery cycles using in-situ neutron diffraction technique, *J. Chin. Chem. Soc.* 67(3) (2020) 344-352.
- [77] D. Lindsay, W. Kerr, Cobalt close-up, *Nat. Chem.* 3(6) (2011) 494-494.
- [78] I.Y.L. Hsieh, M.S. Pan, Y.-M. Chiang, W.H. Green, Learning only buys you so much: Practical limits on battery price reduction, *Appl. Energy* 239 (2019) 218-224.
- [79] T.A. Hewston, B.L. Chamberland, A Survey of first-row ternary oxides LiMO₂ (M = Sc-Cu), *J. Phys. Chem. Solids* 48(2) (1987) 97-108.
- [80] T. Ohzuku, A. Ueda, M. Nagayama, Y. Iwakoshi, H. Komori, Comparative study of LiCoO₂, LiNi₁₂Co₁₂O₂ and LiNiO₂ for 4 volt secondary lithium cells, *Electrochim. Acta* 38(9) (1993) 1159-1167.
- [81] M. Wentker, M. Greenwood, J. Leker, A bottom-up approach to lithium-ion battery cost modeling with a focus on cathode active materials, *Energies* 12(3) (2019) 504.
- [82] M.S. Whittingham, Lithium Batteries and Cathode Materials, *Chem. Rev.* 104(10) (2004) 4271-4302.
- [83] P. Kalyani, N. Kalaiselvi, Various aspects of LiNiO₂ chemistry: A review, *Sci. Technol. Adv. Mater.* 6(6) (2005) 689-703.
- [84] H. Arai, S. Okada, H. Ohtsuka, M. Ichimura, J. Yamaki, Characterization and cathode performance of Li_{1-x}Ni_{1+x}O₂ prepared with the excess lithium method, *Solid State Ion.* 80(3) (1995) 261-269.
- [85] H. Arai, S. Okada, Y. Sakurai, J.-i. Yamaki, Reversibility of LiNiO₂ cathode, *Solid State Ion.* 95(3) (1997) 275-282.
- [86] C. Delmas, J.P. Pérès, A. Rougier, A. Demourgues, F. Weill, A. Chadwick, M. Broussely, F. Perton, P. Biensan, P. Willmann, On the behavior of the Li_xNiO₂ system: an electrochemical and structural overview, *J. Power Sources* 68(1) (1997) 120-125.
- [87] K.-J. Park, M.-J. Choi, F. Maglia, S.-J. Kim, K.-H. Kim, C.S. Yoon, Y.-K. Sun, High-Capacity Concentration Gradient Li[Ni_{0.865}Co_{0.120}Al_{0.015}]O₂ Cathode for Lithium-Ion Batteries, *Adv. Energy Mater.* 8(19) (2018) 1703612.
- [88] K.D.R. Ekawati, A.P. Sholikah, C.S. Yudha, H. Widiyandari, A. Purwanto, Comparative Study of NCA Cathode Material Synthesis Methods towards Their Structure Characteristics, 2018 5th International Conference on Electric Vehicular Technology (ICEVT), 2018, pp. 57-61.

- [89] K. Ghatak, S. Basu, T. Das, V. Sharma, H. Kumar, D. Datta, Effect of cobalt content on the electrochemical properties and structural stability of NCA type cathode materials, *Phys. Chem. Chem. Phys.* 20(35) (2018) 22805-22817.
- [90] K.-J. Park, J.-Y. Hwang, H.-H. Ryu, F. Maglia, S.-J. Kim, P. Lamp, C.S. Yoon, Y.-K. Sun, Degradation Mechanism of Ni-Enriched NCA Cathode for Lithium Batteries: Are Microcracks Really Critical?, *ACS Energy Lett.* 4(6) (2019) 1394-1400.
- [91] R. Alcántara, P. Lavela, P.L. Relano, J.L. Tirado, E. Zhecheva, R. Stoyanova, X-ray Diffraction, EPR, and ^6Li and ^{27}Al MAS NMR Study of $\text{LiAlO}_2\text{-LiCoO}_2$ Solid Solutions, *Inorg. Chem.* 37(2) (1998) 264-269.
- [92] T. Ohzuku, A. Ueda, M. Kouguchi, Synthesis and Characterization of $\text{LiAl}_{1/4}\text{Ni}_{3/4}\text{O}_2$ (R3m) for Lithium-Ion (Shuttlecock) Batteries, *J. Electrochem. Soc.* 142(12) (1995) 4033-4039.
- [93] M. Jo, M. Noh, P. Oh, Y. Kim, J. Cho, A New High Power $\text{LiNi}_{0.81}\text{Co}_{0.1}\text{Al}_{0.09}\text{O}_2$ Cathode Material for Lithium-Ion Batteries, *Adv. Energy Mater.* 4(13) (2014) 1301583.
- [94] M. Guilmard, C. Poullierie, L. Croguennec, C. Delmas, Structural and electrochemical properties of $\text{LiNi}_{0.70}\text{Co}_{0.15}\text{Al}_{0.15}\text{O}_2$, *Solid State Ion.* 160(1) (2003) 39-50.
- [95] S. Madhavi, G.V. Subba Rao, B.V.R. Chowdari, S.F.Y. Li, Effect of aluminium doping on cathodic behaviour of $\text{LiNi}_{0.7}\text{Co}_{0.3}\text{O}_2$, *J. Power Sources* 93(1) (2001) 156-162.
- [96] S. Hwang, W. Chang, S.M. Kim, D. Su, D.H. Kim, J.Y. Lee, K.Y. Chung, E.A. Stach, Investigation of Changes in the Surface Structure of $\text{Li}_x\text{Ni}_{0.8}\text{Co}_{0.15}\text{Al}_{0.05}\text{O}_2$ Cathode Materials Induced by the Initial Charge, *Chem. Mater.* 26(2) (2014) 1084-1092.
- [97] S. Zheng, R. Huang, Y. Makimura, Y. Ukyo, C.A.J. Fisher, T. Hirayama, Y. Ikuhara, Microstructural Changes in $\text{LiNi}_{0.8}\text{Co}_{0.15}\text{Al}_{0.05}\text{O}_2$ Positive Electrode Material during the First Cycle, *J. Electrochem. Soc.* 158(4) (2011) A357.
- [98] X. Zeng, M. Li, D. Abd El-Hady, W. Alshitari, A.S. Al-Bogami, J. Lu, K. Amine, Commercialization of Lithium Battery Technologies for Electric Vehicles, *Adv. Energy Mater.* 9(27) (2019) 1900161.
- [99] H. Kim, M.G. Kim, H.Y. Jeong, H. Nam, J. Cho, A New Coating Method for Alleviating Surface Degradation of $\text{LiNi}_{0.6}\text{Co}_{0.2}\text{Mn}_{0.2}\text{O}_2$ Cathode Material: Nanoscale Surface Treatment of Primary Particles, *Nano Lett.* 15(3) (2015) 2111-2119.
- [100] D. Wang, W. Liu, X. Zhang, Y. Huang, M. Xu, W. Xiao, Review of Modified Nickel-Cobalt Lithium Aluminate Cathode Materials for Lithium-Ion Batteries, *Int. J. Photoenergy* 2019 (2019) 2730849.
- [101] Y. Li, H. Yu, Y. Hu, H. Jiang, C. Li, Surface-engineering of layered $\text{LiNi}_{0.815}\text{Co}_{0.15}\text{Al}_{0.035}\text{O}_2$ cathode material for high-energy and stable Li-ion batteries, *J. Energy Chem.* 27(2) (2018) 559-564.
- [102] S. Yoon, K.-N. Jung, S.-H. Yeon, C.S. Jin, K.-H. Shin, Electrochemical properties of $\text{LiNi}_{0.8}\text{Co}_{0.15}\text{Al}_{0.05}\text{O}_2$ -graphene composite as cathode materials for lithium-ion batteries, *J. Electroanal. Chem.* 683 (2012) 88-93.
- [103] Z. Xie, Y. Zhang, A. Yuan, J. Xu, Effects of lithium excess and SnO_2 surface coating on the electrochemical performance of $\text{LiNi}_{0.8}\text{Co}_{0.15}\text{Al}_{0.05}\text{O}_2$ cathode material for Li-ion batteries, *J. Alloys Compd.* 787 (2019) 429-439.
- [104] B.-S. Liu, X.-L. Sui, S.-H. Zhang, F.-D. Yu, Y. Xue, Y. Zhang, Y.-X. Zhou, Z.-B. Wang, Investigation on electrochemical performance of $\text{LiNi}_{0.8}\text{Co}_{0.15}\text{Al}_{0.05}\text{O}_2$ coated by heterogeneous layer of TiO_2 , *J. Alloys Compd.* 739 (2018) 961-971.
- [105] Z. Zhu, F. Cai, J. Yu, Improvement of electrochemical performance for AlF_3 -coated $\text{Li}_{1.3}\text{Mn}_{4/6}\text{Ni}_{1/6}\text{Co}_{1/6}\text{O}_{2.40}$ cathode materials for Li-ion batteries, *Ionics* 22(8) (2016) 1353-1359.
- [106] A. Kraytsberg, H. Drezner, M. Auinat, A. Shapira, N. Solomatin, P. Axmann, M. Wohlfahrt-Mehrens, Y. Ein-Eli, Atomic Layer Deposition of a Particularized Protective MgF_2 Film on a Li-Ion Battery $\text{LiMn}_{1.5}\text{Ni}_{0.5}\text{O}_4$ Cathode Powder Material, *ChemNanoMat* 1(8) (2015) 577-585.
- [107] Y.-M. Chung, K.-S. Ryu, Surface coating and electrochemical properties of $\text{LiNi}_{0.8}\text{Co}_{0.15}\text{Al}_{0.05}\text{O}_2$ polyaniline composites as an electrode for Li-ion batteries, *Bull. Korean Chem. Soc.* 30(8) (2009) 1733-1737.

- [108] W. Liu, G. Hu, K. Du, Z. Peng, Y. Cao, Q. Liu, Synthesis and characterization of LiCoO_2 -coated $\text{LiNi}_{0.8}\text{Co}_{0.15}\text{Al}_{0.05}\text{O}_2$ cathode materials, *Mater. Lett.* 83 (2012) 11-13.
- [109] J. Chen, L. Zhu, D. Jia, X. Jiang, Y. Wu, Q. Hao, X. Xia, Y. Ouyang, L. Peng, W. Tang, T. Liu, $\text{LiNi}_{0.8}\text{Co}_{0.15}\text{Al}_{0.05}\text{O}_2$ cathodes exhibiting improved capacity retention and thermal stability due to a lithium iron phosphate coating, *Electrochim. Acta* 312 (2019) 179-187.
- [110] D.Y. Wan, Z.Y. Fan, Y.X. Dong, E. Baasanjav, H.-B. Jun, B. Jin, E.M. Jin, S.M. Jeong, Effect of Metal (Mn, Ti) Doping on NCA Cathode Materials for Lithium Ion Batteries, *J. Nanomater.* 2018 (2018) 8082502.
- [111] Y.-Y. Wang, Y.-Y. Sun, S. Liu, G.-R. Li, X.-P. Gao, Na-Doped $\text{LiNi}_{0.8}\text{Co}_{0.15}\text{Al}_{0.05}\text{O}_2$ with Excellent Stability of Both Capacity and Potential as Cathode Materials for Li-Ion Batteries, *ACS Appl. Energy Mater.* 1(8) (2018) 3881-3889.
- [112] J. Zhao, Z. Wang, J. Wang, H. Guo, X. Li, W. Gui, N. Chen, G. Yan, Anchoring K^+ in Li^+ Sites of $\text{LiNi}_{0.8}\text{Co}_{0.15}\text{Al}_{0.05}\text{O}_2$ Cathode Material to Suppress its Structural Degradation During High-Voltage Cycling, *Energy Technol.* 6(12) (2018) 2358-2366.
- [113] L. Zhu, Y. Liu, W. Wu, X. Wu, W. Tang, Y. Wu, Surface fluorinated $\text{LiNi}_{0.8}\text{Co}_{0.15}\text{Al}_{0.05}\text{O}_2$ as a positive electrode material for lithium ion batteries, *J. Mater. Chem. A* 3(29) (2015) 15156-15162.
- [114] Y. Qi, Y. Huang, D. Jia, S.-J. Bao, Z.P. Guo, Preparation and characterization of novel spinel $\text{Li}_4\text{Ti}_5\text{O}_{12-x}\text{Br}_x$ anode materials, *Electrochim. Acta* 54(21) (2009) 4772-4776.
- [115] Y. Yan, Y.-X. Yin, S. Xin, Y.-G. Guo, L.-J. Wan, Ionothermal synthesis of sulfur-doped porous carbons hybridized with graphene as superior anode materials for lithium-ion batteries, *ChemComm* 48(86) (2012) 10663-10665.
- [116] R. Jung, M. Metzger, F. Maglia, C. Stinner, H.A. Gasteiger, Oxygen Release and Its Effect on the Cycling Stability of $\text{LiNi}_x\text{Mn}_y\text{Co}_z\text{O}_2$ (NMC) Cathode Materials for Li-Ion Batteries, *J. Electrochem. Soc.* 164(7) (2017) A1361-A1377.
- [117] O. Tsutomu, M. Yoshinari, Layered Lithium Insertion Material of $\text{LiCo}_{1/3}\text{Ni}_{1/3}\text{Mn}_{1/3}\text{O}_2$ for Lithium-Ion Batteries, *Chem. Lett.* 30(7) (2001) 642-643.
- [118] H.-J. Noh, S. Youn, C.S. Yoon, Y.-K. Sun, Comparison of the structural and electrochemical properties of layered $\text{Li}[\text{Ni}_x\text{Co}_y\text{Mn}_z]\text{O}_2$ ($x = 1/3, 0.5, 0.6, 0.7, 0.8$ and 0.85) cathode material for lithium-ion batteries, *J. Power Sources* 233 (2013) 121-130.
- [119] F. Lin, I.M. Markus, D. Nordlund, T.-C. Weng, M.D. Asta, H.L. Xin, M.M. Doeff, Surface reconstruction and chemical evolution of stoichiometric layered cathode materials for lithium-ion batteries, *Nat. Commun.* 5(1) (2014) 3529.
- [120] W. Hua, B. Schwarz, M. Knapp, A. Senyshyn, A. Missiul, X. Mu, S. Wang, C. Kübel, J.R. Binder, S. Indris, H. Ehrenberg, (De)Lithiation Mechanism of Hierarchically Layered $\text{LiNi}_{1/3}\text{Co}_{1/3}\text{Mn}_{1/3}\text{O}_2$ Cathodes during High-Voltage Cycling, *J. Electrochem. Soc.* 166(3) (2018) A5025-A5032.
- [121] S.-K. Jung, H. Gwon, J. Hong, K.-Y. Park, D.-H. Seo, H. Kim, J. Hyun, W. Yang, K. Kang, Understanding the Degradation Mechanisms of $\text{LiNi}_{0.5}\text{Co}_{0.2}\text{Mn}_{0.3}\text{O}_2$ Cathode Material in Lithium Ion Batteries, *Adv. Energy Mater.* 4(1) (2014) 1300787.
- [122] D. Goonetilleke, N. Sharma, W.K. Pang, V.K. Peterson, R. Petibon, J. Li, J.R. Dahn, Structural Evolution and High-Voltage Structural Stability of $\text{Li}(\text{Ni}_x\text{Mn}_y\text{Co}_z)\text{O}_2$ Electrodes, *Chem. Mater.* 31(2) (2019) 376-386.
- [123] W. Li, A. Dolocan, P. Oh, H. Celio, S. Park, J. Cho, A. Manthiram, Dynamic behaviour of interphases and its implication on high-energy-density cathode materials in lithium-ion batteries, *Nat. Commun.* 8(1) (2017) 14589.
- [124] S.-T. Myung, K. Izumi, S. Komaba, Y.-K. Sun, H. Yashiro, N. Kumagai, Role of Alumina Coating on Li-Ni-Co-Mn-O Particles as Positive Electrode Material for Lithium-Ion Batteries, *Chem. Mater.* 17(14) (2005) 3695-3704.
- [125] K. Liu, Q. Zhang, S. Dai, W. Li, X. Liu, F. Ding, J. Zhang, Synergistic Effect of F^- Doping and LiF Coating on Improving the High-Voltage Cycling Stability and Rate Capacity of

- LiNi_{0.5}Co_{0.2}Mn_{0.3}O₂ Cathode Materials for Lithium-Ion Batteries, *ACS Appl. Mater. Interfaces* 10(40) (2018) 34153-34162.
- [126] Z. Peng, G. Yang, F. Li, Z. Zhu, Z. Liu, Improving the cathode properties of Ni-rich LiNi_{0.6}Co_{0.2}Mn_{0.2}O₂ at high voltages under 5 C by Li₂SiO₃ coating and Si⁴⁺ doping, *J. Alloys Compd.* 762 (2018) 827-834.
- [127] M. Zhang, H. Zhao, M. Tan, J. Liu, Y. Hu, S. Liu, X. Shu, H. Li, Q. Ran, J. Cai, X. Liu, Yttrium modified Ni-rich LiNi_{0.8}Co_{0.1}Mn_{0.1}O₂ with enhanced electrochemical performance as high energy density cathode material at 4.5 V high voltage, *J. Alloys Compd.* 774 (2019) 82-92.
- [128] G. Sun, X. Yin, W. Yang, J. Zhang, Q. Du, Z. Ma, G. Shao, Z.-B. Wang, Synergistic effects of ion doping and surface-modifying for lithium transition-metal oxide: Synthesis and characterization of La₂O₃-modified LiNi_{1/3}Co_{1/3}Mn_{1/3}O₂, *Electrochim. Acta* 272 (2018) 11-21.
- [129] Y.-K. Sun, S.-T. Myung, B.-C. Park, J. Prakash, I. Belharouak, K. Amine, High-energy cathode material for long-life and safe lithium batteries, *Nat. Mater.* 8(4) (2009) 320-324.
- [130] Y.-K. Sun, Z. Chen, H.-J. Noh, D.-J. Lee, H.-G. Jung, Y. Ren, S. Wang, C.S. Yoon, S.-T. Myung, K. Amine, Nanostructured high-energy cathode materials for advanced lithium batteries, *Nat. Mater.* 11(11) (2012) 942-947.
- [131] D. Pasero, N. Reeves, V. Pralong, A.R. West, Oxygen Nonstoichiometry and Phase Transitions in LiMn_{1.5}Ni_{0.5}O_{4-δ}, *J. Electrochem. Soc.* 155(4) (2008) A282.
- [132] C.M. Julien, A. Mauger, Review of 5-V electrodes for Li-ion batteries: status and trends, *Ionics* 19(7) (2013) 951-988.
- [133] M.M. Thackeray, Spinel Electrodes for Lithium Batteries, *J. Am. Ceram. Soc.* 82(12) (1999) 3347-3354.
- [134] M.M. Thackeray, W.I.F. David, J.B. Goodenough, Structural characterization of the lithiated iron oxides Li_xFe₃O₄ and Li_xFe₂O₃ (0<x<2), *Mater. Res. Bull.* 17(6) (1982) 785-793.
- [135] M.M. Thackeray, W.I.F. David, P.G. Bruce, J.B. Goodenough, Lithium insertion into manganese spinels, *Mater. Res. Bull.* 18(4) (1983) 461-472.
- [136] M.Y. Song, D.S. Ahn, H.R. Park, Capacity fading of spinel phase LiMn₂O₄ with cycling, *J. Power Sources* 83(1) (1999) 57-60.
- [137] I. Taniguchi, D. Song, M. Wakihara, Electrochemical properties of LiM_{1/6}Mn_{11/6}O₄ (M = Mn, Co, Al and Ni) as cathode materials for Li-ion batteries prepared by ultrasonic spray pyrolysis method, *J. Power Sources* 109(2) (2002) 333-339.
- [138] L. Yunjian, L. Xinhai, G. Huajun, W. Zhixing, H. Qiyang, P. Wenjie, Y. Yong, Electrochemical performance and capacity fading reason of LiMn₂O₄/graphite batteries stored at room temperature, *J. Power Sources* 189(1) (2009) 721-725.
- [139] J. Vetter, P. Novák, M.R. Wagner, C. Veit, K.C. Möller, J.O. Besenhard, M. Winter, M. Wohlfahrt-Mehrens, C. Vogler, A. Hammouche, Ageing mechanisms in lithium-ion batteries, *J. Power Sources* 147(1) (2005) 269-281.
- [140] T. Ohzuku, M. Kitagawa, T. Hirai, Electrochemistry of Manganese Dioxide in Lithium Nonaqueous Cell: III. X-Ray Diffractational Study on the Reduction of Spinel-Related Manganese Dioxide, *J. Electrochem. Soc.* 137(3) (1990) 769-775.
- [141] M.M. Thackeray, Manganese oxides for lithium batteries, *Prog. Solid State Chem.* 25(1) (1997) 1-71.
- [142] M.M. Thackeray, Structural Considerations of Layered and Spinel Lithiated Oxides for Lithium Ion Batteries, *J. Electrochem. Soc.* 142(8) (1995) 2558-2563.
- [143] J.C. Hunter, Preparation of a new crystal form of manganese dioxide: λ-MnO₂, *J. Solid State Chem.* 39(2) (1981) 142-147.
- [144] O.K. Park, Y. Cho, S. Lee, H.-C. Yoo, H.-K. Song, J. Cho, Who will drive electric vehicles, olivine or spinel?, *Energy Environ. Sci.* 4(5) (2011) 1621-1633.
- [145] N.-S. Choi, J.-G. Han, S.-Y. Ha, I. Park, C.-K. Back, Recent advances in the electrolytes for interfacial stability of high-voltage cathodes in lithium-ion batteries, *RSC Adv.* 5(4) (2015) 2732-2748.

- [146] H.R. Morin, D.G. Graczyk, Y. Tsai, S. Lopykinski, H. Iddir, J.C. Garcia, N. Dietz Rago, S. Trask, L. Flores, S.-B. Son, Z. Zhang, N.M. Johnson, I. Bloom, Transition-Metal Dissolution from NMC-Family Oxides: A Case Study, *ACS Appl. Energy Mater.* 3(3) (2020) 2565-2575.
- [147] Y.K. Sun, K.J. Hong, J. Prakash, The Effect of ZnO Coating on Electrochemical Cycling Behavior of Spinel LiMn_2O_4 Cathode Materials at Elevated Temperature, *J. Electrochem. Soc.* 150(7) (2003) A970.
- [148] M.M. Thackeray, C.S. Johnson, J.S. Kim, K.C. Lauzze, J.T. Vaughey, N. Dietz, D. Abraham, S.A. Hackney, W. Zeltner, M.A. Anderson, ZrO_2 - and Li_2ZrO_3 -stabilized spinel and layered electrodes for lithium batteries, *Electrochem. Commun.* 5(9) (2003) 752-758.
- [149] J.S. Kim, C.S. Johnson, J.T. Vaughey, S.A. Hackney, K.A. Walz, W.A. Zeltner, M.A. Anderson, M.M. Thackeray, The Electrochemical Stability of Spinel Electrodes Coated with ZrO_2 , Al_2O_3 , and SiO_2 from Colloidal Suspensions, *J. Electrochem. Soc.* 151(10) (2004) A1755.
- [150] J. Cao, G. Cao, H. Yu, J. Xie, X. Zhao, Synthesis and electrochemical performance of YF_3 -coated LiMn_2O_4 cathode materials for Li-ion batteries, *Rare Met.* 30(1) (2011) 39-43.
- [151] J. Li, L. Wang, Q. Zhang, X. He, Electrochemical performance of SrF_2 -coated $\text{LiNi}_{1/3}\text{Co}_{1/3}\text{Mn}_{1/3}\text{O}_2$ cathode materials for Li-ion batteries, *J. Power Sources* 190(1) (2009) 149-153.
- [152] C. Qing, Y. Bai, J. Yang, W. Zhang, Enhanced cycling stability of LiMn_2O_4 cathode by amorphous FePO_4 coating, *Electrochim. Acta* 56(19) (2011) 6612-6618.
- [153] D. Liu, Z. He, X. Liu, Increased cycling stability of AlPO_4 -coated LiMn_2O_4 for lithium ion batteries, *Mater. Lett.* 61(25) (2007) 4703-4706.
- [154] C.H. Shen, R.S. Liu, R. Gundakaram, J.M. Chen, S.M. Huang, J.S. Chen, C.M. Wang, Effect of Co doping in LiMn_2O_4 , *J. Power Sources* 102(1) (2001) 21-28.
- [155] L. Xiao, Y. Zhao, Y. Yang, Y. Cao, X. Ai, H. Yang, Enhanced electrochemical stability of Al-doped LiMn_2O_4 synthesized by a polymer-pyrolysis method, *Electrochim. Acta* 54(2) (2008) 545-550.
- [156] A. Bhaskar, D. Mikhailova, N. Kiziltas-Yavuz, K. Nikolowski, S. Oswald, N.N. Bramnik, H. Ehrenberg, 3d-Transition metal doped spinels as high-voltage cathode materials for rechargeable lithium-ion batteries, *Prog. Solid State Chem.* 42(4) (2014) 128-148.
- [157] J.C. Arrebola, A. Caballero, L. Hernán, J. Morales, A high energy Li-ion battery based on nanosized $\text{LiNi}_{0.5}\text{Mn}_{1.5}\text{O}_4$ cathode material, *J. Power Sources* 183(1) (2008) 310-315.
- [158] R. Santhanam, B. Rambabu, Research progress in high voltage spinel $\text{LiNi}_{0.5}\text{Mn}_{1.5}\text{O}_4$ material, *J. Power Sources* 195(17) (2010) 5442-5451.
- [159] C. Li, H. Xiang, M. Xu, Y. Tang, L. Fang, Li_2AGeO_4 (A = Zn, Mg): Two novel low-permittivity microwave dielectric ceramics with olivine structure, *J. Eur. Ceram. Soc.* 38(4) (2018) 1524-1528.
- [160] A.K. Padhi, K.S. Nanjundaswamy, J.B. Goodenough, Phospho-olivines as Positive-Electrode Materials for Rechargeable Lithium Batteries, *J. Electrochem. Soc.* 144(4) (1997) 1188-1194.
- [161] A. Yamada, M. Hosoya, S.-C. Chung, Y. Kudo, K. Hinokuma, K.-Y. Liu, Y. Nishi, Olivine-type cathodes: Achievements and problems, *J. Power Sources* 119-121 (2003) 232-238.
- [162] G. Li, H. Azuma, M. Tohda, LiMnPO_4 as the Cathode for Lithium Batteries, *Electrochem. Solid-State Lett.* 5(6) (2002) A135.
- [163] A. Yamada, S.C. Chung, K. Hinokuma, Optimized LiFePO_4 for Lithium Battery Cathodes, *J. Electrochem. Soc.* 148(3) (2001) A224.
- [164] P. Guan, L. Zhou, Z. Yu, Y. Sun, Y. Liu, F. Wu, Y. Jiang, D. Chu, Recent progress of surface coating on cathode materials for high-performance lithium-ion batteries, *J. Energy Chem.* 43 (2020) 220-235.
- [165] V. Aravindan, J. Gnanaraj, Y.-S. Lee, S. Madhavi, LiMnPO_4 – A next generation cathode material for lithium-ion batteries, *J. Mater. Chem. A* 1(11) (2013) 3518-3539.

- [166] M.G. Fischer, X. Hua, B.D. Wilts, E. Castillo-Martínez, U. Steiner, Polymer-Templated LiFePO_4/C Nanonetworks as High-Performance Cathode Materials for Lithium-Ion Batteries, *ACS Appl. Mater. Interfaces* 10(2) (2018) 1646-1653.
- [167] M. Talebi-Esfandarani, O. Savadogo, Improvement of electrochemical and electrical properties of LiFePO_4 coated with citric acid, *Rare Met.* 35(4) (2016) 303-308.
- [168] C.-s. An, B. Zhang, L.-b. Tang, B. Xiao, J.-c. Zheng, Ultrahigh rate and long-life nano- LiFePO_4 cathode for Li-ion batteries, *Electrochim. Acta* 283 (2018) 385-392.
- [169] Z.-X. Chi, W. Zhang, F.-Q. Cheng, J.-T. Chen, A.-M. Cao, L.-J. Wan, Optimizing the carbon coating on LiFePO_4 for improved battery performance, *RSC Adv.* 4(15) (2014) 7795-7798.
- [170] K. Amine, Olivine LiCoPO_4 as 4.8 V Electrode Material for Lithium Batteries, *Electrochem. Solid-State Lett.* 3(4) (1999) 178.
- [171] S.-M. Oh, S.-W. Oh, C.-S. Yoon, B. Scrosati, K. Amine, Y.-K. Sun, High-Performance Carbon- LiMnPO_4 Nanocomposite Cathode for Lithium Batteries, *Adv. Funct. Mater.* 20(19) (2010) 3260-3265.
- [172] N.-H. Kwon, T. Drezen, I. Exnar, I. Teerlinck, M. Isono, M. Graetzel, Enhanced Electrochemical Performance of Mesoparticulate LiMnPO_4 for Lithium Ion Batteries, *Electrochem. Solid-State Lett.* 9(6) (2006) A277.
- [173] T. Drezen, N.-H. Kwon, P. Bowen, I. Teerlinck, M. Isono, I. Exnar, Effect of particle size on LiMnPO_4 cathodes, *J. Power Sources* 174(2) (2007) 949-953.
- [174] S.K. Martha, J. Grinblat, O. Haik, E. Zinigrad, T. Drezen, J.H. Miners, I. Exnar, A. Kay, B. Markovsky, D. Aurbach, $\text{LiMn}_{0.8}\text{Fe}_{0.2}\text{PO}_4$: An Advanced Cathode Material for Rechargeable Lithium Batteries, *Angew. Chem., Int. Ed.* 48(45) (2009) 8559-8563.
- [175] X. Zhang, M. Hou, A.G. Tamirate, H. Zhu, C. Wang, Y. Xia, Carbon coated nano-sized $\text{LiMn}_{0.8}\text{Fe}_{0.2}\text{PO}_4$ porous microsphere cathode material for Li-ion batteries, *J. Power Sources* 448 (2020) 227438.
- [176] W. Xu, J. Wang, F. Ding, X. Chen, E. Nasybulin, Y. Zhang, J.-G. Zhang, Lithium metal anodes for rechargeable batteries, *Energy Environ. Sci.* 7(2) (2014) 513-537.
- [177] Y.S. Cohen, Y. Cohen, D. Aurbach, Micromorphological Studies of Lithium Electrodes in Alkyl Carbonate Solutions Using in Situ Atomic Force Microscopy, *J. Phys. Chem. B* 104(51) (2000) 12282-12291.
- [178] R. Huggins, *Advanced batteries: Materials science aspects*, Springer US (2009).
- [179] S.-H. Yu, S.H. Lee, D.J. Lee, Y.-E. Sung, T. Hyeon, Conversion Reaction-Based Oxide Nanomaterials for Lithium Ion Battery Anodes, *Small* 12(16) (2016) 2146-2172.
- [180] N.A. Kaskhedikar, J. Maier, Lithium Storage in Carbon Nanostructures, *Adv. Mater.* 21(25-26) (2009) 2664-2680.
- [181] Z.X. Shu, R.S. McMillan, J.J. Murray, Electrochemical Intercalation of Lithium into Graphite, *J. Electrochem. Soc.* 140(4) (1993) 922-927.
- [182] B.J. Marsden, G.N. Hall, A.N. Jones, 4.13 - Graphite in Gas-Cooled Reactors ☆, in: R.J.M. Konings, R.E. Stoller (Eds.), *Comprehensive Nuclear Materials (Second Edition)*, Elsevier, Oxford, 2020, pp. 357-421.
- [183] T.P. Kumar, T.S.D. Kumari, M. Stéphan, Carbonaceous anode materials for lithium-ion batteries - the road ahead, *J. Indian Inst. Sci.* 89 (2012) 393-424.
- [184] M. Winter, J.O. Besenhard, M.E. Spahr, P. Novák, Insertion Electrode Materials for Rechargeable Lithium Batteries, *Adv. Mater.* 10(10) (1998) 725-763.
- [185] X.Y. Song, K. Kinoshita, T.D. Tran, Microstructural Characterization of Lithiated Graphite, *J. Electrochem. Soc.* 143(6) (1996) L120-L123.
- [186] Y. Yamada, A. Yamada, Review—Superconcentrated Electrolytes for Lithium Batteries, *J. Electrochem. Soc.* 162(14) (2015) A2406-A2423.
- [187] K. Xu, A. von Cresce, Interfacing electrolytes with electrodes in Li ion batteries, *J. Mater. Chem.* 21(27) (2011) 9849-9864.

- [188] D. Aurbach, Y. Ein-Eli, B. Markovsky, A. Zaban, S. Luski, Y. Carmeli, H. Yamin, The Study of Electrolyte Solutions Based on Ethylene and Diethyl Carbonates for Rechargeable Li Batteries: II. Graphite Electrodes, *J. Electrochem. Soc.* 142(9) (1995) 2882-2890.
- [189] C. Uhlmann, J. Illig, M. Ender, R. Schuster, E. Ivers-Tiffée, In situ detection of lithium metal plating on graphite in experimental cells, *J. Power Sources* 279 (2015) 428-438.
- [190] Y. Nishi, Lithium ion secondary batteries; past 10 years and the future, *J. Power Sources* 100(1) (2001) 101-106.
- [191] Y. Liu, J.S. Xue, T. Zheng, J.R. Dahn, Mechanism of lithium insertion in hard carbons prepared by pyrolysis of epoxy resins, *Carbon* 34(2) (1996) 193-200.
- [192] F. Beguin, E. Frackowiak, *Carbons for electrochemical energy storage and conversion systems*, CRC Press (2009).
- [193] H.B. Wang, Q. Yu, J. Qu, Synthesis of phosphorus-doped soft carbon as anode materials for lithium and sodium ion batteries, *Russ. J. Phys. Chem. A* 91(6) (2017) 1152-1155.
- [194] N. Loeffler, D. Bresser, S. Passerini, M. Copley, Secondary lithium-ion battery anodes: from first commercial batteries to recent research activities, *Johnson Matthey Technol. Rev.* 59(1) (2015) 34-44.
- [195] V. Aravindan, Y.-S. Lee, R. Yazami, S. Madhavi, TiO₂ polymorphs in 'rocking-chair' Li-ion batteries, *Mater. Today* 18(6) (2015) 345-351.
- [196] V. Aravindan, Y.-S. Lee, S. Madhavi, Research Progress on Negative Electrodes for Practical Li-Ion Batteries: Beyond Carbonaceous Anodes, *Adv. Energy Mater.* 5(13) (2015) 1402225.
- [197] R. Mo, Z. Lei, K. Sun, D. Rooney, Facile Synthesis of Anatase TiO₂ Quantum-Dot/Graphene-Nanosheet Composites with Enhanced Electrochemical Performance for Lithium-Ion Batteries, *Adv. Mater.* 26(13) (2014) 2084-2088.
- [198] Y.-Q. Wang, L. Gu, Y.-G. Guo, H. Li, X.-Q. He, S. Tsukimoto, Y. Ikuhara, L.-J. Wan, Rutile-TiO₂ Nanocoating for a High-Rate Li₄Ti₅O₁₂ Anode of a Lithium-Ion Battery, *J. Am. Chem. Soc.* 134(18) (2012) 7874-7879.
- [199] T.-F. Yi, S.-Y. Yang, Y. Xie, Recent advances of Li₄Ti₅O₁₂ as a promising next generation anode material for high power lithium-ion batteries, *J. Mater. Chem. A* 3(11) (2015) 5750-5777.
- [200] M. Wagemaker, E.R.H. van Eck, A.P.M. Kentgens, F.M. Mulder, Li-Ion Diffusion in the Equilibrium Nanomorphology of Spinel Li_{4+x}Ti₅O₁₂, *J. Phys. Chem. B* 113(1) (2009) 224-230.
- [201] B.-N. Yun, H.L. Du, J.-Y. Hwang, H.-G. Jung, Y.-K. Sun, Improved electrochemical performance of boron-doped carbon-coated lithium titanate as an anode material for sodium-ion batteries, *J. Mater. Chem. A* 5(6) (2017) 2802-2810.
- [202] K. Zaghib, M. Simoneau, M. Armand, M. Gauthier, Electrochemical study of Li₄Ti₅O₁₂ as negative electrode for Li-ion polymer rechargeable batteries, *J. Power Sources* 81-82 (1999) 300-305.
- [203] S. Bach, J.P. Pereira-Ramos, N. Baffier, Electrochemical properties of sol-gel Li_{4/3}Ti_{5/3}O₄, *J. Power Sources* 81-82 (1999) 273-276.
- [204] Y.H. Rho, K. Kanamura, Li⁺ ion diffusion in Li₄Ti₅O₁₂ thin film electrode prepared by PVP sol-gel method, *J. Solid State Chem.* 177(6) (2004) 2094-2100.
- [205] B. Yan, M. Li, X. Li, Z. Bai, J. Yang, D. Xiong, D. Li, Novel understanding of carbothermal reduction enhancing electronic and ionic conductivity of Li₄Ti₅O₁₂ anode, *J. Mater. Chem. A* 3(22) (2015) 11773-11781.
- [206] Z. Zhang, G. Li, H. Peng, K. Chen, Hierarchical hollow microspheres assembled from N-doped carbon coated Li₄Ti₅O₁₂ nanosheets with enhanced lithium storage properties, *J. Mater. Chem. A* 1(48) (2013) 15429-15434.
- [207] H. Li, L. Shen, X. Zhang, J. Wang, P. Nie, Q. Che, B. Ding, Nitrogen-doped carbon coated Li₄Ti₅O₁₂ nanocomposite: Superior anode materials for rechargeable lithium ion batteries, *J. Power Sources* 221 (2013) 122-127.
- [208] Z. Zhu, F. Cheng, J. Chen, Investigation of effects of carbon coating on the electrochemical performance of Li₄Ti₅O₁₂/C nanocomposites, *J. Mater. Chem. A* 1(33) (2013) 9484-9490.

- [209] H. Shim, S. Arnold, Ö. Budak, M. Ulbricht, P. Srimuk, V. Presser, Hybrid Anodes of Lithium Titanium Oxide and Carbon Onions for Lithium-Ion and Sodium-Ion Energy Storage, *Energy Technol.* n/a(n/a) (2020) 2000679.
- [210] Y. Sun, S. Jiang, W. Bi, C. Wu, Y. Xie, Highly ordered lamellar V₂O₃-based hybrid nanorods towards superior aqueous lithium-ion battery performance, *J. Power Sources* 196(20) (2011) 8644-8650.
- [211] D. McNulty, D.N. Buckley, C. O'Dwyer, V₂O₃ Polycrystalline Nanorod Cathode Materials for Li-Ion Batteries with Long Cycle Life and High Capacity Retention, *ChemElectroChem* 4(8) (2017) 2037-2044.
- [212] Ö. Budak, P. Srimuk, A. Tolosa, S. Fleischmann, J. Lee, S.W. Hieke, A. Frank, C. Scheu, V. Presser, Vanadium (III) Oxide/Carbon Core/Shell Hybrids as an Anode for Lithium-Ion Batteries, *Batteries Supercaps* 2(1) (2019) 74-82.
- [213] W.-J. Zhang, Lithium insertion/extraction mechanism in alloy anodes for lithium-ion batteries, *J. Power Sources* 196(3) (2011) 877-885.
- [214] Y. Hamon, T. Brousse, F. Jousse, P. Topart, P. Buvat, D.M. Schleich, Aluminum negative electrode in lithium ion batteries, *J. Power Sources* 97-98 (2001) 185-187.
- [215] D. Chang, H. Huo, K.E. Johnston, M. Ménétrier, L. Monconduit, C.P. Grey, A. Van der Ven, Elucidating the origins of phase transformation hysteresis during electrochemical cycling of Li–Sb electrodes, *J. Mater. Chem. A* 3(37) (2015) 18928-18943.
- [216] R.A. Huggins, Lithium alloy negative electrodes, *J. Power Sources* 81-82 (1999) 13-19.
- [217] W.-J. Zhang, A review of the electrochemical performance of alloy anodes for lithium-ion batteries, *J. Power Sources* 196(1) (2011) 13-24.
- [218] N. Nitta, G. Yushin, High-Capacity Anode Materials for Lithium-Ion Batteries: Choice of Elements and Structures for Active Particles, *Part. Part. Syst. Charact.* 31(3) (2014) 317-336.
- [219] N. Nitta, F. Wu, J.T. Lee, G. Yushin, Li-ion battery materials: present and future, *Mater. Today* 18(5) (2015) 252-264.
- [220] X. Zuo, J. Zhu, P. Müller-Buschbaum, Y.-J. Cheng, Silicon based lithium-ion battery anodes: A chronicle perspective review, *Nano Energy* 31 (2017) 113-143.
- [221] C.J. Wen, R.A. Huggins, Chemical diffusion in intermediate phases in the lithium-silicon system, *J. Solid State Chem.* 37(3) (1981) 271-278.
- [222] M.T. McDowell, S.W. Lee, W.D. Nix, Y. Cui, 25th Anniversary Article: Understanding the Lithiation of Silicon and Other Alloying Anodes for Lithium-Ion Batteries, *Adv. Mater.* 25(36) (2013) 4966-4985.
- [223] C.-M. Park, J.-H. Kim, H. Kim, H.-J. Sohn, Li-alloy based anode materials for Li secondary batteries, *Chem. Soc. Rev.* 39(8) (2010) 3115-3141.
- [224] S.D. Beattie, M.J. Loveridge, M.J. Lain, S. Ferrari, B.J. Polzin, R. Bhagat, R. Dashwood, Understanding capacity fade in silicon based electrodes for lithium-ion batteries using three electrode cells and upper cut-off voltage studies, *J. Power Sources* 302 (2016) 426-430.
- [225] X. Su, Q. Wu, J. Li, X. Xiao, A. Lott, W. Lu, B.W. Sheldon, J. Wu, Silicon-Based Nanomaterials for Lithium-Ion Batteries: A Review, *Adv. Energy Mater.* 4(1) (2014) 1300882.
- [226] C.K. Chan, H. Peng, G. Liu, K. McIlwrath, X.F. Zhang, R.A. Huggins, Y. Cui, High-performance lithium battery anodes using silicon nanowires, *Nat. Nanotechnol.* 3(1) (2008) 31-35.
- [227] J.-Y. Li, Q. Xu, G. Li, Y.-X. Yin, L.-J. Wan, Y.-G. Guo, Research progress regarding Si-based anode materials towards practical application in high energy density Li-ion batteries, *Mater. Chem. Front.* 1(9) (2017) 1691-1708.
- [228] S. Li, J. Niu, Y.C. Zhao, K.P. So, C. Wang, C.A. Wang, J. Li, High-rate aluminium yolk-shell nanoparticle anode for Li-ion battery with long cycle life and ultrahigh capacity, *Nat. Commun.* 6(1) (2015) 7872.
- [229] A.J. McAlister, The Al–Li (Aluminum–Lithium) system, *Bulletin of Alloy Phase Diagrams* 3(2) (1982) 177-183.

- [230] S.P. Kuksenko, Aluminum foil as anode material of lithium-ion batteries: Effect of electrolyte compositions on cycling parameters, *Russ. J. Electrochem.* 49(1) (2013) 67-75.
- [231] X. Chang, Z. Xie, Z. Liu, X. Zheng, J. Zheng, X. Li, Aluminum: An underappreciated anode material for lithium-ion batteries, *Energy Stor. Mater.* 25 (2020) 93-99.
- [232] S. Chatterjee, Titania–germanium nanocomposite for photo-thermo-electric application, *Nanotechnology* 19(26) (2008) 265701.
- [233] P.R. Abel, A.M. Chockla, Y.-M. Lin, V.C. Holmberg, J.T. Harris, B.A. Korgel, A. Heller, C.B. Mullins, Nanostructured $\text{Si}_{(1-x)}\text{Ge}_x$ for Tunable Thin Film Lithium-Ion Battery Anodes, *ACS Nano* 7(3) (2013) 2249-2257.
- [234] J. He, Y. Wei, T. Zhai, H. Li, Antimony-based materials as promising anodes for rechargeable lithium-ion and sodium-ion batteries, *Mater. Chem. Front.* 2(3) (2018) 437-455.
- [235] C. Lupu, J.-G. Mao, J.W. Rabalais, A.M. Guloy, J.W. Richardson, X-ray and Neutron Diffraction Studies on “ $\text{Li}_{4.4}\text{Sn}$ ”, *Inorg. Chem.* 42(12) (2003) 3765-3771.
- [236] A. Darwiche, C. Marino, M.T. Sougrati, B. Fraise, L. Stievano, L. Monconduit, Better Cycling Performances of Bulk Sb in Na-Ion Batteries Compared to Li-Ion Systems: An Unexpected Electrochemical Mechanism, *J. Am. Chem. Soc.* 134(51) (2012) 20805-20811.
- [237] H. Hou, M. Jing, Y. Yang, Y. Zhu, L. Fang, W. Song, C. Pan, X. Yang, X. Ji, Sodium/Lithium Storage Behavior of Antimony Hollow Nanospheres for Rechargeable Batteries, *ACS Appl. Mater. Interfaces* 6(18) (2014) 16189-16196.
- [238] L. Fan, J. Zhang, J. Cui, Y. Zhu, J. Liang, L. Wang, Y. Qian, Electrochemical performance of rod-like Sb–C composite as anodes for Li-ion and Na-ion batteries, *J. Mater. Chem. A* 3(7) (2015) 3276-3280.
- [239] Y. Lu, L. Yu, X.W. Lou, Nanostructured Conversion-type Anode Materials for Advanced Lithium-Ion Batteries, *Chem* 4(5) (2018) 972-996.
- [240] L. Aymard, Y. Oumellal, J.-P. Bonnet, Metal hydrides: an innovative and challenging conversion reaction anode for lithium-ion batteries, *J. Nanotechnol.* 6 (2015) 1821-1839.
- [241] M.D. Bhatt, J.Y. Lee, High capacity conversion anodes in Li-ion batteries: A review, *Int. J. Hydrog. Energy* 44(21) (2019) 10852-10905.
- [242] A.S. ARICÒ, P. BRUCE, B. SCROSATI, J.-M. TARASCON, W.V. SCHALKWIJK, Nanostructured materials for advanced energy conversion and storage devices, *Materials for Sustainable Energy 2005*, pp. 366-377.
- [243] H. Groult, S. Neveu, S. Leclerc, A.G. Porras-Gutierrez, C.M. Julien, A. Tressaud, E. Durand, N. Penin, C. Labrugere, Nano- CoF_3 prepared by direct fluorination with F_2 gas: Application as electrode material in Li-ion battery, *J. Fluor. Chem.* 196 (2017) 117-127.
- [244] S. Chong, Y. Chen, W. Yan, S. Guo, Q. Tan, Y. Wu, T. Jiang, Y. Liu, Suppressing capacity fading and voltage decay of Li-rich layered cathode material by a surface nano-protective layer of CoF_2 for lithium-ion batteries, *J. Power Sources* 332 (2016) 230-239.
- [245] B. Lu, Y. Song, Q. Zhang, J. Pan, Y.-T. Cheng, J. Zhang, Voltage hysteresis of lithium ion batteries caused by mechanical stress, *Phys. Chem. Chem. Phys.* 18(6) (2016) 4721-4727.
- [246] G. Chen, L. Yan, H. Luo, S. Guo, Nanoscale Engineering of Heterostructured Anode Materials for Boosting Lithium-Ion Storage, *Adv. Mater.* 28(35) (2016) 7580-7602.
- [247] D. Bresser, E. Paillard, P. Niehoff, S. Krueger, F. Mueller, M. Winter, S. Passerini, Challenges of “Going Nano”: Enhanced Electrochemical Performance of Cobalt Oxide Nanoparticles by Carbothermal Reduction and In Situ Carbon Coating, *ChemPhysChem* 15(10) (2014) 2177-2185.
- [248] L. Li, R. Jacobs, P. Gao, L. Gan, F. Wang, D. Morgan, S. Jin, Origins of Large Voltage Hysteresis in High-Energy-Density Metal Fluoride Lithium-Ion Battery Conversion Electrodes, *J. Am. Chem. Soc.* 138(8) (2016) 2838-2848.
- [249] X. Zhu, Y. Zhu, S. Murali, M.D. Stoller, R.S. Ruoff, Nanostructured Reduced Graphene Oxide/ Fe_2O_3 Composite As a High-Performance Anode Material for Lithium Ion Batteries, *ACS Nano* 5(4) (2011) 3333-3338.

- [250] L. Zhang, H.B. Wu, S. Madhavi, H.H. Hng, X.W. Lou, Formation of Fe₂O₃ Microboxes with Hierarchical Shell Structures from Metal–Organic Frameworks and Their Lithium Storage Properties, *J. Am. Chem. Soc.* 134(42) (2012) 17388-17391.
- [251] H.S. Kim, Y. Piao, S.H. Kang, T. Hyeon, Y.-E. Sung, Uniform hematite nanocapsules based on an anode material for lithium ion batteries, *Electrochem. Commun.* 12(3) (2010) 382-385.
- [252] M.V. Reddy, T. Yu, C.H. Sow, Z.X. Shen, C.T. Lim, G.V. Subba Rao, B.V.R. Chowdari, α -Fe₂O₃ Nanoflakes as an Anode Material for Li-Ion Batteries, *Adv. Funct. Mater.* 17(15) (2007) 2792-2799.
- [253] S.H. Lee, S.-H. Yu, J.E. Lee, A. Jin, D.J. Lee, N. Lee, H. Jo, K. Shin, T.-Y. Ahn, Y.-W. Kim, H. Choe, Y.-E. Sung, T. Hyeon, Self-Assembled Fe₃O₄ Nanoparticle Clusters as High-Performance Anodes for Lithium Ion Batteries via Geometric Confinement, *Nano Lett.* 13(9) (2013) 4249-4256.
- [254] J. Luo, J. Liu, Z. Zeng, C.F. Ng, L. Ma, H. Zhang, J. Lin, Z. Shen, H.J. Fan, Three-Dimensional Graphene Foam Supported Fe₃O₄ Lithium Battery Anodes with Long Cycle Life and High Rate Capability, *Nano Lett.* 13(12) (2013) 6136-6143.
- [255] Y. Li, C. Zhu, T. Lu, Z. Guo, D. Zhang, J. Ma, S. Zhu, Simple fabrication of a Fe₂O₃/carbon composite for use in a high-performance lithium ion battery, *Carbon* 52 (2013) 565-573.
- [256] S. Petnikota, S.K. Marka, A. Banerjee, M.V. Reddy, V.V.S.S. Srikanth, B.V.R. Chowdari, Graphothermal reduction synthesis of ‘exfoliated graphene oxide/iron (II) oxide’ composite for anode application in lithium ion batteries, *J. Power Sources* 293 (2015) 253-263.
- [257] J. Cabana, L. Monconduit, D. Larcher, M.R. Palacín, Beyond Intercalation-Based Li-Ion Batteries: The State of the Art and Challenges of Electrode Materials Reacting Through Conversion Reactions, *Adv. Mater.* 22(35) (2010) E170-E192.
- [258] H. Jiang, Y. Hu, S. Guo, C. Yan, P.S. Lee, C. Li, Rational Design of MnO/Carbon Nanopeapods with Internal Void Space for High-Rate and Long-Life Li-Ion Batteries, *ACS Nano* 8(6) (2014) 6038-6046.
- [259] H. Wang, L.-F. Cui, Y. Yang, H. Sanchez Casalongue, J.T. Robinson, Y. Liang, Y. Cui, H. Dai, Mn₃O₄–Graphene Hybrid as a High-Capacity Anode Material for Lithium Ion Batteries, *J. Am. Chem. Soc.* 132(40) (2010) 13978-13980.
- [260] X. Yang, K. Fan, Y. Zhu, J. Shen, X. Jiang, P. Zhao, S. Luan, C. Li, Electric Papers of Graphene-Coated Co₃O₄ Fibers for High-Performance Lithium-Ion Batteries, *ACS Appl. Mater. Interfaces* 5(3) (2013) 997-1002.
- [261] F.D. Wu, Y. Wang, Self-assembled echinus-like nanostructures of mesoporous CoO nanorod@CNT for lithium-ion batteries, *J. Mater. Chem.* 21(18) (2011) 6636-6641.
- [262] M.V. Reddy, G.V. Subba Rao, B.V.R. Chowdari, Metal Oxides and Oxysalts as Anode Materials for Li Ion Batteries, *Chem. Rev.* 113(7) (2013) 5364-5457.
- [263] G. KICKELBICK, Introduction to Hybrid Materials, *Hybrid Materials2006*, pp. 1-48.
- [264] C. Draxl, D. Nabok, K. Hannelwald, Organic/Inorganic Hybrid Materials: Challenges for ab Initio Methodology, *Acc. Chem. Res.* 47(11) (2014) 3225-3232.
- [265] S. Fleischmann, A. Tolosa, V. Presser, Design of Carbon/Metal Oxide Hybrids for Electrochemical Energy Storage, *Chem. Eur. J.* 24(47) (2018) 12143-12153.
- [266] J.E. Ritchie, Electronic and Electrochemical Applications of Hybrid Materials, *Hybrid Materials2006*, pp. 401-432.
- [267] M. Kerlau, M. Marcinek, V. Srinivasan, R.M. Kostecki, Reprint of “Studies of local degradation phenomena in composite cathodes for lithium-ion batteries”, *Electrochim. Acta* 53(3) (2007) 1385-1392.
- [268] J.J. Vilatela, D. Eder, Nanocarbon Composites and Hybrids in Sustainability: A Review, *ChemSusChem* 5(3) (2012) 456-478.
- [269] G.V. Zhuang, G. Chen, J. Shim, X. Song, P.N. Ross, T.J. Richardson, Li₂CO₃ in LiNi_{0.8}Co_{0.15}Al_{0.05}O₂ cathodes and its effects on capacity and power, *J. Power Sources* 134(2) (2004) 293-297.

- [270] M. Kerlau, R. Kostecky, Interfacial Impedance Study of Li-Ion Composite Cathodes during Aging at Elevated Temperatures, *J. Electrochem. Soc.* 153(9) (2006) A1644.
- [271] H. Wang, H. Dai, Strongly coupled inorganic–nano-carbon hybrid materials for energy storage, *Chem. Soc. Rev.* 42(7) (2013) 3088-3113.
- [272] W.-D. Zhang, B. Xu, L.-C. Jiang, Functional hybrid materials based on carbon nanotubes and metal oxides, *J. Mater. Chem.* 20(31) (2010) 6383-6391.
- [273] Y. Liang, Y. Li, H. Wang, J. Zhou, J. Wang, T. Regier, H. Dai, Co_3O_4 nanocrystals on graphene as a synergistic catalyst for oxygen reduction reaction, *Nat. Mater.* 10(10) (2011) 780-786.
- [274] Y. Liang, H. Wang, J. Zhou, Y. Li, J. Wang, T. Regier, H. Dai, Covalent Hybrid of Spinel Manganese–Cobalt Oxide and Graphene as Advanced Oxygen Reduction Electrocatalysts, *J. Am. Chem. Soc.* 134(7) (2012) 3517-3523.
- [275] Y. Liang, H. Wang, P. Diao, W. Chang, G. Hong, Y. Li, M. Gong, L. Xie, J. Zhou, J. Wang, T.Z. Regier, F. Wei, H. Dai, Oxygen Reduction Electrocatalyst Based on Strongly Coupled Cobalt Oxide Nanocrystals and Carbon Nanotubes, *J. Am. Chem. Soc.* 134(38) (2012) 15849-15857.
- [276] A.K. Rai, L.T. Anh, J. Gim, V. Mathew, J. Kang, B.J. Paul, J. Song, J. Kim, Simple synthesis and particle size effects of TiO_2 nanoparticle anodes for rechargeable lithium ion batteries, *Electrochim. Acta* 90 (2013) 112-118.
- [277] H. Wang, Y. Yang, Y. Liang, L.-F. Cui, H.S. Casalongue, Y. Li, G. Hong, Y. Cui, $\text{LiMn}_{1-x}\text{Fe}_x\text{PO}_4$ nanorods grown on graphene sheets for ultrahigh-rate-performance lithium ion batteries, *Angewandte Chemie* 123 (2011) 7502-7506.
- [278] L. Li, Z. Guo, A. Du, H. Liu, Rapid microwave-assisted synthesis of Mn_3O_4 –graphene nanocomposite and its lithium storage properties, *J. Mater. Chem.* 22(8) (2012) 3600-3605.
- [279] N. Liu, Z. Lu, J. Zhao, M.T. McDowell, H.-W. Lee, W. Zhao, Y. Cui, A pomegranate-inspired nanoscale design for large-volume-change lithium battery anodes, *Nat. Nanotechnol.* 9(3) (2014) 187-192.
- [280] Q. Yun, X. Qin, W. Lv, Y.-B. He, B. Li, F. Kang, Q.-H. Yang, “Concrete” inspired construction of a silicon/carbon hybrid electrode for high performance lithium ion battery, *Carbon* 93 (2015) 59-67.